OPEN ACCESS

University of BRISTOL

This electronic thesis or dissertation has been downloaded from Explore Bristol Research, http://research-information.bristol.ac.uk

Author:
Denman, Thomas R

Title:
Collisions of Super-Earth and Sub-Neptune Planets.

General rights
Access to the thesis is subject to the Creative Commons Attribution - NonCommercial-No Derivatives 4.0 International Public License. A copy of this may be found at https://creativecommons.org/licenses/by-nc-nd/4.0/legalcode This license sets out your rights and the restrictions that apply to your access to the thesis so it is important you read this before proceeding.

Take down policy
Some pages of this thesis may have been removed for copyright restrictions prior to having it been deposited in Explore Bristol Research. However, if you have discovered material within the thesis that you consider to be unlawful e.g. breaches of copyright (either yours or that of a third party) or any other law, including but not limited to those relating to patent, trademark, confidentiality, data protection, obscenity, defamation, libel, then please contact collections-metadata@bristol.ac.uk and include the following information in your message:

• Your contact details
• Bibliographic details for the item, including a URL
• An outline nature of the complaint

Your claim will be investigated and, where appropriate, the item in question will be removed from public view as soon as possible.

Collisions of Super-Earth and Sub-Neptune Planets.

Thomas Denman

A thesis submitted to the University of Bristol
in accordance with the requirements of the degree of
Doctor of Philosophy
in the Faculty of Science

School of Physics,
H.H. Wills Physics Laboratory,
Tyndall Avenue,
Bristol,
BS8 1TL

October 2021

$\sim 50,000$ words

Abstract

More than half of the planets so far discovered have masses between Earth and Neptune. These 'Super-Earth' planets have a wide array of densities. These planets are sufficiently massive to be able to accrete significant low density hydrogen atmospheres during formation. Post-formation they may experience density enriching erosive processes. One such erosive process is collision. After proto-planetary disc dissipation planet orbits can become unstable, leading to a period of giant impacts. These collisions preferentially eject lighter material, increasing the planet's density.

An example of a system with planets which experienced collisional density enrichment is Kepler-107. Kepler-107c is substantially denser than its closer orbiting neighbour Kepler-107b ($12.65\,\mathrm{g\,cm^{-1}}$ as opposed to $5.3\,\mathrm{g\,cm^{-1}}$), despite probable similar formation environments. Other erosive phenomena, e.g. photo-evaporation, are unlikely as they would affect Kepler-107b more strongly. In chapter 3 of this thesis I present simulations that show collisions can produce Kepler-107c's enriched density.

In the rest of this thesis I examine more general simulations of Super-Earth collisions, focusing specifically on atmospheres. I show the boundary between planets merging together and bouncing off one another strongly correlates with the escape velocity from the point of closest approach. In general I find, while it requires little energy to cause some of the atmosphere to be ejected, total atmosphere ejection requires sufficient energy that the collision will also eject a significant fraction of mantle. Due to the ease of atmosphere removal, I find that all simulated collisions result in a change in both mass and composition, resulting in a corresponding increase in final planet density.

These results underline the importance of giant impacts in explaining the observed Super-Earth density diversity.

Acknowledgements

I thank my supervisors Zoë Leinhardt & Phil Carter, for all the great help and advice they have given me over the course of my PhD. I also thank Christoph Mordasini for his help with dealing with atmospheres. Thanks to Rhys Morris for helping me out whenever I had tech related difficulties. I thank my parents for all the love and support they have given to get me to this stage. Finally I thank Mia Mace and Crispin Logan for keeping me sane during the long hours in the office.

This work was carried out using the computational facilities of the Advanced Computing Research Centre, University of Bristol - http://www.bristol.ac.uk/acrc/. I acknowledges support from an STFC studentship (grant number: ST/R504634/1). This research has made use of NASA's Astrophysics Data System. Much of my analysis also made extensive use of the python libraries: matplotlib, numpy, and scipy.

Declaration

I declare that the work in this dissertation was carried out in accordance with the Regulations of the University of Bristol. This work is original except where indicated by special reference in the text and no part of the dissertation has been submitted for any other degree. Any views expressed in the dissertation are those of the author and in no way represent those of the University of Bristol. The dissertation has not been presented to any other university for examination either in the United Kingdom or overseas.

I note here any contributions to the work from collaborators for each of the individual chapters.

Chapter 3 – Atmosphere-Less Collisions-The Kepler-107 System – This chapter was based on simulations and analysis that I contributed to the paper "A giant impact as the likely origin of different twins in the Kepler-107 exoplanet system" (Bonomo, A.S., Zeng, L., Damasso, M., Leinhardt, Z., ..., Denman, T. et al. A giant impact as the likely origin of different twins in the Kepler-107 exoplanet system. Nat Astron 3, 416–423 (2019). https://doi.org/10.1038/s41550-018-0684-9). The observational data from this paper came from the HARPS-N collaboration. Isocomposition contours were generated by L. Zeng. My contribution to the paper was running, analysing and summarising SPH simulations to test the collision hypothesis. This chapter is a more detailed discussion of the simulations I ran for this paper.

Chapter 4 – Head-On Collisions – This chapter is a paper I have written (Thomas R Denman, Zoë M. Leinhardt, Philip J Carter, Christoph Mordasini, Atmosphere loss in planet–planet collisions, Monthly Notices of the Royal Astronomical Society, Volume 496, Issue 2, August 2020, Pages 1166–1181, https://doi.org/10.1093/mnras/staa1623). Initial atmosphere fractions and atmosphere profiles were provided by C. Mordasini. The modifications to GADGET-2

to model hydrogen atmospheres were done by P. Carter. Simulations, analysis and writing were done by me.
Chapter 5 – Oblique Collisions – This chapter is a paper I have submitted to MNRAS (Thomas R. Denman, Zoë M. Leinhardt and Philip J. Carter, Atmosphere Loss in Oblique Super-Earth Collisions). All major components of the paper, including simulations, analysis and writing were done by me.

Thomas Denman
October 2021

Contents

List of Figures

List of Tables

1

Introduction

The study of exoplanets is a rapidly expanding field. In the quarter of a century since the first confirmed exoplanet was detected orbiting a main sequence star in 1995 more than 4000 planets have been so far detected (4472 as of 19/08/21). Many of the planets we have detected have no close analogues in our own solar system, for example we have detected an abundance of planets of masses that lie between that of Earth and Neptune. These are typically called Super-Earths, although they are sometimes referred to as Sub-Neptunes if they have thick atmospheres. The large diversity of different densities in this mass range implies they must not all form in the same way.

This thesis focuses on one particular planetary formation process that is believed to be a cause for this diversity in density: giant collisions between planets which occur in the late stages of a solar system's formation. In particular it looks at the effect of collisions on Super-Earth mass planets with thick atmospheres of masses $\sim 1\,\mathrm{M}_{\oplus}$.

1.1 Planet Detection

At the time of writing 4472 exoplanets have so far been detected according to the NASA exoplanet archive NASA (2021). Since the first detection in 1995 (Mayor & Queloz, 1995) many new methods have been developed to detect exoplanets. The proportion of

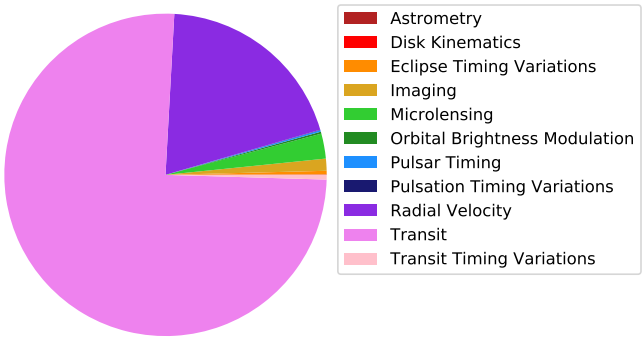

Figure 1.1: The relative proportions of different verified planet detections by each method according to the NASA exoplanet archive (19/08/21. NASA 2021).

exoplanets detected by each method is given by figure 1.1. The most successful exoplanet detection methods so far are as follows:

- Direct Imaging: The easiest method to conceptualise, direct imaging requires high resolution imaging to image directly the light reflected by the planet from the central star. High resolution requirements mean this method works best when the planet orbits at a large separation from the star and is large enough to reflect more of the incident light.
- Radial Velocity: This is the method that produced the first confirmed exoplanet observations. A star's orbit about the combined centre of mass of it and its orbiting planets will cause light from it to be doppler shifted from higher to lower to higher frequencies as the planets orbit about it. Higher mass closer planets cause larger wobbles and thus are easier to detect.
- Microlensing: When one star passes in front of another, gravitational lensing will bend light from the star behind it making the combined object appear brighter, this increase and then decrease in intensity creating a characteristic curve that can be observed. The same process occurs with planets but to a much lesser extent due to their lower masses. If a star with a planet passes in front of another star we would expect both intensity curves to be overlaid on one another. Due to gravitational lensing's dependence on mass this method is better at detecting larger planets.
- Transits: When an orbiting planet passes in front of its host star it will block some of the light from it, the amount of light blocked being proportional to the planets radius.

To confirm the detection is a planet multiple repeat detections are required, the time between them being the planets orbital period. These requirements of an observable decrease in light and multiple detections mean this method is most successful at detecting large short period planets.

The two graphs of figure 1.2 compare measured parameters for all currently discovered planets. The top graph shows planet mass compared to radius. Most detected planets (including those in our own solar system) are distributed around a single mass-radius relation, for masses below $100\,M_\oplus$ there is a positive relation between mass and radius with an obvious steepening at $2\,M_\oplus$, beyond $100\,M_\oplus$ the median radius begins a shallow decline with increasing mass. This well defined mass radius relation implies a consistency in formation materials and processes for all exoplanets. The initial steepening is thought to be due to planets being large enough to accrete significant hydrogen atmospheres as they are forming from the proto-planetary disc. The later downturn on the other hand is due to the planets being sufficiently massive that they reach electron degeneracy pressure. The spread of densities about this main mass-radius relation implies that some formation processes are system dependant.

The bottom graph in figure 1.2 shows planet masses and semi-major axes, displaying in colour the different detection methods used to observe them. Few planets have been discovered in the same parameter space as our solar system so far, larger closer orbiting planets are easier to detect with most modern methods, however, so this is likely because of the current limits on each detection method.

The success of the transit method in detecting exoplanets (helped in no small part by dedicated space telescopes such as Kepler) has meant the detection of a large number (2610 by 19/08/21 NASA (2021)) of planets of masses between Earth's and Neptune's unlike any detected in our own solar system. These planets are typically called either Super-Earth's or Sub-Neptune's depending on how high their atmosphere fraction is. Of these Super-Earths 2498 have been discovered orbiting at $a < 1\,\text{au}$.

Considering this proliferation of observations of close-orbiting Super-Earth mass planets, how they form is a topic of much active research.

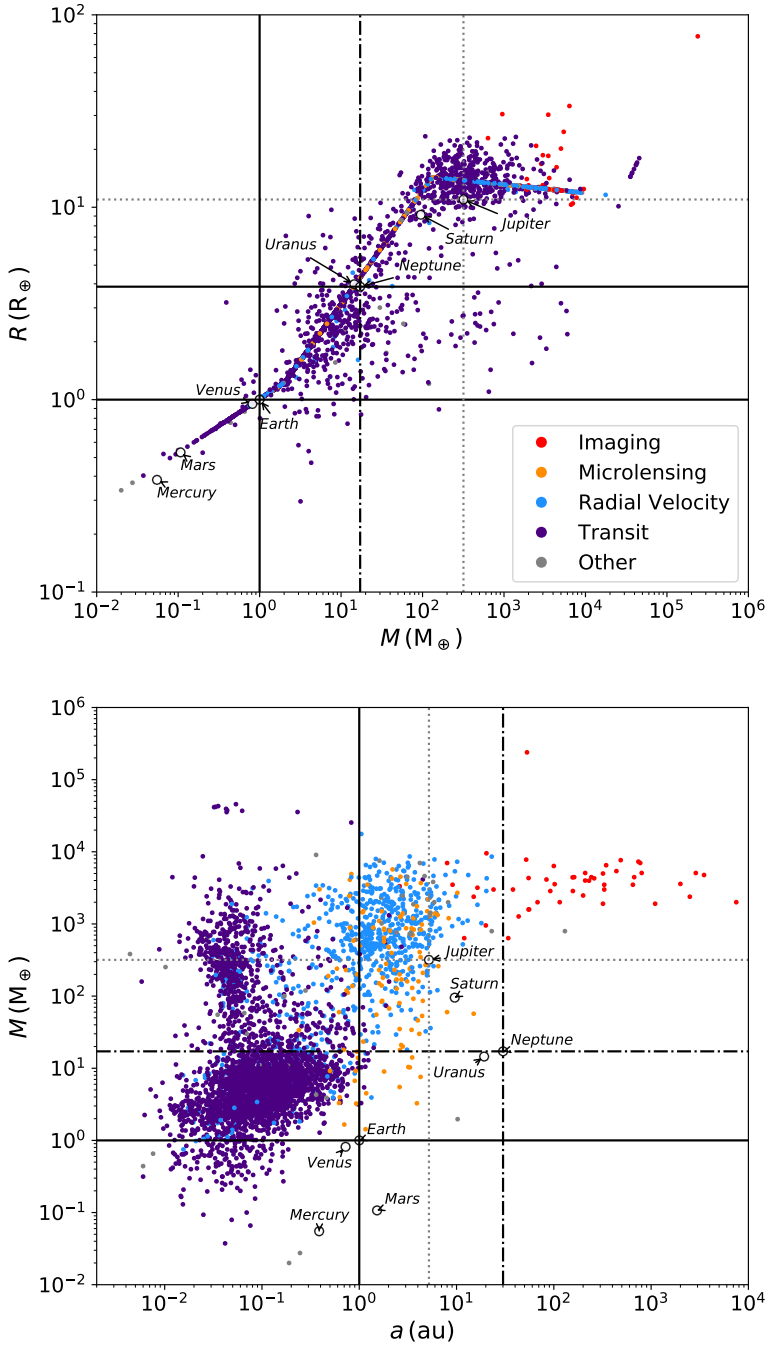

Figure 1.2: Top: Planet mass compared with radius Bottom: Exoplanet mass compared with semi-major axis of its orbit about its host star, compared with solar system planets. This illustrates each methods biases towards detection of a particular type of planet. Solid lines are show the values for Earth for each parameter, dash-dotted for Neptune, and dotted Jupiter. All data obtained from the NASA exoplanet archive (19/08/21).

1.2 Planetary Formation

I shall focus here mostly on the processes in Super-Earth formation as the majority of collisions I consider are between Super-Earths.

1.2.1 Protoplanetary discs

Planet formation begins with the formation of a star. As a star forms material falling into it tends to create a disc due to conservation of angular momentum. It is from this proto-planetary disc that planets form. The main constituents of a proto-planetary disc are gas and dust. The majority of the opacity of the disc is due to dust, and it is thus the easier component to observe despite only forming a small fraction of the initial disc's mass. Assuming it starts with the same composition as the interstellar medium, the main constituent of dust should be silicate grains which start with sizes $\lesssim 0.1\,\mu$m (Draine, 2003). Gas on the other hand initially forms a much greater percentage of the disc's mass, but it is more difficult to detect as emission from gas molecules occurs at set frequencies and so high resolution spectroscopy is required to identify it (Williams & Cieza, 2011). The main constituent gas is H_2. Figure 1.3 shows a series of cross-sectional diagrams of the proto-planetary disc and how it is theorised to evolve over time.

The simplest way to model the proto-planetary disc is the viscous disc model. In this model angular momentum is transported through the disc by its viscosity. Inner parts of the disc, which under Keplerian motion move faster than outer material, exert a positive frictional torque on material external to it accelerating it and vice versa. This overall torque on the disc is negative meaning that the motion of gas is typically sub-Keplerian.

In this model it is assumed that the disc is in a steady state, i.e. the mass flow is constant independent of orbital distance. Under this assumption it can be shown that the gas will flow inwards at a radial velocity v_r of

$$v_\mathrm{r} = -\frac{3}{2}\frac{\nu}{r} \tag{1.1}$$

where r is the orbital distance and ν the viscosity (Raymond & Morbidelli, 2020). The vertical height of a steady state disc can be calculated by comparing the gravitational and pressure forces above and below the mid-plane. Because pressure is dependent on temperature, which itself is dependent on both irradiation of the disc from the central

star and viscous mixing, we end up with discs with scale heights that increase slowly initially at small radii, but flare out at large radii (Dullemond et al., 2007).

The viscous accretion model is a good first order estimate for the physics of discs, but it has many flaws. For example only infinite discs can truly follow steady state accretion, so the approximation only really works particularly well for the inner disc (Lynden-Bell & Pringle, 1974). Another issue is that the molecular viscosity of the gas is multiple orders of magnitude too low to account for disc viscosity and the right conditions for such viscosity to be generated by turbulence only occur in the higher temperatures of the inner disc. Another potential disc model is that of a wind dominated disc (Bai & Stone, 2013; Bai, 2013).

The motion of the gas about the central star is sub-Keplerian small dust particles are carried along by the gas due to their large surface areas compared to their mass. When grains collide and coagulate this effect lessens and they decouple from the gas disc. They still experience a strong drag force from it however which causes grains to settle towards the mid-plane, further increasing grain growth (Williams & Cieza, 2011). These growing grains are the first steps towards planet formation.

1.2.2 Planetesimal Formation and Growth

Observations show that the lifetimes of proto-planetary discs are typically in the region of a few Myrs (Haisch, Jr. et al., 2001), for planets to form quick enough to accrete substantial atmospheres from the disc they therefore need to grow in size from dust by many orders of magnitude very rapidly.

The solid material in the proto-planetary disc starts off as sub-micron to cm sized dust. When such material collides with similar mass objects, if the collision is slow enough, it will stick together. This sticking velocity is material dependent, it is lower for silicates than it is for ices for example, potentially indicating faster building of objects beyond the 'snow line' of a proto-planetary disc where material becomes cold enough for ices to condense out. Blum & Wurm (2008) give an in depth review of these processes.

When objects reach the order of cm − m in size, growth processes are less well understood. We know that growth of this sized objects must be very quick because, as they grow larger, they steadily become uncoupled from the gas disc. Their motion can be described as Keplerian plus gas drag, which results in them rapidly spiralling towards the

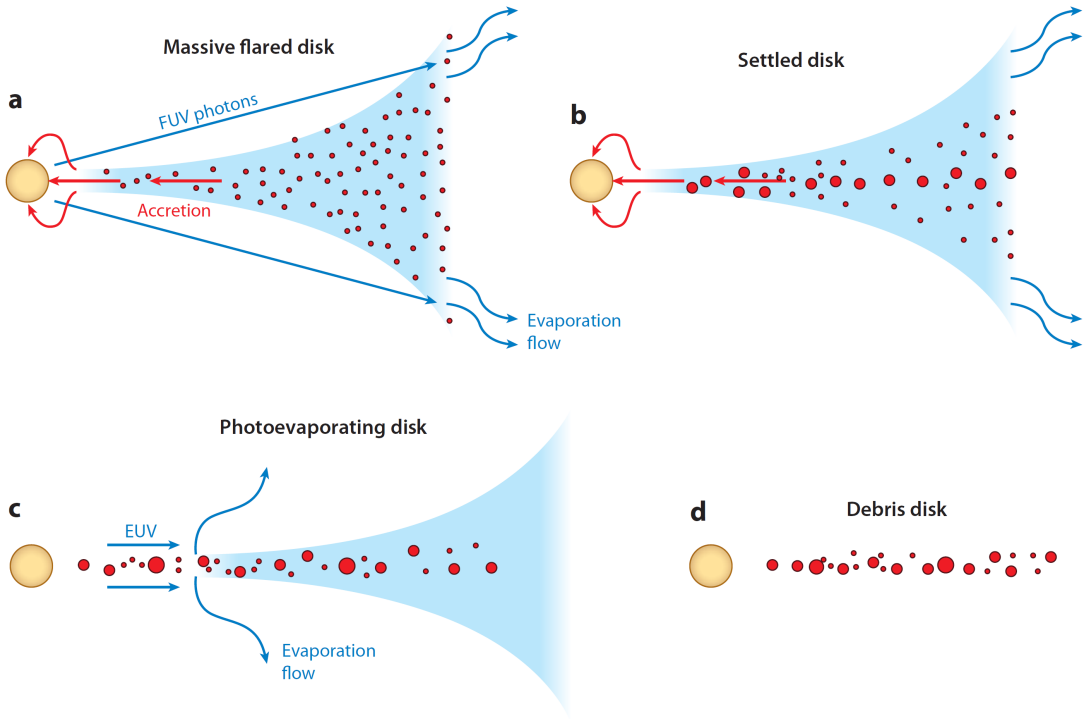

Figure 1.3: A series of diagrams showing the structure of a protoplanetary disc and how it evolves (Williams & Cieza, 2011). Initially the disc forms from material accreting onto the forming star, some photo-evaporation occurs generating an outer limit, but it is not enough to overpower the accretion rate. As time progresses dust particles coagulate and settle down towards the mid-plane. The accretion rate onto the central star eventually slows, once it has become sufficiently slow that photo-evaporation can overpower it the disc is evaporated away from the inner disc outwards. Eventually we are left with a disc of planets and planetary embryos, these continue to collide and scatter with one another until we are left with a system of planets that is stable for long time periods.

central star (Armitage, 2007). From experiment however, we know that vacuum collisions of cm sized objects at the expected velocities however should be disruptive (Blum et al., 2000). There are multiple possible methods by which this bouncing boundary can be increased or bypassed such as invoking special conditions such as sticky organic materials (Kouchi et al., 2002), aerodynamic re-accretion (Wurm et al., 2001) or electromagnetic attraction (Blum & Wurm, 2008), to fully account for the very rapid growth required to turn material at this scale into planetesimal mass objects, however, we need to invoke some other process.

One promising growth process is 'streaming instability' first proposed in Youdin & Goodman (2005), this is a process in which any overdensity of dust particles will heat up the gas at that radius causing it to rotate at closer to Keplerian speeds, meaning the dust at that overdense point will experience less drag. Less drag means it will spiral inwards slower. This slowing of inward migration in turn causes the overdense region to grow in density as more and more material from greater radii conglomerates at this 'speed bump'. Overall this process becomes a positive feedback loop which can create areas of higher dust density which are sufficiently high that they can cause large planetesimal mass objects to form from dust and larger material via self-gravitation.

Once an object has reached km scale or larger it is known as a planetesimal. Planetesimals continue to grow via collisions, their mass is sufficiently great that their collision cross section is increased by a gravitational focusing factor:

$$F_{\mathrm{g}} = 1 - \frac{v_{\mathrm{esc}}^2}{v_{\mathrm{rel}}^2} \tag{1.2}$$

(Safronov, 1972). v_{rel} is the relative velocity of the two objects in a collision and v_{esc} is their mutual escape velocity:

$$v_{\mathrm{esc}} = \sqrt{\frac{2G\left(M_1 + M_2\right)}{\left(R_1 + R_2\right)}}, \tag{1.3}$$

where M_1 and M_2 are the masses of the two objects and R_1 and R_2 their radii.

When a planetesimal is growing quickly in comparison to others, its increasing mass will increase the escape velocity compared to the average relative velocity, and this sets up a positive feedback loop of increasing mass. This process is known as runaway growth (Wetherill & Stewart, 1989). When approaching objects scatter without colliding however their relative velocities are excited such that on the next approach they will be

roughly at the escape velocity. This scattering process is what eventually stops the runaway growth regime. For runaway growth to occur the majority of the solid material in the disc needs to be in small planetesimals, some formation routes, such as streaming instability may therefore bypass this stage.

Once $v_{\mathrm{esc}} \approx v_{\mathrm{rel}}$, we enter the oligarchic growth regime (Kokubo & Ida, 1998, 2000). Unlike runaway growth in this regime growth rate slows with increasing mass. As such we would expect the masses of protoplanets in this regime to converge to similar values. In practice what simulations of this regime observe are higher mass 'oligarchs' embedded roughly equidistantly in the planetesimal disc. The remaining planetesimals are typically smaller by a few orders of magnitude and their orbits are excited to high eccentricities by close encounters with the oligarchs.

Runaway followed by oligarchic growth can explain the masses of terrestrial planets, but it is potentially not quick enough to grow planets large enough to accrete substantial atmospheres while the gas disc is still present, like Super-Earths and giant planets are thought to (Morbidelli et al., 2015). This is true even if we assume that they formed outside the snow line where there is a large increase in solids due to ices condensing out.

The method by which these planets are proposed to grow to such a size so rapidly is via hydrodynamically assisted accretion of much smaller objects, this process is known as 'pebble accretion' (Ormel & Klahr, 2010). When material passes within the gravitational influence of a planet embedded in the proto-planetary disc, the drag force from the gas lowers its momentum and makes it less likely to escape. The collision cross section for pebble accretion can be significantly larger than that for planetesimal accretion because gas drag has a stronger effect on smaller objects with lower momenta. This can induce a very rapid growth in mass of the planetesimal, as pebbles will be continuously drifting inwards into a planetesimals path until the gas disc dissipates. An in depth discussion of this process is given in Johansen & Lambrechts (2017). Pebble accretion stops at the 'pebble isolation mass' which occurs when the core becomes large enough to create a pressure bump which will attenuate the flux of pebbles arriving from greater orbital distances. Although turbulent mixing can cause some inwards transfer of dust (Weber et al., 2018) this pressure bump also puts a stop to pebble accretion for planets orbiting interior to the planet causing it. Bitsch et al. (2018) discuss the relation of this isolation mass to various disc parameters.

1.2.3 Orbital Migration

Planet orbits are not static, and there are multiple reasons why they can change over time, such as gravitational interactions with other planets or passing stars. The interaction between a planet and the protoplanetary disc is in general complex and beyond the scope of this work, so I shall briefly summarise the important results for Super-Earth mass planets. The most important orbital migration method for terrestrial and Super-Earth mass planets is 'type I' migration.

Type I migration occurs due to the spiral density wave a planet will create in the protoplanetary disc as it orbits through it. Gravitational interactions between this spiral density wave and the planet will apply a torque to the planet affecting its motion. Material internal to the planet's orbit causes a positive torque, whereas material external causes a negative torque. For a typical rotationally symmetric protoplanetary disc with a density that is a power law function of distance from the star the negative torque is stronger which will result in inward migration (Ward, 1986) at a rate that dependent is on the planets mass. Higher mass planets migrate quicker than low mass ones. For a full analytic description of this process see Paardekooper et al. (2010) and Paardekooper et al. (2011).

There are other potential processes for orbital migration of planets, planets large enough to generate a gap in the proto-planetary disc around their orbit can undergo 'type II' migration. Here the significant torques on the planet caused by the steep density gradients at the edge of the gap cause the planet's migration to be governed by the motion of the gas within the disc. This motion can be inwards or outwards depending on whether the disc is expanding or contracting, for a steady disc far from any other boundaries it will cause an inward migration at a rate of $v_{\mathrm{r}} = -3\nu/2r$, where ν is a measure of disc viscosity. This only happens for planets of masses large enough to generate a disc gap, which is only true for planets on the scale of Jupiter, as such it is not typically an important process for Super-Earths.

Considering that both types of migration typically cause inwards movement of orbiting planets, what stops them from spiralling all the way into the central star? For type I migration if the disc density increases as radius does sufficiently rapidly then the positive torque can overpower the external torque, such a location is know as a 'planet trap' (Masset et al., 2006). These planet traps occur at local density maxima, and at

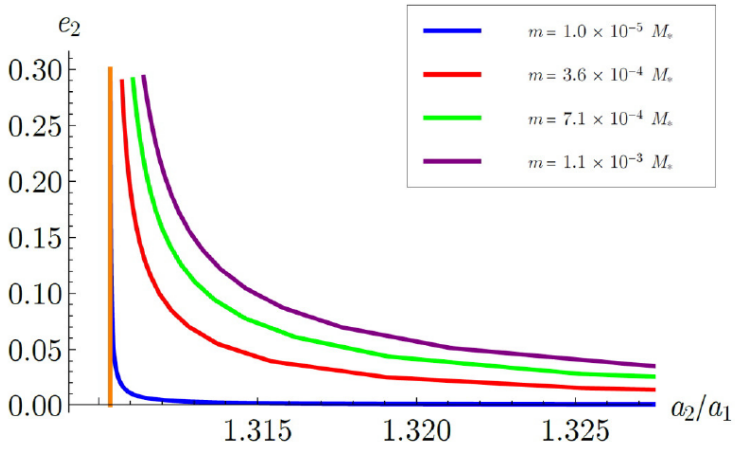

Figure 1.4: The equilibrium eccentricities for the 3:2 resonance for different mass planets migrating towards resonance with another planet of equal mass. The more massive the planets are, the wider the resonance is. Figure 13 from Raymond & Morbidelli (2020).

the outer edges of any gaps in the disc. A planet's orbital evolution once it has reached a planet trap then becomes tied with the evolution of the gas disc in a similar fashion to type II migration (Lyra et al., 2010; Paardekooper et al., 2010). Another important process by which a planet's inward migration can be paused is if it gets trapped in mean motion resonance with another planet.

1.2.4 Resonant trapping

As the planets migrate inwards, they often get trapped in resonant orbits with one another, this can lead to long resonant chains of multiple planets. The simplest type of orbital resonance is mean motion resonance, this occurs when the ratio of the two planets period of orbit, P, is close to the ratio of small integer numbers (i,j):

$$\frac{P_1}{P_2} = \frac{i}{j} \tag{1.4}$$

(Armitage, 2007). A very brief overview of why resonant trapping occurs is as follows: A general solution to the 3 body problem is impossible to find, but there are equilibrium solutions one can find (see figure 1.4). We can describe motion close to these equilibrium solutions using perturbation theory on the systems Hamiltonian. One such equilibrium

solution is resonance, for a planet on a circular orbit approaching resonance with another this equilibrium solution acts like a potential minimum, which the approaching planets orbit will oscillate or 'librate' around. As the two planets approach resonance the equilibrium orbit becomes more and more eccentric (see figure 1.4. Inward migration stops when the circularising effects of gas drag on the approaching planet equal the eccentricity amplifying effect. Slow approaching planets are trapped by this process, but fast approaching planets will not be as their librations will be sufficiently large to break out of the local potential minimum. For an in depth description of the process, see Pichierri et al. (2018).

A similar process of migration and then resonant trapping is thought to have resulted in Jupiter's trio of moons in $2:1$ resonances with one another, although in this particular case tidal dissipation is thought to be the circularising force (Goldreich, 1965).

Due to the rapid inwards migration that Super-Earths undergo, resonant trapping is thought to be an important process in their formation. Many of the systems with multiple Super-Earths in we observe have them orbiting close to resonance, but few have them orbiting in resonance (Fabrycky et al., 2014). This is in part because the longer a resonant chain gets the stronger the perturbing forces on each of the planets have on the others, making the system less stable over long time periods.

1.2.5 Gas Disc Dissipation

As mentioned a couple of times previously, proto-planetary discs are not permanent. We observe them to have lifetimes of a few Myrs (Haisch, Jr. et al., 2001). When they dissipate they do so very rapidly compared to the dynamical timescale of the viscous transport processes of the disc, this is known as the 'two time-scale problem' (Williams & Cieza, 2011).

The main process which governs gas disc dissipation is believed to be photo-evaporation from X-ray or high energy UV emission from the central star. The precise importance of particular frequencies is still a topic of ongoing research (Williams & Cieza, 2011). This photo-evaporation process occurs throughout the lifetime of the disc, for most of the time the disc is present however the accretion rate of the star from the disc is faster than the photo-evaporation rate. As soon accretion can no longer keep up with the rate of photo-evaporation the gas disc rapidly dissipates from the inside out leaving only solid

debris and any planets which had already formed while the disc was present (Alexander et al., 2006a,b).

While the gas disc is present it has a circularising effect on the orbits of planets and planetesimals orbiting within it. When the disc dissipates this effect vanishes and with nothing to damp interplanetary forces increasing eccentricity even small perturbations can cause orbits to destabilise (Barnes & Raymond, 2004). Such destabilisation can cause collisions between (or ejections of) planets. When we have a group of multiple planets in a resonant chain the mutual amplification of their eccentricities until it destabilises is known as a 'breaking the chains' scenario (Izidoro et al., 2017). It is thought to commonly occur in systems with Super-Earths, as when we do find multiple in the same system it is rare to find them in resonance, but we do find them quite often close to it (Fabrycky et al., 2014). Volk & Gladman (2015) suggest that such resonant chain breaking scenarios are very common in the formation of inner solar systems and that a system of close orbiting planets might have even existed in our own early solar system at $a < 0.5\,\mathrm{au}$ that has since destabilised, with the planets in question either being ejected, disrupted or accreted onto the sun, leaving iron rich Mercury as the only remnant.

A useful tool for determining whether close encounters of planets are statistically more likely to cause ejection or collision is the Safronov number Θ (Raymond & Morbidelli, 2020), this is given by

$$\Theta^2 = \left(\frac{Gm_{\mathrm{pl}}}{R_{\mathrm{pl}}}\right)\left(\frac{a_{\mathrm{pl}}}{GM_*}\right) = \frac{m_{\mathrm{pl}}}{M_*}\frac{a_{\mathrm{pl}}}{R_{\mathrm{pl}}} \tag{1.5}$$

where R_{pl} is the planets physical radius, a_{pl} its orbital radius, m_{pl} is its mass, and M_* is the mass of the central star. If $\Theta > 1$ then encounters are more likely to result in scattering and ejection, if $\Theta < 1$ then they are more likely to result in collision. Figure 1.5 shows the Safronov number for the planets in the NASA exoplanet archive. From this graph we can see that close orbiting low mass planets are more likely to experience collisions, whereas higher mass giant planets are more likely to experience scattering or ejection. This shows that, unless they have since undergone significant inwards migration, for most of the Super-Earths we have detected so far any close approaches of neighbours post disc-dissipation would likely have caused collisions. It is these late formation giant collisions that form the focus of this work.

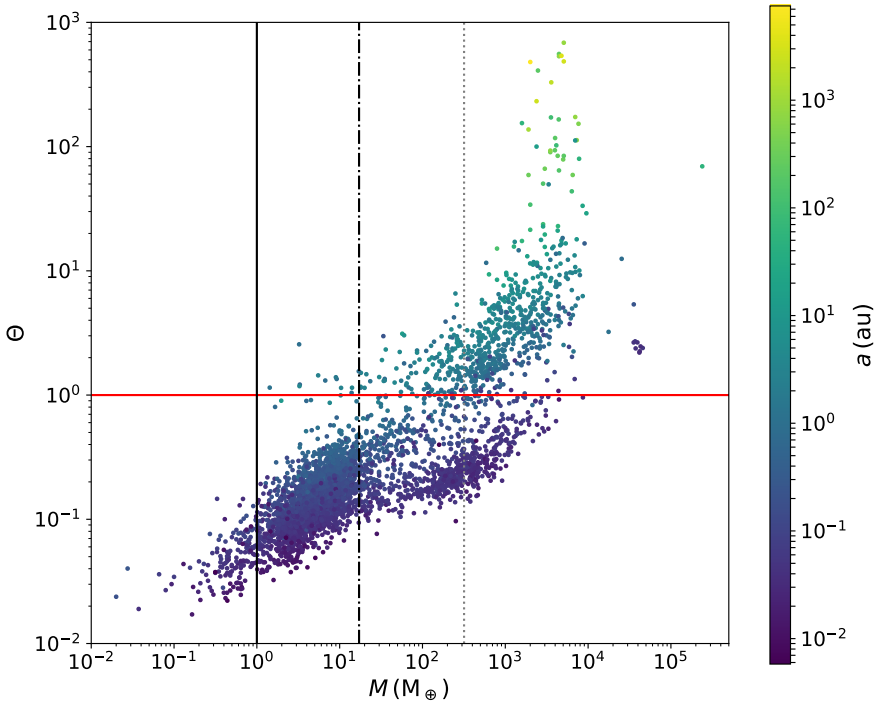

Figure 1.5: The Safronov number for planets in the NASA exoplanet archive (NASA, 2021) as a function of planet mass. The colour of the line gives orbital distance. Lines are drawn for comparison with the masses of Earth (solid black), Neptune (dash-dotted black) and Jupiter (dotted grey). Below the solid red line planets are more likely to undergo collision, above it they are more likely to scatter or eject other objects they encounter.

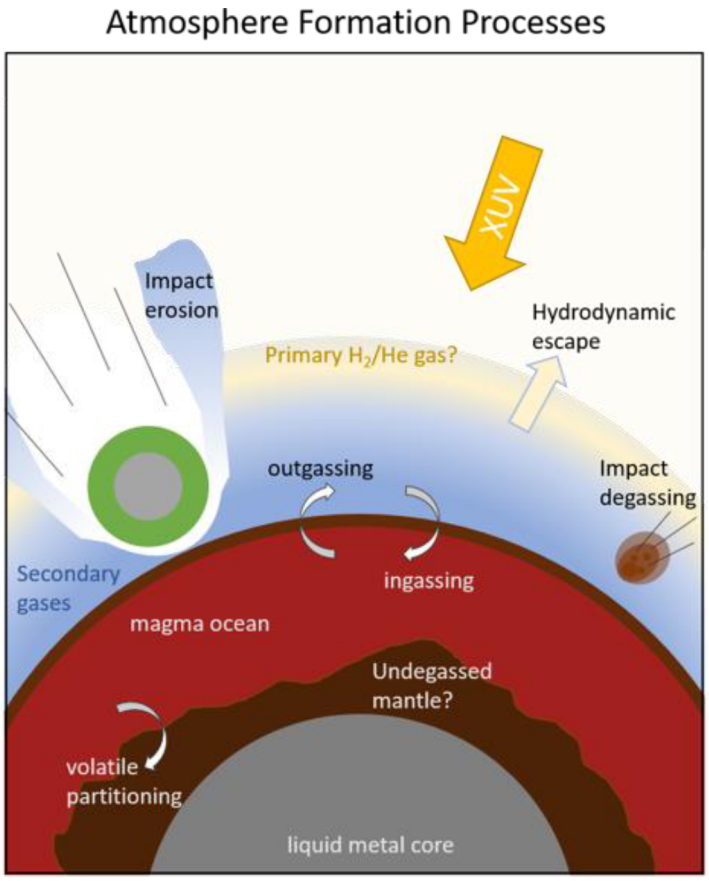

Figure 1.6: A diagram of the various processes important to the formation of atmospheres, figure 1 from Schaefer & Parmentier (2021)

1.3 Atmosphere Formation

We can tell from the low densities of many observed Super-Earths that they must have significant atmosphere fractions often on the order of an Earth mass or more in mass Lopez & Fortney (2014). How do such atmospheres form though and why aren't they present about all planets of this mass?

Typically two main types of atmosphere are considered; hydrogen rich 'primary atmospheres' are formed from the planet accreting an atmospheric envelope from the proto-planetary disc, and 'secondary atmospheres' which are typically made of heavier volatiles that have been outgassed from porous rocks or delivered by captured comets.

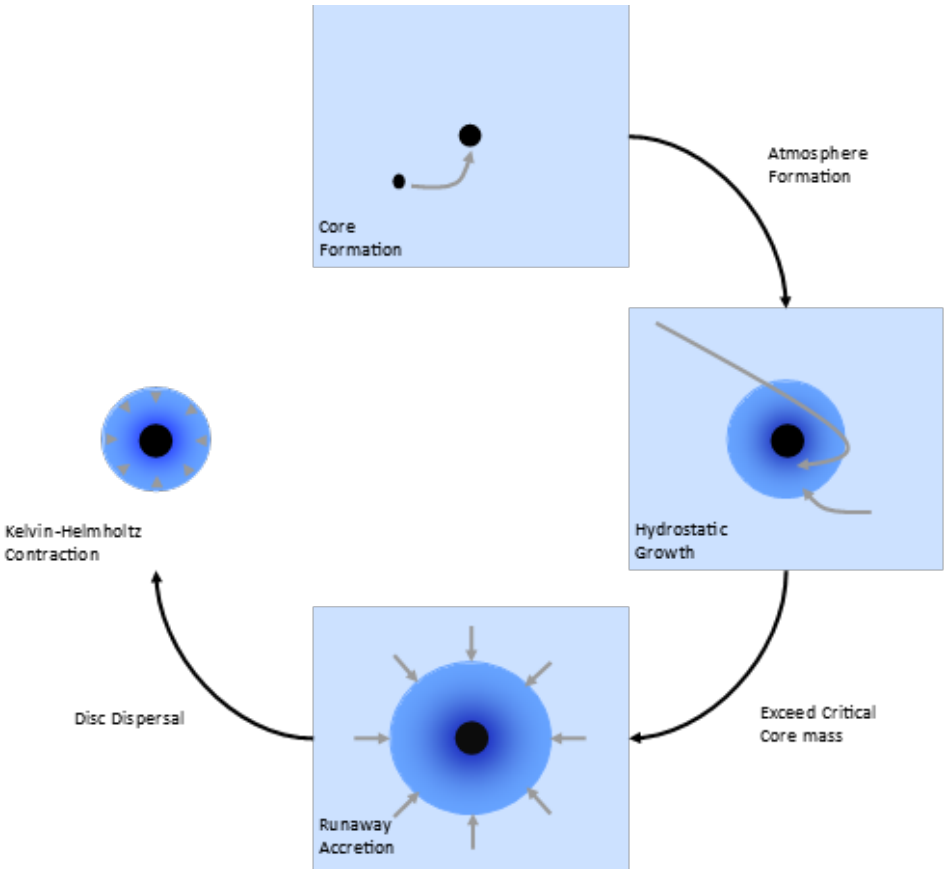

Figure 1.7: The main steps in accretion of a primary atmosphere from the protoplanetary disc (adapted from figure 6.1 Armitage 2010). Super-Earths do not experience the same extent of runaway growth that giant planets do and so either skip or undergo an attenuated 3rd stage.

The atmospheres of real planets tend to be formed from a mixture of material coming from both formation methods. At the two extremes of planet mass we have giant planets which formed earlier when more of the gas disc was present and have large mostly primary atmospheres, and terrestrial planets, which are more likely to lose any accreted hydrogen to erosive effects, have much thinner mostly secondary atmospheres. Super-Earths lie somewhere between the two.

Figure 1.6 is a diagram showing some of the main processes that occur in the formation of atmosphere, I shall summarise these below:

1.3.1 Accretion from the Protoplanetary Disc

When a protoplanet reaches a sufficiently large mass, if the protoplanetary disc is still present, it will begin to accrete a gaseous envelope. This is the method by which Super-Earths and core accretion formed gas giants accrete the majority of their atmospheres.

The main steps in this process are summarised in figure 1.7, they are as follows (Armitage, 2010):

Firstly a solid core needs to form of sufficient mass for it to have a gravitationally bound envelope about it. For this to occur the velocity of individual gas particles needs to be less than the escape velocity of the planet.

The second growth phase is hydrostatic growth. During the hydrostatic growth phase the rate of growth is dependent on the rate of thermal diffusion and convection of the planet. This is because contraction of the envelope is required for more of the gas disc to be able to approach close enough to be accreted, and initially for lower mass planets the pressure of the envelope is in equilibrium with the gravity of the protoplanet so it needs to contract to grow.

The third growth phase is called runaway growth. This was first proposed in Perri & Cameron (1974) and Mizuno (1980) and occurs when the protoplanet has grown sufficiently massive that its gravity can overpower the thermal pressure of the gas and we get hydrodynamic accretion. This critical mass typically occurs at around $10\,M_\oplus$. This process is called runaway growth because it is a positive feedback loop, the more material that becomes bound to the protoplanet the greater its mass, the more the envelope can be compressed, meaning that more material can be added. Growth in this stage is limited by the the gas supply in the disc. Although the runaway growth phase is short, ($\sim 10^5$ yrs), a giant planet will accrete the majority of its mass in this growth phase.

Once the gas supply has been exhausted runaway growth will end and the planet will begin the long process of Kelvin-Helmholtz contraction and cooling back to hydrostatic stability. There are a multiple ways in which atmosphere growth can be stopped, for giant planets it typically stops when either the gas disc dissipates or, more likely, the planet grows sufficiently large to create a gap in the disc.

The method which attenuates Super-Earth growth is less clear, they should form early enough to undergo runaway accretion during the disc lifetime (Piso & Youdin,

2014), despite their much greater abundance in inner solar systems (Super-Earth abundance rate being $30 - 50\,\%$, Fressin et al. 2013 as opposed to $< 1\,\%$ for Hot Jupiters, Udry & Santos 2007). There are multiple proposed solutions including atmosphere loss during accretion (Ikoma & Hori, 2012), heating from small grains stopping contraction (Lambrechts & Lega, 2017), late assembly (Lee et al., 2014) and rapid disc dispersal (Ogihara et al., 2020).

1.3.2 Outgassing

Outgassing (or degassing) is the process in which volatiles, which get trapped in the silicate material that forms a planet during its formation, escape to the surface. For this to occur prior conditions need to be met however: We need a magma ocean with an oversaturation of the volatiles, and we need the bubbles formed by this oversaturation to be able to reach the surface and burst (Elkins-Tanton, 2012).

This oversaturation can be triggered by re-solidification of the magma ocean, water for example is incompatible with some of the silicate mineral crystals which form Elkins-Tanton & Seager (2008). The precise level of re-solidification required for bubble formation is dependant on the concentration of the volatile in question. Once one gas species has reached sufficient oversaturation to form bubbles however other volatiles can diffuse into them. Once these bubbles grow sufficiently large they will decouple from the fluid flow in the mantle and rise to the surface, bursting and releasing their volatiles.

The precise species which will be degassed by the mantle in these processes is also dependant on chemical interactions in the mantle, for example Hirschmann & Withers (2008) show that magma oceans able to form stable graphite will retain a significant fraction of the carbon as the magma solidifies, whereas Elkins-Tanton & Seager (2008) show that when magma oceans which aren't reducing enough for graphite to be stable carbon species dominate the degassing. This volatile degassing process can form liquid oceans eventually, as is thought may have happened on Earth, but it takes the water millions of years to condense out from the hot steam it was degassed as (Abe & Matsui, 1986).

Volatiles from outgassing form a higher percentage of the atmosphere for lower mass planets due to their lower mass, and thus lower gravitational potential, meaning that they accrete less of the gas disc and also lose more atmosphere to erosive processes. For

Super-Earths outgassing typically produces atmosphere fractions of a few percent of the entire planet by mass, although in extreme cases it can be up to 20 % (Elkins-Tanton & Seager, 2008).

1.3.3 Thermal Escape

One of the main ways in which atmospheres get eroded over time is by thermal escape, to understand the processes involved we shall consider the two extremes; Jeans escape and hydrodynamic escape (also known as 'Blowoff').

The kinetic energy of the particles in a gas will follow a distribution defined by the temperature of the atmosphere. For a gas in equilibrium this is the Maxwell-Boltzmann distribution. This distribution of energies has a long tail at high energy, meaning that some particles have kinetic energies significantly higher than the average. If this kinetic energy is greater than that particle's escape velocity then it can be lost from the atmosphere. This process is known as Jeans escape (Jeans, 1924).

Hydrodynamic escape on the other hand is escape caused by thermal expansion propelling particles with sufficient force that they are ejected from the planet, such a process can be treated analogously to a Parker (1958) solar wind model (Hunten, 1973). Hydrodynamic blowoff in the extreme of isothermal expansion can be shown to be analogous to Jeans escape (Hunten, 1982).

For thermal expansion to occur the atmosphere must typically be heated by some process. One of the most important heat sources is X-ray and extreme ultraviolet (XUV) radiation from the central star, especially for close orbiting planets such as Hot Jupiters (Lammer et al., 2003) and Kepler detected Super-Earths (Lopez & Fortney, 2013; Owen & Wu, 2013). This is not the only heat source however, Ginzburg et al. (2016) for example consider the effects of the heat emitted by the cores of recently formed planets as they cool.

The other way hydrodynamic escape of the atmosphere can be triggered is by removing a confining ambient pressure. When the gas disc dissipates, for example, a planet's atmosphere will no longer be in hydrostatic equilibrium with its surroundings and thus a Parker wind will be generated (Owen & Wu, 2016).

In a system with no migration occurring and photo-evaporation being the sole erosive effect on planetary atmospheres we would expect to observe planet densities to follow a

consistent pattern. We would expect the higher density objects being closer to the central star as closer objects would experience more of the stars radiation following the inverse square law. Planets orbiting closer to the star are therefore expected to experience more photo-evaporation, which preferentially removes lighter material, making them denser. We observe exoplanets with significantly different densities orbiting adjacent to one another in the same system, however, such as the Kepler-36 (Liu et al., 2015) or Kepler-107 (Bonomo et al., 2019) systems. Considering these planets likely formed in the same region of the disc and so should have initially had the same composition, their close orbits imply that photo-evaporation cannot be the only erosive process.

1.3.4 Collisions

Another method by which planets can lose atmosphere mass is by collision. Shockwaves from an impact will propel material outwards, if the force of the impact is large enough it can impart sufficient momentum on the material it is passing through to eject it. Ejection is especially likely for atmosphere because it is typically high up a planet's potential well and thus more loosely gravitationally bound than the core or mantle. The heat added to the system by a collision will also increase the rate of thermal escape (Liu et al., 2015). The collision process is covered more fully in section 1.4. As stated previously, it is thought that after the proto-planetary disc dissipates planetary systems undergo a period of significant instability in which collisions are common, this is the time period we would expect most of these atmosphere eroding collisions to occur. Inamdar & Schlichting (2016) and Liu et al. (2015) suggest that these collisions are vital for explaining the density diversity we observe in Super-Earth systems.

This model of dispersion formed by collisions is supported by the Swain et al. (2019) study of NASA exoplanet archive planets of radius $\leqslant 3R_{\oplus}$. They show that terrestrial planets, which they denote as all planets of radius $< 1.75R_{\oplus}$, are split into two distinct groups in insolation-density-radius space. One of these groups experiences low levels of radiation and their densities decrease with increasing mass so they conclude that they formed solely from accreting smaller objects like the solar system's terrestrial planets. The other group experienced much higher levels of solar radiation and thus photo-evaporation of any atmosphere is much more likely to have occured. They note

that for the many examples of this second case, however, the planets have higher densities than would be expected from total atmosphere erosion due to photo-evaporation, indicating that collisions likely have stripped the outer mantle layers leaving a much higher iron core content.

Bonomo et al. (2019) provide observational evidence for the potential aftermath of such a mantle stripping giant collision in the Kepler-107 system. This particular system is covered in more depth in chapter 3 but, in brief, Kepler-107b orbits closer to the star than Kepler-107c but has a significantly lower density, considering the large difference in density and the closeness of orbits Bonomo et al. (2019) consider a giant collision in Kepler-107c's past to be the most likely cause.

Bulk removal of atmosphere via collisions should leave a different signature in the chemical and isotope abundances of atmospheres. Jeans escape will preferentially remove lighter material, whereas, with an impact, proximity to the point of impact has a stronger effect on whether material is likely to escape. For example evidence of collisions in the Earth's history can be inferred by noble gas abundances (Schlichting & Mukhopadhyay, 2018).

Collisions can also cause atmosphere growth. Asteroids and comets, for example, can cause an atmosphere to both grow or shrink. Which process occurs is very dependent on both the colliding objects size and also its impact velocity. Collision of asteroids and comets at slower impact velocities can cause significant atmospheric growth via delivery of volatiles trapped in ices or porous rocks. Faster more energetic collisions on the other hand will generate larger shockwaves which will erode the atmosphere. This dependence on collision parameters means inner planets in a star system are more likely to experience erosion whereas outer planets experience more atmosphere growth (Wyatt et al., 2020). Sinclair et al. (2020) apply this model to collisions against the Earth post Moon-forming impact, they show that larger asteroids can deliver more volatiles, but they are rarer and as such growth due to them is more stochastic. Another way impacts can trigger changes in atmosphere composition is by creating magma oceans on the surface from which outgassing can occur (Elkins-Tanton, 2012).

1.3.5 This works choice of atmosphere

The main method for determining the atmospheres of exoplanets is via transmission spectra. We observe the spectroscopic differences between light from the planet's star with and without the planet in between, as these differences should be caused by scattering and absorption of stellar photons within the planet's atmosphere. This methodology was initially formulated in Seager & Sasselov (2000) for transiting Hot-Jupiters. The precise frequency of photons that get scattered or absorbed is dependent on a variety of factors including temperature structures, clouds and hazes, and molecular composition (Madhusudhan, 2019).

Super-Earth and Sub-Neptune atmospheres lie on the cutting edge of what is feasibly detectable. The first detected atmosphere by this method was by Fraine et al. (2014), since then there have been multiple further detections including Knutson et al. (2014), Demory et al. (2016), Tsiaras et al. (2016), Wakeford et al. (2017) and Benneke et al. (2019). The majority of Super-Earths detected, however, we still have no spectroscopic data for. The launch of the James Webb Space Telescope should provide a great advancement in this field and multiple studies focus on utilising its increased capacity (e.g. Sotzen et al. 2021, Phillips et al. 2021).

Despite our lack of data on the exact make up of Super-Earth atmospheres there are some predictions we can make about their composition based on their masses, radii and orbital distances. Perhaps one of the simplest models we can make is that of a differentiated rocky core, like we would expect for a terrestrial planet, surrounded by a thick hydrogen atmosphere accreted from the proto-planetary disc for example the models used by Lopez & Fortney (2014) or Bodenheimer et al. (2018). For reasons of simplicity we have followed these models and assumed an atmosphere of solely Hydrogen for this work. It should be noted however, that depending on how oxidised the planet's magma is even a world which begins with an atmosphere of this composition may result in equilibrium atmospheres with a high content of water (Kite et al., 2020).

1.4 Giant Impacts

As discussed previously orbital instability after dissipation of the proto-planetary disc is thought to be a common occurrence in the formation of planets. For planets of Super-Earth mass such instability often results in collisions. A collision between two planets will preferentially eject less strongly bound material higher up in a planet's gravitational potential, for example any atmosphere. A single collision can therefore have a significant effect on the density of a planet, for example the second closest orbiting planet in the Kepler-107 system (Bonomo et al., 2019). Inamdar & Schlichting (2016) even suggest that such collisions are vital for producing the overall observed density diversity in Super-Earth mass exoplanets. In this section I will summarise some of the important previous works in the field:

1.4.1 Theoretical Models

a) Scaling Laws

For planetary collisions, we typically consider two separate collision regimes dependant on which is the dominant binding force that has to be overcome for erosion to occur. At low masses the dominant binding force is the material strength of an object (i.e. how difficult an object is to shatter), whereas at higher masses however the dominant binding force is an object's self-gravity (i.e how well material in an object is gravitationally bound to it). Housen & Holsapple (1990) use dimensional analysis to provide a scaling law that predict the minimum specific energy (i.e the ratio of projectile kinetic energy and target mass) required for the largest collisional fragment to be half the mass of the original target.

Leinhardt & Stewart (2012) expand this scaling law analysis to impactors of similar size to the target. Instead of specific impact energy the energy measure they use is specific relative kinetic energy measured at the point of impact Q_{R}, which is defined as:

$$Q_{\mathrm{R}} = \frac{1}{2}\frac{\mu v_{\mathrm{imp}}^2}{M_{\mathrm{tot}}} \tag{1.6}$$

where μ is the reduced mass of the system, M_{tot} the total mass of projectile and target combined and v_{imp} the collision velocity.

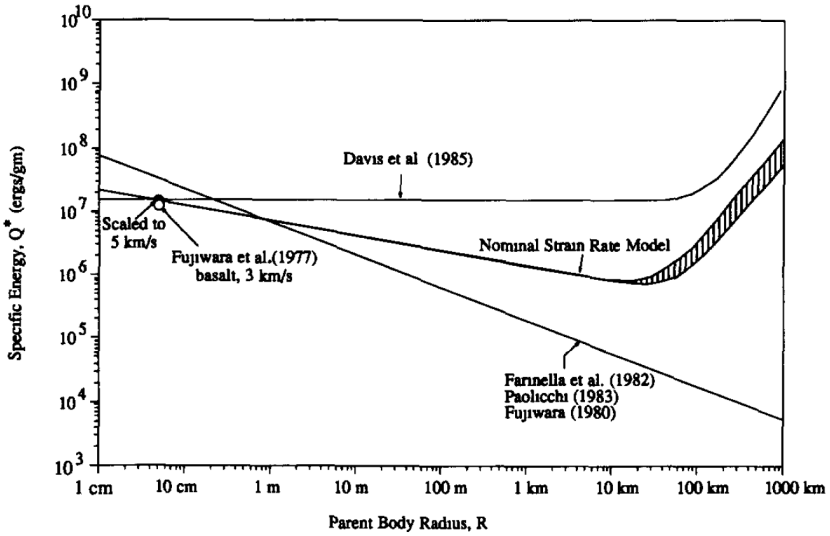

Figure 1.8: Three different models for how the catastrophic fragmentation energy depends on target radius (from Housen & Holsapple (1990)). Models based on material strength predict the fragmentation energy to decrease with increasing target mass as the momentum of shockwaves caused by a collision become too large for material strength to withstand. Models based on gravitational binding however predict the catastrophic fragmentation energy increases with increasing mass due to the corresponding greater gravitational potential .

Leinhardt & Stewart (2012) define the catastrophic disruption threshold, Q^*_{RD}, the minimum Q_{R} for the largest collision remnant to be less than half the combined mass of projectile and target. Using the catastrophic fragmentation threshold scaling law derived by Housen & Holsapple (1990), they predict that the scaling law for the catastrophic disruption threshold should be:

$$Q^*_{\mathrm{R}} = q_{\mathrm{s}} \left(\frac{S}{\rho_1} \right)^{\frac{3\bar{\mu}(\phi+3)}{2\phi+3}} R_{\mathrm{C1}}^{\frac{9\bar{\mu}}{3-2\phi}} V^{*(2-3\bar{\mu})} + q_{\mathrm{g}} \left(\rho_1 G \right)^{\frac{3\bar{\mu}}{2}} R_{\mathrm{C1}}^{3\bar{\mu}} V^{*(2-3\bar{\mu})} \tag{1.7}$$

where q_{s} and q_{g} are dimensionless coefficients with values close to unity, S is a material strength measure (in units of $\mathrm{Pa\,s}^{\frac{3}{\phi+3}}$), V^* is the collision velocity at the catastrophic fragmentation threshold, ϕ is a dimensionless constant of values between 6 and 9 which measures the dependence of the material strength on strain rate, and $\bar{\mu}$ is a measure of energy and momentum coupling. From Holsapple & Schmidt (1987) $\bar{\mu} = 1/3$ is equivalent to to pure momentum scaling, which we would expect for a more solid body, and $\bar{\mu} = 2/3$ is equivalent to pure energy scaling, this is what we would expect to observe for a perfect gas. $\rho_1 = 1000\,\mathrm{kg\,m}^3$ and R_{C1} is the radius of a spherical object with density ρ_1 and a mass equal to the total mass of the system:

$$R_{\mathrm{C1}} = \left(\frac{3M_{\mathrm{tot}}}{4\pi\rho_1} \right)^{\frac{1}{3}}. \tag{1.8}$$

For collisions of two objects of Super-Earth mass we would expect them to be overwhelmingly in the gravitationally dominated regime, as illustrated in figure 1.8, where they are off the right hand edge of the graph. Even when material properties are important, such as providing drag in glancing collisions, the materials the planets are made of behave more like fluids at the temperatures and pressures they are under, so we would not be able to use a classical definition of material strength as the ease by which a material gets fractured.

This dimensional analysis derived scaling forms the basis for many empirical models based on cratering experiments and collision simulations. The scaling law which we most commonly use in this work is the one from Leinhardt & Stewart (2012) which was empirically derived from the results of their simulations. It gives, for a head on collision for a projectile and target of equal mass, a catastrophic disruption threshold of:

$$Q^*_{\mathrm{RD}} = \frac{4}{5} c^* \pi \rho_1 G R_{\mathrm{C1}}^2 \tag{1.9}$$

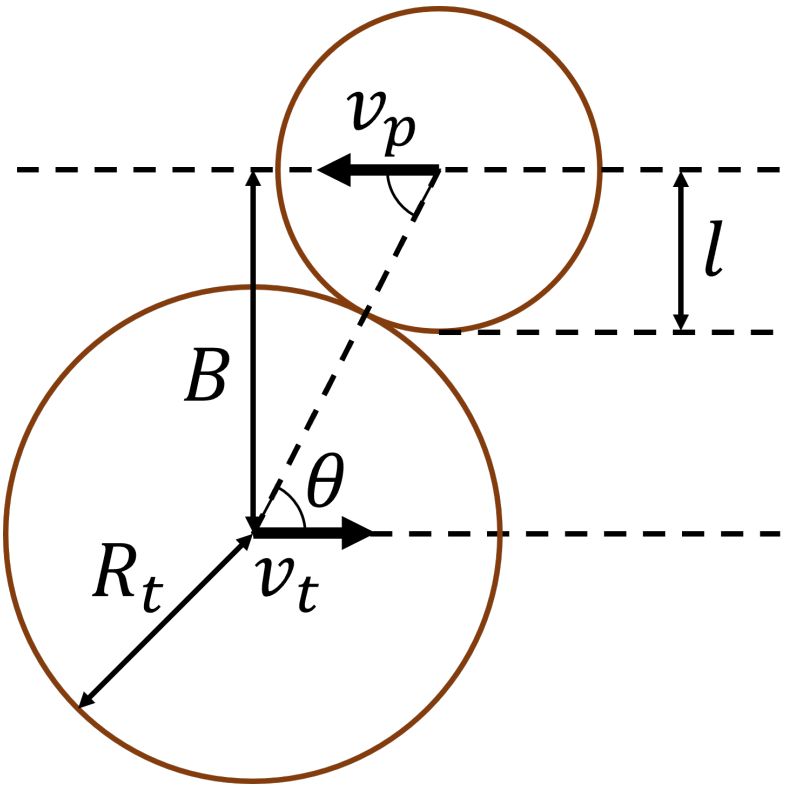

Figure 1.9: A graph showing the geometry of a glancing collision, as well as the parameters Leinhardt & Stewart (2012) use to measure it, most calculations use the relative velocity of the projectile compared to the target for the collision velocity $v_{\rm imp} = v_{\rm p} - v_{\rm t}$.

where c^* is a parameter that details the difference between the equal mass disruption criterion and the binding energy and so can be considered a measure of energy dissipation in the system. They measured a value of $c^* = 1.9 \pm 0.3$ for their smoothed particle hydrodynamics simulations of planetary sized bodies.

For higher impact angle collisions and different projectile-target mass ratios this initial value is further modified. For projectiles and targets of different masses to one another, the catastrophic disruption threshold is also dependent on planet mass and impact velocity. We shall modify the equal mass $Q^*_{\rm RD}$ using the projectile-target mass ratio ($\gamma = M_{\rm p}/M_{\rm t}$). To derive this modification we compare our definition of impact energy from equation 1.6 to the catastrophic disruption scaling for the gravitational

regime from equation 1.7:

$$\frac{\mu V^{*(2)}}{2M_{\rm tot}} = q_{\rm g}\left(\rho_1 G\right)^{\frac{3\bar{\mu}}{2}} R_{\rm C1}^{3\bar{\mu}} V^{*(2-3\bar{\mu})}. \tag{1.10}$$

If we note that $\mu = \gamma M_{\rm t}/\left(\gamma+1\right)$ and $M_{\rm tot} = M_{\rm t}\left(\gamma+1\right)$ then from this, with some rearranging, we can derive:

$$V^* = \left[\frac{2\left(\gamma+1\right)^2}{\gamma} q_{\rm g}\left(\rho_1 G\right)^{\frac{3\bar{\mu}}{2}} R_{\rm C1}^{3\bar{\mu}}\right]^{\frac{1}{3\bar{\mu}}}. \tag{1.11}$$

Considering that for $\gamma = 1$, we have both $\mu = M_{\rm t}/2$ and $M_{\rm tot} = 2M_{\rm t}$ this means that $Q^*_{\rm RD}(\gamma=1) = V^{*(2)}/8$, therefore:

$$V^*\left(\gamma\right) = V^*\left(\gamma=1\right)\left(\frac{\left(\gamma+1\right)^2}{4\gamma}\right)^{\frac{1}{3\bar{\mu}}}. \tag{1.12}$$

From equation 1.7, the following must be true

$$Q^*_{\rm RD}(\gamma) = Q^*_{\rm RD}(\gamma=1)\left(\frac{V^*\left(\gamma\right)}{V^*\left(\gamma=1\right)}\right)^{2-3\bar{\mu}}. \tag{1.13}$$

Combining these together we thus arrive at the final effect that different projectile-target mass ratios should have on the catastrophic disruption threshold

$$Q^*_{\rm RD}(\gamma) = Q^*_{\rm RD}(\gamma=1)\left(\frac{\left(\gamma+1\right)^2}{4\gamma}\right)^{\frac{2}{3\bar{\mu}}-1}. \tag{1.14}$$

Leinhardt & Stewart (2012) measured a value of $\bar{\mu} = 0.36 \pm 0.01$ for their SPH planet collision simulations.

Corrections to the catastrophic disruption threshold due to the projectile hitting the target at an oblique impact angle make use of the fact that only a percentage of the projectile's mass will interact with the target. This interacting mass $m_{\rm int}$ is given by;

$$m_{\rm int} = \rho\int_0^l \pi a^2 dz = \rho\pi\left(R_{\rm p} l^2 - \frac{l^3}{3}\right) \tag{1.15}$$

where, to complete the integral we have used the parameter $a^2 = R_{\rm p}^2 - \left(R_{\rm p} - z\right)^2$, where z measures the vertical distance in the plane of collision from the base of the projectile, $R_{\rm p}$ is the projectile's radius, and l is the vertical distance from the projectile's base to the top of the target at the point of collision (see figure 1.9). l can be calculated from

the un-normalised impact parameter, B, by $l = R_{\rm p} + R_{\rm t} - B$, where $R_{\rm t}$ is the target planet's radius.

Using this interacting mass and comparing it to the total projectile mass, $M_{\rm p}$, with the parameter $\alpha = m_{\rm int}/M_{\rm p}$ we can generate the following modification μ_α to the reduced mass :

$$\mu_\alpha = \frac{\alpha M_{\rm p} M_{\rm t}}{\alpha M_{\rm p} + M_{\rm t}}, \tag{1.16}$$

where $M_{\rm t}$ is the target planet's mass.

This implies that a collision of energy $Q_{\rm R}$ is equivalent to a head on collision of energy:

$$Q_{\rm R} = Q_{\rm R}^{\rm Head\,On} \frac{\mu}{\mu_\alpha}, \tag{1.17}$$

The magnitude of the catastrophic disruption threshold is modified further however due to it being proportional to the impact velocity as given by equation 1.7 $Q^*_{\rm RD} \propto V^{*(2-3\bar{\mu})}$, this gives a catastrophic disruption threshold change of

$$Q^*_{\rm RD} = Q^{*\rm Head\,On}_{\rm RD} \frac{\mu}{\mu_\alpha} \left(\frac{V^*}{V^{*\rm Head\,On}} \right)^{2-3\bar{\mu}}. \tag{1.18}$$

Because of equation 1.6,

$$\frac{V^*}{V^{*\rm Head\,On}} = \sqrt{\frac{\mu}{\mu_\alpha}}. \tag{1.19}$$

This therefore gives a final transformation for the catastrophic disruption threshold of:

$$Q^*_{\rm RD} = Q^{*\rm Head\,On}_{\rm RD} \left(\frac{\mu}{\mu_\alpha} \right)^{2-\frac{3\bar{\mu}}{2}}. \tag{1.20}$$

A more complicated type of scaling law is one that models the mass loss for a collision of arbitrary impact energy. An example of this is the empirically derived disruption regime prediction from Stewart & Leinhardt (2009) for the mass of the largest remnant, $M_{\rm LR}$:

$$\frac{M_{\rm LR}}{M_{\rm tot}} = -0.5 \left(\frac{Q_{\rm R}}{Q^*_{\rm RD}} - 1 \right) + 0.5 \tag{1.21}$$

Marcus et al. (2009), from their simulations of Super-Earth collisions, show that disruptive collisions of Super-Earths with a composition of one part iron core to two parts forsterite mantle follow the prediction of this model. They also show that such collisions typically increase the iron fraction of the largest remnant as the forsterite

mantle is preferentially ejected, which they model as a power law of Q_{R}. They measure the iron content of their largest remnant cores to follow:

$$\frac{M_{\mathrm{Fe}}}{M_{\mathrm{LR}}} = 0.33 + 0.25 \left(\frac{Q_{\mathrm{R}}}{Q^*_{\mathrm{RD}}} \right)^{1.65}. \tag{1.22}$$

The exponent and coefficient of this model are likely dependent on initial composition (Carter et al., 2018), however, this was beyond the scope of their initial study.

It should be noted that not all scaling law models use specific kinetic energy (Q_{R}). Movshovitz et al. (2016) and Gabriel et al. (2020), for example, use un-normalised kinetic energy K:

$$K = \frac{1}{2} \mu v_{\mathrm{imp}}^2. \tag{1.23}$$

Movshovitz et al. (2016) show the kinetic energy required for catastrophic disruption K^* for their simulated $100 - 1000\,\mathrm{km}$ objects to be linearly related to the systems binding gravitational energy at the point of impact, U:

$$K^* = cU \tag{1.24}$$

where c is a constant and

$$U = \frac{3GM_{\mathrm{t}}^2}{5R_{\mathrm{t}}} + \frac{3GM_{\mathrm{p}}^2}{5R_{\mathrm{p}}} + \frac{3GM_{\mathrm{t}}M_{\mathrm{p}}}{(R_{\mathrm{t}} + R_{\mathrm{p}})}. \tag{1.25}$$

b) Self-Similar Hydrodynamic Models

One commonly used method to determine the atmosphere loss after a collision is to consider the collision as an explosion and to model the shockwave in each direction from this point 1-dimensionally. Yalinewich & Remorov (2021) discuss how the behaviour of the shockwave depends upon the distance it is from the collision point. Close to the shock the density profile is roughly constant and can be well described by a Sedov-Taylor explosion (Sedov, 1946; Taylor, 1950). When the shockwave distance becomes of the order of the atmosphere's scale height the shockwave will begin to accelerate due to declining density, Sakurai Akira (1960) provide a model for this regime. The regime which typically gets focused on for atmosphere stripping due to impacts, however, is when the shockwave distance is much larger than the scale height. The shock in this region tends to be self-similar with the effective shock radius from the centre of the explosion being $R \propto t^{\alpha}$ i.e a power law function of time. Multiple papers discuss atmosphere loss

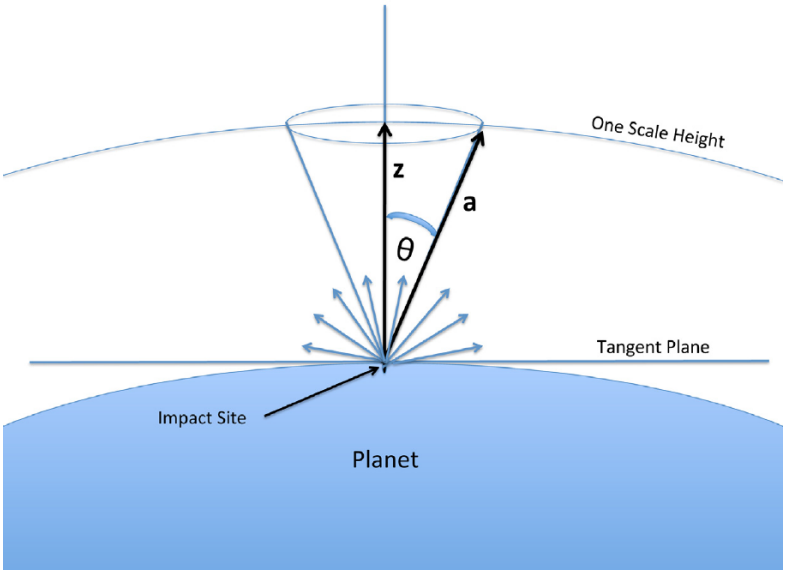

Figure 1.10: A diagram showing the important geometry for small collisions. If an impactor is sufficiently small it will not create a shock in the mantle large enough to generate atmosphere loss. All material ejected from such a collision will be due to atmospheric shockwaves confining this loss to material above the tangent plane of the planet at the point of impact. Figure 10 from Schlichting et al. (2015).

due to collisions in this regime, for example Yalinewich & Schlichting (2018), Yalinewich & Remorov (2021) and Schlichting et al. (2015).

One particular example of a self similar model being used to predict atmosphere losses is Schlichting et al. (2015). They outline two methods of atmosphere ejection which occur during an impact: ejection from shockwaves in the atmosphere directly from the point of impact, and material that gets ejected due to shockwaves through the mantle from the impact. When these mantle shocks reach the surface they generate further atmosphere shockwaves expelling material.

For smaller collisions only the direct shockwaves from the point of impact will cause atmosphere loss. The theoretical maximum amount of atmosphere that can be lost from such an impact (assuming atmosphere scale height, h, is much less than planet radius, R_t) is the entire material cap above the tangent plane at the point of impact. Schlichting et al. (2015) calculate this cap to be

$$M_\mathrm{cap} = 2\pi\rho_0 h^2 R_\mathrm{t}, \tag{1.26}$$

where ρ_0 is the density of atmosphere at the surface. Thicker atmospheres are more complicated as it is more possible for the shockwave to travel around the planet. Schlichting et al. (2015) use a simplified model where they look at the projectile mass required to eject all material above the impact in a cone of opening angle θ (see figure 1.10). They show that for typical impact velocities comparable to the escape velocity this requires a minimum impactor mass of

$$M_{\mathrm{p}} = 4\pi\rho_0 h^3, \tag{1.27}$$

with total cap removal occurring at an impactor mass of

$$M_{\mathrm{p}} = \sqrt{2}\rho_0 \left(\pi h R_{\mathrm{p}}\right)^{\frac{3}{2}}. \tag{1.28}$$

Such a simplification neglects that a shock can eject some atmosphere in a particular direction without losing all of it. Yalinewich & Remorov (2021) covers a more complicated model generated by treating the shock from the collision 1-dimensionally in all directions from the point of impact. This allows them to treat the explosion as a particular type of self similar problem known as an impulsive piston problem (Zel'dovich & Raizer, 1967).

Not all of the atmosphere is lost due to direct atmospheric shockwaves however, a shockwave will also be generated in the mantle of the planet due to the collision, and, if this is energetic enough, the movement of the crust due to this shockwave can remove atmosphere above it, unlike direct atmospheric shockwaves, this process can remove material from all points on the planet. To predict the velocity of this shockwave Schlichting et al. (2015) assume that the system can be well represented by a constant density target planet and an explosion at the point of impact, using momentum conservation this means that the velocity of the shockwave, v_{s}, can be calculated via $M_{\mathrm{p}} v_{\mathbf{v}_{\mathrm{imp}}} = M_{\mathrm{shock}} v_{\mathrm{s}}$, where M_{shock} is the mass of projectile behind the shockwave. Assuming all projectile material is dissipated by the explosion of the impact and that the shockwave spreads out in all directions through the target at constant velocity due to the constant density the volume V contained behind the shockwave is:

$$V = \frac{\pi l^3 \left(4 - 3\frac{l}{2R}\right)}{6} \tag{1.29}$$

where R is the target radius and l is the distance the shockwave has travelled so far (see figure 1.11). Using this and our assumption of constant density the velocity of the

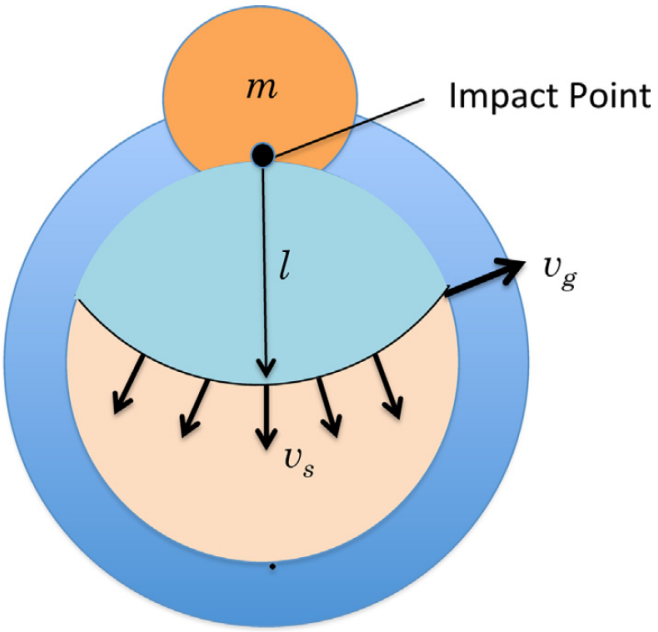

Figure 1.11: A diagram showing the mantle shockwave caused by a large impact, and the ground velocity generated as it passes. Figure 6 from Schlichting et al. (2015).

shockwave should therefore be:

$$v_{\mathrm{s}} = v_{\mathrm{imp}} \frac{M_{\mathrm{p}}}{M_{\mathrm{t}}} \frac{1}{\left(\frac{l}{2R}\right)^3 \left(4 - 3\frac{l}{2R}\right)}. \tag{1.30}$$

It's not the speed of the shock that dictates the amount of material above a point of crust that gets jettisoned, but the vertical ground velocity v_{g} at that point. This can determined by decomposing the shock velocity into components parallel and perpendicular to the ground, this gives $v_{\mathrm{g}} = v_{\mathrm{s}} \frac{l}{2R}$. From v_{g} we can determine the amount of material lost. It should be noted that minimum ground velocity doesn't occur at the antipode but at $l/2R = 8/9$.

From this ground velocity they then solve to work out the fraction of material above that point that gets jettisoned, χ, by using their self-similar solutions to the fluid equations. They have two separate solutions, for adiabatic and isothermal atmospheres respectively, these are:

$$\chi_{\mathrm{Adi}} = 0.4 \left(\frac{v_{\mathrm{imp}} M_{\mathrm{p}}}{v_{\mathrm{esc}} M_{\mathrm{t}}}\right) + 1.8 \left(\frac{v_{\mathrm{imp}} M_{\mathrm{p}}}{v_{\mathrm{esc}} M_{\mathrm{t}}}\right)^2 - 1.2 \left(\frac{v_{\mathrm{imp}} M_{\mathrm{p}}}{v_{\mathrm{esc}} M_{\mathrm{t}}}\right)^3 \tag{1.31}$$

for an adiabatic atmosphere, and

$$\chi_{\mathrm{Iso}} = 0.4 \left(\frac{v_{\mathrm{imp}} M_{\mathrm{p}}}{v_{\mathrm{esc}} M_{\mathrm{t}}}\right) + 1.4 \left(\frac{v_{\mathrm{imp}} M_{\mathrm{p}}}{v_{\mathrm{esc}} M_{\mathrm{t}}}\right)^2 - 0.8 \left(\frac{v_{\mathrm{imp}} M_{\mathrm{p}}}{v_{\mathrm{esc}} M_{\mathrm{t}}}\right)^3 \tag{1.32}$$

for an isothermal one.

Yalinewich & Schlichting (2018) improve upon this model by comparing it to hydrodynamical simulations of such collisions. In particular they discuss the importance of the rarefaction wave on the velocity of the shockwave in the core and mantle of the planet. In qualitative terms what happens to the pressure waves passing through the planets is as follows: The initial shockwave is caused by the force of the impact, this impact will cause shockwaves in both target and projectile that move away from the point of impact. Once these shockwaves reach a surface they will cause a rarefaction wave in the other direction which decompresses all the material compressed by the shock. Typically this rarefaction wave starts in the projectile as it is smaller. Rarefaction waves travel at the speed of sound through the material, because the sound speed for the shocked material is faster than unshocked material they are thus faster than shockwaves. For small impactors rarefaction waves can therefore catch up with the shockwave, weakening it and

decreasing its velocity. Because of this effect Yalinewich & Schlichting (2018) predict a new ground velocity of

$$ln\left(\frac{v_{\rm g}}{v_{\rm imp}}\right) = \frac{14.2x^2 - 25.3x + 11.3}{1.0x^2 - 2.5x + 1.9} + 2ln\left(\frac{R_{\rm p}}{R_{\rm t}}\right) \tag{1.33}$$

where $x = sin\left(\frac{\theta}{2}\right)$ is the position of the point on the surface atmosphere ejection is being calculated for, θ being the angle between the perpendicular to the surface at that point and the perpendicular at the point of impact.

For large impactors on the other hand where the rarefaction wave cannot catch up they propose the mass contained within the shocked material is proportional to that of the projectile, analogous to the physics of Newton's cradle. They predict the velocity at the antipode to be $v_{\rm antipode} = v_{\rm imp}$, i.e the collision velocity.

Yalinewich & Schlichting (2018) use the same transformation between this ground velocity and the material above it that gets ejected (χ) as Schlichting et al. (2015). From this calculated χ the total fraction of the atmosphere lost from the collision is given by;

$$\frac{\Delta M_{\rm t}^{\rm atmos}}{M_{\rm t}^{\rm atmos}} = \frac{1}{2R_{\rm t}^2}\int_0^{2R_{\rm t}} \chi_{\rm loss}\left(\frac{v_{\rm g}}{v_{\rm esc}}\right) ldl. \tag{1.34}$$

Figure 1.12 shows a series of cross sectional plots of SPH simulations of collisions illustrating shockwaves and rarefaction waves, SPH particles with higher density than they started are red, while lower density ones are in blue. Despite our planets having two component cores with a significant density difference between the centre and the surface, assumption of a spherical shock wavefront appears a good first order approximation. Rather than staying spherical and having a shock wave passing through it, though, the target planet is significantly deformed. This deformation is even more exaggerated for larger impactors.

1.4.2 Simulations of Giant Impacts

Multiple methods have been used so far to simulate planet collision and smaller impacts, each having their own strengths and drawbacks. I shall briefly summarise a few of the methods here, as well as giving examples of previous works which have used each method.

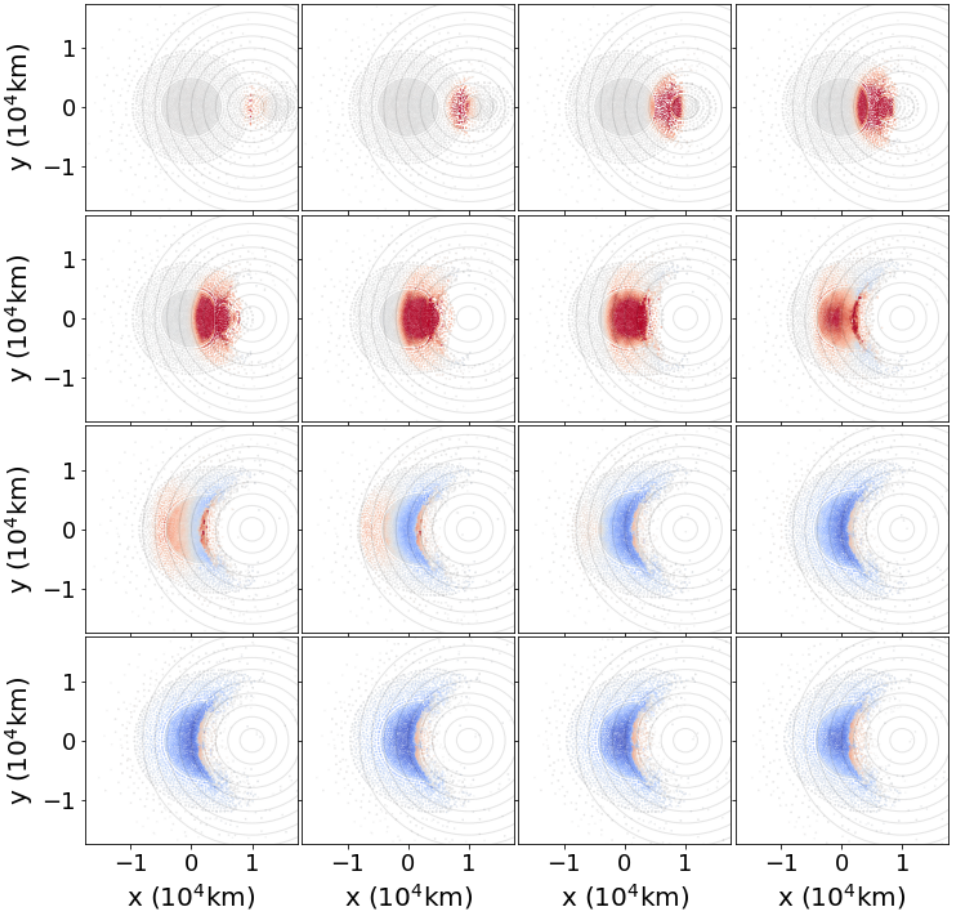

Figure 1.12: A series of snapshots showing a simulation of a collision in process between a 5.9 $M_\oplus$ target and a 0.25 $M_\oplus$ projectile. Red areas show particles higher than initial pressure, blue shows particles below initial pressure. Grey circles about the point of impact are for comparison with the shape of the shockwave.

a) N-body codes

One of the simplest ways one can simulate collisions is by N-body simulations, here each object is split into many smaller particles of set mass and radius (hence N bodies). In the simplest versions of such codes these particles can interact with one another in two ways, gravitationally or collisionally. Collisions occur when the locations of the centre of masses of two particles end up within the sum of their radii after a simulation step. This lack of other types of interaction for the simplest versions of these codes means they are best suited to collisions in the gravity dominated regime.

Whilst atmospheres can be modelled by looking at the collisional interactions of hard particles, as this forms the basis of the assumptions used to derive the ideal gas model, to do so requires particles that would be far too small to be practical to compute for any planetary scale collision. As such N-body simulations of astronomical collisions are best suited to collisions of solid material, for example rubble pile models of asteroids Korycansky & Asphaug (2009).

b) Mesh Methods

Both mesh methods and smoothed particle hydrodynamics (see below) consider the material that constitutes the colliding planets to be best represented by a fluid. Where mesh methods differ is how they represent the fluid. Mesh methods use the Eulerian description of fluids where values are measured at fixed points as the fluid flows past them. These fixed points of measurement are the nodes of the titular mesh. The properties of points in the mesh can be determined for each timestep by using numerical approximations to the Eulerian versions of the fluid equations. Mesh methods are good for materials that are mixing, and adaptive meshes, where the grid points get refined at each step to be higher density in important areas, can be very good for representing both shocks and regions of sparsity well. One large downside to mesh methods however is they can only represent material within the physical extent of the mesh, so anything that gets ejected with sufficient force to leave the simulation area is lost.

One previous work which has modelled giant collisions with planets with atmospheres using a mesh is Liu et al. (2015), they look at the examples of Kepler-11 and Kepler-36 where comparatively volatile rich Sub-Neptunes and volatile poor Super-Earths exist on

adjacent orbits. They propose giant collisions as a potential cause for this and use mesh methods to model two such collisions. They show it is possible that Kepler-36b could have been significantly devolatilised by giant collisions relative to Kepler-36c. Because of this devolatilisation they suggested giant collisions as a potential cause for the large density dispersion observed in close orbiting Super-Earths and Sub-Neptunes

c) Smoothed Particle Hydrodynamics codes

Whilst mesh methods use the Eulerian description of fluids, Smoothed particle hydrodynamics (SPH) use the Lagrangian representation, where the points that are measured follow the flow of the fluid. How this works is that the fluid is split into many small particles, which interact gravitationally like in N-body codes, but instead of them having fixed densities, their densities as well as other thermodynamical properties are calculated by particle proximity. This allows us to model materials with different equations of state with particles many orders of magnitude larger than any real particle in question. The downside with SPH methods is how well they represent shocks and also how they represent boundaries between materials, as the properties of each particle are dependent on the properties of neighbouring particles. Particles at a surface will have a different amount of neighbours to particles in the bulk, and so their properties are less well described.

An example of using SPH to simulate planetary collisions is Marcus et al. (2009) where they introduce the modified version of Gadget-2 this work was built upon (see numerical methods). In this paper they consider the collisions of closely orbiting super-Earth mass objects made of a silicate and iron without atmospheres and show that such collisions can result in Mercury-like iron enriched remnants. In Marcus et al. (2010) they build upon these results by looking at rock-ice planets and show that in both this and the previous case, less dense surface material is removed preferentially, and that accretionary impacts also preferentially accrete heavier material from the projectile.

Leinhardt & Stewart (2012), Stewart & Leinhardt (2012) and Movshovitz et al. (2016) all use SPH simulations to generate scaling laws (see section a)) to predict the amount of material that a collision is likely to eject. Leinhardt & Stewart (2012) construct a model intended to be broadly applicable at all scales, whereas Movshovitz et al. (2016) focus specifically on the $100 - 1000\,\mathrm{km}$ range of radii.

Gabriel et al. (2020) and Genda et al. (2012) use SPH to look at the boundary between merging collisions (where the target and projectile combine to form one large remnant), and hit-and-run collisions (where the projectile bounces off and there are two comparably sized large remnants). They both show the boundary to be dependent on both impact velocity and impact angle, with faster, higher impact angle collisions being more likely to result in hit-and-runs.

Most previous SPH simulations have been of atmosphere-less collisions, this is because of the considerable differences in density between planetary mantles and atmospheres. Gas atmospheres are much lower density than rocky mantles, this means a much lower spatial resolution for the atmosphere. Also, because particle properties in SPH are dependent on those of their neighbours, the physical boundary between mantle and atmosphere (the 'crust') isn't dealt with well.

Despite these limitations there are some examples in the literature of SPH being used to model atmospheres for example Hwang et al. (2017a), Hwang et al. (2017b), Kegerreis et al. (2018) and Kegerreis et al. (2020). These two groups take different approaches to these issues:

Hwang et al. (2017a) and Hwang et al. (2017b) only consider highly grazing collisions where the planets' mantles only pass through one another's atmospheres, this reduces the effects of the material boundary. They use these collision simulations to look at the evolution of systems of close orbiting Super-Earths.

Kegerreis et al. (2018) and Kegerreis et al. (2020) on the other hand get around this problem by using a very high resolution, this decreases the effect of the atmosphere being comparatively low resolution. In Kegerreis et al. (2018) they use this method to test collisional theories of Uranus's formation whereas in Kegerreis et al. (2020) they look at the erosion of atmospheres in collisions of terrestrial planets (i.e rocky planets of mass $< 1\,\mathrm{M}_\oplus$).

This work in comparison only considers the large scale final results of a simulation, such as final mass ejected or fraction of material in each remnant of each type. We also deal with substantially larger atmosphere fractions than Kegerreis et al. (2020). This means we can use a lower resolution.

1.4.3 Modelling Collisions in our Solar System

The strongest evidence we have for giant collisions are our current formation theories for planets and moons of our own solar system, in particular giant collisions are thought to have played an important part in the formation of Mercury, Earth and Uranus.

Mercury, for example, has a very high iron core content compared to the other terrestrial planets. Whilst this could potentially be explained by a combination of photo-evaporation and the inner disc where it formed being enriched in iron due to the silicates melting, a giant collision occurring allows us to have a similar result without requiring the early solar system sun to be quite as active. Benz et al. (1988) use SPH simulations to show that a $20 - 30\,\mathrm{km\,s^{-1}}$ impactor with $1/6^{th}$ Mercury's mass could have generated the required iron enrichment.

Giant collisions are also thought to be the leading formation mechanism for the Earth-moon system. A large planetesimal by the name of Theia is thought to have collided with the early Earth Cameron & Ward (1976), mixing with the Earth and ejecting sufficient debris into orbit to form the Moon. One current model for this is that the collision generated an extended cloud of vapourised material, called a synestia from which the Moon is thought to have formed as it condensed (Lock et al., 2020). This high temperature extended vapour cloud explains an important property of the Earth and the Moon, which is how they appear to be so isotopically similar.

Uranus is also thought to have undergone a giant collision at some point in the past, with it being hypothesised that this could be a cause for both its peculiar axis of rotation (roughly perpendicular to the plane of the solar system) and also the unusual shape of its magnetic field. Kegerreis et al. (2018), for example, use SPH codes to model the deposition of the mantle material of a potential impactor and show that it is definitely possible to deposit a sufficient amount of the projectile's core and mantle material to cause the observed effect in the magnetic field. They also show that an impactor of at least $2\,\mathrm{M_\oplus}$ can provide a sufficient change in angular momentum to affect the rotation enough to reproduce Uranus' tilt. They also show that such collisions can also cause a sufficient amount of material to be ejected to account for the formation of Uranus's satellites.

1.4.4 Applications for Simulation Results

Using simulations we can not only analyse individual collisions which we have evidence have occurred, but also provide models which can be used to understand how planets and whole solar systems evolve over longer time periods. This section looks at a few ways this can be done:

a) N-body Planetary System Models

One place where the results of simulations of collisions gets used is in improving models for the evolution of an entire planetary system. For example N-body simulations of oligarchic growth of planetesimals or destabilising of resonant super-earth chains. Early models of planetesimal growth, for example, initially assumed perfect merging on all collisions (e.g. Chambers 2001) which leads under-predictions of the processes' timescale. More modern simulations will use fragmentation models from local simulations of collisions, such as Chambers (2013) which uses Leinhardt & Stewart (2012) and Genda et al. (2012) to predict the results when particles collide, they observe a similar time for planetesimals to grow to half their mass as previous simulations, but a lengthened time for full formation. Indicating the importance of including fragmentation.

A more recent example is Hwang et al. (2017a) and Hwang et al. (2017b) where they use an N-body code to model the evolution of 'Kepler-multi's' (the close orbiting systems of Super-Earths detected by Kepler), but they model the collisions of such objects using an SPH code. Their N-body code shows highly grazing impacts where the mantles do not touch to be more common than direct head on impacts, so they focus their analysis on these.

b) Population synthesis Models

Population synthesis models take current theories of planet formation and use them to predict the population distribution of planets such models would generate to see if these predictions tally with current observations. As such an improvement in the understanding of a particular stage of formation can improve the entire model. One such population synthesis model is the Bern model (Alibert et al., 2005; Mordasini, 2018). These synthesis models can also provide realistic initial conditions for collision

simulations, for example this work also uses the results of the Bern model when deciding the mass of atmosphere of each target. For an in depth review of population synthesis models see Mordasini (2018).

c) Atmosphere Evolution Models

In a smaller scale than population synthesis, models which combine atmosphere formation processes can better understand how atmospheres evolve from the initial material accreted by a planet. Sinclair et al. (2020) for example use previous giant collisions and smaller scale cratering models to look at various possible paths an Earth-like planet's atmosphere might evolve along since the Moon-forming impact. They show that smaller atmospheres tend to grow, whilst larger ones lose mass, so a variety of initial compositions could result in the current Earth atmosphere. Atmospheres significantly thicker than the Earth's current one however would need to be initially primordial in composition to lose enough material to end up with the current Earths atmosphere, due to the reduced amount of material available for collision after the Moon-forming impact.

1.5 Thesis Outline

My thesis focuses on the results SPH simulations I have run of Super-Earth collisions. The next chapter (2) will summarise the SPH code as well as any other analytical processes that I have used. Chapter 3 focuses on initial atmosphere-less collisions, specifically the simulations which were run for Bonomo et al. (2019). Chapter 4 focuses on the results of simulating head-on collisions into a barotropic ideal gas atmosphere. Chapter 5 focuses on expanding out this formalism to include different impact angles. The final chapter (6) will detail current and potential future work as well as summarising the most important overall results.

2

Numerical Methods

This chapter is a summary of all the processes I have used to model and understand planetary collisions throughout this thesis. In particular it contains an in depth summary of a modified version of GADGET-2, which is the SPH code I have used to simulate the collisions, as well as a run through the processes of setting up and running collision simulations and some analysis methods.

2.1 GADGET-2

2.1.1 Smoothed Particle Hydrodynamics (SPH)

Smoothed particle hydrodynamic (SPH) methods for modelling fluids are based around the principle of splitting the fluid into individual particles and modelling their motions and interactions. For this to be feasible we need a way of calculating continuous fluid properties from the array of particles. This is done using a smoothing Kernel W. The density ρ_i of a particle for example can be calculated from

$$\rho_i = \sum_{j=1}^{N} m_j W(|r_{ij}|, h_i), \tag{2.1}$$

where $r_{ij} = r_i - r_j$ is the separation between particles located at r_i and r_j, and h_i are the smoothing lengths. For GADGET-2 these smoothing lengths are given by

$$\frac{4\pi}{3} h_i^3 \rho_i = N_{\text{sph}} \bar{m} = M_{\text{sph}}, \tag{2.2}$$

where N_{sph} is the number of smoothing neighbours, $\bar{m}$ the average mass per particle and M_{sph} the mass contained within a smoothing volume. For GADGET-2 it is the mass contained within the smoothing volume which remains constant, meaning that smoothing lengths can vary.

The Smoothing kernel which GADGET-2 uses is:

$$W(r,h) = \frac{8}{\pi h^3} \begin{cases} 1 - 6\left(\frac{r}{h}\right)^2 + 6\left(\frac{r}{h}\right)^3 & 0 \leqslant \frac{r}{h} \leqslant \frac{1}{2} \\ 2\left(1 - \frac{r}{h}\right)^3 & \frac{1}{2} \leqslant \frac{r}{h} \leqslant 1 \\ 0 & \frac{r}{h} > 1 \end{cases} \tag{2.3}$$

where $r = |r_{ij}|$ and $h = h_i$.

To construct the equations of motion we need to start with the Lagrangian $L = T - V$, where T is kinetic energy and V potential energy. For SPH fluid equations T is the standard result for the sum of an array of particles whereas the potential needs to encapsulate the mechanics required for fluids and so we construct it from equations of the fluid pressure. GADGET-2 uses a Lagrangian designed to conserve both energy and entropy (Springel, 2005) so that explosions are well represented compared to SPH equations which use temperature instead of entropy as the independent variable (Springel & Hernquist, 2002). Although designed to account for galaxy cluster scale phenomena, such as active galactic nucleii, entropy conservation is also useful for planets as planetary impacts can be modelled as explosions (Schlichting et al., 2015). Entropy conservation is also useful for modelling phase changes (Davies et al., 2020). In its original formulation the potential energy of fluid particles is derived from the pressure equation of a barotropic gas $p = A\rho^\gamma$ (see section a)). We use this Lagrangian to model atmospheres. In general, however, the pressure of the materials we simulate, and thus their potential, is derived using tabulated equations of state and so the exact Lagrangian used is more complicated.

The Lagrangian for gas particles in GADGET-2 is:

$$L(q, \dot{q}) = \frac{1}{2} \sum_{i=1}^{N} m_i \dot{r}_i^2 - \frac{1}{\gamma - 1} \sum_{i=1}^{N} m_i A_i \rho_i^{\gamma - 1}, \tag{2.4}$$

where q and $\dot{q}$ are the generalised coordinates. The solutions to the Lagrangian, can be derived using the calculus of variations and are given by:

$$\frac{d}{dt}\left(\frac{\partial L}{\partial \dot{q}_i}\right) - \frac{\partial L}{\partial q_i} = \sum_{j=1}^{N} \lambda_j \frac{\partial \phi_j}{\partial q_i}. \tag{2.5}$$

These are known as Lagrange equations of the first kind. λ_i here are Lagrange multipliers, while ϕ_i are a series of constraints on the coordinates of the lagrangian based on the particular problem we are dealing with. GADGET-2 uses the size of its variable smoothing lengths as its constraint:

$$\phi_i(q) = \frac{4}{3}\pi h_i^3 \rho_i - M_{sph} = 0. \tag{2.6}$$

Using the Lagrangian, the Lagrange equations for each of the smoothing lengths h_i, and our holonomic constraints we can derive a formula for the Lagrange multipliers:

$$\lambda_i = \frac{3 m_i P_i}{4\pi h_i^3 \rho_i^2}\left(1 + \frac{3\rho_i}{h_i}\left(\frac{\partial \rho_i}{\partial h_i}\right)^{-1}\right)^{-1}. \tag{2.7}$$

Using this and the Lagrange equation for our position coordinates we can now derive that,

$$m_i \frac{dv_i}{dt} = -\sum_{j=1}^{N} \frac{m_j P_j}{\rho_j^2}\left(1 + \frac{h_j}{3\rho_j}\frac{\partial \rho_j}{\partial h_j}\right)^{-1} \nabla_i \rho_j. \tag{2.8}$$

To determine the gradient of density we use its definition in 2.1, to obtain the following,

$$\nabla_i \rho_j = m_i \nabla_i W_{ij}(h_j) + \sum_{k=1}^{N} m_k \nabla_i W_{ki}(hi)\delta_{ij}. \tag{2.9}$$

Where

$$W_{ij}(h) = W(|r_{ij}|, h). \tag{2.10}$$

Applying this to equation 2.8, we thus obtain the bulk of the equation of motion that GADGET-2 uses:

$$\frac{dv_i}{dt} = -\sum_{j=1}^{N} m_j \left[f_i \frac{P_i}{\rho_i^2}\nabla_i W_i j(h_i) + f_j \frac{P_j}{\rho_j^2}\nabla_i W_i j(h_j)\right], \tag{2.11}$$

where

$$f_i = \left(1 + \frac{h_i}{3\rho_i}\frac{\partial \rho_i}{\partial h_i}\right)^{-1}. \tag{2.12}$$

This is not complete however, numerical codes in general struggle with representing shocks due to their discontinuous nature. To confront this an artificial viscosity force is also included (see section b)).

a) Barotropic Gases and Pseudoentropy

A barotropic equation of state is an equation of state where pressure can be defined solely as a function of density. These are typically used for systems where the density has a clear dependence on temperature, as they allow for construction of simpler models which don't need to account for heat transfer processes.

Reversible processes for example can be well described by barotropic equations of state, because they are adiabatic (i.e. thermally isolated from their surroundings). To derive the equation of state for such a gas, lets begin with the first law of thermodynamics:

$$đQ < d\epsilon + pdV \tag{2.13}$$

where pdV is the work done per unit mass of fluid for a volume change of dV, $d\epsilon$ the change in internal energy, and $đ$ is the quantity of heat absorbed by the unit mass of fluid from its surroundings. For a process that isn't dissipative this becomes an equality. Considering we are talking about an adiabatic process $đQ = 0$ and so:

$$d\epsilon + pdV = 0. \tag{2.14}$$

An ideal gas has an equation of state of $p = R\rho T/\mu_{\mathrm{mol}}$, where R is a gas specific constant and μ_{mol} the molar mass. If we consider V to be the volume for a unit mass of fluid our equation then becomes

$$0 = \frac{d\epsilon}{dT}dT + \frac{RT}{\mu_{\mathrm{mol}}V}dV = C_{\mathrm{V}}dT + \frac{RT}{\mu_{\mathrm{mol}}V}dV \tag{2.15}$$

where we have defined the specific heat capacity at constant volume C_{V}. This equation can be rearranged to

$$C_{\mathrm{V}}d\ln T + \frac{R}{\mu_{\mathrm{mol}}}d\ln V \tag{2.16}$$

which implies a solution of:

$$V \propto T^{C_{\mathrm{V}}\mu_{\mathrm{mol}}/R}. \tag{2.17}$$

Using our ideal gas equation of state we can thus derive

$$p \propto T^{1+C_{\mathrm{V}}\mu_{\mathrm{mol}}/R}, \tag{2.18}$$

$$p \propto V^{-1+C_{\mathrm{V}}\mu_{\mathrm{mol}}/R}. \tag{2.19}$$

The final of these exponential relations is our barotropic equation of state. Normally however this equation is written in a slightly different form, which is derived from the ratio of specific heat capacities at constant pressure to constant temperature $\gamma = C_{\mathrm{p}}/C_{\mathrm{V}}$. These specific heat capacities are related to one another by

$$C_{\mathrm{p}} - C_{\mathrm{V}} = \frac{R}{\mu_{\mathrm{mol}}}. \tag{2.20}$$

This gives us our final barotropic equation of state of

$$p = A\rho^{\gamma}. \tag{2.21}$$

The variable A is known as the pseudo-entropy of the fluid because its value is closely related to that of entropy. If we note that heat is $đQ = TdS$ then for our non-dissipative adiabatic process we would have zero entropy change, which corresponds to a constant pseudo-entropy. This implies that a fluid where all elements have the same pseudo-entropy should itself be isentropic.

b) Shock representation and Artificial Viscosity

The typical analytic representation of a shock front is as a surface where there is a discontinuity in velocity, temperature and entropy. The boundary conditions which relate the partial differential equation solutions on either side of this discontinuity are called the Rankine-Hugoniot equations. While this is a powerful tool for determining analytical solutions it is not as useful for numerical methods of solving fluid motion (which are often required due to the non-linear nature of the fluid flow equations), as the shock surfaces themselves are capable of motion described by non-linear differential equations which are computationally expensive to solve.

Real systems don't have a perfect discontinuity however, the shock front of a real system has a finite width of transition which is dependent on the strength of dissipative processes occuring such as viscosity and heat conduction. Inspired by this VonNeumann & Richtmyer (1950) proposed the solution of using an artificial viscosity, which has been tuned such that it has a strength sufficient that the shock front has a thickness comparable to (and preferably greater) than the separation between measurement points. This artificial viscosity allows the motion of the shock front to be described to a reasonable degree of accuracy solely by numerically solving the equations for fluid motion.

For a Lagrangian method of solving fluid problems such as SPH the problem of representing shocks is further compounded by the ability of particles to move. They tend to mimic molecules exhibiting random movements of the size of the width of a shock front. To account for this the artificial viscosity needs to be formulated in such a fashion as to also damp these random motions (Monaghan & Gingold, 1983). SPH artificial velocity forces typically take the form

$$\frac{dv_i}{dt}|_{visc} = -\sum_{j=1}^{N} m_j \Pi_{ij} \nabla_i \bar{W_{ij}}, \tag{2.22}$$

where $\bar{W_{ij}}$ is the arithmetic mean of $W_{ij}(h_i)$ and $W_{ij}(h_j)$ and Π_{ij} is a tensor describing the strength of the artificial velocity.

GADGET-2 uses the Monaghan (1997) formulation of the artificial viscosity tensor which is constructed using the concept of signal velocity v_{ij}^{sig}. This allows it to provide good solutions for systems with special relativity, which was important for GADGET-2's original purpose as a cosmological code. This signal velocity is

$$v_{ij}^{\text{sig}} = c_i + c_j - 3w_{ij}, \tag{2.23}$$

where c_i is the sound speed at particle i and w_{ij} is given by

$$w_{ij} = \begin{cases} \frac{\underline{v}_{ij}.\underline{r}_{ij}}{|\underline{r}_{ij}|} & \underline{v}_{ij}.\underline{r}_{ij} < 0 \\ 0 & otherwise \end{cases}. \tag{2.24}$$

From this the artificial viscosity tensor is given by

$$\Pi_{ij} = -\frac{\alpha}{2} \frac{v_{ij}^{\text{sig}} w_{ij}}{\rho_{ij}}, \tag{2.25}$$

where ρ_{ij} is the mean density of particles i and j.

2.1.2 Gravitational Algorithms

Gravitational forces have a significant effect on phenomena of the scale of planets, it is therefore important that our simulations model these forces well. The simplest method one can consider for constructing a code that calculates the gravitational interaction between each particle in an array of particles is to individually calculate the interaction between each particle and each other particle. This method however becomes very slow

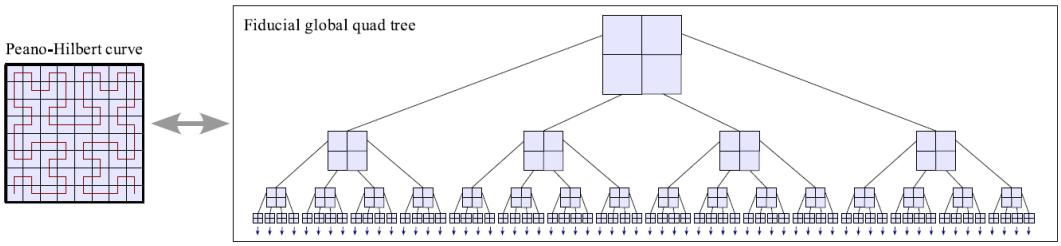

Figure 2.1: A 2D representation of a the hierarchical tree used by GADGET-2, along with a representation of how the data is stored in memory. In 3D the code uses Oct-trees stored using 3D Peano-Hilbert curves (From Springel 2005).

for large numbers of particles, the time it takes scales as roughly $O(n^2)$ where n is the number of particles. As such for large scale simulations approximations are often made to shorten the time. The two main approximation algorithms in common usage are as follows:

a) Particle Mesh methods

For particle mesh methods a potential is determined by transforming our particle distribution into a grid or mesh, (we are essentially transforming to an Eulerian method of doing fluid calculations here) the density and thus the gravitational potential for each point can be defined, and therefore we can calculate the acceleration for each particle by extrapolating the grid potential to the particles' positions.

b) Hierarchical Trees

For the hierarchical tree method used by GADGET-2, for each timestep the total volume covered by the simulation is split into 8 equally sized chunks (i.e split in half along each coordinate axis, see figure 2.1). The total mass and centre of mass of each chunk is measured. This process is repeated iteratively for each chunk until at the lowest level there is only 1 particle in every 'leaf' node.

To determine the gravitational attraction on a particle, P_i, within the fluid from the surrounding array of particles we use an opening criterion to determine how deep to go in the heirarchical tree for each part of the total volume. The gravitational forces are then calculated for P_i from each of the last branch nodes to follow the criterion. The simplest version of this method uses an opening angle, where nodes which have a smaller

angular size when observed from P_i do not get opened. GADGET-2 on the other hand uses the following force dependent measure:

$$\frac{GM}{r^2}\left(\frac{l}{r}\right)^2 \leqslant \alpha|\underline{a}|, \tag{2.26}$$

where M is the mass of the node, l its extension, and r its distance from P_i. $\underline{a}$ is the previous timestep's acceleration and α a tolerance parameter. This method is chosen over the constant opening angle method as it means that the typical relative error on the force remains roughly constant over the course of the simulation independent of the dynamics at that particular point in time.

GADGET-2 also includes another criterion to ensure that errors from extremely small distances don't become unbound:

$$|r_k - c_k| \leqslant 0.6l \tag{2.27}$$

where $c = (c_x, c_y, c_z)$, i.e this inequality applies separately to each coordinate axis. Essentially what this inequality does is that it requires that the particle in question is outside a box roughly 20% larger than the tree node.

c) Our Choice of Algorithm

These two methods of calculating gravitational interactions can be combined, such that long range forces are calculated via mesh methods and short range ones by tree methods, such methods are known as treePM methods. While GADGET-2 has the capability to perform such calculations we have chosen to use solely the Hierarchical tree formulation, as the forces we were most interested in were the close up forces during the collision process.

2.1.3 Tabulated Equations of State

The main difference between the version of GADGET-2 used for these simulations and the release version is the modifications that have been made so that GADGET-2 can use tabulated equations of state, which means it can better model the core and mantle of planetary bodies (further detail on these modifications can be found in Marcus et al. 2009 and Ćuk & Stewart 2012). The specific equations of state used were derived from ANEOS/MANEOS models (Melosh & Vickery, 1989). Instead of calling these models

every time we needed to determine thermodynamic values, they were instead used to generate grids of tabulated values, and when a value is needed it was interpolated from neighbouring points in the grid (Marcus et al., 2009). These equation of state tables therefore needed to be finely gridded to ensure phase boundaries were well resolved. This method was used as it is a much more rapid process than calling ANEOS every time a thermodynamic variable is needed. The equations of state which we used were: iron for the inner core of planets, and forsterite for their mantles, these can be found in full at Carter et al. (2019).

The ID number N_{ID} of a particle is used to tell which material it is and thus which equation of state should be used. The code uses an $IDSKIP$ variable which denotes the range of N_{ID} values possible for each material. All particles with an ID number in the range $(n-1) \times IDSKIP \leqslant N_{\mathrm{ID}} < n \times IDSKIP$ are of the same material and use the same equation of state. A similar ID number offset was also used to distinguish which planet the particles originated in.

2.1.4 Ideal Gas Atmospheres

We have elected to use the simplest model of a gas we could, that of an ideal gas. We use the built in methods GADGET-2 already has for representing hydrogen, as that is what we expect the primordial atmospheres of planets to primarily be made of. This method is not without its flaws however, ideal gas models do not behave realistically at high densities and temperatures, for example those we observe near the surface of the mantle. This is because ideal gases make the unrealistic assumption that particles are infinitesimal in extent and collide inelastically, at high temperatures and densities particles are close and collide often so accurate representation of collisions is much more important, and as such ideal gas models are less useful. Despite these flaws the ideal gas model has been chosen because it is the simplest and most universally understood gas model. It thus provides a good baseline for further tests that more accurately model the atmosphere.

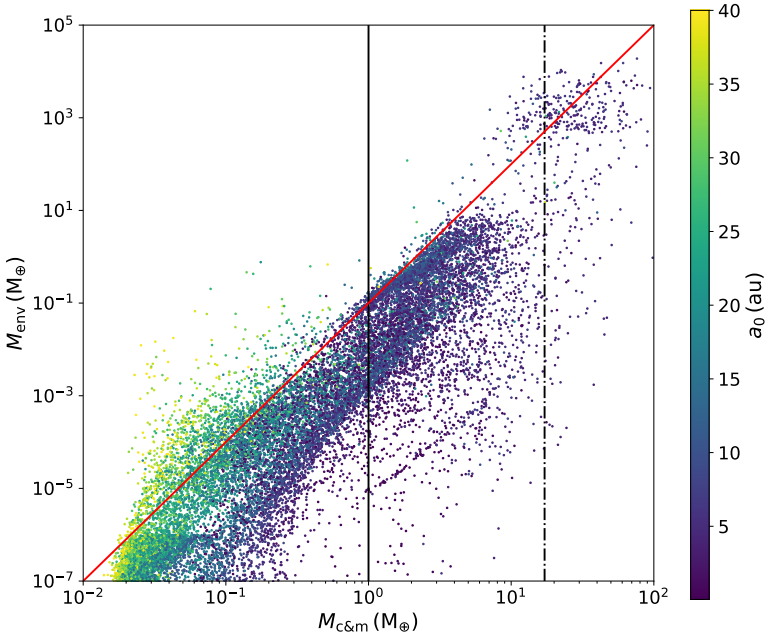

Figure 2.2: The envelope mass compared with the core and mantle mass of 10 Myr old planets derived from Bern Model formation simulations. The red line shows equation 2.28, the solid black line gives the Earth's mass, while the dash-dotted one is Neptune's mass. Data provided by Christoph Mordasini.

2.2 Simulation Setup

We model each of our planets as being made out of 2 or 3 separate layers of different materials, an iron core, a forsterite (silicate) mantle and an ideal gas model of a hydrogen atmosphere. The steps we take in generating these planets and setting them up for a collision simulation are detailed below. These planets had twice the mass of mantle as they had of core, following the works of Ćuk & Stewart (2012) and Marcus et al. (2009).

If we were modelling an atmosphere a hydrogen atmosphere was then added on top of the mantle. The mass of atmosphere, M_{atmos}, we added was predicted from the total core and mantle mass, $M_{\text{c\&m}}$, using the following equation:

$$M_{\text{atmos}} = 0.1 \times \left(\frac{M_{\text{c\&m}}}{\text{M}_\oplus} \right)^3 . \tag{2.28}$$

This equation was generated empirically from population synthesis data to describe the trend in the mean atmosphere mass as core and mantle mass increases seen in the Bern global planet Model (Alibert et al., 2005; Mordasini, 2018). This equation best describes planets between 1 and $7M_\oplus$. It should be noted however that there was a significant spread around these atmosphere masses for planets generated in the Bern model simulation that this result is derived from, so this was only treated as a first order estimate to ensure we were testing envelope masses of the right order of magnitude. Figure 2.2 shows a small sample from a later set of Bern model simulations, these include more erosive phenomena so instead of providing the average atmosphere mass the relation of equation 2.28 appears as an upper limit.

2.2.1 Planet Generation

An outline of the processes we used to generate each planet is as follows:

1. Begin by determining radial density and temperature profiles for the core and mantle material.
2. Turn these radial profiles into an array of particles by splitting the planet into an array of shells and using the density of each shell to determine the number of particles.
3. Run an equilibration simulation to ensure the planet is stable
4. If the planet has an atmosphere, determine radial density profiles for it.
5. Add atmosphere particles in the same fashion as step 2.

6. Repeat equilibration simulation to ensure atmosphere is stable

This section covers each step in detail.

a) Radial Profiles

The initial temperature-radius profiles that we work from for the core and mantle of objects are those from Valencia et al. (2006). The initial input to our set-up code are these radial profiles, as well as the amount of particles we wish to use, and radii for the surface of the core and the surface of the mantle along with estimates for the bulk density of each part.

This initial input density profile is a top hat function which isn't stable and so we do the following process to determine a stable one from it:

First the cumulative mass and gravity radial profiles are generated from the inside out. These mass and gravity profiles are then used to generate a radial pressure profile from the outside in. The pressure and temperature profiles are then used along with the equation of state to generate a radial density profile. From this density profile mass, gravity and pressure radial profiles are regenerated. This process is continued iteratively until the density profile no longer changes. Using these profiles and the input parameters the next step is to split the object into radial shells and start placing a number of particles dependent on a shells volume and assumed density at random positions in each radial shell. Particle composition is determined based on shell location.

The iterative profile refinement method doesn't work with an ideal gas however. This is because of the use of an ideal gas equation, at high temperatures and pressures an ideal gas will compress a lot more easily than a real gas because the model ignores interparticle effects. When combined with the process used to refine initial density estimates this results in the atmosphere particles becoming far too dense. This unphysical density was sufficiently bad it resulted in particles sinking to the planet's core during equilibration.

To avoid these unphysically high densities we instead chose to set the density and other thermodynamic parameters of the particles in each radial shell directly from radial profiles. The GADGET-2 equilibration runs (see section b)) were relied upon for ensuring a stable planet. These radial atmospheric profiles were the work of my collaborator Christoph Mordasini, they were generated with the planetary interior structure model COMPLETO21 (Mordasini et al., 2012; Jin et al., 2014; Linder et al., 2019). In brief, this

code determines atmosphere structure by solving the equations for mass conservation, energy generation, hydrostatic equilibrium and energy transport using the assumption that planets are spherically symmetrical, these equations are given below:

$$\frac{\partial m}{\partial r} = 4\pi r^2 \rho \tag{2.29}$$

$$\frac{\partial l}{\partial r} = 0 \tag{2.30}$$

$$\frac{\partial P}{\partial r} = -\frac{GM}{r^2}\rho \tag{2.31}$$

$$\frac{\partial T}{\partial r} = \frac{T}{P}\frac{\partial P}{\partial r}\nabla\left(T, P\right). \tag{2.32}$$

The parameters here are the mass m inside a given radius r, the gas density ρ, the intrinsic luminosity l, the pressure P, the temperature T and the temperature gradient $\nabla\left(T, P\right)$. The Schwarzschild criterion was used to determine whether or not a layer was stable against convection and thus whether or not the main component of energy transport would be convection or radiative diffusion. This criterion is, a system is stable against convection if

$$-\frac{dT}{dZ} < \frac{g}{C_{\mathrm{p}}}. \tag{2.33}$$

where g is the gravitational acceleration at that point, and C_{p} the heat capacity at constant pressure.

Our atmospheres were modelled using an ideal gas equation of state for reasons of simplicity, so we use that here to solve these hydrodynamic equations. The opacities which were used were those corresponding to a condensate free gas with solar material composition as per Freedman et al. (2014). The final piece that is needed to solve these structure equations is the intrinsic luminosity, l, of the planets. This was obtained in a similar fashion to relation 2.28 where Bern model formation simulations were used to generate an array of planets of different masses from which a function describing the mean luminosity for each mass could be generated:

$$\frac{L}{L_{\mathrm{J}}} = 0.1 \times \left(\frac{M_{\mathrm{planet}}}{\mathrm{M}_{\oplus}}\right)^{1.5}. \tag{2.34}$$

L here is the planets luminosity, L_{J} the luminosity of Jupiter, and M_{planet} is the total mass of the planet in question. Like for equation 2.28 there is a large degree of spread about the result here, this equation is merely a first order estimate for the distributions

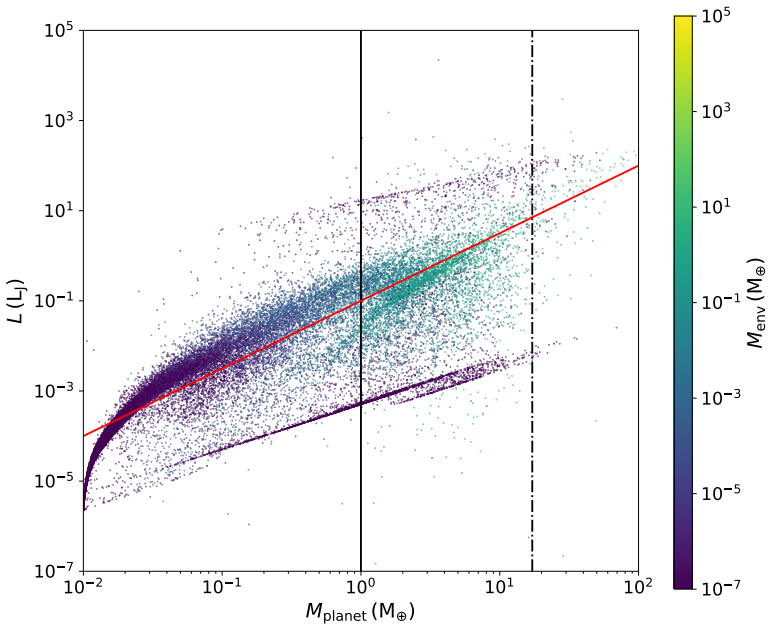

Figure 2.3: Luminosity of 10 Myr old planets modelled using Bern model formation simulations. The estimate of equation 2.34 is given by the red line, the solid black line is an Earth mass and the dash-dotted line is the mass of Neptune. Data provided by Christoph Mordasini.

peak (see figure 2.3). This particular luminosity relation corresponds to planets of $\sim$ 10 Myr which corresponds to a time soon after protoplanetary gas disc dispersal. This time was chosen because protoplanetary disc dispersal is when we would expect giant collisions to begin occurring as the disc is no longer damping the eccentricities in the planets orbits.

Once these hydrodynamic equations have been solved we then have our radial density and temperature profiles for the atmosphere.

b) Equilibration

While the above methods generate radial profiles that are analytically stable, they do not account for any instabilities that may be generated from SPH forces between particles, for example if our random placement of particles has caused there to be overdensities or underdensities at particular points in the planet. As such, before we run collisions with our input planets, we first do an equilibration run for each planet. To hasten this stabilisation process we use a couple of cooling methods

The first of these methods is velocity damping, for this method we apply a multiplicative restitution factor to the velocity of each particle at each time step (we chose 50% as per Carter et al. 2018). This ensures that the movement of particles to reduce any over or underdensities does not overshoot and oscillate.

The second method is entropy forcing, for this method we reset the entropy (or pseudo-entropy for the atmosphere) of each particle to a constant value at each time step. Amongst other things this ensures that our planets have isentropic layers. The entropy values used in this work were $1.3\,\mathrm{kJ\,K^{-1}\,kg^{-1}}$ for the iron core and $3.2\,\mathrm{kJ\,K^{-1}\,kg^{-1}}$ for the mantle as per Carter et al. (2018). For the atmosphere we instead modify the pseudo-entropy A, this is a value that behaves very similarly to the entropy but isn't precisely the same thing (see section a)). This was set at different values for different stages of the work in this paper, initially in chapter 4 we used a value of $5 \times 10^{11}\mathrm{Ba\,g^{-\gamma}\,cm^{3\gamma}}$ due to it giving a more reasonable temperature and density near the surface, but for chapter 5 we decided $1.3 \times 10^{12}\mathrm{Ba\,g^{-\gamma}\,cm^{3\gamma}}$ would be better as this provided the closest overall final profile to Christoff Mordasini's initial predictions (see figure 2.4).

To determine whether or not our planets had reached a stable equilibrium we looked at the velocities and radial distances of the planet particles. At equilibrium the values for bulk radial velocity for each material and also the radial velocity for surface particles for each material should be zero, whereas the average and furthest radial distances of particles to the planet's centre of mass should have asymptoted to a constant value. This equilibration was continued until change in radius per timestep was less than $10^{-3}\,R_\oplus$. Typically we equilibrated the core and mantle before adding an atmosphere on top, as this meant we also generated a stable equilibrated atmosphereless planet we could use as a projectile. For the initial core at the typical resolutions we used of 10^5 particles per $5\,\mathrm{M_\oplus}$ this took runs of roughly 28 hrs in simulation time. Atmosphere equilibration took approximately four times longer, likely because of the decrease in spatial resolution meaning that particles interacted less. Figure 2.5 shows the radial profiles of an equilibrated target planet.

2.2.2 Collision Setup

Typical parametrisations of collisions (see figure 2.6) tend to be dependent upon a point of impact, impact angle and impact velocity for example are both measured at this point

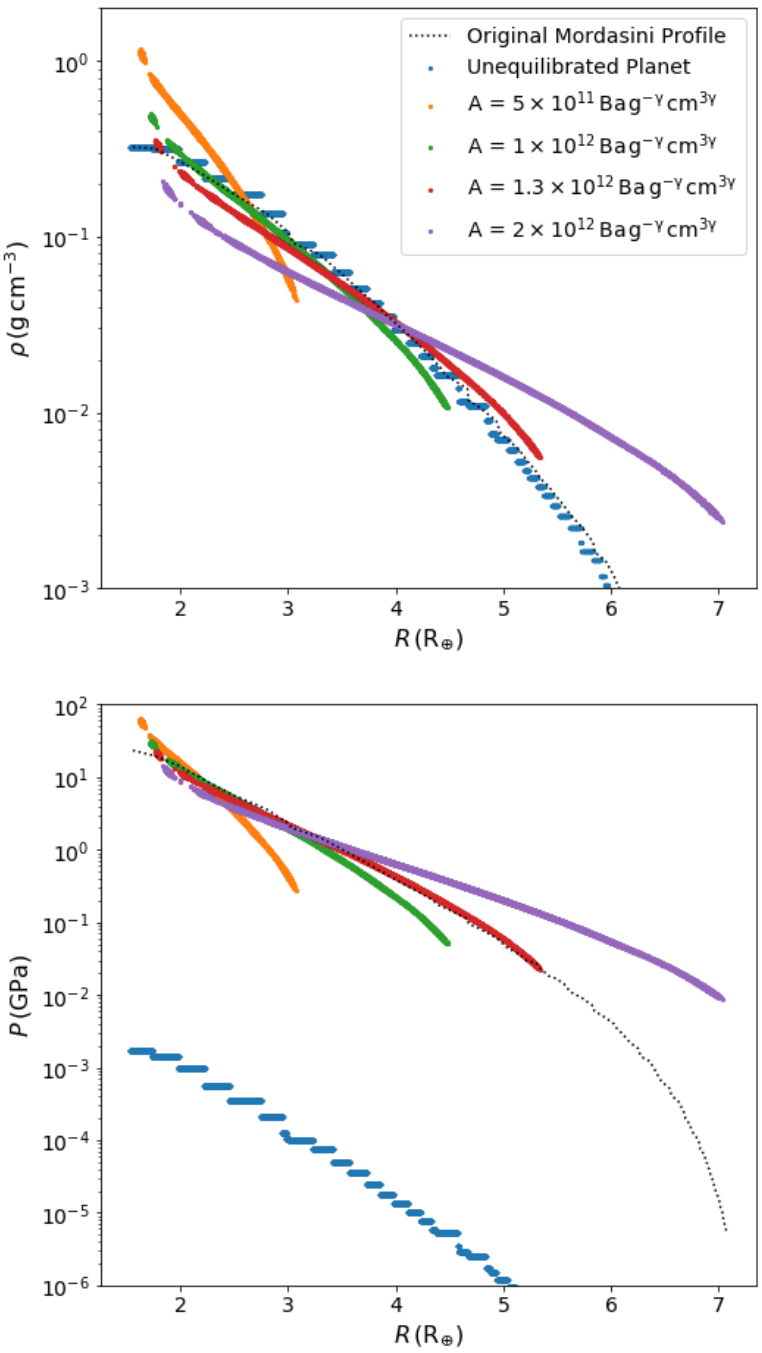

Figure 2.4: Comparisons of the different radial density and pressure profiles after equilibration for different forced pseudo-entropy values for a 6.25 $M_\oplus$ planet, of which 1.25 $M_\oplus$ was atmosphere.

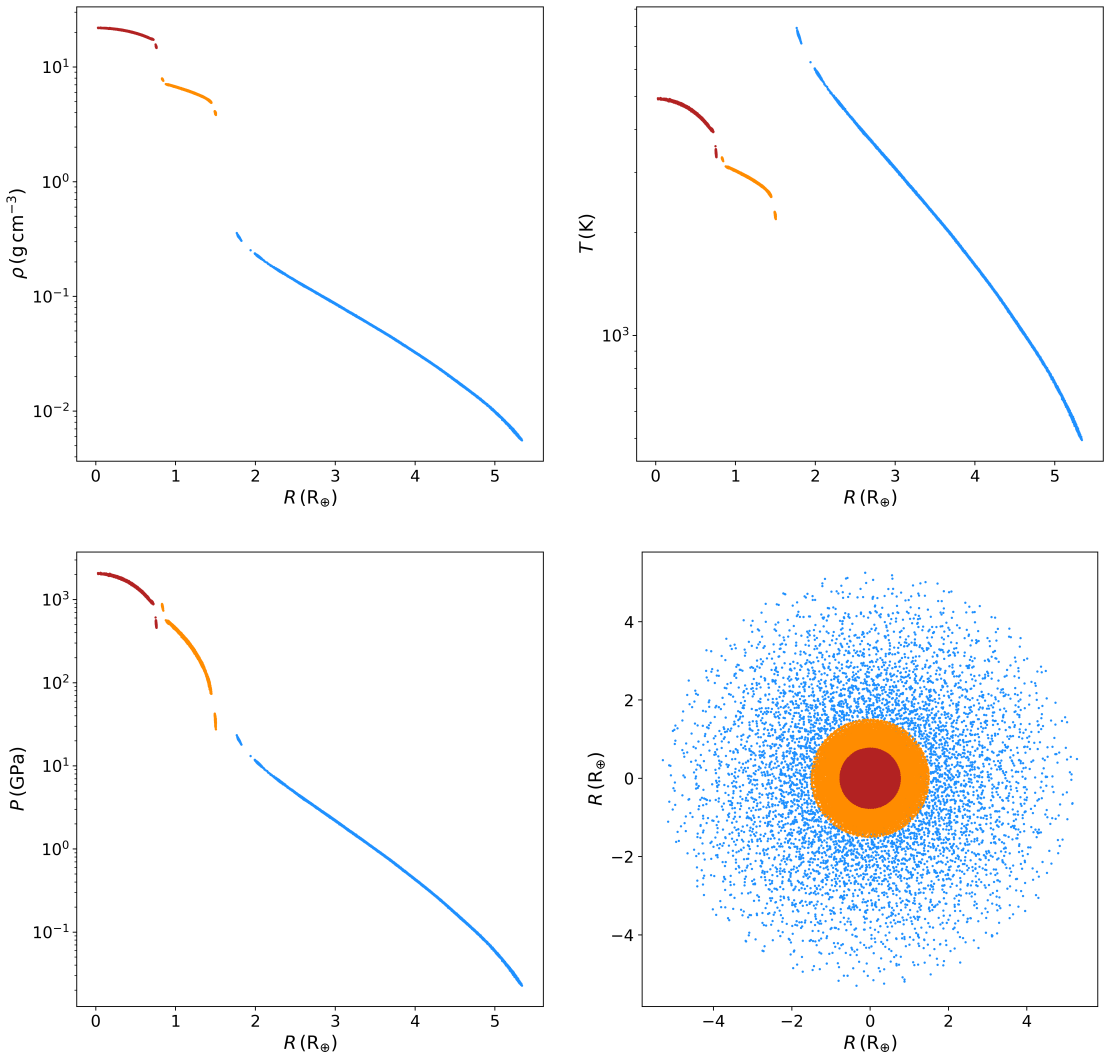

Figure 2.5: Example radial profiles of an equilibrated 6.25 $M_\oplus$ planet for density (top left), temperature (top right), and pressure (bottom left). Colour indicates material type: red for iron particles, orange for forsterite, and blue for hydrogen. The bottom right graph shows a cross-sectional slice of the planet.

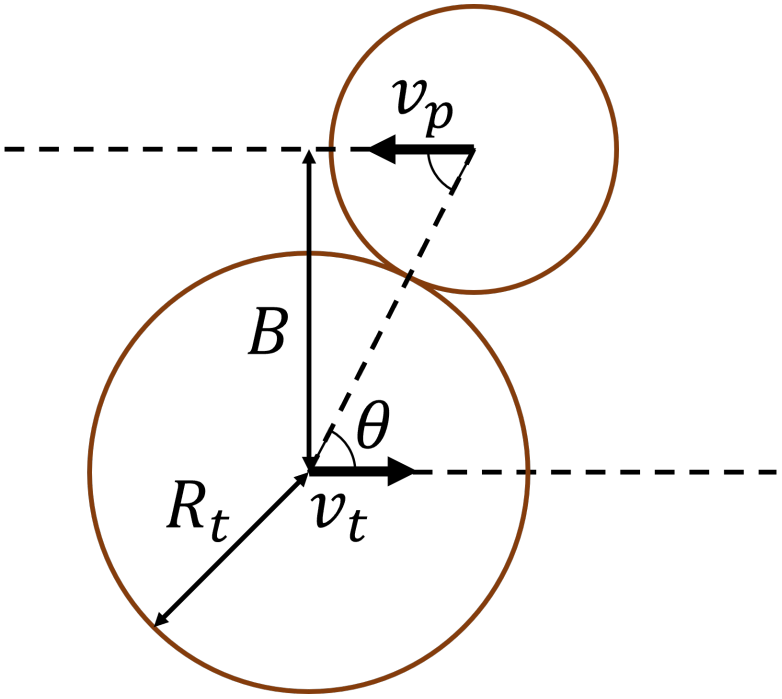

Figure 2.6: A diagram of an atmosphere-less collision, along with the parameters typically used to describe them. Usually we are more interested in the relative velocity $v_{\mathrm{rel}} = v_{\mathrm{p}} - v_{\mathrm{t}}$ than either the projectile or target velocities. Typically we also normalise the impact parameter B by the sum of the two planets radii $b = B/(R_{\mathrm{p}} + R_{\mathrm{t}})$.

of impact. For atmosphere-less planets this point has a simple definition, it occurs when the mantles of the two planets touch.

Because of how particles are defined in relation to others in SPH, determining the outer radius of the mantle requires some assumptions. Each SPH particle has a mass and a density, which is defined by the particle's position relative to neighbouring ones, but no set shape. To define a hard outer boundary for simulated planets we have chosen to assume that each particle is spherical and has constant density equal to its SPH density. We consider a collision to have occurred when these spheres from the projectile particles first overlap those from the target.

A further complication comes when we add atmospheres to our planets. Atmospheres decrease in density approximately exponentially with increasing radius asymptoting to zero at large radii, meaning that we cannot define a clear boundary where the planets impact one another. As such we have chosen to consider our point of impact instead as when the mantles of the two planets collide.

Further complications to this method arise when we deal with highly grazing impacts, that is, collisions where the mantles do not collide at all, but projectile and target do pass through one another's atmosphere. For such collisions we chose to measure the impact parameter and impact velocity at the point of closest approach of the two centres of mass. Both of these two methods are illustrated in figure 2.7. We also chose to use impact parameter over impact angle as a measure of obliqueness of collision as if we took the measurement at the point of closest approach all impact angles for highly grazing impacts would be 90°, which doesn't measure how deep in the atmosphere the approach gets. Impact parameter on the other hand, which can be defined as the distance between the planets centre of mass in the plane of collision perpendicular to their relative velocity, can be used to differentiate different highly grazing collisions. In this work we chose to normalise impact parameter with respect to mantle surface radii for ease of comparison with previous works which did not include atmospheres (e.g. Leinhardt & Stewart 2012).

To set up the initial conditions for the beginning of each simulation we used a simple model of the system. We assumed that the planets could each be well represented by point particles and used the time reversal symmetry of a two body system and a basic Verlet integrator to run the projectile back until it had reached the initial seperation required. We arbitrarily elected to use initial separations of 5 times the sum of the

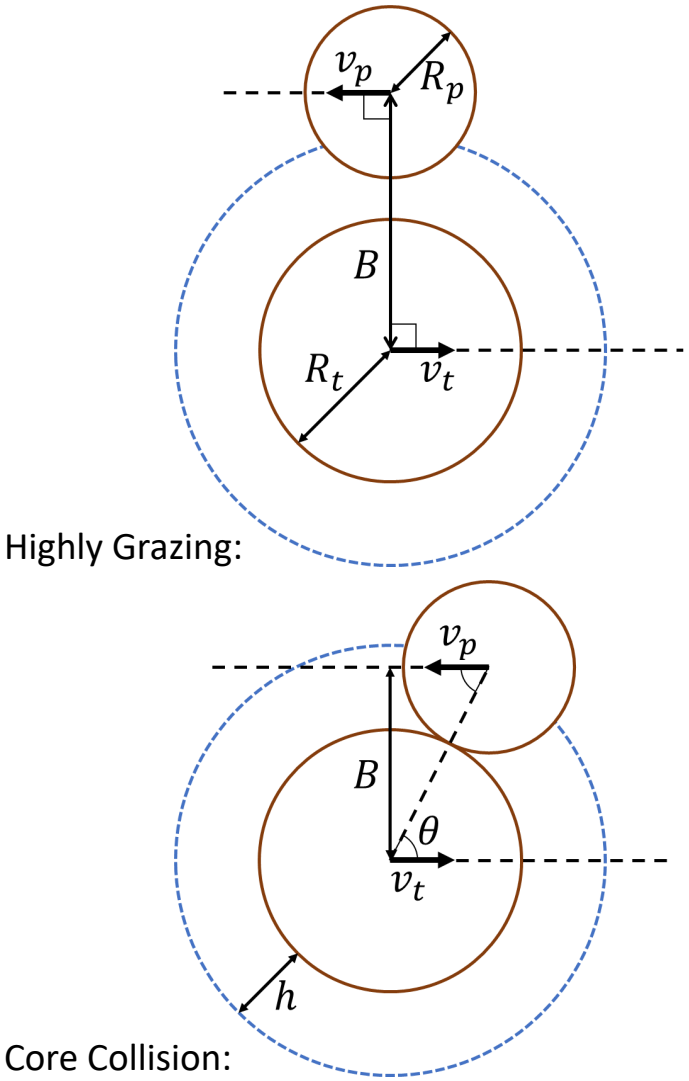

Figure 2.7: The collision geometry for collisions with an atmosphere. We have elected to use a method of parametrising collisions that is independent of the scale height of an atmosphere, and so the normalised impact parameter $b = B/(R_\mathrm{p} + R_\mathrm{t})$ will be > 1 for highly grazing collisions.

projectile and target mantle surface radii as this meant the separation was substantially larger than the atmosphere height and thus tidal forces on the two planets would be reduced, meaning the planets for the simulation could be equilibrated in isolation.

2.2.3 Collision Point Resimulation

Because our setup process neglects the effects of tidal forces and we do not have a good model for atmospheric drag the collision parameters it predicted were not the same as those at the point of impact, this thus meant that we needed to test the accuracy of our initial predictions for collision parameters by analysing each simulated collision in high time resolution at the point of collision. Simulating the entire collision at such a high time resolution would produce many GB of unneeded data however, so to determine the strength of these effects we re-simulate the moment when the impact happens with a significantly higher output frequency for snapshot data files than the rest of the collision. The precise time resolution used was dependent on the hard drive space available, so it varied between the sets of simulations used for each chapter, as an example however, in chapter 5 we used 1000 s per snapshot in simulation time for the main simulations and 10 s for the collision point resimulation.

To determine the precise point of collision we needed to define it in terms of the simulation particles. We defined it as the first snapshot in which two mantle particles were closer to one another than the sum of their particle radii. To calculate this radius r_{particle} we assumed each particle was spherically symmetric and had a constant density ρ_{particle} equal to its SPH density. This gives a radius of

$$r_{\text{particle}} = \left(\frac{3m_{\text{particle}}}{4\pi\rho_{\text{particle}}} \right)^{\frac{1}{3}}, \tag{2.35}$$

where m_{particle} is the particles mass. Our corrected collision parameters were then measured using the bulk properties of each planet, for example impact velocity from the relative bulk velocity of the two initial objects, or impact parameter from the distance between the two planets centre of mass perpendicular to their relative velocity.

To increase the speed of our detection of the collision point for collisions when the mantles collide, instead of measuring the separation between all particles in the projectile and target, we instead selected the outermost ‘crust’ layer of mantle particles and only measured the separations for those. Because measuring particle separation for all particle

pairs is a process which scales as n^2 using this smaller selection of particles significantly increases the speed of the process. We defined the outermost layer as the mantle particles which in the initial equilibrated snapshot for a planet had distances from the centre of mass of greater than ~ 0.99 times the most distant mantle particle. To ensure both short calculation times and also good coverage of crust particles all over the planet's surface, this cutoff was fine tuned for each different mass planet.

2.2.4 Physical and Simulation based limits on collision parameters

The precise values for collision parameters were dependent on what was being tested in that batch of collisions. There are however some boundaries on what is feasible to test, I shall outline some of these here:

a) Simulation Run time

How long we wish to simulate for depends upon which processes we wish to simulate as different processes have different timescales which they work over. A good way of estimating the timescale for a process is by calculating its 'dynamical time'.

The gravitational dynamical time, $t_{\rm dyn}$, gives a good estimate for the amount of time required for gravitational resettling to occur. It is given by

$$t_{\rm dyn} = \sqrt{\frac{R^3}{GM_{\rm tot}}} \tag{2.36}$$

where $M_{\rm tot}$ is the total mass of the system and R the largest separation between projectile and target. For typical collision parameters used in this work (i.e. two Super-Earth mass planets starting at a separation 5 times their combined radius) this value was $\sim 8\,$hrs. To ensure that we have simulated for long enough for the mass of bound material in each remnant mass to be stable we should simulate for long enough to model multiple gravitational dynamical times.

After a collision the majority of the material is a superheated vapour, and planets are typically quite extended in radius. We do not consider the cooling of such objects, in part because it is difficult to model such processes as they can be very dependent on precise composition and for the sake of simplicity we model planets with single composition layers. The timescale for cooling processes on this scale also tends to be substantially

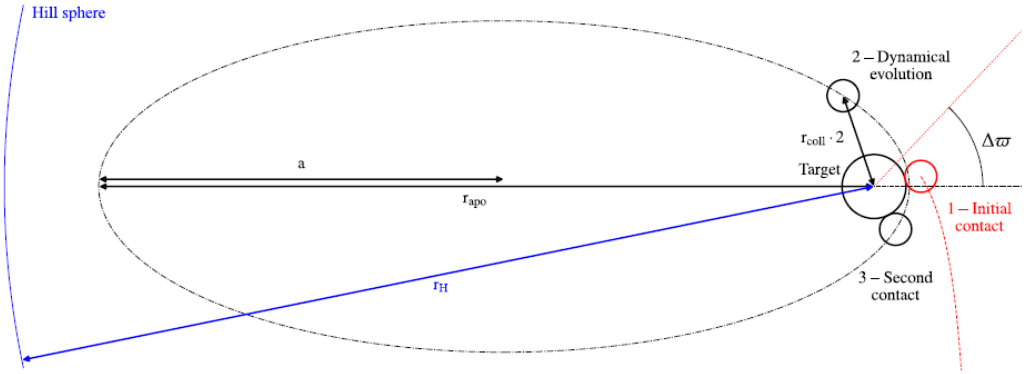

Figure 2.8: A diagram from Emsenhuber & Asphaug (2019b) detailing the dynamics of a graze-and-merge collision. For a graze-and merge collision to occur the initial collision must slow the projectile down sufficiently that the apoapsis of its post-collision orbit around the target is less far than the Hill radius.

longer than for gravitational ones. Liu et al. (2015) for example approximate the cooling time for a Super-Earth planet after a collision to be in the range of $10\,\mathrm{kyr} < t_{\mathrm{cool}} < 1\,\mathrm{Myr}$ depending on collision speed. We would expect the cooling times of our post-collision planets to be of the same order of magnitude, and this time is multiple orders of magnitude larger than the gravitational dynamical time.

For glancing collisions, there is a possibility of the projectile rebounding off the target. If, when the projectile rebounds, no mass is lost from the target then the collision is called a 'hit-and-run'. If the rebounding projectile has insufficient kinetic energy to escape from the gravitational pull of the target it is pulled back for a secondary collision. These multi-collision events are known as 'graze-and-merge' collisions and are covered in depth in Emsenhuber & Asphaug (2019b). The time needed for a re-collision to occur depends upon the time required for the projectile to orbit back round to collide with the target (see figure 2.8 for a diagram of this orbit). For real planets in solar systems the Hill sphere of the target is a physical limit on the size of such a re-collision orbit. If a projectile reaches the edge of the Hill sphere it will no longer be bound to the target and the main object gravitationally affecting it will be the solar system's star. A re-collision may occur after the projectile escapes the Hill sphere, but it may be multiple more stellar orbits later. If we know the masses of the planets and star and the orbital distance we can thus estimate the maximum time required to observe a secondary collision, the first

thing we need to do is to determine the Hill radius of the target planet, this is:

$$r_{\rm H} = a_{\rm i} \sqrt[3]{\frac{M_{\rm t}}{3M_*}}, \tag{2.37}$$

where $a_{\rm i}$ is the orbital distance of the target from the star, $M_{\rm t}$ the target mass and M_* the star's mass. From this we can calculate the semi-major axis of the maximal graze-and merge orbit, this should be:

$$a_{\rm ii} = \frac{r_{\rm H} + R_{\rm t} + R_{\rm p}}{2}, \tag{2.38}$$

where $R_{\rm t}$ is the projectile planet's radius and $R_{\rm p}$ the target planet's radius. The orbital period, T, for this limiting orbit should therefore be:

$$T = 2\pi \sqrt{\frac{a_{\rm ii}^3}{G\left(M_{\rm t} + M_{\rm p}\right)}}, \tag{2.39}$$

where $M_{\rm p}$ is the projectile mass. When considering a Mercury-like orbit of a Sun-like star by a Super-Earth mass target, like the Kepler-Multi's in Hwang et al. (2017a), this gives a re-collision time of $5 - 7$ hours, well within the typical simulation run time of 27.7 hours. The majority of our simulations allowed enough time for a re-collision for close orbiting planets at 0.1 au, but not enough for one orbiting at 1 au. Because we do not model the gravitational effects of the central star, unless we were specifically graze-and-merge collisions, we removed these results from our equation fitting process as whether or not the projectile escapes is system dependent and we were attempting to generate collision scaling laws that were agnostic to orbital distance.

b) Planet Masses and Atmosphere masses

The key limit on what masses can be used in simulations is resolution. Because the properties of SPH particles depend on the proximity of their neighbouring particles, this means that there is a minimum amount of particles required to accurately describe an object. Because of this we chose to assume objects with fewer than 500 particles were below the resolution limit. This puts a limit on the maximum mass ratio of target to projectile that we can simulate, the smallest targets we used had at least ten times as many particles as this. For a $6.25\,{\rm M}_\oplus$ planet with 10^5 particles in its core and mantle, like those we use in chapters 4 and 5, this means the minimum resolvable object is

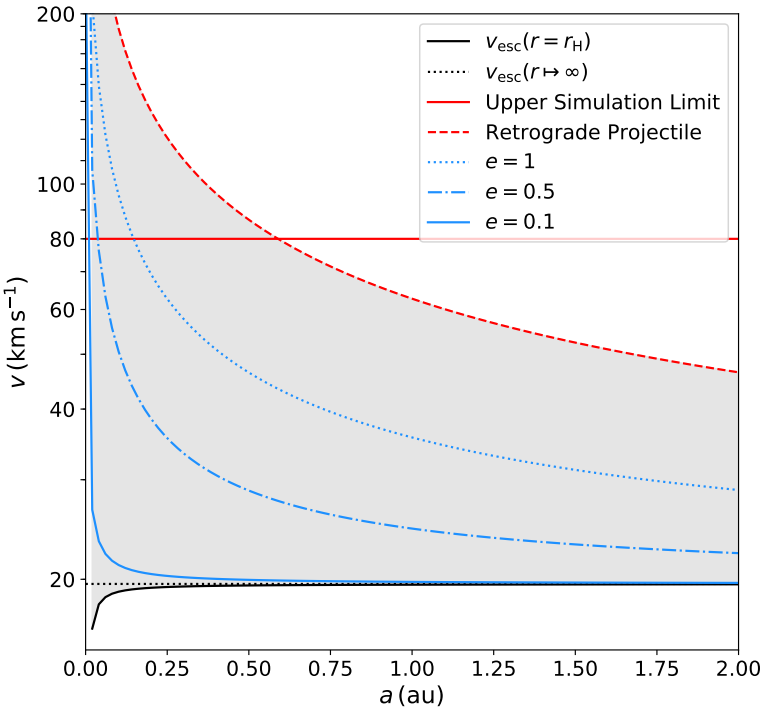

Figure 2.9: The probable velocities of collision at different orbital radii for a $6.25\,\mathrm{M}_\oplus$ target, and $2\,\mathrm{M}_\oplus$ projectile orbiting a sun-like star. Black lines show the lower limit of probable collision, dashed red the upper limit, and blue the rough velocity we would expect for a particular projectile eccentricity.

$0.025\,\mathrm{M}_\oplus$, this means we are unable to resolve impactors on the scale of Earth's Moon ($0.012\,\mathrm{M}_\oplus$). In practice the minimum mass impactors used were $0.25\,\mathrm{M}_\oplus$ an order of magnitude within the resolution limit.

A similar restriction holds true for atmospheric mass, where each atmosphere particle needs sufficient neighbours to be described properly. For each particle to have enough neighbours the atmosphere layer needs to be sufficiently thick that there are multiple layers of particles present once it has been equilibrated. The thinnest atmosphere which was used was thus 9000 particles, which, after equilibration, was approximately 4 layers of particles thick.

c) Collision velocities

The minimum velocity that two planets can collide into one another with is their mutual escape velocity (Süli, 2021). When we consider real systems this essentially is equivalent

to the two planets having zero relative velocity when they enter one anothers Hill sphere, with the relative kinetic energy of impact coming from the gravitational potential the two planets have at that separation. This limit is shown by the black lines in figure 2.9 for a typical target and projectile from our simulations.

A major limiting factor on the upper velocity was the range of applicability of the equations of state being used. In particular we had issues with the equation of state for iron, which had reduced accuracy at higher temperatures and pressures that resulted in un-physical vapourisation. These iron equation of state issues meant we could not simulate collisions faster than $80\,\mathrm{km\,s^{-1}}$ (solid red line, figure 2.9). For many of the collisions modelled this velocity was already in the super-catastrophic disruption regime (see section b)) where the planets are nearly completely disrupted. Theoretically the maximum velocity we would expect a collision to occur at would be if a prograde and retrograde planet collided. The velocity of these retrograde collisions is twice the Keplerian velocity, plus the additional velocity gained from the the projectile planet's acceleration within the targets Hill sphere (dashed red line, figure 2.9). For typical simulation planets orbiting at $\sim 0.1\,\mathrm{au}$ this velocity is greater than our simulation limit. Retrograde planets are very uncommon though so reaching this limit is very unlikely (Gabriel et al., 2020).

Previous works (e.g. Süli 2021) show that impacts at the mutual escape velocity are the most probable, with the probability distribution following a convex curve that trails off at higher velocities. Typical velocities of approach to the Hill sphere tend to be $\sim ev_{\mathrm{Keplerian}}$ (Gabriel et al., 2020) where e is the eccentricity and $v_{\mathrm{Keplerian}}$ the Keplerian orbital velocity at that distance from the star (blue lines, figure 2.9). Higher eccentricities are more likely to cause a collision with another planet as orbits are more likely to cross, but in planet formation orbits begin circularised by the gas disc. After the disc dissipates gravitational interactions amplify eccentricity until collisions or scattering occur. Reaching very high eccentricities is therefore unlikely, so collisions are more likely to occur at close to the mutual escape velocity.

Because of the higher probability of collisions at close to the escape velocity, for studies like ours it makes sense to have a larger array of lower velocities than greater ones, as we wish to give a good description of overall trends, and these are the most likely impacts.

2.2.5 Analysis Methods

a) Determining Bound material

To determine whether simulation particles were bound or not, like Benz & Asphaug (1999) and Marcus et al. (2009) we used the following process; firstly we found the particle lowest in the gravitational potential well. This particle was used as a seed particle. We then determined which particles were gravitationally bound to the seed particle (i.e. their kinetic energies were less than the gravitational potential energy between them and the seed.) The combined mass and centre of mass of all these new particles and the original seed are combined to make a new seed. This process was repeated until the change in mass per step went below a threshold value. To determine the bound mass for multiple objects in the same simulation, when we have completed determining all the bound mass in one object we remove all particles that are in that object and begin the process again, finding a new seed particle for the next object. This process can be repeated multiple times.

b) Categorisation and Definitions

There are various different classifications of collision regimes in the literature. An example classification system would be that used by Leinhardt & Stewart (2012), a diagram of the velocities and impact parameters characteristic of the different collision regimes they define is given in 2.10. I shall provide here an example of the definitions of some of the important collision classifications for this work:

- Merger: Merging collisions are ones where the end result is only one large remnant that is a combination of the two initial objects, if no material is lost in the process such a collision is known as a 'perfect merger'.
- Partial Accretion: A collision in the partial accretion regime is one where the largest remnant is more massive than the target planet in the collision (Leinhardt & Stewart, 2012). For this to be true the target needs to have accreted some of the projectile's mass.
- Erosion: An erosive collision is one where the largest remnant is smaller than the target planet in the collision (Leinhardt & Stewart, 2012). For these collisions the projectile has eroded the target, decreasing its mass.

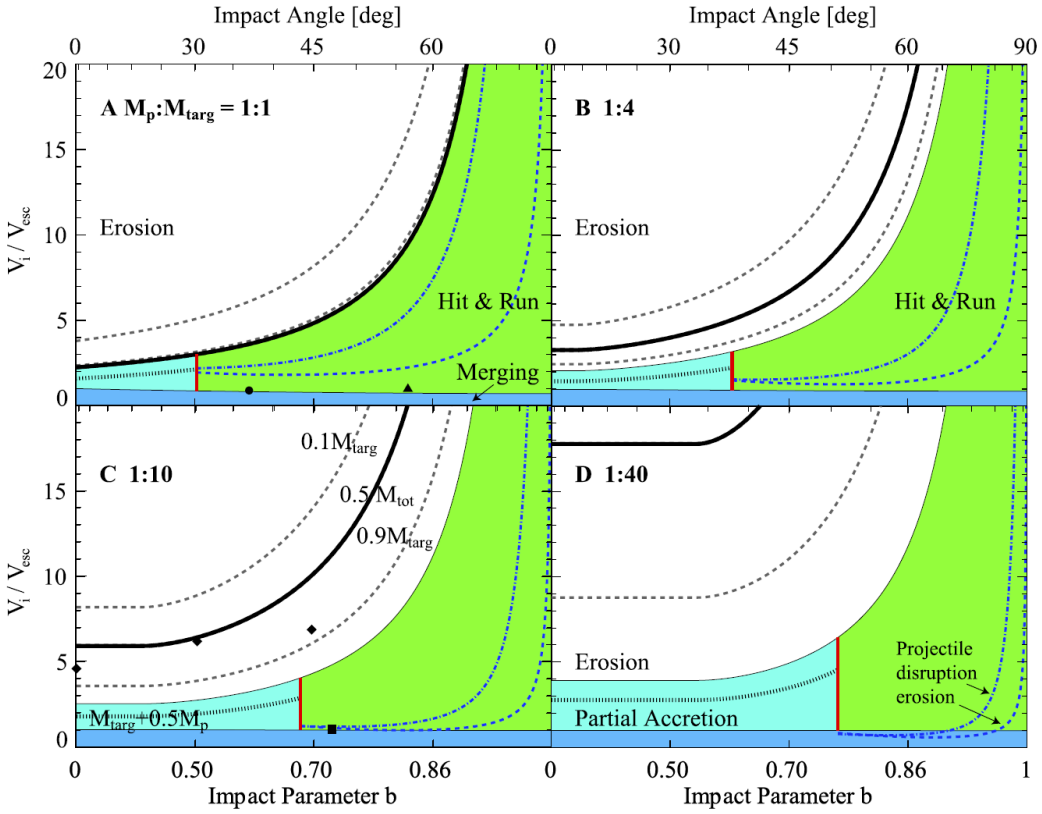

Figure 2.10: A diagram showing the different collision categorisations used in Leinhardt & Stewart (2012) and the velocities and impact angles they occur at for 4 different projectile-target mass ratios. Dark blue here is perfect mergers, light blue partial accretion, green hit-and-run and white are erosive collision. The solid black line here is the catastrophic disruption threshold. Diagram from Leinhardt & Stewart (2012).

- Hit-and-Run: Glancing collisions of a projectile of sufficient velocity will have the projectile rebound off the target having minimal effect on its mass, it is common to call such collisions hit-and-run collisions (Leinhardt & Stewart, 2012).
- Erosive Hit-and-Run: Gabriel et al. (2020) show that for highly stratified objects projectiles can rebound off the target at a lower impact angle than otherwise, but they often erode a substantial amount of the target in the process, they call such collisions 'erosive hit-and-runs' as they rebound like classical hit-and-runs but unlike them they are erosive to the target. Considering the large difference in density between mantle and atmosphere these are likely to be common in collisions between planets with atmospheres (see chapter 5).
- Graze-and-Merge: Sometimes the velocity of the projectiles remnants after a hit-and-run or erosive hit-and-run collision are insufficient for it to leave the gravitational influence of the target remnant. In such a case the projectile remnant will come back round to re-collide and merge with the target remnant. Such a collision is known as a graze-and-merge collision. They are covered in depth by Genda et al. (2012) and Emsenhuber & Asphaug (2019a).
- Disruption: These collisions result in a largest remnant of mass $0.1M_{\rm tot} < M_{\rm LR} < 0.9M_{\rm tot}$. This regime was defined by Leinhardt & Stewart (2012) due to linear dependence they observed of largest remnant mass on specific energy of impact in this range for simulations of collisions between atmosphere-less planets. Due to the large impedance mismatch between atmosphere and mantle and the effect that this has on shocks this may not be the case for Super-Earth planets with thick atmospheres.
- Catastrophic Disruption: Catastrophic disruption is where the collision is sufficiently energetic that the mass of the largest remnant is only half the total mass of the projectile-target system, this is a commonly used tool to build scaling laws, for example Housen & Holsapple (1990) or Leinhardt & Stewart (2012).
- Super-catastrophic Disruption: Super-catastrophic disruption collisions are those where the largest remnant mass is a small percentage of the initial system mass. This region is typically defined as $< 0.1M_{\rm tot}$ as both simulation (Korycansky & Asphaug, 2009) and experiment (e.g. Kato et al. 1995 and Matsui et al. 1982) show a change in the material loss curve at this point to a power law dependence on energy.

3

Atmosphere-less Collisions – The Kepler-107 System

This chapter is based on work I contributed to Bonomo et al. (2019). The first part summarises the observation and contributions from other collaborators, the second part is a detailed overview of the simulated collisions which constituted my contribution to the paper.

3.1 The Kepler-107 system

3.1.1 Initial Detection

The Kepler-107 system is an example of a system which likely underwent a giant collision. The system consists of 4 sub-Neptune sized planets labelled b, c, d and e. These were initially detected by the Kepler space telescope. The four planets have orbital periods that are close to integer ratios of one another, implying that the planets are close to resonance. These near resonance orbits in turn imply that the planets evolved at a greater distance from the central star and migrated inwards. The full data for the system is given in tables 3.1(star) and 3.2(planets).

Parameter	Value
Host star	Kepler-107, KIC-10875245, KOI-117, 2MASS 19480677 + 4812309
Magnitudes	B = 13.34, V = 12.70, J = 11.39, K = 11.06
Distance (pc)	525.5 ± 5.5
Systemic radial velocity V_r ($\mathrm{km\,s^{-1}}$)	$5.64423 \pm 4.5 \times 10^{-4}$
Effective Temperature, T_{eff} (K)	5854 ± 61
Metallicity [Fe/H] (dex)	0.321 ± 0.065
Spectroscopic surface gravity log g (cgs)	4.28 ± 0.10
Asteroseismic surface gravity log g (cgs)	4.210 ± 0.013
Rotational velocity $V \sin i$ ($\mathrm{km\,s^{-1}}$)	3.6 ± 0.5
Mass $M_*(\mathrm{M_\odot})$	1.238 ± 0.029
Radius $R_*(\mathrm{R_\odot})$	1.447 ± 0.014
Density ρ_* ($\mathrm{g\,cm^{-3}}$)	0.574 ± 0.029
Age, t (Gyr)	$4.29^{+0.56}_{-0.70}$
Limb-darkening coefficients	u1 = 0.26 ± 0.08, u2 = 0.56 ± 0.12

Table 3.1: Stellar parameters of The star Kepler-107, from table 1 Bonomo et al. (2019).

Planets	b	c	d	e
Orbital period, P (d)	$3.1800218 \pm 2.9 \times 10^{-6}$	$4.901452 \pm 1.0 \times 10^{-5}$	$7.95839 \pm 1.2 \times 10^{-4}$	$14.749143 \pm 1.9 \times 10^{-5}$
Transit epoch, $T_c - 2{,}450{,}000$ ($\mathrm{BJD_{TDB}}$)	$5701.08414 \pm 3.7 \times 10^{-4}$	$5697.01829 \pm 7.9 \times 10^{-4}$	5702.9547 ± 0.0060	$5694.48550 \pm 4.6 \times 10^{-4}$
Transit duration (h)	3.633 ± 0.021	4.269 ± 0.037	4.18 ± 0.36	6.117 ± 0.031
Radius ratio R_p/R_*	$0.00973 \pm 1.3 \times 10^{-4}$	$0.01012 \pm 1.3 \times 10^{-4}$	$0.00544 \pm 3.6 \times 10^{-4}$	$0.01839 \pm 1.4 \times 10^{-4}$
Inclination, i (deg)	89.05 ± 0.67	$89.49^{+0.34}_{-0.44}$	$87.55^{0.64}_{-0.48}$	89.67 ± 0.22
Eccentricity, e	0 (fixed)	0 (fixed)	0 (fixed)	0 (fixed)
Radial-velocity semi-amplitude, K ($\mathrm{m\,s^{-1}}$)	1.32 ± 0.57	3.06 ± 0.57	< 1.06	1.95 ± 0.82
Radius, R_p($\mathrm{R_\oplus}$)	1.536 ± 0.025	1.597 ± 0.026	0.86 ± 0.06	2.903 ± 0.035
Mass, M_p($\mathrm{M_o plus}$)	3.51 ± 1.52	9.39 ± 1.77	< 3.8	8.6 ± 3.6
Density, ρ_p ($\mathrm{g\,cm^{-3}}$)	5.3 ± 2.3	12.65 ± 2.45	< 33.1	2.00 ± 0.82
Semi-major axis, a (au)	$0.04544 \pm 3.5 \times 10^{-4}$	$0.06064 \pm 4.7 \times 10^{-4}$	$0.08377 \pm 6.5 \times 10^{-4}$	$0.12639 \pm 9.9 \times 10^{-4}$
Equilibrium temperature (K)	1593 ± 19	1379 ± 17	1173 ± 14	955 ± 12

Table 3.2: Measured parameters of each of the planets in the Kepler 107 system, from table 1 Bonomo et al. (2019).

3.1.2 Unusual Masses

The planet masses and radii in table 3.2 were measured using the transit method by the Telescopio Nazionale Galileo in La Palma. Of the Kepler-107 planets, the two orbiting closest to the star have similar orbits but quite different densities, c is $12.65\,\mathrm{g\,cm^{-3}}$ whereas b is $5.3\,\mathrm{g\,cm^{-3}}$. There are a few phenomena which can cause such density diversity, which I shall detail below:

One method for a planet to obtain a high density is via XUV photo-evaporation stripping the lighter material from the planet (as is outlined in Lopez et al. 2012). Typically if photo-evaporation were to be the cause we would expect the denser planet to be closer to the star, due to the inverse square law meaning that the interior planet would experience a greater flux of incident light and thus greater erosion of less dense, more easily evaporated material. We do not observe this to be the case here however, 107-c is denser but orbits at a greater semi-major axis.

Another method by which a planet can form with a high density is the denser planet could have formed in the silicate poor inner region of the proto-planetary disc. This is one of the processes which gives rise to Mercury's high density (Ebel & Stewart, 2018). Like for photo-evaporation, if forming in a silicate poor region were the cause of the density difference between 107-c and 107-b we would expect the denser planet to be orbiting closer to the star, which is not the case. All the planets in the system have close to circular orbits so if the two planets' orbits were to have crossed we would expect this to have occurred when the protoplanetary disc was still present to damp the resulting eccentricities. This would require the process to occur very rapidly, however and it also seems unlikely that this wouldn't cause the orbits of the lower mass planets in the system to destabilise.

Considering the arguments against both the above possibilities this implies that giant impacts are the most likely cause for the density difference. Previous simulation work shows that impacts between Super-Earths will result in a largest remnant with an enriched iron content and thus higher density (Marcus et al., 2009). Unlike other phenomena, like photo-evaporation, giant impact occurrence can be modelled stochastically, having very little dependence on orbital distance. Kepler-107c therefore, likely experienced one or more large impacts which stripped its mantle, while Kepler-107b did not.

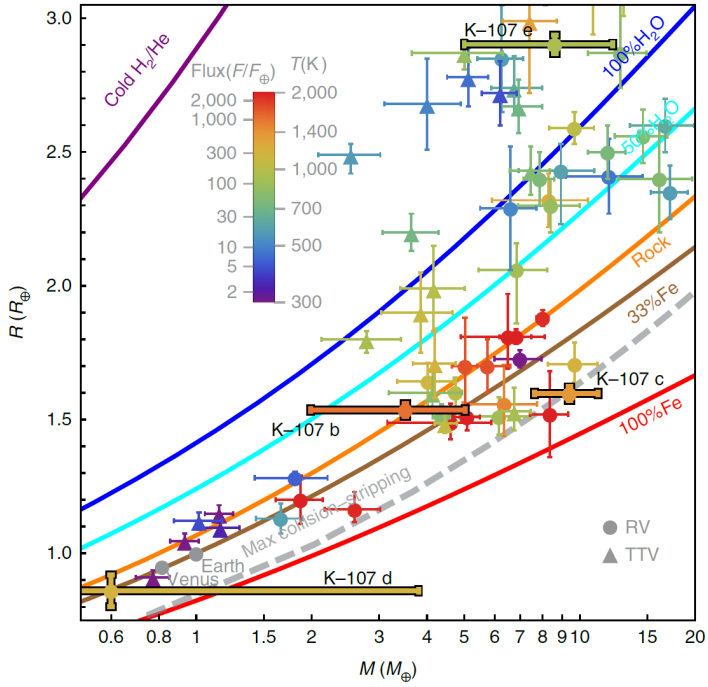

Figure 3.1: Detected exoplanets masses and radii compared to isocomposition contours. The Kepler-107 planets are outlined in black, both Kepler-107c and 107b are consistent with a rocky composition, with 107c's density implying a much higher iron core content than 107b. 107b's low density potentially implies an outer water shell. Graph from Bonomo et al. (2019).

3.1.3 Planet Compositions

The observed density is a clue as to the internal composition of a planet. Zeng & Sasselov (2013) describe a method to construct isocomposition contours in radius/mass space for any given composition. I shall give a brief overview of this methodology here.

The core of this method is solving the coupled differential equations below: Firstly we have

$$\frac{dr}{dm} = \frac{1}{4\pi\rho r^2}, \tag{3.1}$$

where r is the radius from the planet centre, ρ the density at that radius, and m the mass internal to that radius. Secondly we have

$$\frac{dp}{dm} = -\frac{Gm}{4\pi r^4}, \tag{3.2}$$

where p is the pressure at that radius. To solve these differential equations we need an equation of state for each material of form $\rho = \rho(p, T)$. Using the pressure-temperature

relations calculated by Valencia et al. (2006) this is then simplified to $\rho = \rho(p)$. The final tool needed for solving these equations are the boundary conditions, these are as follows: the pressure at the centre of the planet, the pressure at the surface, and the pressure at each material interface.

Figure 3.1 shows exoplanets with measured masses and radii compared with isocomposition contours derived using Zeng & Sasselov (2013). Planets of all compositions are larger if they have more mass, with planets that contain a higher percentage of heavier main components (such as iron) being denser overall compared to those that have a higher percentage lighter components (such as water or hydrogen). The grey dashed line shows an empirically derived limit for collisional stripping of mantle for a planet that starts with an Earth-like iron core/rocky mantle ratio (Marcus et al., 2010).

Using this isocomposition method, and assuming Kepler-107c is currently made of solely iron and rock, it was predicted that 107c should be roughly 70% iron core by mass with a silicate mantle of roughly 30%. Kepler-107b on the other hand should have a much lower iron core content, and potentially a water outer shell or an atmosphere.

The objective of the simulations I ran for Bonomo et al. (2019) was to see whether Kepler-107c's composition and mass could be reached by a collision assuming reasonable collision velocities and initial planets with an Earth-like composition.

3.2 Collision Modelling

3.2.1 Numerical Methods

My work for Bonomo et al. (2019) was to use simulations of collisions to determine whether we could obtain the predicted 70% iron core composition for an object of Kepler-107c's mass if we start with an Earth like rock-iron compositional ratio. Focusing on obtaining the correct core fraction over obtaining the correct final density meant we did not need to worry about accurate modelling of post-collision cooling of bound material. It is acceptable to ignore cooling processes for the collision modelling because they occur over much greater timescales (kyr as opposed to hr, see section a)).

In Marcus et al. (2009) the authors detail how, in collisions between simulated Super-Earths constructed from an iron core and a silicate mantle, the iron fraction, f_{Fe}, in the largest remnant changes with changing specific impact energy, Q_{R}, from a starting value

of one third in projectile and target:

$$f_{\mathrm{Fe}} = 0.33 + 0.25 \left(\frac{Q_{\mathrm{R}}}{Q^*_{\mathrm{RD}}} \right)^{1.65}, \tag{3.3}$$

where Q^*_{RD} is the catastrophic disruption energy, i.e the energy required for the final largest remnant to be half the total mass of the system. Specific impact energy Q_{R} is defined as:

$$Q_{\mathrm{R}} = \frac{1}{2} \frac{\mu}{M_{\mathrm{tot}}} v^2_{\mathrm{imp}}, \tag{3.4}$$

where v_{imp} is the collision velocity, M_{tot} is the sum of projectile mass M_{p} and target mass M_{t}, and $\mu = M_{\mathrm{t}} M_{\mathrm{p}} / M_{\mathrm{tot}}$ is the reduced mass. For a 70% iron core equation 3.3 this implies a collision energy of roughly $1.3 Q^*_{\mathrm{RD}}$ for a head-on impact.

We do not start with exactly the same projectile-target mass ratio as Marcus et al. (2009) so we start with a collision energy of Q^*_{RD} and explored the parameter space from there as a starting place.

The initial estimate we use for the catastrophic disruption threshold, Q^*_{RD}, comes from Leinhardt & Stewart (2012). We have a collision which is well within the gravitational scaling regime so we use their empirical measure of

$$Q^*_{\mathrm{RD}} = \frac{4}{5} c^* \pi \rho_1 G R^2_{\mathrm{C1}}, \tag{3.5}$$

where $\rho_1 = 1000\,\mathrm{kg\,m^{-3}}$ is a standard density, R_{C1} is the radius of an object with the mass of the system with a density of ρ_1, and c^* is a dimensionless parameter that represents the offset between the gravitational binding energy and the equal mass disruption criterion, their larger scale collisions gave a value of $c^* = 1.9$. For higher impact angle collisions and collisions where the projectile was not the same mass as the target we used the corrections from Leinhardt & Stewart (2012). These corrections are detailed in section a).

The overall process of running the simulations is described in chapter 2. We used tabulated equations of state for the thermodynamic properties of the forsterite mantle and iron core as per Marcus et al. (2009) and Ćuk & Stewart (2012), while initial radial profiles were determined using Valencia et al. (2006).

Our final tests were done with a resolution of 10^5 particles, but some initial resolution testing trial runs were also done at a resolution of 10^4 particles. The majority of collisions simulated were between $10\,\mathrm{M_\oplus}$ planets although we also experimented with $5\,\mathrm{M_\oplus}$ and

$7.5\,M_\oplus$ planets. Using the predictions detailed above in equations 3.3, 3.4 and 3.5, this meant collision velocities of $\sim 60\,\mathrm{km\,s^{-1}}$. All initial planets had an approximately Earth-like composition of 33 % iron core and 67 % forsterite mantle. After each collision we measured the mass of material gravitationally bound in the largest remnant, and the fraction of the largest remnant which was iron core particles.

3.2.2 Results

Graphs of all the collisions tested are given in figure 3.2. The process to find the best candidate collision was as follows: firstly we tested equal mass collisions at different masses to determine how large the initial planets needed to be to generate approximately Kepler-107c's mass ($9.39\,M_\oplus$) post-collision. We observed the $10\,M_\oplus$ planets to give the closest largest remnant masses. Then we tested different impact velocities and different impact angles to work out which was best for obtaining the right iron fraction (70 % iron). As was observed in Marcus et al. (2009), higher velocity (and thus impact energy) collisions result in a larger final iron core fraction. The simulations we ran at non-zero impact angles at the same impact energy as a head-on result produced successively less mantle stripping, as expected from Leinhardt & Stewart (2012). The graphs in Figure 3.2 detail the resulting final mass and iron fraction for each of the collisions tested.

One of the best candidate collisions we simulated was a $62.5\,\mathrm{km\,s^{-1}}$ head-on collision between two $10\,M_\oplus$ bodies, figure 3.3 shows snapshots of this simulation. This collision is sufficiently energetic that both projectile and target are flattened into a pancake shape, from which the material that is still gravitationally bound collapses back down into a single large remnant. At this stage a significant percentage of the bound material is a low density high temperature vapour. Eventually this vapour will cool back down again to equilibrium with its surroundings. This collision produces a final planet which is slightly too low a mass ($8.2\,M_\oplus$) and which doesn't have quite high enough an iron fraction (64 %) but it is sufficiently close that it shows a collisional density enrichment of the required magnitude is possible.

3.2.3 Discussion and Conclusion

The collisions detailed in figure 3.2 illustrate that a single high-energy impact can result is significant iron enrichment. An example collision from these which closely resembles

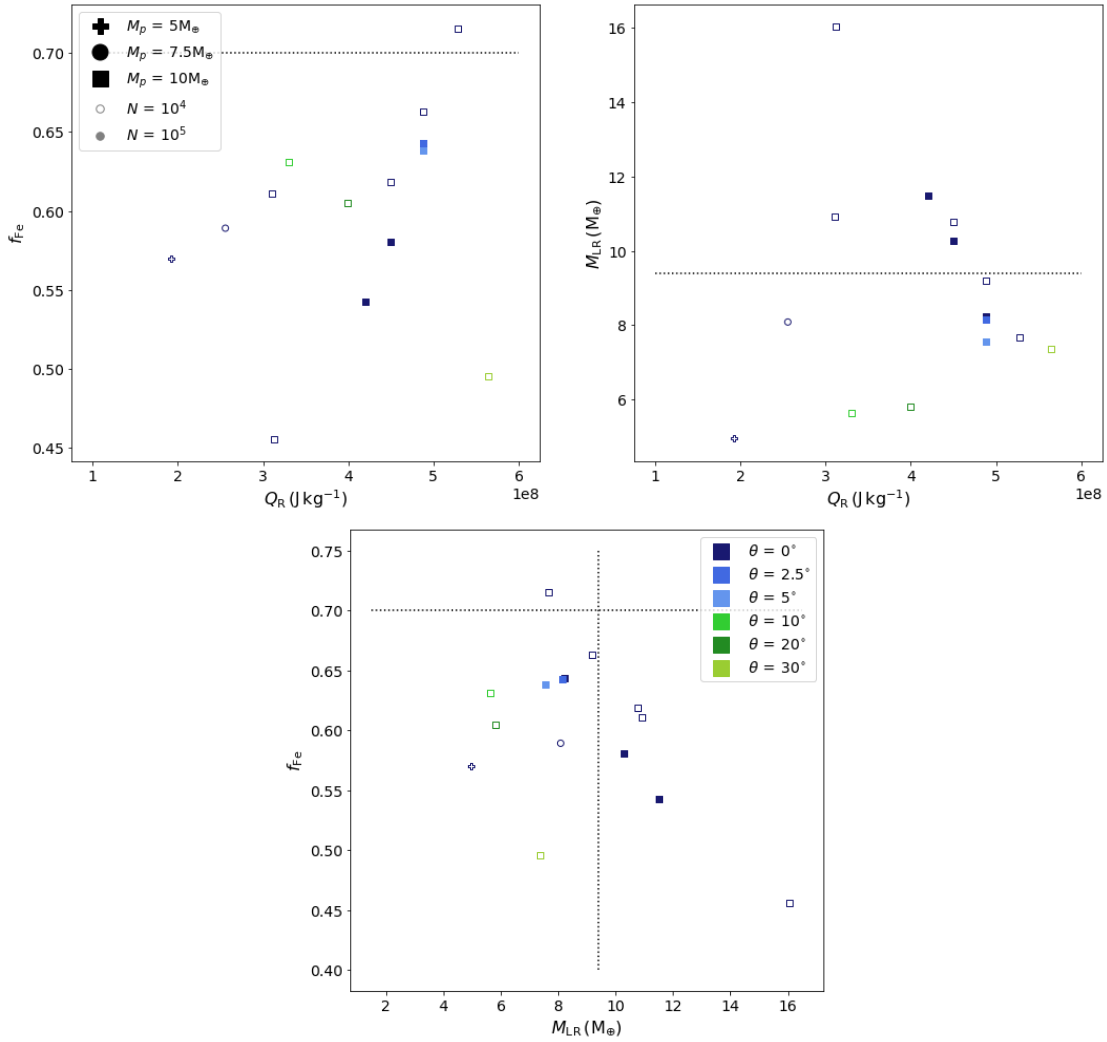

Figure 3.2: A series of graphs comparing the mass and iron fraction of the largest remnants for our simulated collisions to predicted values for Kepler-107c (dotted line). Open symbols are the lower 10^4 particles per planet resolution whereas filled ones were 10^5 particles per planet. top left: Iron fraction of the largest remnant compared with impact energy. Higher impact energies typically correspond to more mantle being ejected and therefore a higher final iron fraction. Higher impact angles counteract this effect due to the lower interacting mass. top right: Total mass of the largest remnant compared to the impact energy. Higher impact energies typically mean lower mass largest remnants for the same reason as they produce a higher iron fraction. bottom: A comparison of our final largest remnant masses and iron fractions for each simulated collision. We have not quite hit the predicted mass and iron fraction of Kepler-107c with a single simulation alone. Obtaining the same result as the prediction would require further simulations measuring the effects of different projectile and target masses, multiple collisions on the same target, or modelling of post collisional vapour erosion. The result is sufficiently close however to show that it is not unreasonable that this system could have been formed by a single collision.

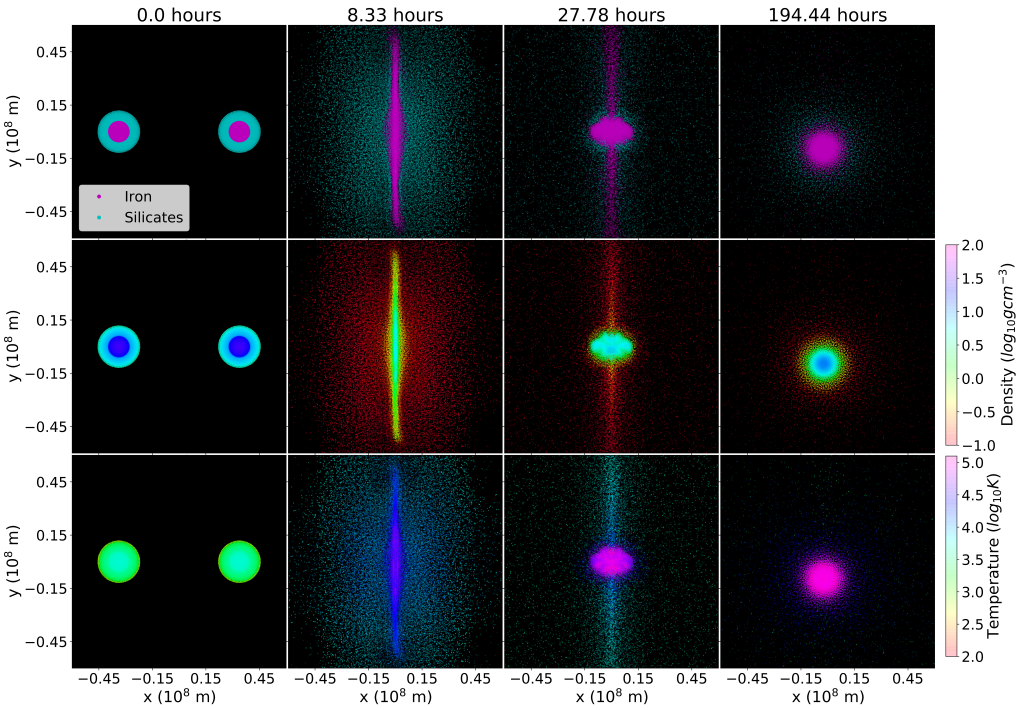

Figure 3.3: Snapshots from an example collision simulation, showing material composition (top), density (middle) and temperature (bottom). The material in the final panel is extended compared to the initial panel. This is due to it being much hotter. Because of time constraints we don't simulate collisions until the material has cooled and re-equilibrated, instead simulations are run until the bound material in the largest remnant asymptotes to a constant value.

what is hypothesised to have happened in the Kepler-107 system is given in the cross-sectional snapshots of figure 3.3. These snapshots show a collision which began with two large mantle dominated planets similar in composition to what we expect for Kepler-107b, after the collisions sufficient mantle had been ejected from the largest remnant that it resembled a high density iron dominated planet similar to Kepler-107c. It should be noted that a series of multiple energetic collisions (as described in Chau et al. (2018)) may also produce a similar density enrichment as is observed here. A full survey of the various series of collisions that could generate the desired result is however beyond the scope of this work.

For the sake of simplicity our analyses have neglected to include the cooling process. After a collision the material that makes up the largest remnant is likely to be heavily vapourised and extended over a much larger radius than an equilibrium planet. We would expect some of this material to be eroded away via thermal escape processes such as the Parker winds described by Owen & Wu (2016). We would also expect the extended vapour to intercept more incident XUV flux due to its greater extent and thus also experience greater photo-evaporative erosion. We would expect both of these erosive effects to affect the lighter vapour more strongly, so we would also expect these processes to have a further density enriching effect. Precise calculation of this effect was beyond the scope of this work however.

Kepler-107b is potentially less dense than would be expected for a planet of Earth-like composition, so it could have a sizeable atmosphere or outer water shell. There is degeneracy between different compositions at this mass and radius so precise determination would require spectroscopic analysis which is currently unavailable. If Kepler-107c formed in the same region of the disc then it should have a similar initial composition. An advantage of picking an Earth-like composition, however, (which is within the error for 107b) is that it allowed us to use previous work by Marcus et al. (2009) to predict roughly what energy and mass collisions we should simulate. Assuming however that an Earth-like composition is not the case, and 107c initially had a water outer shell or atmosphere, we would still expect to observe similar results. Lighter material, higher up a planet's potential well, is, in general, more likely to be ejected via a collision (Marcus et al., 2010), and so we would expect density enrichment to be a result regardless of initial composition. The main difference we would expect to observe would be the impact

energy required for a sufficient increase in density. For a more detailed analysis of the effect of collisions on atmospheres see chapters 4 and 5.

In summary, while we have not exactly replicated the mass and predicted core fraction of Kepler-107c with our simulations, we have shown that it is feasible for collisions to produce a sufficient density enrichment for Kepler-107c to have been created from planets of initially Earth-like composition. Considering that Kepler-107c orbits close to a much less dense interior neighbour a formation mechanism via solely photo-evaporation is unlikely, because of this a collisional origin is the most likely cause for its comparatively high density.

4

Head-On Collisions

This chapter is a paper published in MNRAS (Denman et al., 2020).

4.1 Introduction

There have been a wealth of exoplanet discoveries over recent years, bringing the total number of confirmed planets to more than 4000. About twenty percent have a mass between that of Earth and Neptune (henceforth 'Super-Earth mass'). Of these, two thirds orbit at a distance less than that of Mercury from their host stars, and more than three quarters are in systems with at least one other planet (NASA, 2019) .

Planets in this mass and orbital distance range are very diverse, with measured densities ranging from between 0.03 and 12.7 $\mathrm{g\,cm^{-3}}$. Even planets within the same solar system at similar orbital radii can be vastly dissimilar. The two innermost planets of the Kepler-107 system (Bonomo et al., 2019), for example, both have similar radii ($1.5 - 1.6\,\mathrm{R_\oplus}$), but Kepler-107b has a density of $5.3\,\mathrm{g\,cm^{-3}}$ compared to Kepler-107c's $12.6\,\mathrm{g\,cm^{-3}}$. This high density implies that Kepler-107c must have a different composition from 107b.

There are two main theories that explain the diversity of densities observed in Super-Earths and Mini-Neptunes: 1) XUV radiation from the central star (Lopez et al., 2012;

Lopez & Fortney, 2013; Owen & Wu, 2013; Jin et al., 2014) strips close orbiting planets of some of their lighter elements, leaving them denser. 2) Giant impacts eject the lighter outer material (such as crust or atmosphere) from both bodies leaving a denser remnant planet (Inamdar & Schlichting, 2016; Bonomo et al., 2019).

XUV radiation cannot always explain large differences in density for planets orbiting at similar semi-major axes in the same planetary system, for example, Kepler-107b and c. These two planets orbit at a similar distance from their parent star and have similar physical radii but differ significantly in planetary mass. The outer Kepler-107c is more than twice as dense as the inner-most 107b. Kepler-107c's density can not be explained by XUV radiation because it is orbiting outside of the less massive and also less dense Kepler-107b which would have lost more material due to irradiation. Thus, a giant impact is the best explanation (Bonomo et al., 2019).

Giant impacts have been suggested as the explanation for density diversity in several planetary systems (Liu et al., 2015; Inamdar & Schlichting, 2016). In addition, many of the tightly orbiting high-multiplicity systems detected by Kepler appear to be on the borders of stability (Fang & Margot, 2013). Therefore, it is not unreasonable to consider the planets gravitationally interacting with one another in such a way that either they eject one or both planets or that they collide with one another. Barnes & Raymond (2004) showed that small perturbations in orbit will lead to such ejections or collisions. Volk & Gladman (2015) even suggested close orbiting groups of planets are common in the formation of inner solar systems ($a < 0.5$au), including our own, but that they are not stable long term, and will undergo collisional disruption and consolidation. This suggests that the high multiplicity systems that we observe are either these initial unstable systems, or that the planets are in an arrangement that is stable for long time periods.

Several previous works (e.g. Schlichting et al., 2015; Inamdar & Schlichting, 2016) have demonstrated that giant impacts have the potential to remove large fractions of these planets' atmospheres, leading to substantial density enhancement. In this chapter we directly calculate atmosphere stripping via 3D modelling of head-on giant impacts between Mini-Neptune mass planets with significant atmospheres and lower mass bare Super-Earth impactors.

4.1.1 Previous Work

Until recently, simulations of atmospheric losses due to such giant collisions were too computationally expensive to run within a reasonable time frame. Recent advances, however, have meant high resolutions are now much more attainable.

Because of computational demands much early work focused on analytical predictions (some of which focus on significantly lower mass atmospheres than we consider here, such as Earth-like atmospheres), for example Genda & Abe (2003) which discusses how much of an Earth-like protoplanet's atmosphere is likely to survive the giant impact phase. They used one dimensional models to calculate the amount of material jettisoned after a collision from the ground velocity beneath it, showing that for the canonical Moon-forming impact only ≈ 20 per cent of mass would be lost. Genda & Abe (2003) also showed that the ground velocity needs to reach the escape velocity for total atmosphere erosion. Schlichting et al. (2015) expanded upon this by formulating a method of predicting atmospheric loss from a wide range of projectiles colliding with terrestrial planets. This method is the one used by Inamdar & Schlichting (2016) when discussing the density diversity of Super-Earth mass exoplanets. Inamdar & Schlichting (2016) showed that a single collision between similarly sized exoplanets can cause a decrease in the mass ratio of atmospheric envelope to central core material by a factor of 2, which in turn leads to a density increase of a factor of 2–3. Inamdar & Schlichting (2016) thus suggested giant impacts as a cause for the observed density diversity.

Despite computational limitations some progress has been made in simulating collisions of planets with gaseous envelopes. Liu et al. (2015) considered a model of the Kepler-36 system (with target planets of 6–8% atmosphere by mass). They found that a collision could cause the density difference observed between the two planets in this system, and suggested that giant collisions might therefore be the cause of the dispersion we observe in the mass-radius relationship for Super-Earth mass planets. Hwang et al. (2017a) and Hwang et al. (2017b) used an N-body code to model the evolution and stability of high multiplicity planetary systems (specifically Kepler-11 and Kepler-36). For the collisions they used a smoothed particle hydrodynamics (SPH) code and assumed atmosphere mass fractions of 5–15% to determine the results of highly grazing collisions (collisions where only the atmospheres overlap), they showed that typically the higher mass core will accrete more of the disrupted gas envelope leading to increasing density

contrasts between the two planets. Due to problems with their equation of state however, they where unable to simulate the results of head-on collisions. Kegerreis et al. (2018) also used SPH to model collisions involving targets with atmospheres, to see if they could model the formation of Uranus' off axis rotation and unusual magnetic field. Unlike the simulations in this chapter, Kegerreis et al. (2018) focus mostly on higher impact parameter collisions in order to study the change in rotation. They considered ice giants as opposed to the metal and silicate planets with atmospheres studied in this work.

In this chapter results are presented from a series of head-on collisions between Super-Earth mass planets where each of the three different mass targets is a Mini-Neptune with a significant hydrogen envelope (8–33%). We run a large series of numerical simulations with a wide array of atmosphere-less Super-Earth projectiles. We provide scaling relations for material loss applicable to a wide range of masses that can be used in N-body simulations and population synthesis models.

4.2 Methods

Here I shall summarise the specific processes used for running the simulations in this chapter, for a more in general overview see chapter 2.

4.2.1 Numerical code

The simulations presented in this chapter were run using the SPH code GADGET-2 (Springel, 2005). Although GADGET-2 was initially designed for simulations on cosmological scales, we have used a modified version to model our planets that includes tabulated equations of state for the planetary constituents. For further detail on these modifications see Marcus et al. (2009) and Ćuk & Stewart (2012). We further modified GADGET-2 to include an ideal gas atmosphere component.

In SPH codes, such as GADGET-2, the material is split into separate particles each representing an ensemble of material. The continuous fluid properties, such as the density, for each ensemble of particles are calculated using kernel interpolation methods. The gravitational forces on the other hand are calculated using hierarchical tree methods

(Springel, 2005). We ran GADGET-2 in 'Newtonian' mode with timestep synchronisation, and the standard relative cell-opening criterion. We use the standard timestep criterion as described in Springel (2005), where the smaller of the timestep based on the gravitational softening and the acceleration, or the courant condition is used (with a courant factor of 0.1). We use the standard artificial viscosity formulation for GADGET-2 as described in Springel (2005), with a strength parameter of 0.8.

We modelled the planets as two or three material systems, each planet (both projectile and target) consisting of iron core, forsterite (silicate) mantle, and a hydrogen atmosphere for the target only. In a similar fashion to prior studies (Ćuk & Stewart, 2012; Marcus et al., 2009), the mantle was twice the mass of core. We modelled the atmosphere as a monatomic ideal gas for simplicity and ease of comparison (see section 4.4.1). Tabulated ANEOS/MANEOS equations of state (EOS) from Melosh (2007) were used for the iron and forsterite (these tables are available from Carter et al. 2019).

For the initial hydrogen atmosphere mass, we used the results of the Bern global planet formation model (Alibert et al., 2005; Mordasini, 2018) which was based on the core accretion paradigm. The model calculated the accretion of H/He of forming planets embedded in a protoplanetary disk by solving the 1D spherically symmetric interior structure equations (Pollack et al., 1996). In these calculations, the grain opacity in the protoplanetary atmospheres was reduced by a factor 0.003 relative to interstellar medium grain opacities following Mordasini et al. (2014) so it has a value consistent with observed metal enrichment of giant planets. Other effects considered were the accretion of planetesimals, orbital migration, disk evolution, and N-body interactions. These models predicted that for planets with masses between 1 and 7 $\mathrm{M}_\oplus$, the mass of the H/He envelope, M_{atmos}, at the end of the disk lifetime can be approximated by

$$\frac{M_{\mathrm{atmos}}}{\mathrm{M}_\oplus} = 0.01 \times \left(\frac{M_{\mathrm{c\&m}}}{\mathrm{M}_\oplus}\right)^3, \tag{4.1}$$

where $M_{\mathrm{c\&m}}$ is the combined mass of iron core and forsterite mantle. This yields an envelope mass of $M_{\mathrm{atmos}} = 1.25\ \mathrm{M}_\oplus$ for a combined mantle and core mass of of $M_{\mathrm{c\&m}} = 5\ \mathrm{M}_\oplus$ and $M_{\mathrm{atmos}} = 10\ \mathrm{M}_\oplus$ for 10 $\mathrm{M}_\oplus$ of core and mantle. A 10 $\mathrm{M}_\oplus$ core is close to the critical mass for runaway gas accretion which sets in when $M_{\mathrm{c\&m}} \approx M_{\mathrm{atmos}}$, which is approximately captured by this relation. One should, however, note that in the Bern model simulations, a large spread around this mean relation of about one order in

magnitude is observed.

4.2.2 Hardware

The simulations were each run using a full node on the University of Bristol's Bluecrystal supercomputers, either on phase 3 or phase 4. Phase 3 nodes consist of 16 core 2.6 GHz SandyBridge processors with 59.7 GiB RAM altogether (Gardiner, 2015), whilst phase 4 nodes have two 14 core 2.4 GHz Intel E5-2680 v4 (Broadwell) CPUs with the whole node having a combined 128 GiB of RAM (Gardiner, 2017). Each collision took between half a day and a day depending on the masses and impact energies involved.

4.2.3 Initial conditions

To generate the initial planets, we began by creating the central core and mantle. To generate density profiles we used radial temperature profiles (from Valencia et al., 2006) as well as estimates for the average bulk density of each type of material (i.e core or mantle) and the radial range that the core and mantle occupies. From this initial assumption of constant density per material layer we iteratively generated new density profiles using gravitational and hydrostatic pressure calculations, until we obtained a density profile that was consistent with our equation of state, the expected hydrostatic pressure and the input temperature profile.

Once a consistent profile was obtained it was then used to generate the position of each of the particles by splitting the planet into a number of radial bins based on its mass and randomly positioning a number of particles within each bin proportional to the bin's mass. The final number of bins being adjusted so that we could reach our desired mass to a tolerance of 1 per cent. The type of material being added to each bin was decided by the material ranges given for the initial density profile. After generating an initial SPH planet it was then equilibrated in isolation for 10^5s (simulated seconds) using a preliminary run of GADGET-2, to ensure that we were running simulations with a planet that was stable. During equilibration we used two 'artificial cooling' methods, velocity damping of the particles, i.e applying a restitution factor of 50% each timestep (see Carter et al., 2018), and also entropy forcing, the entropy of each particle is reset to a constant value for each material at every timestep ($1.3\,\mathrm{kJ\,K^{-1}\,kg^{-1}}$ for the iron core, $3.2\,\mathrm{kJ\,K^{-1}\,kg^{-1}}$ for the mantle). This entropy forcing ensures that we produce planets

with isentropic layers.

To generate a planet with an atmosphere, we added an atmosphere to the previously generated core and mantle only planets. The radial profiles of the planetary atmospheres were generated with the planet interior structure and evolution model completo21, which has already been described in several publications (Mordasini et al., 2012; Jin et al., 2014; Linder et al., 2019). Therefore we only give a short overview here. The structure of the atmosphere was found in the 1D spherically symmetric approximation by solving the usual equations of mass conservation, hydrostatic equilibrium, energy generation, and energy transport

$$\frac{\partial m}{\partial r} = 4\pi r^2 \rho \qquad \frac{\partial P}{\partial r} = -\frac{Gm}{r^2}\rho \tag{4.2}$$

$$\frac{\partial l}{\partial r} = 0 \qquad \frac{\partial T}{\partial r} = \frac{T}{P}\frac{\partial P}{\partial r}\nabla(T,P) \tag{4.3}$$

where m is the mass inside of a radius (distance to the planet's centre) r, ρ the gas density, P the pressure, G the gravitational constant, l the (intrinsic) luminosity, T the temperature, and $\nabla(T,P)$ the temperature gradient. The Schwarzschild criterion was used to decide whether the energy transport occurs in a layer via radiative diffusion or convection, meaning that ∇ is always the smaller of the radiative and the adiabatic gradient. When solving the structure equations, we assumed opacities corresponding to a condensate-free gas of solar composition (Freedman et al., 2014), and, in contrast to past publications, an ideal gas EOS. For the (intrinsic) luminosity, l, of the planets, which needs to be specified in order to solve the structure equations, we employed a simple power law scaling with planet mass. Like equation 4.1, the luminosity scaling was also based on formation simulations with the Bern model. The results obtained correspond to planet ages of 10 Myr. This age corresponds to a time when the systems are still dynamically active (soon after the dispersion of the eccentricity damping gas disk), so many collisions should occur. This gives,

$$L/\mathrm{L_J} \simeq 0.1 \times \left(\frac{M_{\mathrm{planet}}}{\mathrm{M}_\oplus}\right)^{1.5}, \tag{4.4}$$

where $\mathrm{L_J}$ is Jupiter's luminosity and M_{planet} is the total mass of the planet (again there is scatter around this relation).

We then used this radial mass profile for the atmosphere to determine the position of atmosphere particles, by splitting the profile into radial bins and placing particles

proportionally to the mass of the bins at random positions within them, in a similar fashion to the core and mantle. This new body was equilibrated for a longer time of 4–8$\times 10^5$ s until the radius of the planet had converged to a constant value. The pseudo-entropy of the atmosphere was forced to a value of $5 \times 10^{11}\,\mathrm{Ba\,g^{-\gamma}\,cm^{3\gamma}}$ where the adiabatic index was $\gamma = 5/3$, this ensured that the atmosphere would not reach densities where it would sink underneath the mantle and core material, but also that the base of the ideal gas atmosphere was as close as possible to our predicted temperatures.

For the core and mantle of our targets we used a resolution of 10^5 particles. All other particles in each simulation were made the same mass as the core and mantle particles, resulting in a total resolution between 1.2×10^5 and 2.5×10^5 particles. This results in an atmosphere 'thickness' of between 5 and 10 layers of particles. Our total particle number is smaller than that suggested by Kegerreis et al. (2019), however, we are interested in large changes in mass of the largest remnant so our resolution should be sufficient. We have run resolution tests of head-on collisions of 5 $M_\oplus$ planets with 0.9 $M_\oplus$ atmospheres against one another at both half and double our standard resolution (of 10^5 particles in the target core and mantle) at impact velocities of 20 and 40 $\mathrm{km\,s^{-1}}$. The key quantities we measure: mass of the largest remnant, atmosphere loss fraction and core and mantle loss fraction, each vary from the mean value at that velocity by less than 5% except for the core and mantle loss fraction at low velocity where only a very small number of particles are being lost. We did not consider losses or remnants of only a few hundred particles resolvable with SPH methods.

a) The Point of Impact

In collisional studies impact parameters such as velocity, impact energy etc. are normally measured in terms of the point of first physical contact between the two planetary bodies (e.g. Leinhardt & Stewart, 2012). For planets with atmospheres this becomes more complex, however, as atmosphere densities decay approximately exponentially so there is no clear boundary at which the atmosphere ends. Tidal forces between planets also have a stronger distorting effect on the atmosphere than the core and mantle. Thus we use the time when mantle surfaces touched as our point of impact because this can be clearly defined.

To obtain an initial start position from our desired collision parameters (for example

velocity and impact angle), the following process was used: 1) the two planets were represented by point masses at their centres, these two planets were placed at their position at the point of impact and set at the predicted velocity; 2) Time reversal symmetry was then used to trace the path of the projectile back to a separation of five times the sum of the projectile and target mantle radii (excluding atmosphere). To determine the projectiles path we used a simple Verlet integrator, set the target planet to be centred on the origin, and calculated the acceleration as given by the relative gravitational force between two point particles. The choice of starting separation was a somewhat arbitrary one intended to reduce the tidal forces compared to the starting distances of previous similar studies due to us equilibrating planets in isolation and atmospheres being more easy to tidally distort.

Note using the point where mantles touch as our point of impact is not without its drawbacks. As can be observed in Figure 4.1 the presence of the atmosphere causes a significant observable slowing of the relative impact velocity. This slowing is due to atmospheric drag which distorts the projectile planet. For some collisions this distortion is even present when the leading edge of the projectile is greater than an atmospheric scale height from the target. In further calculations, which use impact energy, we used the measured velocity instead of the predicted input value. To measure this collision point precisely we re-simulated the point of impact for our collisions with a higher output frequency (snapshots were taken every 3 seconds as opposed to every 100).

b) Input Parameters

All collisions presented in this chapter were head-on, involving a projectile with no atmosphere and a target with atmosphere. Head-on collisions were chosen as they are the most energetic and are, therefore, expected to be the most efficient at removing material (Leinhardt & Stewart, 2012). The three target masses simulated were: a) a $3.0\,M_\oplus$ core and mantle with a $0.27\,M_\oplus$ atmosphere (Table 4.5), b) a $5.01\,M_\oplus$ core and mantle with a $1.25\,M_\oplus$ atmosphere (Table 4.1), and c) a $7.07\,M_\oplus$ core and mantle with a $3.43\,M_\oplus$ atmosphere (Table 4.6). Projectiles had masses between 0.05 to 1 times the core and mantle mass of the target, giving 6–7 mass ratios per target distributed approximately evenly between 0.04 and 0.92. These masses were chosen to sample a wide range of parameter space with a limited number of runs. 7–8 collision velocities

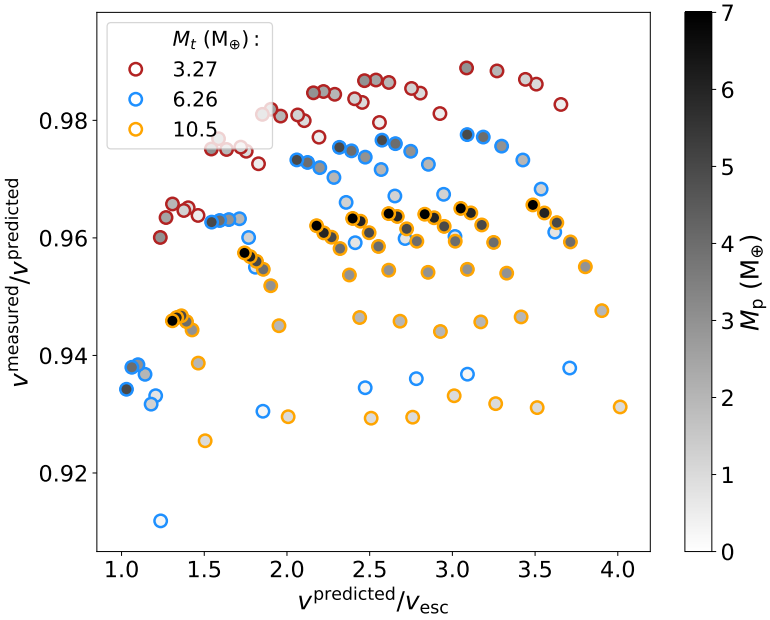

Figure 4.1: Comparisons of the predicted velocity for the three targets and the ratio between measured and predicted impact velocities. Impact velocities are given in terms of the mutual escape velocity ($v_{\rm esc} = \left(2GM_{\rm tot}/R^{'}\right)^{\frac{1}{2}}$ where $R^{'} = (3M_{\rm tot}/4\pi\rho_{\rm bulk})^{\frac{1}{3}}$ and $\rho_{\rm bulk}$ is the bulk density of the simulated target). Edge colours show target mass while central colours show projectile mass. The reduced velocity compared to the prediction can be considered a measure of the drag caused by the atmosphere. As might be expected, the denser, higher mass atmospheres around the larger targets tend to cause more drag, the lower mass and lower velocity projectiles tend to experience proportionally more drag as well due to their lower momenta.

per target were distributed approximately evenly between 20 and 80 $\rm km\,s^{-1}$. These velocities were 1–4 times the mutual escape speed, which we define in a similar fashion to Leinhardt & Stewart (2012),

$$v_{\rm esc} = \left(2GM_{\rm tot}/R^{'}\right)^{\frac{1}{2}}, \tag{4.5}$$

where $M_{\rm tot}$ is total mass and $R^{'}$ is the radius of a spherical body of mass $M_{\rm tot}$ and the same density as the bulk density of the simulated target. This measure for mutual escape velocity was chosen due to it being a minimum velocity at which we might expect to see ejection of material. This velocity range meant that we could sample well both collision regimes detailed in section 4.3.1, as well as the transition between them.

4.2.4 Run Parameters

To determine the length of time we needed for our simulations (the run time) we used the dynamical time for gravitational interactions $t_{\rm dyn}$. A dynamical time for a process is a prediction of the rough timescale it will take to finish, generated from a few system parameters. For gravity dominated systems the dynamical time is given by:

$$t_{\rm dyn} = \sqrt{\frac{R^3}{GM}} \tag{4.6}$$

Taking the largest initial separation as R and the smallest total mass as M, the largest dynamical time we obtain is 27000 s. We elected to use a run time of 10^5 s, a value slightly under 4 dynamical times. Whilst a longer run time gives a more reliable estimate of the long term final state after a collision, we were constrained by computation time, and the results we were most interested in (bound mass for each material component of our planets) had already converged to a constant value by this time for all our simulations.

4.2.5 Analysis Methods

a) Determining Bound Material

To determine what material was bound in the largest post-collision remnant we used the same iterative method as Marcus et al. (2009) and Carter et al. (2018). We began by locating the particle closest to the potential minimum and using kinetic energy and gravitational potential to determine which other particles were gravitationally bound to this deepest particle. Using the total mass and centre of mass of these particles as our new seed, we then iteratively ran through the process of determining which extra particles were bound to the seed, and then adding them to the seed, until either the change in mass of the seed was below a set tolerance or a maximum number of iterations had been reached. For our simulations we obtained single particle differences in mass within a few iterations so our tolerance was set to a single particles mass, and the maximum number of iterations was never reached. Material type was also tracked, to determine the mass of each type of material which was unbound or part of the largest remnant.

Table 4.1: Simulation parameters and results for head-on collisions between a $6.26\,\mathrm{M}_\oplus$ target, with a mantle surface radius of $1.49\,\mathrm{R}_\oplus$, and an atmosphere scale height of $0.60\,\mathrm{R}_\oplus$, and a projectile of mass M_p and radius R_p. The first digit of the collision ID denotes the non-atmospheric target mass ($M_\mathrm{t}^\mathrm{core} = 5.01\,\mathrm{M}_\oplus$, therefore, $M_\mathrm{t}^\mathrm{atmos} = 1.25\,\mathrm{M}_\oplus$). v_init is the initial relative speed of the projectile with respect to the target, at an initial separation of S to give a predicted impact speed of $v_\mathrm{imp}^\mathrm{pred}$, the measured velocity at the point where the mantles touch is $v_\mathrm{imp}^\mathrm{meas}$. M_LR is the total mass of the largest post-collision remnant, where $M_\mathrm{LR}^\mathrm{atmos}$ and $M_\mathrm{LR}^\mathrm{core}$ are the atmospheric and non-atmospheric masses, respectively, the final column gives the category we have given that collision. We have used '-' to denote final snapshots where there where too few particles in the largest remnant to be able to properly resolve. Simulation data for $M_\mathrm{t} = 3.27\,\mathrm{M}_\oplus$ and $M_\mathrm{t} = 10.5\,\mathrm{M}_\oplus$ can be found in Tables 4.5 & 4.6.

ID	M_p	R_p	$v_\mathrm{imp}^\mathrm{pred}$	$\frac{v_\mathrm{imp}^\mathrm{pred}}{v_\mathrm{esc}}$	$v_\mathrm{imp}^\mathrm{meas}$	$\frac{v_\mathrm{imp}^\mathrm{meas}}{v_\mathrm{esc}}$	v_init	$\frac{v_\mathrm{init}}{v_\mathrm{esc}}$	S	M_LR	$M_\mathrm{LR}^\mathrm{atmos}$	$M_\mathrm{LR}^\mathrm{core}$	$\frac{M_{LR}}{M_\mathrm{tot}}$	$X_\mathrm{loss}^\mathrm{atmos}$	$X_\mathrm{loss}^\mathrm{c\&m}$	Category
	$\mathrm{M}_\oplus$	$\mathrm{R}_\oplus$	$\mathrm{km\,s^{-1}}$		$\mathrm{km\,s^{-1}}$		$\mathrm{km\,s^{-1}}$		$\mathrm{R}_\oplus$	$\mathrm{M}_\oplus$	$\mathrm{M}_\oplus$	$\mathrm{M}_\oplus$				
5-0	0.25	0.62	20.00	1.24	18.24	1.13	9.38	0.58	11.15	6.50	1.24	5.26	1.0	0.01	-0.0	AM-CM
5-1	0.25	0.62	30.00	1.85	27.92	1.73	24.25	1.50	11.16	6.43	1.17	5.26	0.99	0.06	-0.0	AL-CM
5-2	0.25	0.62	40.00	2.47	37.38	2.31	35.89	2.22	11.15	6.30	1.05	5.26	0.97	0.16	-0.0	AL-CM
5-3	0.25	0.62	45.00	2.78	42.12	2.60	41.39	2.56	11.18	6.22	0.97	5.25	0.96	0.22	0.0	AL-CM
5-4	0.25	0.62	50.00	3.09	46.84	2.90	46.77	2.89	11.15	6.14	0.89	5.25	0.94	0.29	0.0	AL-CM
5-5	0.25	0.62	60.00	3.71	56.27	3.48	57.34	3.54	11.18	5.94	0.71	5.23	0.91	0.43	0.01	AL-CM
5-6	0.75	0.88	20.00	1.21	18.66	1.13	10.22	0.62	11.93	6.90	1.13	5.76	0.98	0.1	0.0	AL-CM
5-7	0.75	0.88	30.00	1.81	28.65	1.73	24.58	1.48	11.93	6.66	0.91	5.75	0.95	0.27	0.0	AL-CM
5-8	0.75	0.88	40.00	2.41	38.37	2.31	36.11	2.18	11.96	6.29	0.56	5.73	0.9	0.55	0.01	AL-CM
5-9	0.75	0.88	45.00	2.71	43.20	2.61	41.58	2.51	11.94	6.11	0.41	5.69	0.87	0.67	0.01	AL-CM
5-10	0.75	0.88	60.00	3.62	57.66	3.48	57.48	3.47	11.96	4.62	0.07	4.55	0.66	0.94	0.21	AL-CE
5-11	1.25	1.02	20.00	1.18	18.63	1.10	10.11	0.60	12.35	7.28	1.02	6.26	0.97	0.18	0.0	AL-CM
5-12	1.25	1.02	30.00	1.77	28.80	1.70	24.54	1.45	12.35	6.92	0.68	6.25	0.92	0.46	0.0	AL-CM
5-13	1.25	1.02	45.00	2.65	43.52	2.57	41.56	2.45	12.37	5.86	0.19	5.68	0.78	0.85	0.09	AL-CA
5-14	1.25	1.02	50.00	2.95	48.37	2.85	46.93	2.77	12.36	5.04	0.09	4.95	0.67	0.93	0.21	AL-CE
5-15	1.25	1.02	60.00	3.54	58.10	3.42	57.46	3.39	12.36	2.94	0.00	2.94	0.39	1.0	0.53	TAL-CE
5-16	2.00	1.18	20.00	1.14	18.74	1.07	9.66	0.55	12.81	7.89	0.91	6.99	0.95	0.27	0.0	AL-CM
5-17	2.00	1.18	30.00	1.71	28.90	1.65	24.36	1.39	12.82	7.49	0.53	6.96	0.91	0.58	0.01	AL-CM
5-18	2.00	1.18	40.00	2.28	38.81	2.22	35.96	2.05	12.83	6.42	0.21	6.22	0.78	0.83	0.11	AL-CA
5-19	2.00	1.18	45.00	2.57	43.72	2.50	41.45	2.37	12.81	5.48	0.09	5.38	0.66	0.93	0.23	AL-CA
5-20	2.00	1.18	50.00	2.85	48.63	2.78	46.83	2.67	12.84	4.15	0.01	4.14	0.5	0.99	0.41	TAL-CE
5-21	2.00	1.18	60.00	3.43	58.40	3.33	57.39	3.28	12.83	1.12	0.00	1.12	0.14	1.0	0.84	TAL-CE
5-22	3.01	1.32	20.00	1.10	18.77	1.03	8.69	0.48	13.24	8.73	0.81	7.92	0.94	0.35	0.01	AL-CM
5-23	3.01	1.32	30.00	1.65	28.89	1.59	23.99	1.32	13.25	8.38	0.49	7.89	0.9	0.61	0.02	AL-CM
5-24	3.01	1.32	40.00	2.20	38.88	2.14	35.71	1.96	13.25	6.76	0.17	6.59	0.73	0.86	0.18	AL-CA
5-25	3.01	1.32	45.00	2.47	43.82	2.41	41.24	2.27	13.25	5.45	0.07	5.39	0.59	0.94	0.33	AL-CA
5-26	3.01	1.32	50.00	2.75	48.74	2.68	46.64	2.56	13.26	3.78	0.00	3.78	0.41	1.0	0.53	TAL-CE
5-27	3.01	1.32	60.00	3.30	58.54	3.22	57.23	3.15	13.28	-	-	-	-	1.0	-	SCD
5-28	4.01	1.43	20.00	1.06	18.76	1.00	7.47	0.40	13.58	9.66	0.81	8.85	0.94	0.35	0.02	AL-CM
5-29	4.01	1.43	30.00	1.59	28.89	1.53	23.57	1.25	13.60	9.37	0.51	8.86	0.91	0.59	0.02	AL-CM
5-30	4.01	1.43	40.00	2.12	38.91	2.07	35.43	1.88	13.60	7.46	0.17	7.29	0.73	0.86	0.19	AL-CA
5-31	4.01	1.43	45.00	2.39	43.87	2.33	41.00	2.18	13.59	5.95	0.06	5.89	0.58	0.95	0.35	TAL-CA
5-32	4.01	1.43	50.00	2.66	48.80	2.59	46.43	2.47	13.60	4.05	0.00	4.05	0.39	1.0	0.55	TAL-CE
5-33	4.01	1.43	60.00	3.19	58.63	3.11	57.06	3.03	13.59	0.30	0.00	0.30	0.03	1.0	0.97	SCD
5-34	5.01	1.52	20.00	1.03	18.68	0.96	5.80	0.30	13.84	10.72	0.79	9.93	0.95	0.37	0.01	AL-CM
5-35	5.01	1.52	30.00	1.54	28.88	1.49	23.10	1.19	13.85	10.38	0.53	9.85	0.92	0.58	0.02	AL-CM
5-36	5.01	1.52	40.00	2.06	38.93	2.00	35.12	1.81	13.84	8.34	0.20	8.14	0.74	0.84	0.19	AL-CA
5-37	5.01	1.52	45.00	2.32	43.89	2.26	40.73	2.10	13.85	6.93	0.08	6.85	0.62	0.94	0.32	AL-CA
5-38	5.01	1.52	50.00	2.57	48.83	2.51	46.19	2.38	13.86	4.80	0.00	4.80	0.43	1.0	0.52	TAL-CE
5-39	5.01	1.52	60.00	3.09	58.65	3.02	56.86	2.93	13.88	0.93	0.00	0.93	0.08	1.0	0.91	SCD

b) Collision categorisation

To categorise the collision outcomes for our data we consider separately atmosphere ('A') and core and mantle material ('C'). For atmospheres if there was greater than 95 per cent of the initial atmosphere mass in the final remnant we considered there to be a merger ('AM'), on the other hand if there was less than 5 per cent remaining we categorised this as total loss ('TAL'), the rest were considered to undergo partial loss ('AL'). Although hydrogen atmospheres as small as $0.1-1\%$ of a planet's total mass can have a significant effect on its radius, we do not have the resolution to accurately probe atmosphere mass losses that small. For core and mantle, we define mergers ('CM') for > 95 per cent of the total mass of core and mantle from both projectile and target remaining in the largest remnant. If the mass of core and mantle in the largest remnant is greater than that initially in the target we have an accretion event ('CA'), if it is less we have an erosion event ('CE'). If there was less than 10 per cent of the total mass remaining in the largest remnant we define it as a super-catastrophic disruption ('SCD'). Tables 4.1, 4.5 and 4.6, categorise our final results for each collision using this system.

4.3 Results

The main aim of the simulations for this chapter is to determine scaling laws for atmosphere loss as well as total material loss during head-on giant impacts. The wide breadth of impact energies that are simulated in this work have uncovered a broad range of outcomes from near perfect merging events to highly energetic catastrophic disruption (see Figure 4.2).

In the process of determining the loss scaling laws we have found that the atmosphere loss, core and mantle material loss, and the largest remnant mass are well behaved functions of specific impact energy: $Q_{\rm R} = \frac{1}{2}\mu V_{\rm imp}^2/M_{\rm tot}$, where μ is the reduced mass, $V_{\rm imp}$ is the impact velocity, and $M_{\rm tot}$ is the sum of the projectile and target masses (see Leinhardt & Stewart, 2012). We find that atmosphere dominates the material lost until the impact energy is large enough to remove more than 80% of the atmosphere at which point mantle and core material begin to be removed significantly as well. It is also at this point that there is a break and steepening in slope of the largest post collision remnant mass ($M_{\rm lr}$) as a function of $Q_{\rm R}$ (Figure 4.4). In other words, the atmosphere of the

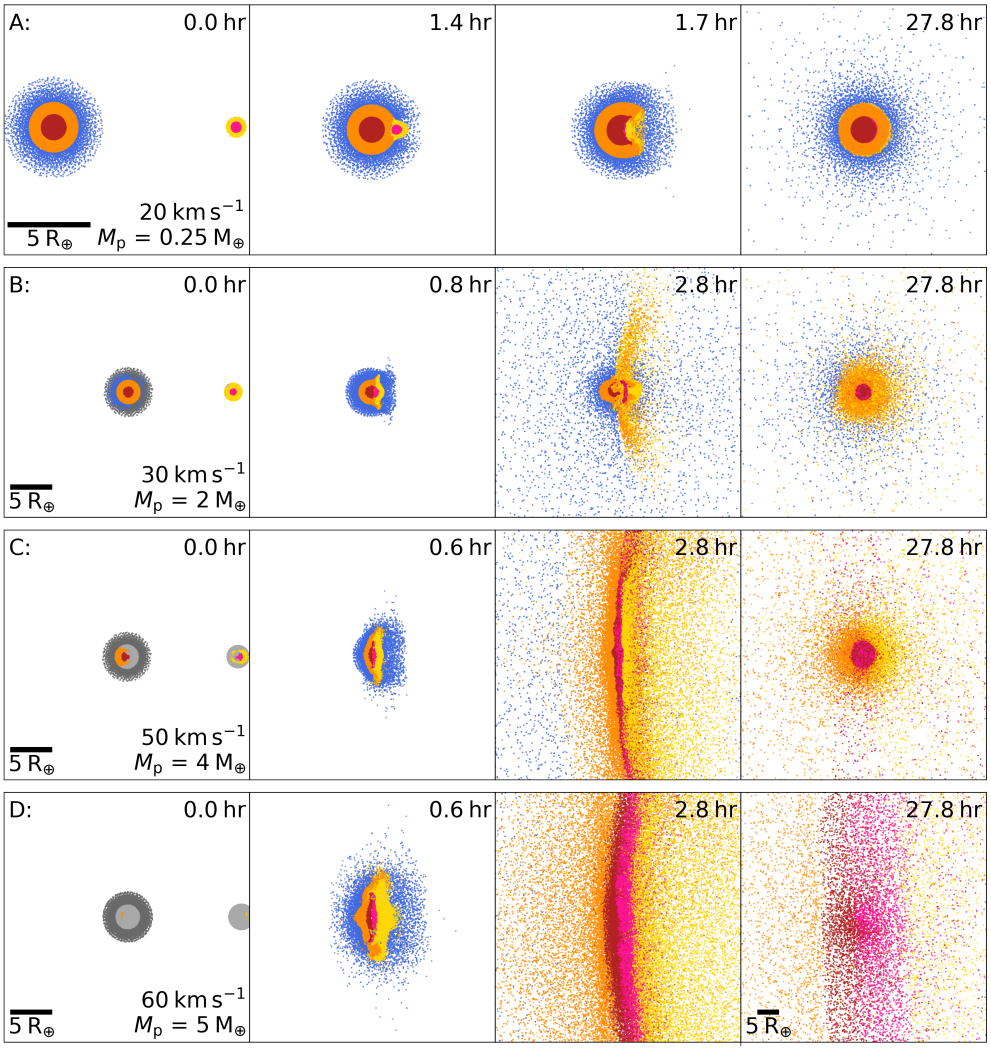

Figure 4.2: Cross-sectional snapshots sliced through the midplane for a series of head-on collisions showing different collision outcomes from merging to catastrophic disruption as the specific relative kinetic energy Q_R increases from row A to row D. Colour denotes material, red and pink – iron core, orange and yellow – forsterite mantle, and blue – hydrogen atmosphere. The additional colours in the first panel denote material that will not be bound by the end of the simulation, black being atmosphere, and grey core or mantle. All collisions shown have the same target mass ($M_t = 6.26\,M_\oplus$) but differ in projectile mass (M_p) and impact speed ($\mathbf{v}_{imp}$): A) Atmosphere and core and mantle merger – $\mathbf{v}_i = 20$ km s^{-1}, $M_p = 0.25\,M_\oplus$ (Table 4.1 5-0); B) Atmosphere loss and core and mantle merger– $\mathbf{v}_i = 30$ km s^{-1}, $M_p = 2\,M_\oplus$ (Table 4.1 5-17); C) Total atmosphere loss and core and mantle erosion – $\mathbf{v}_i = 50$ km s^{-1}, $M_p = 4\,M_\oplus$ (Table 4.1 5-32); D) Supercatastrophic disruption $\mathbf{v}_i = 60$ km s^{-1}, $M_p = 5\,M_\oplus$ (Table 4.1 5-39). Post collision remnants were inflated in comparison to the initial planets and the expected radius of the resultant planet. This 'puffiness' is because we do not cool our final remnants until they reach equilibrium, we only run the simulations until the mass of bound material converges.

target planet cannot be completely removed in one giant impact without significantly eroding the planet.

4.3.1 Mass Loss

We begin by comparing our simulation results to the prescription described in Leinhardt & Stewart (2012) based on collisions of planetesimals and planetary embryos constructed using solely rocky material. A key result from Leinhardt & Stewart (2012) was that the mass of the largest post-collision remnant, $M_{\rm LR}$, scales with $Q_{\rm R}$:

$$\frac{M_{\rm LR}}{M_{\rm tot}} = -0.5 \left(\frac{Q_{\rm R}}{Q^*_{\rm RD}} - 1 \right) + 0.5, \tag{4.7}$$

where $Q^*_{\rm RD}$ is the catastrophic disruption threshold (the energy required to disperse enough material that the largest post-collision remnant is half the total system mass). Normalising $Q_{\rm R}$ by $Q^*_{\rm RD}$ causes the largest remnant mass fraction for different target and projectile masses to fit on the same line.

Figure 4.3 shows the largest remnant mass from our simulations as a function of specific impact energy for collisions with a target of mass $M_{\rm t} = 10.5\,{\rm M}_\oplus$. Each different colour represents a different projectile mass ($M_{\rm p}$). Instead of a straight line (as in Leinhardt & Stewart 2012) our results appear to show two separate linear regimes: a shallower low energy one and a steeper high energy one.

While the existence of the atmosphere means that results split into two regimes, we test $Q^*_{\rm RD}$ to determine whether it still scales $Q_{\rm R}$ such that we obtain a mass independent fit (see Figure 4.4). To determine $Q^*_{\rm RD}$, we fit our data with the following broken linear equation:

$$\frac{M_{\rm LR}}{M_{\rm tot}} = \begin{cases} m_1 \left(Q_{\rm R} - Q_{\rm piv} \right) + c^{\rm LR} & Q_{\rm R} \leqslant Q_{\rm piv} \\ m_2 \left(Q_{\rm R} - Q_{\rm piv} \right) + c^{\rm LR} & Q_{\rm R} > Q_{\rm piv}, \end{cases} \tag{4.8}$$

where $Q_{\rm piv}$ is the specific energy at the transition between the two regimes, measured to be the point where the two linear sections intersect, $c^{\rm LR}$ is the fraction of mass that has been lost at this transition energy, and m_1 and m_2 are the gradients of the two linear sections. Since jettisoning material should require input of energy, we fix this fit such that all mass is in the largest remnant for zero energy input. The gradient for the initial

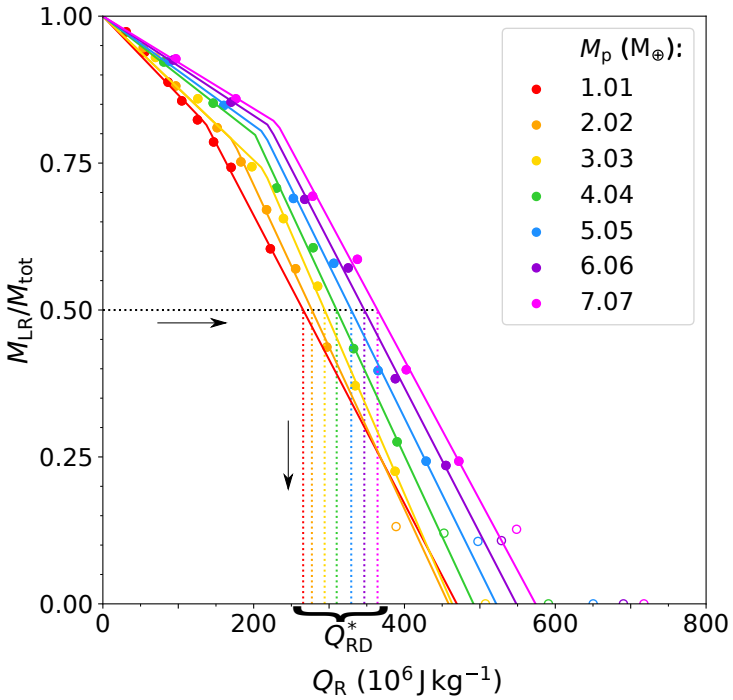

Figure 4.3: A comparison of the mass of the largest remnant for each collision compared with its specific impact energy, overlaid with a graphical representation of the process used to determine Q^*_{RD}. The circles represent the fraction of the total mass which remains in the largest remnant after a collision with a target mass of $M_{\mathrm{t}} = 10.5\,\mathrm{M}_\oplus$ as a function of specific impact energy Q_{R}. Each colour indicates one of seven M_{p} values. A filled circle represents a point used for fits, whilst open circles are points with $\frac{M_{\mathrm{LR}}}{M_{\mathrm{tot}}} < 0.2$ which we considered too close to the super-catastrophic disruption regime which our fit is not designed to cover, for all collisions where < 100 particles were observed in the largest remnant, we also considered the results to be below the resolution limit of the simulation. The solid lines represent our fit to the data for each projectile-target mass ratio, following equation 4.8. From this fit the empirically determined value of Q^*_{RD} is shown on the horizontal axis by the intersection of a coloured dotted line matching the M_{p} colour and $M_{\mathrm{LR}}/M_{\mathrm{tot}} = 0.5$ on the y-axis.

section thus becomes:

$$m_1 = \frac{c^{\mathrm{LR}} - 1}{Q_{\mathrm{piv}}}. \tag{4.9}$$

To ensure a robust fitting method, despite the low number of data points, we began by generating multiple random sets of input parameters for least squares fitting. We determined a best fitting set of output parameters for each input set, and chose the fit with the smallest squared residuals as our final best fit. The fits we obtain for each set of projectile and target masses can then be used to determine the catastrophic disruption threshold by measuring the energy at which half the mass of the system is in the largest remnant (as shown in Figure 4.3). The errors on Q^*_{RD} were determined by propagating errors generated by the least squares fitting algorithm.

For solely rocky objects Leinhardt & Stewart (2012) showed that normalising the impact energy by the catastrophic disruption threshold will mean that mass fraction in the largest remnant will overlap for each set of different targets and projectiles (following equation 4.7). Marcus et al. (2010) showed that this relationship remains true for planets without atmospheres using similar SPH simulations with GADGET-2. The top panel of Figure 4.4 shows the mass of the largest remnant versus normalised specific impact energy for our simulations. The Q^*_{RD} scaling appears to be preserved for all projectile and target masses although the location of the pivot energy changes depending on the target. We fitted each of the targets individually in order to quantify this target dependence. The equation used for the fits is similar to that used for the un-normalised fits (equation 4.8):

$$\frac{M_{\mathrm{LR}}}{M_{\mathrm{tot}}} = \begin{cases} m_1^{\mathrm{LR}} \left(\frac{Q_{\mathrm{R}} - Q_{\mathrm{piv}}}{Q^*_{\mathrm{RD}}} \right) + c^{\mathrm{LR}} & Q_{\mathrm{R}} \leqslant Q_{\mathrm{piv}}, \\ m_2^{\mathrm{LR}} \left(\frac{Q_{\mathrm{R}} - Q_{\mathrm{piv}}}{Q^*_{\mathrm{RD}}} \right) + c^{\mathrm{LR}} & Q_{\mathrm{R}} > Q_{\mathrm{piv}} \end{cases} \tag{4.10}$$

where we again assume that zero mass is lost for zero impact energy as in equation 4.9. The parameters obtained via these fits are found in Table 4.2. This table shows that there is a significant target mass dependence in the pivot energy, the pivot occurs at higher energies for higher target masses and atmosphere fractions.

The middle panel of Figure 4.4 shows the fraction of atmosphere lost from the target versus specific impact energy normalised by the catastrophic disruption threshold. Our results show three separate curves, one for each target mass. The results show that less massive atmospheres of less massive planets are removed more easily than higher

Table 4.2: Parameters for fits using equation 4.10 to the largest remnant mass with $Q^*_{\rm RD}$ normalised specific impact energy.

M_t ($M_\oplus$)	m_2^{LR}	c^{LR}	Q_{piv}/Q^*_{RD}
3.27	-0.68 ± 0.01	0.92 ± 0.01	0.39 ± 0.01
6.26	-0.78 ± 0.02	0.86 ± 0.01	0.54 ± 0.02
10.5	-0.85 ± 0.02	0.76 ± 0.01	0.69 ± 0.02

Table 4.3: Parameters for fits to the fraction of atmosphere lost from the largest remnant with $Q^*_{\rm RD}$ normalised specific energy using equation 4.11

Target Mass ($M_\oplus$)	A
3.27	2.42 ± 0.06
6.26	1.89 ± 0.03
10.5	1.54 ± 0.02

mass atmospheres of higher mass planets. We fit the atmosphere loss fraction, $X^{\rm atmos}_{\rm loss}$, for each target with a quadratic curve fixed to go through the origin and peak at total atmosphere removal:

$$X^{\rm atmos}_{\rm loss} = \frac{-A^2}{4}\left(\frac{Q_{\rm R}}{Q^*_{\rm RD}}\right)^2 + A\frac{Q_{\rm R}}{Q^*_{\rm RD}}, \tag{4.11}$$

where A is the fit parameter. For results of these fits see Table 4.3. Some deviation from the quadratic fits is observed at higher energies, especially for the low mass target ($3.27\,M_\oplus$), this deviation may be due to resolution because there are fewer particles representing the atmosphere for lower mass targets.

We also investigate the dependence of core and mantle loss on the impact energy (bottom panel Figure 4.4). We observe a similar broken linear relation to the broken linear relation seen for the mass of the largest remnant (Figure 4.3 and Figure 4.4, top). In this case we have a shallow gradient below the pivot energy (negligible for the two larger mass targets) indicating very little core and mantle mass loss, and a much steeper

Table 4.4: Parameters for fits using equation 4.12 to the fraction of core material lost from the largest remnant with $Q^*_{\rm RD}$ normalised specific energy.

M_t ($M_\oplus$)	m_1	m_2	$c^{c\&m}$	Q_{piv}/Q^*_{RD}
3.27	0.28 ± 0.02	0.73 ± 0.01	0.08 ± 0.01	0.45 ± 0.01
6.26	0.03 ± 0.03	0.88 ± 0.02	0.02 ± 0.01	0.53 ± 0.01
10.5	0.07 ± 0.03	1.02 ± 0.02	0.03 ± 0.01	0.67 ± 0.01

gradient (therefore much greater loss) above. For lower mass targets (lower atmosphere fractions) there is greater loss of core and mantle at low energies.

In order to compare the energies of the pivots in the mass of the largest remnant and the core and mantle mass loss fraction, we fit the core and mantle loss fraction using the following equation:

$$X_{\rm loss}^{\rm c\&m} = \begin{cases} m_1^{\rm c\&m}\left(\frac{Q_{\rm R}-Q_{\rm piv}}{Q^*_{\rm RD}}\right) + c^{\rm c\&m} & Q_{\rm R} \leqslant Q_{\rm piv}, \\ m_2^{\rm c\&m}\left(\frac{Q_{\rm R}-Q_{\rm piv}}{Q^*_{\rm RD}}\right) + c^{\rm c\&m} & Q_{\rm R} > Q_{\rm piv}. \end{cases} \tag{4.12}$$

Parameters for these fits are given in Table 4.4. As can be seen from the coloured vertical bars in the bottom panel of Figure 4.4, there appears to be a correlation between this pivot energy and the pivot energy found for the mass of the largest remnant. The similar energies of these pivot points implies that the break in slope for largest remnant mass is due to the break in slope for loss of core and mantle material. We therefore categorise impacts into two energy loss regimes: below the pivot energy we have atmosphere dominated loss, and above it we have substantial core and mantle loss.

An important point to note here is that at this pivot energy, the amount of atmosphere remaining is consistently $20-30\%$. This means that a single giant impact cannot remove all of a planet's atmosphere without also removing core and mantle material.

4.3.2 Atmospheric Loss Scaling Law

As we saw in Figure 4.4, the atmosphere mass loss fraction coinciding with the pivot energy is consistently $70-80$ per cent. We therefore suggest a normalisation based on this pivot energy instead of $Q^*_{\rm RD}$. The results for this are shown in the top panel of Figure 4.5. To build a scaling law for atmosphere loss, we have fitted the loss fraction using a quadratic curve (again with a constraint of zero mass loss at zero input energy and a peak at total atmosphere mass loss)

$$X_{\rm loss}^{\rm atmos} = \frac{-A^2}{4}\left(\frac{Q_{\rm R}}{Q_{\rm piv}}\right)^2 + A\frac{Q_{\rm R}}{Q_{\rm piv}}, \tag{4.13}$$

where our fitting parameter $A = 0.94 \pm 0.01$. The other ingredient we require for building a scaling law for atmosphere loss is a way of predicting the pivot energy. After some experimentation we found a linear relation between the pivot energy divided by

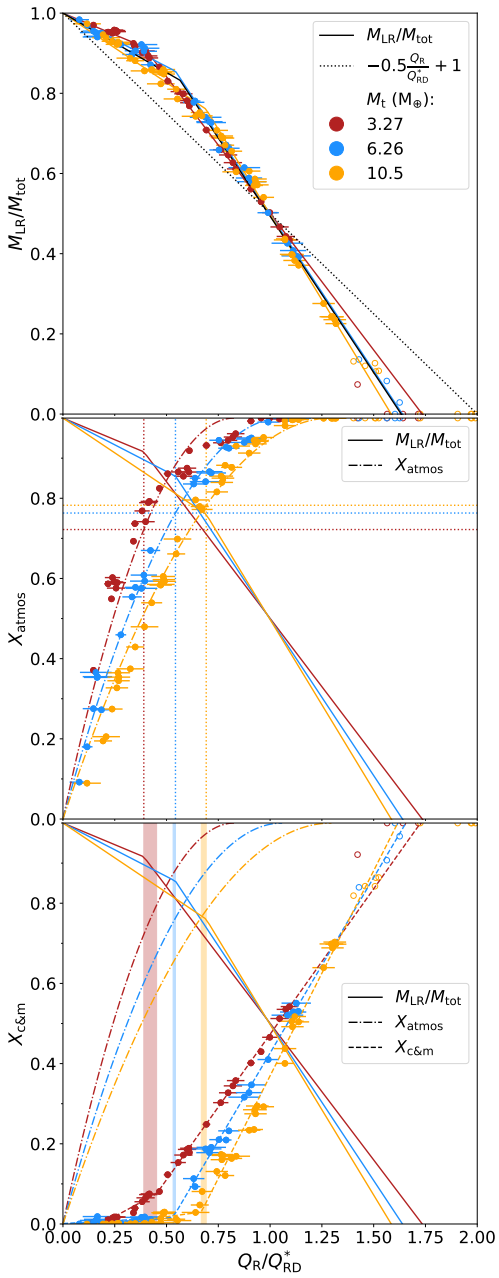

Figure 4.4: Top: M_{LR} versus Q_R/Q^*_{RD} for all simulations. Colour indicates target mass, open circles represent points that were excluded from the fit. Coloured solid lines are best fits to data for a given M_t. The black solid line is the best fit to the entire data set. The dotted black line is the universal law from Leinhardt & Stewart (2012). Middle: Fraction of atmosphere lost versus Q_R/Q^*_{RD}. The dashed coloured lines indicate best fits. The dotted vertical and horizontal lines show the specific energy of the break in the M_{LR} fit and the respective fraction of atmosphere loss. Bottom: Fraction of core and mantle lost versus Q_R/Q^*_{RD}. Dashed lines are a broken linear fit. Shaded vertical sections show the difference between the specific energy of the break in the M_{LR} fit and the break in the core loss fit. For all 3 graphs the horizontal error bars represent the error in the Q^*_{RD} determination method.

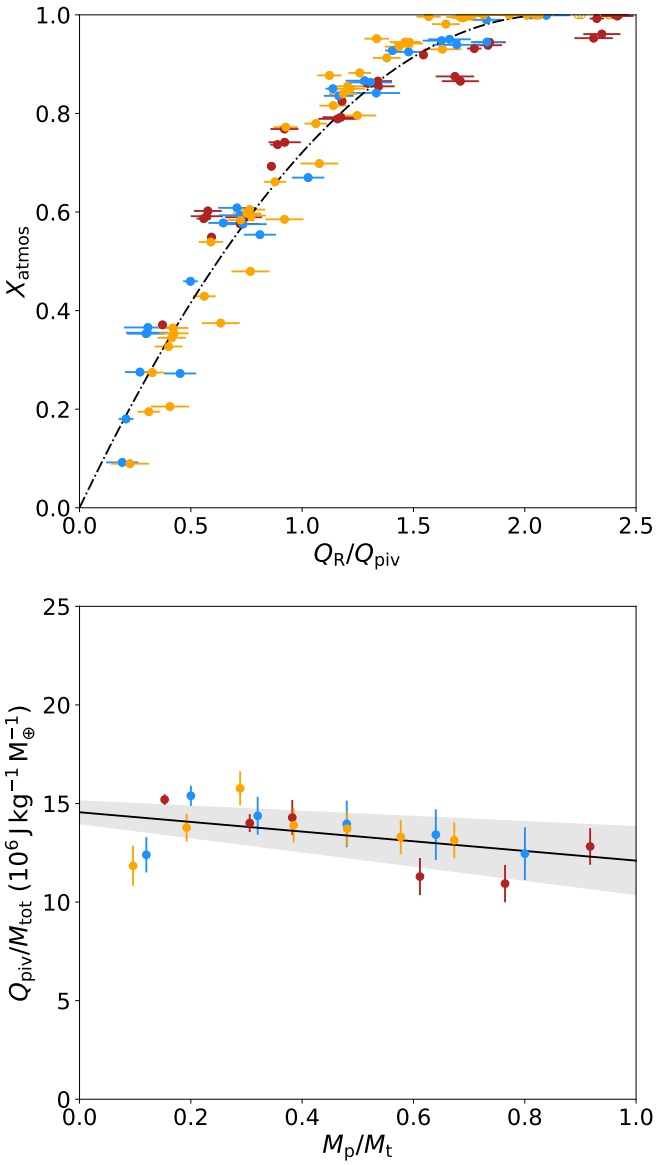

Figure 4.5: Top: Fractional atmosphere loss compared to specific impact energy scaled with respect to the pivot energy for each target mass. The amount of energy required to remove more atmosphere increases as the amount of atmosphere removed increases. Fitted to the data is a simple quadratic which has been fixed to cross the origin and have a peak at total atmosphere loss (equation 4.13). Bottom: Specific energy of the pivot normalised by the total mass of the system compared with projectile-target mass ratio. Mass normalised pivot energy appears to be approximately constant, decreasing slightly as projectile masses increase. The fit is given by equation 4.14.

the total mass and the projectile target mass ratio for all atmosphere fractions tested (see bottom panel of Figure 4.5):

$$\frac{Q_{\mathrm{piv}}}{M_{\mathrm{tot}}} = -\left(2.5 \pm 1.1\right) \frac{M_{\mathrm{p}}}{M_{\mathrm{t}}} + \left(14.6 \pm 0.6\right) \quad [10^6\,\mathrm{J\,kg^{-1}\,M_{\oplus}^{-1}}]. \tag{4.14}$$

Equation 4.14 has quite a shallow gradient, meaning that the specific energy of the pivot is strongly dependent on the the total mass, i.e. the impact energy is strongly dependent on the square of the total mass, implying it is related to the total gravitational binding energy of the system. The error envelope in Figure 4.5 is generated from the variance of the fit parameters. Together Equations 4.13 and 4.14 can be used to predict the mass fraction of atmosphere lost from the target for any head-on giant impact in the regime tested.

4.4 Discussion

4.4.1 Caveats

a) Atmosphere fraction effects

We chose the initial atmosphere fraction for each target planet based on the most likely atmosphere fractions from the Bern global planet formation model (equation 4.1). One issue with this method is that it makes distinguishing between the effects of target mass and atmosphere fraction somewhat difficult, as both are directly related. An important result that requires further investigation is the relation between atmosphere fraction and pivot energy. One might expect that less massive atmospheres would require less energy to remove and thus core and mantle material would begin to be removed earlier, decreasing the pivot energy. We observe a decrease in pivot energy but we cannot distinguish whether this is due to a smaller atmosphere fraction or a shallower gravitational potential well from a less massive target. In the future we could test the cause of the decrease in pivot energy by simulating collisions involving targets of the same masses with different atmosphere fractions.

b) Equation of State effects

One simplification we have made in this work is to use ideal gas atmospheres as opposed to a more realistic equation of state. For Earth atmospheric pressures this would have a

negligible effect, but we are dealing with significantly more massive atmospheres (roughly seven orders of magnitude). For such massive atmospheres the pressures and densities at the base of the atmosphere are such that the assumption that molecules do not interact (inherent in using an ideal gas) may not be realistic. The lack of inter-particle interactions means that we have unrealistically high densities at high pressures, (the base of our atmospheres post equilibration being 1.2–19.2 $\times 10^5$ atm or 1.2–19.2 $\times 10^9$ GPa). One effect of this is a significant compression of the atmosphere when equilibrating a GADGET-2 planet. During the equilibration the radii of atmospheres shrank on average by a factor of two. Despite these issues, we have used an ideal gas as a starting point, more realistic equations of state should be the subject of a future study.

c) Impact Angle effects

For impact angle we have also elected to investigate the simplest case – head-on collisions. In general, we would expect an average collision angle of 45° (Shoemaker & Hackman, 1962). Leinhardt & Stewart (2012) present in their prescription a method to relate the mass loss of an off angle collision with a head-on one, which uses an interacting mass. In the impact scenarios considered in this work we would expect the impact angle correction to become more complicated due to the density contrast between atmosphere and mantle. Hwang et al. (2017b) and Hwang et al. (2017a) have previously done work on grazing collisions where the cores and mantles did not touch. Their results show that mass loss follows a power-law dependence on impact parameter. We plan to investigate this further in future work.

4.4.2 Catastrophic Disruption threshold Scaling

Leinhardt & Stewart (2012) predict that for equal mass impacts the catastrophic disruption threshold should obey:

$$Q^*_{\mathrm{RD}(\gamma=1)} = c^* \frac{4}{5} \pi \rho_1 G R^2_{\mathrm{C1}}, \tag{4.15}$$

where $\gamma = M_{\mathrm{p}}/M_{\mathrm{t}}$, c^* is a measure of the catastrophic disruption threshold in units of the gravitational binding energy (measured to be $c^* = 1.9 \pm 0.3$ for hydrodynamical simulations of large rocky planets), $\rho_1 = 1000\,\mathrm{kg\,m^{-3}}$, and $R_{\mathrm{C1}} = \left(\frac{3M_{\mathrm{tot}}}{4\pi\rho_1}\right)^{\frac{1}{3}}$ is the radius a spherical body would have if it had the total system mass and a density of ρ_1.

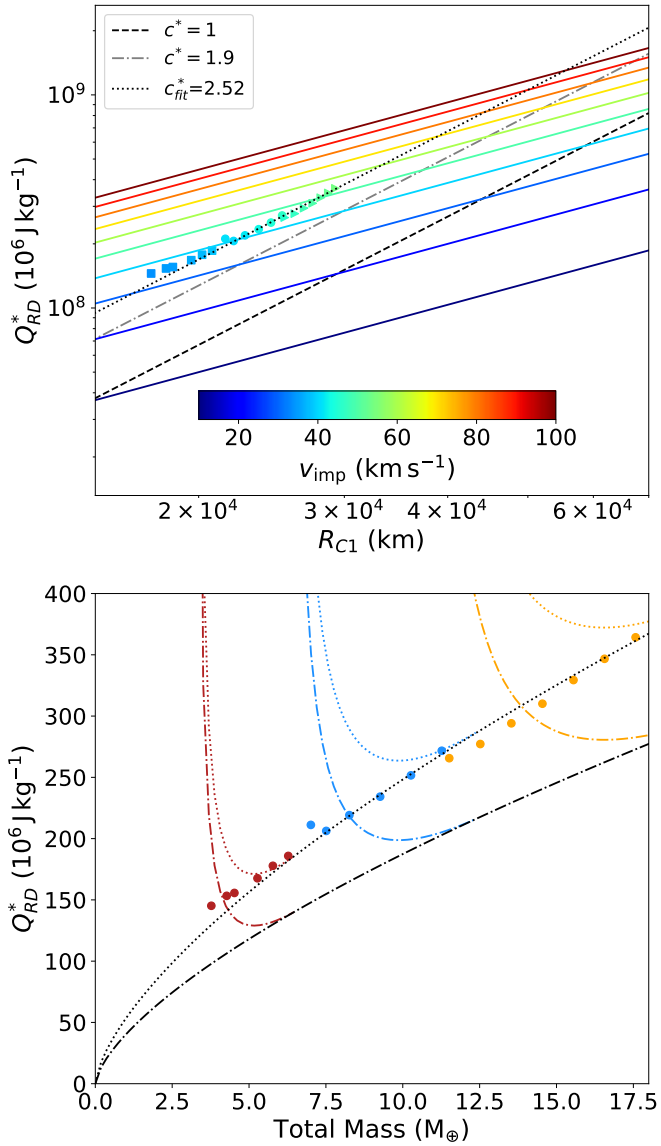

Figure 4.6: Top: Catastrophic disruption threshold $Q^*_{\rm RD}$ compared with $R_{\rm C1}$ the radius a spherical body would have if it had the total system mass and a density of 1000 kg m^{-3}, with black and grey lines showing their predicted relationship for different values of the strength parameter c^* following equation 4.15. We observe a value of $c^* = 2.52$, which is a 32% increase compared to Leinhardt & Stewart (2012)'s value of 1.9 for solely rocky bodies. Coloured lines show the predicted catastrophic disruption threshold for equal mass collisions for particular velocities. The colour of each data point indicates the relative velocity the pair of planets would have for each collision if they were equal mass. Bottom: Comparison between the catastrophic disruption threshold, and the total mass of each set of collisions. Black lines detail predictions of the catastrophic disruption threshold for each total mass for pure energy scaling for different values of c^*, dotted is our measured value of 2.52, dot-dashed is Leinhardt & Stewart (2012)'s value of 1.9, coloured lines show predictions for pure momentum scaling. Our results (dots with colours representing target mass as per figure 4.4) appear to follow the prediction for pure energy scaling.

Leinhardt & Stewart (2012) also propose a further correction for this catastrophic disruption threshold for collisions of different mass projectiles and targets,

$$Q^*_{\mathrm{RD}} = Q^*_{\mathrm{RD}(\gamma=1)} \left(\frac{(\gamma+1)^2}{4\gamma} \right)^{\frac{2}{3\bar{\mu}}-1}, \tag{4.16}$$

which is dependent upon a parameter $\bar{\mu}$ where $\bar{\mu}$ has values between 1/3 (pure momentum scaling) and 2/3 (pure energy scaling). This multiplicative correction becomes unity for all mass ratios with perfect energy scaling because the index becomes zero.

Figure 4.6 details how our results compare to Leinhardt & Stewart's predictions. Our results run parallel to the prediction of equation 4.15 indicating a larger c^* value of 2.52 (compared to the value given in Leinhardt & Stewart 2012). The larger c^* means that a greater excess over the binding energy is required to remove material from planets with atmospheres than those without. This is presumably due to the increased compressibility and decreased viscosity of atmosphere compared to mantle and core material.

It should be noted that we appear to be observing pure energy scaling for these collisions as no mass ratio correction is required, this is illustrated best in the bottom part of Figure 4.6. Here, black lines represent the predicted catastrophic disruption threshold using energy scaling, whilst coloured lines represent the momentum scaling which Leinhardt & Stewart (2012) predicts we should be close to. As can be observed, our results follow the energy scaled prediction closely. This runs contrary to the results in Leinhardt & Stewart (2012) which predicts near perfect momentum scaling. Presumably this difference is due to the presence of the atmosphere, as the Leinhardt & Stewart (2012) method is based on Holsapple & Schmidt (1987)'s crater scaling, where they show that porous materials tend to follow momentum scaling, while perfect gases tend to follow energy scaling.

4.4.3 Mass loss efficiency comparisons

Leinhardt & Stewart (2012) predict that the mass of the largest post-collision remnant scales with normalised specific impact energy (equation 4.7). This equation gives a gradient with respect to Q_{R} for the largest remnant mass of

$$\frac{d\left(M_{\mathrm{LR}}/M_{\mathrm{tot}}\right)}{dQ_{\mathrm{R}}} = -\frac{0.5}{Q^{*(\mathrm{LS12})}_{\mathrm{RD}}}. \tag{4.17}$$

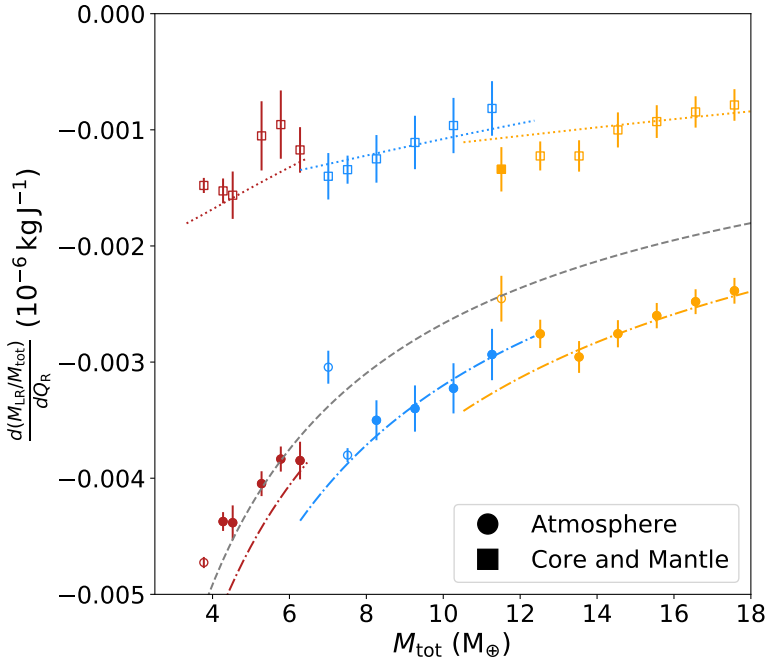

Figure 4.7: Comparisons between the mass loss efficiency for core and mantle, and for atmosphere to the total mass of the system. Atmosphere loss shows a decreased efficiency in comparison to core and mantle loss, as might be expected considering the increased compressibilty of atmosphere material. Filled shapes are gradients where we obtained 4 or greater data points for that line, open are where we have 3 or fewer. The grey line shows the loss efficiency predicted by Leinhardt & Stewart (2012) for rocky material, the coloured line beneath them is this value multiplied by 1 plus the atmosphere fraction for that particular target as per equation 4.18. This appears to show reasonable correlation with our results especially for higher mass targets. The coloured dotted line above this shows a prediction of what the atmosphere gradient must be that uses all previously derived scaling laws, is linear and passes through zero mass loss for zero input energy (equation 4.19). Our results show some degree of correlation with this value, but we do not have a high enough density of data in this region to effectively probe the accuracy of this prediction.

In this work we found that the largest remnant mass as a function of specific energy falls into two regimes (see Figure 4.3) with two different gradients. Figure 4.7 compares the gradients measured from our results to Leinhardt & Stewart's prediction.

We can consider these gradients as a measurements of the efficiency of mass loss in each regime. The efficiency of mass loss for the core and mantle loss region is typically at least double that for the atmosphere dominated loss regime, this is presumably due to the increased compressibility of the atmosphere.

As can be observed, the Leinhardt & Stewart (2012) model (equation 4.17 above) appears to under predict the efficiency of mantle and core material loss for planets with substantial envelopes. This is likely due to the pressure of the atmosphere above providing a resisting force to reduce mantle loss. Once the atmosphere is removed the specific energy of the impact is higher than would have been necessary to remove significant mantle if no atmosphere was present, so more material is being removed per unit of specific energy.

We have found that an approximate prediction of the gradient in the core and mantle loss regime is given by:

$$\frac{d\left(M_{\rm LR}/M_{\rm tot}\right)}{dQ_{\rm R}} = -\frac{0.5(1+f_{\rm atmos})}{Q_{\rm RD}^{*\rm (LS12)}}, \tag{4.18}$$

where $f_{\rm atmos}$ is the atmosphere fraction of the target. For our higher mass targets with more massive atmospheres, this seems to be a reasonably good predictor of loss efficiency; for the smallest target with the lowest mass atmosphere, however, the initial prediction from equation 4.17 seems to match more closely.

To predict the loss efficiency (gradient) in the atmosphere loss dominated regime, we assume that there is zero mass loss for zero input energy, and use our scaling laws for the pivot energy (equation 4.14) and catastrophic disruption threshold (equation 4.15) along with our correction to the gradient in the core and mantle loss regime (equation 4.18) to predict the fraction of material in the largest remnant at the pivot energy. We also assume that the gradient in the atmosphere loss regime is constant with respect to energy (as in Equations 4.8 and 4.9). Combining these equations we obtain the following relation,

$$\frac{d\left(M_{\rm LR}/M_{\rm tot}\right)}{dQ_{\rm R}} = \frac{-0.5 - m_2^{\rm LR}(Q_{\rm RD}^{*\rm (New)} - Q_{\rm piv})}{Q_{\rm piv}}. \tag{4.19}$$

Our results show a reasonable match with this prediction for the gradient in the atmosphere loss regime. However, we do not have a sufficient data in this region to fully probe the accuracy of this scaling; for example we cannot test whether atmosphere loss begins at zero impact energy (as we have assumed in deriving the scaling) or requires some small initial energy input.

4.4.4 Implications

This study was motivated by the density disparity observed in exoplanet systems. The post-impact bodies in our simulations are hot and inflated, often with a large mass of vaporised silicate, and thus do not represent the structure of planets millions of years after their final giant impacts (Lock & Stewart, 2017; Carter et al., 2020; Lock et al., 2020). To determine the bulk density of the remnants from their post-collision material composition, we use the approximation suggested in Lopez & Fortney (2014). In their model the total radius of a planet, $R_{\rm planet}$, from which we determine the density, can be calculated from summing the radial contributions of the following three components: the core and mantle, which has a power law relation to mass; the convective envelope, which is dependent on the temperature of the atmosphere, which itself is a function of stellar flux and planet age; and the radiative atmosphere (also dependent on temperature). Here, we ignore the contribution of the radiative atmosphere due to its small effect ($\sim 0.1 \mathrm{R}_{\oplus}$) We used an age of 5 Gyr for our comparison planets (see Figure 4.8) as this is the most common age for stars in the local galactic neighbourhood. We used a flux, $F_{\rm planet}$, of $100\,\mathrm{F}_{\oplus}$ as the type of planets we simulated are most commonly observed at ~ 0.1 au around Sun-like stars. Figure 4.8 shows contour plots of the radius (top) and density (bottom) as a function of mass and atmosphere fraction according to the Lopez & Fortney (2014) approximation described above.

The prediction we obtained for the envelope radius of our initial targets using the Lopez & Fortney (2014) model was within 10 per cent of the radius of our initial thermodynamic profiles. This radius was, however, significantly larger than our GADGET-2 targets due to the compression caused by using an ideal gas. We also note that we could not reach the 20 mBar pressures which Lopez & Fortney (2014) consider to be the edge of the atmosphere with computationally practical resolutions.

For our collisions, we always observe a decrease in atmosphere fraction. This decrease

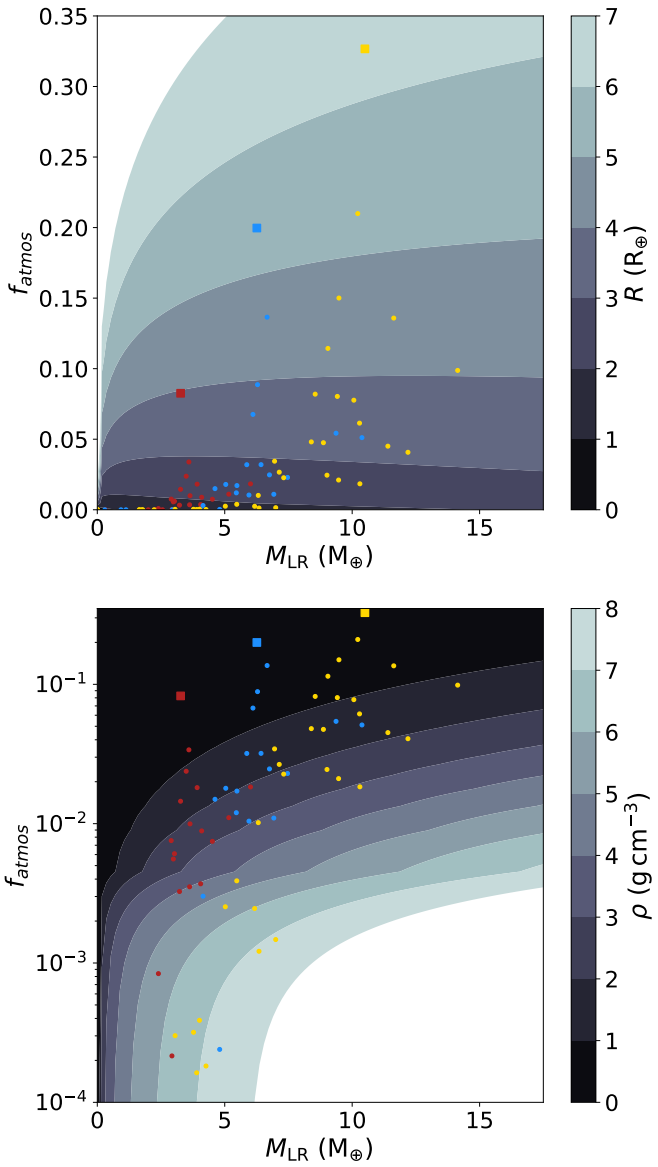

Figure 4.8: Top: Radius as a function of mass following the prescription of Lopez & Fortney (2014), compared against our initial targets (squares) and also our post-collision largest remnants (circles), the same colour scheme for target masses is used as for the rest of the chapter. Bottom: Density as a function of mass calculated using the radius above, this is similarly compared against our initial targets (squares) and also our post-collision largest remnants (circles), collisions with full atmosphere removal have been removed so atmosphere fraction could be plotted logarithmically.

in atmosphere fraction means that for all the collisions we simulate, except for those resulting in largest remnants below the resolution limit, we observe an increase in density as shown in the bottom panel of Figure 4.8.

4.4.5 New prescriptions for atmosphere loss and largest remnant mass

Here we summarise the process one would need to use to predict the atmosphere loss from any giant impact in the regime probed by the simulations run for this chapter, as well as the modifications to the Leinhardt & Stewart (2012) prescription for largest post-collision remnant mass for an arbitrary head on collision between a Mini-Neptune with a significant gaseous envelope and a lower mass Super-Earth without an atmosphere. This algorithm can be incorporated into N-body codes and population synthesis models.

1. For a given collision scenario ($M_{\rm p}$, $M_{\rm t}$ and $V_{\rm imp}$), calculate the specific relative kinetic energy of the impact,
$$Q_{\rm R} = \frac{1}{2}\mu\frac{V_{\rm imp}^2}{M_{\rm tot}}, \tag{4.20}$$
where $M_{\rm tot} = M_{\rm t} + M_{\rm p}$, and $\mu = M_{\rm t}M_{\rm p}/(M_{\rm t} + M_{\rm p})$ is the reduced mass, $M_{\rm t}$ is the target mass, $M_{\rm p}$ the projectile mass and $V_{\rm imp}$ is the impact velocity.
2. Then, calculate the specific kinetic energy of the transition between the atmosphere loss and core and mantle loss regimes,
$$Q_{\rm piv} = \left(\frac{M_{\rm tot}}{M_{\oplus}}\right)\left(-2.45\frac{M_{\rm p}}{M_{\rm t}} + 14.56\right) \quad [10^6\,{\rm J\,kg^{-1}}]. \tag{4.21}$$
3. Calculate the catastrophic disruption threshold,
$$Q^*_{\rm RD} = c^*\frac{4}{5}\pi\rho_1 G R_{\rm C1}^2, \tag{4.22}$$
using a value of $c^* = 2.52$ for collisions involving planets with atmospheres ($Q^{*({\rm New})}_{\rm RD}$) and $c^* = 1.9$ ($Q^{*({\rm LS12})}_{\rm RD}$, as in Leinhardt & Stewart 2012) for targets with no atmosphere. $\rho_1 = 1000\,{\rm kg\,m^{-3}}$, and $R_{\rm C1} = \left(\frac{3M_{\rm tot}}{4\pi\rho_1}\right)^{\frac{1}{3}}$ is the radius a spherical body would have if it had the total system mass and a density of ρ_1.

4. Calculate the gradients of each of the linear sections of the largest remnant mass fraction relation. For the core and mantle loss regime this is
$$m_{\rm c\&m} = \frac{-0.5(1 + f_{\rm atmos})}{Q^{*({\rm LS12})}_{\rm RD}}, \tag{4.23}$$

where $f_{\rm atmos}$ is the mass fraction of the target which is atmosphere.

5. Zero impact energy means zero mass loss, therefore the gradient for the atmosphere loss dominated part of the relation is, from equation 4.9,

$$m_{\rm atmos} = \frac{m_{\rm c\&m}(Q_{\rm piv} - Q_{\rm RD}^{*(\rm New)}) - 0.5}{Q_{\rm piv}}. \tag{4.24}$$

6. Next, calculate the super-catastrophic disruption threshold, taking this to be where <10 per cent of the initial mass ends up in the largest remnant (following Leinhardt & Stewart (2012)) we obtain

$$Q_{\rm supercat} = Q_{\rm RD}^{*(\rm New)} - \frac{0.4}{m_{\rm c\&m}}. \tag{4.25}$$

7. Then, the total mass in the largest remnant is:

$$\frac{M_{\rm LR}}{M_{\rm tot}} = \begin{cases} m_{\rm atmos} Q_{\rm R} + 1 & 0 < Q_{\rm R} < Q_{\rm piv} \\ \\ m_{\rm c\&m}(Q_{\rm R} - Q_{\rm RD}^{*(\rm New)}) + 0.5 & Q_{\rm piv} < Q_{\rm R} < Q_{\rm supercat}. \end{cases} \tag{4.26}$$

We did not probe the super-catastrophic disruption regime in this study due as this would require much higher resolution; for collisions in this energy regime we recommend using the prescription of Leinhardt & Stewart (2012).

8. Finally, the atmosphere fraction lost is,

$$\chi_{\rm loss}^{\rm atmos} = \begin{cases} \frac{-0.94^2}{4}\left(\frac{Q_{\rm R}}{Q_{\rm piv}}\right)^2 + 0.94\frac{Q_{\rm R}}{Q_{\rm piv}} & \frac{Q_{\rm R}}{Q_{\rm piv}} < 2.12 \\ 1 & \frac{Q_{\rm R}}{Q_{\rm piv}} > 2.12. \end{cases} \tag{4.27}$$

4.5 Summary

In this chapter we present the results from a series of SPH simulations of head-on collisions of planets in which the target has a significant atmosphere. Our findings are summarised below:

- Giant impacts can have sufficient energy to remove large fractions of mass from the target planet; the mass lost is dependent upon the specific kinetic energy of the impact.

- Giant impacts can result in substantial increases in the densities of Mini-Neptune planets by ejecting a fraction of their atmospheres.
- The fraction of mass lost splits into two regimes – at low specific impact energies only the outer layers are ejected corresponding to atmosphere dominated loss, at higher energies material deeper in the potential is excavated resulting in significant core and mantle loss.
- Approximately twenty per cent of the initial atmosphere remains at the transition between the two regimes.
- A single collision cannot remove all the atmosphere without also removing a significant percentage of mantle material.
- Mass removal is less efficient in the atmosphere loss dominated regime compared to the core and mantle loss regime.
- The specific energy of this transition (pivot energy, $Q_{\rm piv}$) scales linearly with the ratio of projectile to target mass for all projectile-target mass ratios measured: $Q_{\rm piv} = M_{\rm tot}\left(-2.45\frac{M_{\rm p}}{M_{\rm t}} + 14.56\right)$ $[10^6\,{\rm J\,kg^{-1}\,M_\oplus^{-1}}]$.
- The fraction of atmosphere lost is well approximated by a quadratic in terms of the ratio of specific energy to transition energy: $X_{\rm loss}^{\rm atmos} = \frac{-0.94^2}{4}\left(\frac{Q_{\rm R}}{Q_{\rm piv}}\right)^2 + 0.94\frac{Q_{\rm R}}{Q_{\rm piv}}$, for $Q_{\rm R} < 2.12\,Q_{\rm piv}$, and total atmosphere loss for energies greater than this.

4.6 Appendix

4.6.1 Further Impacts

We present results in this chapter for collisions against 3 separate simulated Super-Earth targets, a $3.27\,{\rm M_\oplus}$ target with a $0.27\,{\rm M_\oplus}$ atmosphere, $1\,{\rm M_\oplus}$ core and $2\,{\rm M_\oplus}$ mantle (initial conditions and results given in Table 4.5); a $6.26\,{\rm M_\oplus}$ one with a $1.25\,{\rm M_\oplus}$ atmosphere, $1.67\,{\rm M_\oplus}$ core and $3.34\,{\rm M_\oplus}$ mantle (Table 4.1); and a $10.5\,{\rm M_\oplus}$ one with a $3.43\,{\rm M_\oplus}$ atmosphere, $2.36\,{\rm M_\oplus}$ core and $4.71\,{\rm M_\oplus}$ mantle (Table 4.6).

Table 4.5: Parameters for head-on collisions between a $3.27\,\mathrm{M}_\oplus$ target ($M_\mathrm{t}^\mathrm{core} = 3.0\,\mathrm{M}_\oplus$, $M_\mathrm{t}^\mathrm{atmos} = 0.27\,\mathrm{M}_\oplus$) with a mantle surface radius of $1.31\,\mathrm{R}_\oplus$, and an atmosphere scale height of $0.52\,\mathrm{R}_\oplus$, and projectiles of mass M_p. Similar to Tables 4.1 and 4.6.

ID	M_p	R_p	$v_\mathrm{imp}^\mathrm{pred}$	$\frac{v_\mathrm{imp}^\mathrm{pred}}{v_\mathrm{esc}}$	$v_\mathrm{imp}^\mathrm{meas}$	$\frac{v_\mathrm{imp}^\mathrm{meas}}{v_\mathrm{esc}}$	v_init	$\frac{v_\mathrm{init}}{v_\mathrm{esc}}$	S	M_LR	$M_\mathrm{LR}^\mathrm{atmos}$	$M_\mathrm{LR}^\mathrm{core}$	$\frac{M_\mathrm{LR}}{M_\mathrm{tot}}$	$X_\mathrm{loss}^\mathrm{atmos}$	$X_\mathrm{loss}^\mathrm{c\&m}$	Category
	$\mathrm{M}_\oplus$	$\mathrm{R}_\oplus$	$\mathrm{km\,s^{-1}}$		$\mathrm{km\,s^{-1}}$		$\mathrm{km\,s^{-1}}$		$\mathrm{R}_\oplus$	$\mathrm{M}_\oplus$	$\mathrm{M}_\oplus$	$\mathrm{M}_\oplus$				
3-0	0.50	0.78	20.00	1.46	19.28	1.41	14.98	1.10	9.59	3.66	0.17	3.49	0.97	0.37	0.0	AL-CM
3-1	0.50	0.78	25.00	1.83	24.32	1.78	21.20	1.55	9.59	3.59	0.12	3.47	0.95	0.56	0.01	AL-CM
3-2	0.50	0.78	30.00	2.19	29.31	2.14	26.92	1.97	9.59	3.49	0.08	3.41	0.92	0.7	0.03	AL-CM
3-3	0.50	0.78	35.00	2.56	34.29	2.51	32.39	2.37	9.60	3.27	0.05	3.22	0.87	0.81	0.08	AL-CA
3-4	0.50	0.78	40.00	2.92	39.25	2.87	37.74	2.76	9.59	2.90	0.02	2.88	0.77	0.93	0.18	AL-CE
3-5	0.50	0.78	50.00	3.66	49.14	3.59	48.21	3.53	9.59	2.00	0.00	2.00	0.53	1.0	0.43	TAL-CE
3-6	1.00	0.97	20.00	1.40	19.30	1.35	14.77	1.04	10.13	4.07	0.11	3.96	0.95	0.59	0.01	AL-CM
3-7	1.00	0.97	25.00	1.75	24.37	1.71	21.05	1.48	10.12	3.92	0.07	3.85	0.92	0.74	0.04	AL-CM
3-8	1.00	0.97	30.00	2.10	29.40	2.06	26.80	1.88	10.14	3.55	0.04	3.51	0.83	0.85	0.12	AL-CA
3-9	1.00	0.97	35.00	2.46	34.41	2.41	32.30	2.27	10.13	3.03	0.02	3.01	0.71	0.93	0.25	AL-CA
3-10	1.00	0.97	40.00	2.81	39.39	2.76	37.66	2.64	10.12	2.40	0.00	2.40	0.56	1.0	0.4	TAL-CE
3-11	1.00	0.97	50.00	3.51	49.31	3.46	48.15	3.38	10.14	0.32	0.00	0.32	0.07	1.0	0.92	SCD
3-12	1.25	1.03	20.00	1.38	19.29	1.33	14.60	1.00	10.31	4.30	0.11	4.19	0.95	0.59	0.02	AL-CM
3-13	1.25	1.03	25.00	1.72	24.39	1.68	20.93	1.44	10.31	4.08	0.06	4.02	0.9	0.78	0.06	AL-CA
3-14	1.25	1.03	30.00	2.06	29.43	2.03	26.70	1.84	10.31	3.64	0.04	3.60	0.8	0.85	0.15	AL-CA
3-15	1.25	1.03	35.00	2.41	34.43	2.37	32.22	2.22	10.31	2.98	0.02	2.97	0.66	0.93	0.3	AL-CE
3-16	1.25	1.03	40.00	2.75	39.42	2.71	37.59	2.59	10.32	2.27	0.00	2.27	0.5	1.0	0.47	TAL-CE
3-17	1.25	1.03	50.00	3.44	49.35	3.40	48.09	3.31	10.31	-	-	-	-	1.0	-	SCD
3-18	2.00	1.18	20.00	1.31	19.32	1.26	14.03	0.92	10.77	5.03	0.11	4.92	0.95	0.59	0.02	AL-CM
3-19	2.00	1.18	25.00	1.63	24.38	1.59	20.54	1.34	10.78	4.69	0.06	4.63	0.89	0.78	0.07	AL-CA
3-20	2.00	1.18	30.00	1.96	29.42	1.92	26.39	1.73	10.79	4.10	0.04	4.06	0.78	0.85	0.19	AL-CA
3-21	2.00	1.18	35.00	2.29	34.46	2.25	31.96	2.09	10.78	3.23	0.01	3.21	0.61	0.96	0.36	TAL-CA
3-22	2.00	1.18	40.00	2.62	39.46	2.58	37.37	2.44	10.78	2.29	0.00	2.29	0.43	1.0	0.54	TAL-CE
3-23	2.00	1.18	50.00	3.27	49.42	3.23	47.92	3.13	10.79	-	-	-	-	1.0	-	SCD
3-24	2.50	1.26	20.00	1.27	19.27	1.22	13.59	0.86	11.01	5.52	0.11	5.41	0.96	0.59	0.02	AL-CM
3-25	2.50	1.26	25.00	1.59	24.42	1.55	20.24	1.28	11.01	5.16	0.06	5.10	0.89	0.78	0.07	AL-CA
3-26	2.50	1.26	30.00	1.90	29.46	1.87	26.17	1.66	11.01	4.52	0.03	4.48	0.78	0.89	0.19	AL-CA
3-27	2.50	1.26	35.00	2.22	34.47	2.19	31.78	2.02	11.00	3.62	0.01	3.61	0.63	0.96	0.34	TAL-CA
3-28	2.50	1.26	40.00	2.54	39.47	2.50	37.21	2.36	11.01	2.56	0.00	2.56	0.44	1.0	0.53	TAL-CE
3-29	3.00	1.33	20.00	1.23	19.20	1.19	13.14	0.81	11.20	6.01	0.11	5.90	0.96	0.59	0.02	AL-CM
3-30	3.00	1.33	25.00	1.54	24.38	1.50	19.94	1.23	11.21	5.68	0.07	5.61	0.91	0.74	0.07	AL-CA
3-31	3.00	1.33	30.00	1.85	29.43	1.82	25.93	1.60	11.22	5.01	0.04	4.97	0.8	0.85	0.17	AL-CA
3-32	3.00	1.33	35.00	2.16	34.46	2.13	31.58	1.95	11.21	4.06	0.02	4.04	0.65	0.93	0.33	AL-CA
3-33	3.00	1.33	40.00	2.47	39.47	2.44	37.05	2.29	11.22	2.93	0.00	2.93	0.47	1.0	0.51	TAL-CE
3-34	3.00	1.33	50.00	3.09	49.45	3.05	47.67	2.94	11.21	-	-	-	-	1.0	-	SCD

Table 4.6: A summary of collision parameters and results for head-on collisions between a $10.50\,M_\oplus$ target ($M_\mathrm{t}^\mathrm{core} = 7.07\,M_\oplus$, $M_\mathrm{t}^\mathrm{atmos} = 3.43\,M_\oplus$) with a mantle surface radius of $1.60\,R_\oplus$, and an atmosphere scale height of $0.70\,R_\oplus$, and projectiles of mass M_p. Similar to Tables 4.1 and 4.5.

ID	M_p	R_p	$v_\mathrm{imp}^\mathrm{pred}$	$\frac{v_\mathrm{imp}^\mathrm{pred}}{v_\mathrm{esc}}$	$v_\mathrm{imp}^\mathrm{meas}$	$\frac{v_\mathrm{imp}^\mathrm{meas}}{v_\mathrm{esc}}$	v_init	$\frac{v_\mathrm{init}}{v_\mathrm{esc}}$	S	M_LR	$M_\mathrm{LR}^\mathrm{atmos}$	$M_\mathrm{LR}^\mathrm{core}$	$\frac{M_\mathrm{LR}}{M_\mathrm{tot}}$	$X_\mathrm{loss}^\mathrm{atmos}$	$X_\mathrm{loss}^\mathrm{c\&m}$	Category
	$M_\oplus$	$R_\oplus$	$\mathrm{km\,s^{-1}}$		$\mathrm{km\,s^{-1}}$		$\mathrm{km\,s^{-1}}$		$R_\oplus$	$M_\oplus$	$M_\oplus$	$M_\oplus$				
7-0	1.01	0.95	30.00	1.51	27.76	1.39	21.07	1.06	13.54	11.20	3.12	8.08	0.97	0.09	0.0	AL-CM
7-1	1.01	0.95	40.00	2.01	37.18	1.87	33.82	1.70	13.54	10.81	2.73	8.08	0.94	0.2	0.0	AL-CM
7-2	1.01	0.95	50.00	2.51	46.47	2.33	45.21	2.27	13.55	10.22	2.15	8.07	0.89	0.37	0.0	AL-CM
7-3	1.01	0.95	55.00	2.76	51.12	2.57	50.68	2.54	13.57	9.85	1.79	8.07	0.86	0.48	0.0	AL-CM
7-4	1.01	0.95	60.00	3.01	55.99	2.81	56.07	2.81	13.57	9.48	1.42	8.06	0.82	0.59	0.0	AL-CM
7-5	1.01	0.95	65.00	3.26	60.57	3.04	61.39	3.08	13.56	9.05	1.03	8.01	0.79	0.7	0.01	AL-CM
7-6	1.01	0.95	70.00	3.51	65.18	3.27	66.66	3.35	13.58	8.55	0.70	7.85	0.74	0.8	0.03	AL-CM
7-7	1.01	0.95	80.00	4.01	74.50	3.74	77.10	3.87	13.55	6.96	0.24	6.72	0.6	0.93	0.17	AL-CE
7-8	2.02	1.17	30.00	1.46	28.16	1.37	21.11	1.03	14.17	11.85	2.76	9.09	0.95	0.2	0.0	AL-CM
7-9	2.02	1.17	40.00	1.95	37.80	1.84	33.85	1.65	14.19	11.03	1.96	9.08	0.88	0.43	0.0	AL-CM
7-10	2.02	1.17	50.00	2.44	47.32	2.31	45.23	2.21	14.18	10.15	1.16	8.98	0.81	0.66	0.01	AL-CM
7-11	2.02	1.17	55.00	2.68	52.02	2.54	50.70	2.47	14.19	9.42	0.76	8.66	0.75	0.78	0.05	AL-CM
7-12	2.02	1.17	60.00	2.93	56.64	2.76	56.09	2.74	14.19	8.40	0.40	7.99	0.67	0.88	0.12	AL-CA
7-13	2.02	1.17	65.00	3.17	61.47	3.00	61.41	3.00	14.16	7.14	0.19	6.95	0.57	0.94	0.24	AL-CE
7-14	2.02	1.17	70.00	3.42	66.26	3.23	66.67	3.25	14.21	5.47	0.02	5.45	0.44	0.99	0.4	TAL-CE
7-15	2.02	1.17	80.00	3.90	75.81	3.70	77.11	3.76	14.19	1.65	0.00	1.65	0.13	1.0	0.82	TAL-CE
7-16	3.03	1.32	30.00	1.43	28.33	1.35	20.89	0.99	14.62	12.58	2.49	10.09	0.93	0.27	0.0	AL-CM
7-17	3.03	1.32	40.00	1.90	38.07	1.81	33.71	1.60	14.61	11.63	1.58	10.05	0.86	0.54	0.01	AL-CM
7-18	3.03	1.32	50.00	2.38	47.68	2.27	45.13	2.15	14.64	10.07	0.78	9.28	0.74	0.77	0.08	AL-CA
7-19	3.03	1.32	55.00	2.62	52.50	2.50	50.61	2.41	14.65	8.87	0.42	8.45	0.66	0.88	0.16	AL-CA
7-20	3.03	1.32	60.00	2.85	57.25	2.72	56.00	2.66	14.64	7.31	0.17	7.15	0.54	0.95	0.29	TAL-CA
7-21	3.03	1.32	65.00	3.09	62.05	2.95	61.33	2.92	14.65	5.02	0.01	5.01	0.37	1.0	0.5	TAL-CE
7-22	3.03	1.32	70.00	3.33	66.78	3.18	66.61	3.17	14.62	3.05	0.00	3.05	0.23	1.0	0.7	TAL-CE
7-23	3.03	1.32	80.00	3.80	76.41	3.63	77.05	3.66	14.64	-	-	-	-	1.0	-	SCD
7-24	4.04	1.43	30.00	1.39	28.37	1.32	20.53	0.95	14.94	13.41	2.31	11.10	0.92	0.33	0.0	AL-CM
7-25	4.04	1.43	40.00	1.86	38.19	1.77	33.49	1.55	14.95	12.39	1.43	10.96	0.85	0.58	0.01	AL-CM
7-26	4.04	1.43	50.00	2.32	47.91	2.22	44.96	2.09	14.97	10.29	0.63	9.66	0.71	0.82	0.13	AL-CA
7-27	4.04	1.43	55.00	2.55	52.72	2.45	50.46	2.34	14.94	8.81	0.30	8.51	0.61	0.91	0.23	AL-CA
7-28	4.04	1.43	60.00	2.79	57.57	2.67	55.87	2.59	14.96	6.32	0.06	6.25	0.43	0.98	0.44	TAL-CE
7-29	4.04	1.43	65.00	3.02	62.36	2.89	61.20	2.84	14.98	4.01	0.00	4.01	0.28	1.0	0.64	TAL-CE
7-30	4.04	1.43	70.00	3.25	67.15	3.12	66.49	3.09	14.98	1.75	0.00	1.75	0.12	1.0	0.84	TAL-CE
7-31	4.04	1.43	80.00	3.71	76.75	3.56	76.95	3.57	14.99	-	-	-	-	1.0	-	SCD
7-32	5.05	1.52	30.00	1.36	28.40	1.29	20.11	0.91	15.21	14.36	2.25	12.11	0.92	0.34	0.0	AL-CM
7-33	5.05	1.52	40.00	1.82	38.24	1.74	33.23	1.51	15.22	13.19	1.38	11.81	0.85	0.6	0.03	AL-CM
7-34	5.05	1.52	50.00	2.27	48.01	2.18	44.77	2.03	15.21	10.73	0.55	10.18	0.69	0.84	0.16	AL-CA
7-35	5.05	1.52	55.00	2.50	52.85	2.40	50.29	2.28	15.24	9.01	0.22	8.79	0.58	0.94	0.27	AL-CA
7-36	5.05	1.52	60.00	2.72	57.69	2.62	55.71	2.53	15.25	6.17	0.02	6.16	0.4	0.99	0.49	TAL-CE
7-37	5.05	1.52	65.00	2.95	62.53	2.84	61.07	2.77	15.25	3.78	0.00	3.77	0.24	1.0	0.69	TAL-CE
7-38	5.05	1.52	70.00	3.18	67.35	3.06	66.37	3.01	15.21	1.65	0.00	1.65	0.11	1.0	0.86	TAL-CE
7-39	5.05	1.52	80.00	3.63	77.01	3.50	76.84	3.49	15.25	-	-	-	-	1.0	-	SCD
7-40	6.06	1.60	30.00	1.33	28.39	1.26	19.67	0.87	15.46	15.33	2.22	13.11	0.93	0.35	0.0	AL-CM
7-41	6.06	1.60	40.00	1.78	38.27	1.70	32.97	1.47	15.46	14.14	1.40	12.74	0.85	0.59	0.03	AL-CM
7-42	6.06	1.60	50.00	2.22	48.04	2.14	44.57	1.98	15.47	11.40	0.51	10.89	0.69	0.85	0.17	AL-CA
7-43	6.06	1.60	55.00	2.44	52.96	2.35	50.12	2.23	15.46	9.47	0.20	9.27	0.57	0.94	0.29	AL-CA
7-44	6.06	1.60	60.00	2.67	57.82	2.57	55.56	2.47	15.48	6.35	0.01	6.34	0.38	1.0	0.52	TAL-CE
7-45	6.06	1.60	65.00	2.89	62.62	2.78	60.92	2.71	15.46	3.90	0.00	3.90	0.24	1.0	0.7	TAL-CE
7-46	6.06	1.60	70.00	3.11	67.50	3.00	66.23	2.94	15.49	1.78	0.00	1.78	0.11	1.0	0.86	TAL-CE
7-47	6.06	1.60	80.00	3.56	77.14	3.43	76.72	3.41	15.50	-	-	-	-	1.0	-	SCD
7-48	7.07	1.67	30.00	1.31	28.38	1.24	19.18	0.84	15.67	16.30	2.18	14.12	0.93	0.36	0.0	AL-CM
7-49	7.07	1.67	40.00	1.74	38.30	1.67	32.68	1.42	15.67	15.10	1.36	13.75	0.86	0.6	0.03	AL-CM
7-50	7.07	1.67	50.00	2.18	48.10	2.10	44.36	1.93	15.67	12.19	0.50	11.69	0.69	0.85	0.17	AL-CA
7-51	7.07	1.67	55.00	2.40	52.98	2.31	49.93	2.18	15.65	10.30	0.19	10.11	0.59	0.94	0.29	AL-CA
7-52	7.07	1.67	60.00	2.61	57.85	2.52	55.39	2.41	15.66	7.00	0.01	6.99	0.4	1.0	0.51	TAL-CE
7-53	7.07	1.67	65.00	2.83	62.66	2.73	60.77	2.65	15.70	4.27	0.00	4.26	0.24	1.0	0.7	TAL-CE
7-54	7.07	1.67	70.00	3.05	67.55	2.94	66.09	2.88	15.69	2.23	0.00	2.23	0.13	1.0	0.84	TAL-CE
7-55	7.07	1.67	80.00	3.49	77.25	3.37	76.60	3.34	15.67	-	-	-	-	1.0	-	SCD

5

Oblique Collisions

This chapter is a paper submitted to MNRAS (Denman et al., 2021).

5.1 Introduction

The detection of thousands of extra-solar planets demonstrates that planet formation is a ubiquitous process. Both observations and numerical simulations indicate that planet formation often results in multiple planet systems. Gravitational interactions with the proto-planetary disc cause planets embedded within to migrate. This migration is typically inward and is dependent on planet mass (Ward, 1986). In systems with multiple Super-Earth mass planets this process forms resonant chains at the inner edge of the disc. The large rocky cores of these Super-Earths can accrete significant primordial atmospheres from the proto-planetary disc (Rogers et al., 2011).

When the proto-planetary disc dissipates it ceases to provide the drag force that circularises the orbits of the planets. Small orbital perturbations can destabilise any resonant chain of close orbiting Super-Earths that may have formed within the disc (Barnes & Raymond, 2004) as they are often already on the borders of stability (Fang & Margot, 2013). Eventually, the instability will lead to collisions between the planets or gravitational ejection of a planet from the system. As such, the systems we observe with

Super-Earth mass planets typically only have a few planets. Observed Super-Earths in multiple planet systems are often detected orbiting close to, but not in, mean motion resonance (Fabrycky et al., 2014). Very rarely we observe a system of multiple planets in a meta-stable resonant chain (for example Trappist-1, Gillion et al. 2017, and Kepler-223, Mills et al. 2016). Volk & Gladman (2015) suggest such resonant chains of close orbiting planets are common in planetary formation and potentially even occurred in the early stages of our own solar system's formation but that over long time periods they become unstable leading to either destruction or collisional consolidation.

Giant impacts are not only thought to be an important formation mechanism for Super-Earths. The dissipation of the proto-planetary disc can result in orbit destabilisation for objects from planetesimals all the way up to giant planets, leading to orbital crossings and collisions. A similar resonant chain breaking scenario to the Super-Earth formation process is thought to be a possible formation scenario for Hot Jupiter systems (Raymond & Morbidelli, 2020). Giant impacts are thought to be a common process in planet formation, and may allow us to observe ongoing planet formation in young planetary systems (e.g. Watt et al., 2021). Our own solar system has multiple examples of planets for which giant collisions are the most probable formation mechanism, for example there is strong evidence for a giant impact having formed the Earth-Moon system (e.g. Hartmann & Davis, 1975; Asphaug, 2014; Lock et al., 2018) and also for a giant collision causing Uranus' unusual axis of rotation and magnetic field (Kegerreis et al., 2018).

Another impetus for the study of giant collisions between Super-Earth sized objects is the large degree of diversity in their measured densities, both overall and between Super-Earths observed in the same system. This density diversity as a whole cannot solely be accounted for by other methods, such as XUV radiation from the central star. XUV erodes the less dense outer layers of close orbiting planets. XUV radiation should lead to a simple orbital distance density relation due to the reduction in XUV flux with orbital distance Inamdar & Schlichting (2015). XUV radiation can explain differences in density between planets orbiting different stars but not a large amount of density difference within a multiple planet system, especially when the density does not correlate with orbital distance (e.g. Bonomo et al., 2019).

Inamdar & Schlichting (2016) shows theoretically that giant collisions are a potential

explanation to the observed density diversity because collisions can cause a significant percentage of a planet's atmosphere to be ejected. In addition, Bonomo et al. (2019), present observational evidence for a giant impact in the Kepler 107 system. In this system planet Kepler-107b is less dense ($\rho = 5.3\,\mathrm{g\,cm^{-3}}$) than its neighbour Kepler-107c orbiting externally to it ($\rho = 12.6\,\mathrm{g\,cm^{-3}}$). The K-107 system exhibits exactly the opposite situation as we would expect to occur due to XUV, which has a stronger effect on planets closer to the central star. However, as shown in the paper, a large collision could have stripped the lighter material from Kepler-107c, increasing its density.

Our research in this chapter involves modelling such giant impacts between Super-Earth mass exoplanets. In particular we focus on collisions involving a target which has accreted a thick hydrogen atmosphere form the proto-planetary disc.

5.1.1 Previous Work

Due to the density disparity between mantle and atmosphere most previous numerical work on giant impacts have modelled the targets without atmosphere. This approximation works well for smaller terrestrial objects with masses $\lesssim 1\mathrm{M}_\oplus$ which typically have low atmosphere mass fractions (of the order of 1% or less). However, Kegerreis et al. (2020) modelled these thin atmospheres, which required simulations with resolutions at the upper end of what is currently typically feasible at order 10^7 particles.

The assumption of a thin atmosphere is no longer accurate for Super-Earth mass objects, however, which can often accrete large amounts of gas from the proto-planetary disk. Fortunately these thicker atmospheres do not require as high a total simulation resolution to model, as the higher atmosphere fraction means a greater percentage of the total particles in the simulation are in the atmosphere.

Whilst not going so far as to include atmosphere, Gabriel et al. (2020) investigate the effects of density stratification in planetary bodies on collisions involving Earth mass objects, i.e the effect of a planet with an internal density that decreases with radius from its centre, either due to pressure or composition. They look at the effects of this stratification in objects that are comprised of a combination of iron, silicate, and water. They show that density stratification can lead to hit-and-run style collisions at lower impact angles than constant bulk density models predict. The densities of some Super-Earths analysed in this chapter are even more highly stratified than those covered in

Gabriel et al., in part due to the higher masses involved and also due to the density contrast between the core and mantle material and the atmosphere.

Whilst we make comparisons to Gabriel et al. (2020), this chapter does not follow the same method; they use raw relative kinetic energy, K, and its relationship to the binding energy of material in the system, as suggested by Movshovitz et al. (2016). In this chapter, we instead use the specific relative kinetic energy measure of Leinhardt & Stewart (2012), which is given by:

$$Q_{\mathrm{R}} = \frac{1}{2}\mu\frac{v^2}{M_{\mathrm{tot}}}, \tag{5.1}$$

where M_{tot} is the total mass in the system, μ the reduced mass, and v the impact velocity. This is consistent with our previous work (Denman et al., 2020), which examined solely head-on collisions involving similar mass bodies to those covered in this chapter. This chapter expands on our previous work by examining collisions at many different impact parameters.

5.1.2 Collision Outcomes

The head-on impacts from our previous work (Denman et al., 2020) resulted in either the majority of the projectile merging with the target, or, at higher energies, one or both being disrupted. Real collisions are unlikely to be head-on, in general we would expect an impact angle closer to 45° (Shoemaker & Hackman, 1962).

At these higher impact angles additional impact outcomes can occur. For example, if a collision is sufficiently glancing a hit-and-run can occur in which the projectile bounces off the target (and in the classical definition does not erode it Leinhardt & Stewart 2012). Another possible impact outcome is graze-and-merge (Genda et al., 2012), these start similar to hit-and-run collisions but the collision saps enough kinetic energy from the projectile that it can not escape the gravitational influence of the target and the projectile and target eventually merge.

5.2 Methods

Here we provide a brief summary of the numerical methods used in this chapter, a more in depth description of which is given in chapter 2.

5.2.1 Numerical code

The simulations in this chapter were carried out using the same build of the SPH code GADGET-2 (Springel, 2005) as used in chapter 4 (Denman et al., 2020). This version of GADGET-2 has been modified so it can use tabulated equations of state to model planets (Marcus et al., 2009; Ćuk & Stewart, 2012). GADGET-2 was run in 'Newtonian mode' with timestep synchronisation and the standard relative cell-opening criterion. We use the standard timestep criterion described in Springel (2005), with a Courant factor of 0.1. We also use the standard artificial viscosity formulation with a strength parameter of 0.8.

5.2.2 Initial Conditions

Planets were modelled as either two or three component objects, with an iron core, a forsterite mantle, and a hydrogen atmosphere (target only). For all planets we built an iron core surrounded by a forsterite mantle of double the mass of the core. We ran a preliminary equilibration for each planet to ensure they were stable, the same set up process as was used in Marcus et al. (2009) and Ćuk & Stewart (2012). For the target object we then added a hydrogen atmosphere as an outer layer and re-equilibrated as per Denman et al. (2020). The mass of this atmosphere $M_{\rm atmos}$ was determined via the following relation:

$$\frac{M_{\rm atmos}}{M_\oplus} = 0.01 \times \left(\frac{M_{\rm c\&m}}{M_\oplus}\right)^3, \tag{5.2}$$

where $M_{\rm c\&m}$ is the combined mass of the core and mantle. This rule was determined empirically from the results of Bern model population synthesis simulations (Alibert et al., 2005; Mordasini, 2018), and is the same as was used in Denman et al. (2020).

We used tabulated ANEOS/MANEOS equations of state (from Melosh & Vickery 1989) to describe the iron and forsterite (full tables are available from Carter et al. 2019). The hydrogen atmospheres on the other hand were modelled using the ideal gas equation of state (built in to GADGET-2) for simplicity. Initial radial density and temperature profiles for the core and mantle were taken from Valencia et al. (2006), and we used the same initial profiles for the atmosphere as in Denman et al. (2020).

We used the same equilibration times as given in Denman et al., 4×10^5 s for core equilibration and twice this for equilibrating the atmosphere on top. Core and mantle

entropies were set to $1.3\,\mathrm{kJ\,K^{-1}\,kg^{-1}}$ and $3.2\,\mathrm{kJ\,K^{-1}\,kg^{-1}}$ respectively. Unlike in our previous work, here the initial value of the atmosphere's pseudo-entropy was set to the higher value of $1.3 \times 10^{11}\mathrm{Ba\,g^{-\gamma}\,cm^{3\gamma}}$ (where $\gamma = \frac{5}{3}$ was the value of the adiabatic index). This higher pseudo-entropy meant a more extended atmosphere than Denman et al. (2020) which better matched the initial radial density profile after equilibration was completed.

Most simulations had a resolution of 10^5 particles in the target core and mantle as this allowed us to run a large number of them. We also ran a smaller group of simulations at both higher and lower resolutions, which typically showed good agreement with the equivalent intermediate resolution results that our analysis is based on (a more in depth discussion of this is given in appendix 5.6.1).

5.2.3 Run Parameters

The simulations were run for about four times the gravitational dynamical time, t_{dyn}, to allow enough time for gravitational resettling of material after the collision to occur. This interaction time (one dynamical time) is given by:

$$t_{\mathrm{dyn}} = \sqrt{\frac{R^3}{GM_{\mathrm{tot}}}}, \tag{5.3}$$

where R is initial separation between target and projectile centres of mass, M_{tot} the total mass of the system, and G is the gravitational constant.

The other time constraint we considered was the time required to observe the secondary impact for graze-and-merge collisions. At higher impact parameters as energy increases from perfect merging to hit-and-run, graze-and-merge collisions can occur where the remnants of the projectile have sufficient energy to escape from the initial collision but not enough energy to escape from the gravitational influence of the largest remnant (Genda et al., 2012; Emsenhuber & Asphaug, 2019b). In such a situation, these projectile remnants will eventually fall back to the target for a secondary collision. Our collisions were run for sufficiently long that we could simulate graze-and merge collisions at orbits as large as 0.4 au (see appendix 5.6.3 for details). We do not include the effects of the central star in our simulations, however, as we want our results to be agnostic to orbital distance; as such, graze-and-merge collisions are removed from most analyses in the rest of this work.

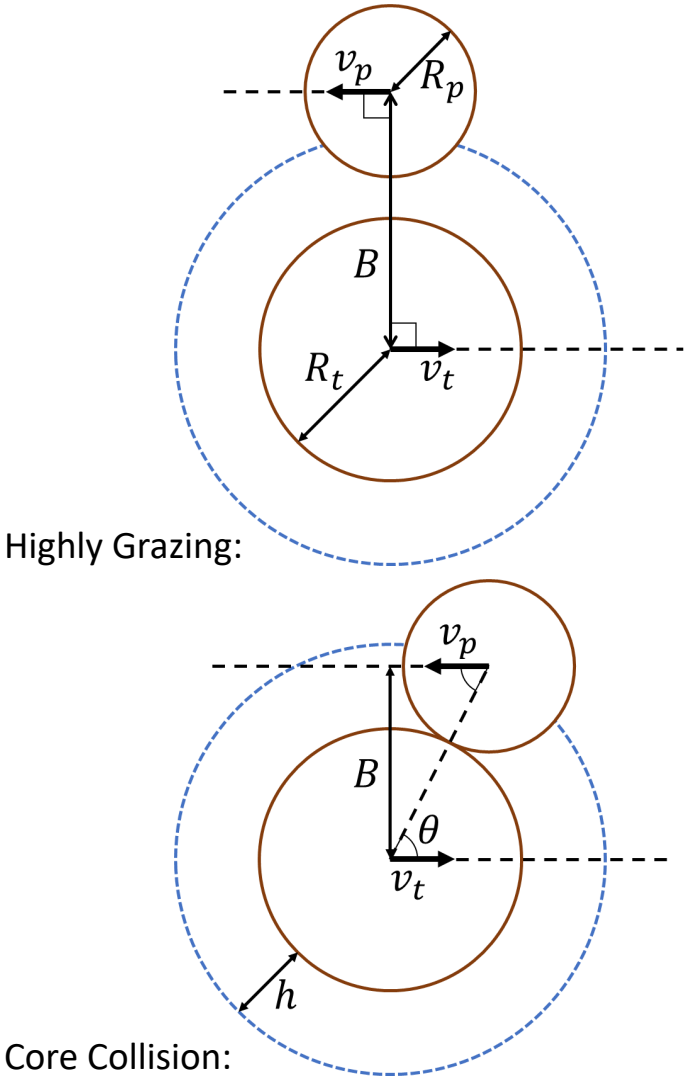

Figure 5.1: Collision geometry showing the parameters used to describe both highly grazing impacts (top) and collisions where the mantles collide (bottom). A normalised impact parameter is used, $b = B/(R_\mathrm{p} + R_\mathrm{t})$. The relative velocity of an impact is $v = v_\mathrm{t} - v_\mathrm{p}$. The brown solid lines indicate the surface of the mantle of the projectile and target and the blue dotted line represents one scale height within the target's atmosphere.

All collisions used the same target, which had a total mass of $6.25\,M_\oplus$. Using only one target meant we could test collisions at a larger range of velocities and impact angles. This target planet consisted of a $1.67\,M_\oplus$ iron core, $3.33\,M_\oplus$ forsterite mantle and $1.25\,M_\oplus$ hydrogen atmosphere. We used 5 different projectiles evenly spaced in mass from $1\,M_\oplus$ to $5\,M_\oplus$. These projectiles did not have atmospheres because we were not simulating at a high enough resolution for the smaller atmospheres to be well resolved. We kept the larger mass projectiles without atmosphere for ease of comparison. Target and projectiles had a 1 : 2 ratio of iron core to forsterite mantle particles. We chose eight different velocities: $20, 25, 30, 35, 40, 50, 60\,\&\,70\,\mathrm{km\,s^{-1}}$, the slowest of these is approximately escape velocity, whereas the fastest is approximately the expected collision velocity of a prograde and retrograde planet at 0.1 au; lower collision velocities are more probable (Gabriel et al., 2020) so we carried out a wider range of collisions at low velocities.

For simplicity, instead of defining an edge to the atmosphere, we defined the point of collision as follows: for most collisions we define the collision point to be when the mantle surfaces of target and projectile touch. For highly grazing collisions, in which the projectile only passes through the target atmosphere, however, we define the point of collision to be the point of closest approach. We have also used the mantle surface radius to define the radius of the target, R_t. Likewise the impact parameter, b, is normalised by the sum of the target and projectile mantle surface radii following

$$b = \frac{B}{R_\mathrm{t} + R_\mathrm{p}}, \tag{5.4}$$

where B is the vertical distance between the centres of mass of target and projectile as shown in Figure 5.1. This normalisation means that highly grazing collisions where the cores do not touch will have impact parameter $b > 1$, this is in contrast to previous atmosphere-less works on planet collision where $b > 1$ meant a collision would not occur. (Impact angle is defined as $\theta_\mathrm{imp} = sin^{-1}(b)$, because this is undefined for $b > 1$ we do not use it in our analyses.)

We chose a range of seven different impact parameters roughly evenly spaced, from head-on ($b = 0$) to a series of collisions that only passed through the atmosphere at $b = 1.3$ (these were $b = 0$, 0.1, 0.34, 0.5, 0.71, 0.94, 1.1 & 1.3). Full data of all of these collisions and their precise collision parameters is given in Tables 5.2–5.6 in appendix 5.6.5.

To determine the required positions of planets at the beginning of our simulation runs we used the above collision parameters, assumed target and projectile were perfectly spherical and thus well represented by a point mass, and used a Verlet integrator to trace the path of the projectile backwards in time until the centres of mass of both target and projectile were separated by a distance of five times the sum of their mantle surface radii.

5.3 Results

In this chapter we simulate collisions between Super-Earths at a wide array of impact angles, from head-on, to the projectile barely grazing the surface of the target atmosphere, as well as a wide variety of impact speeds, from the escape velocity, to twice the orbital velocity of the target. An array of these results is shown in Figure 5.2 detailing some of the more common outcomes.

Overall we find that the results are a strong function of specific impact energy, Q_{R}. We see a separation of the results into two regimes. At higher impact parameters and energies a large percentage of the projectile has enough energy to escape the larger target remnant resulting in two large remnant objects with masses of a similar order of magnitude (for example collisions C and D in Figure 5.2). At lower energies and impact angles the projectile remnant cannot escape and we observe behaviour as described in Denman et al. (2020), where we obtain a single large remnant containing core material from both target and projectile (e.g. collision A in Figure 5.2). In between these two regimes we observe a narrow band of graze-and-merge collisions in which the projectile escapes the target on its first collision but does not have enough energy to escape the gravitational influence of the target and thus merges in a later secondary collision (e.g. collision B in Figure 5.2).

5.3.1 Largest Remnant Mass

The two graphs on the left and centre in Figure 5.3 show the dependence of the mass of the largest remnant on the relative specific kinetic energy of the collision, Q_{R}. In the rightmost graph of Figure 5.3 we observe two separate collision regimes which result in different masses for the second largest collision remnant. We find that the transition

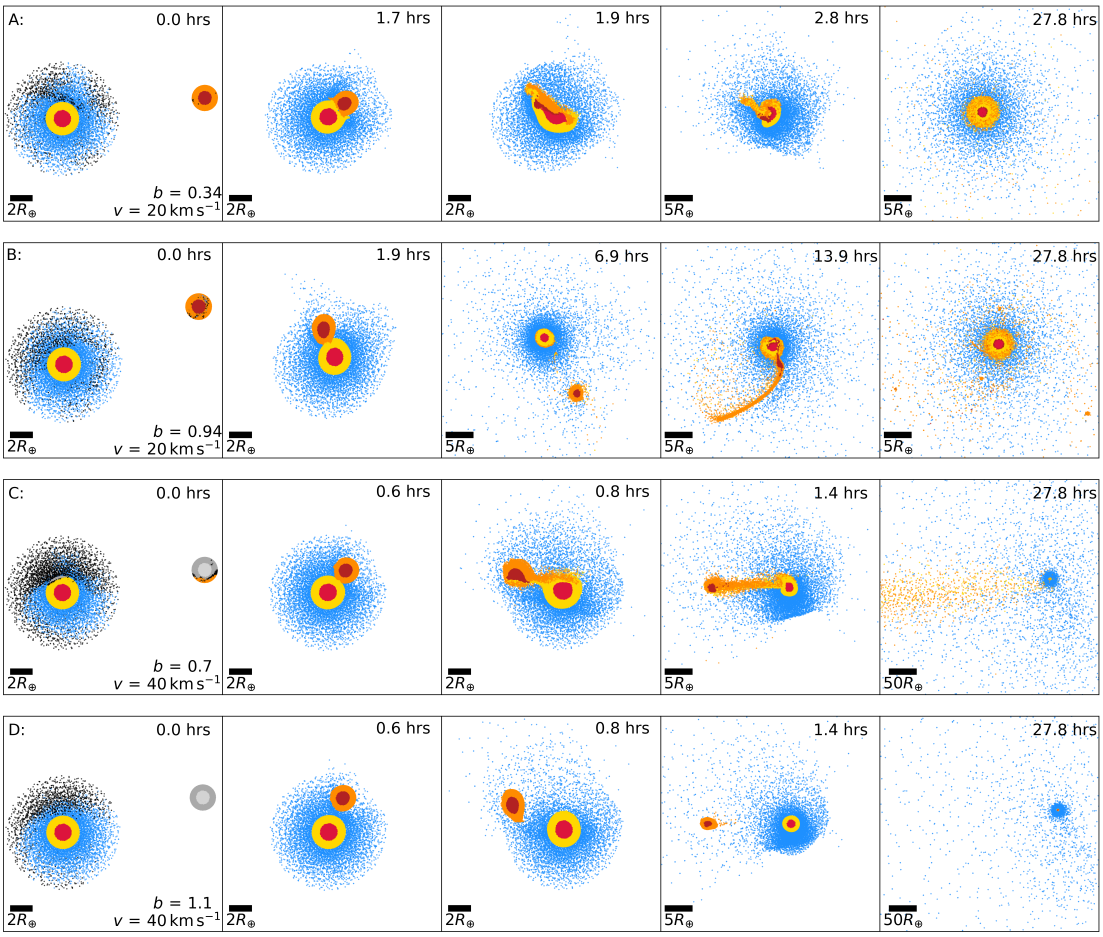

Figure 5.2: Snapshots showing cross-sectional slices of collisions in progress for four different types of collision between a 6.25 $M_\oplus$ target and a 2 $M_\oplus$ projectile. Colours indicate material type, with different shades to distinguish between projectile and target: iron cores are red, forsterite mantle particles are orange/yellow, and atmosphere particles are blue. Colours in the first panel indicate the final location of each particle, black for unbound material, shades of grey are for the second largest remnant, and largest remnant particles retain the colours described previously. The four different collisions are as follows: A) a head-on like collision – the majority of target and projectile merge to form a new planet as described in Denman et al. (2020), the remaining mass is ejected. B) A collision in the transition region between merge and hit-and-run – this particular example is a graze-and-merge in which the remnants of the projectile undergo a secondary collision with the target; tidal forces tear apart the projectile as it comes back for the second collision resulting in chunks of projectile remaining in orbit. C) An erosive hit-and-run collision – the mantles of both objects collide causing both to lose mass during the collision; a stream of mantle debris is left between the two objects after the collision. D) A highly grazing collision – the projectile only passes through the atmosphere of the target, shockwaves eject some of the atmosphere but the projectile and target lose a negligible mass of core and mantle.

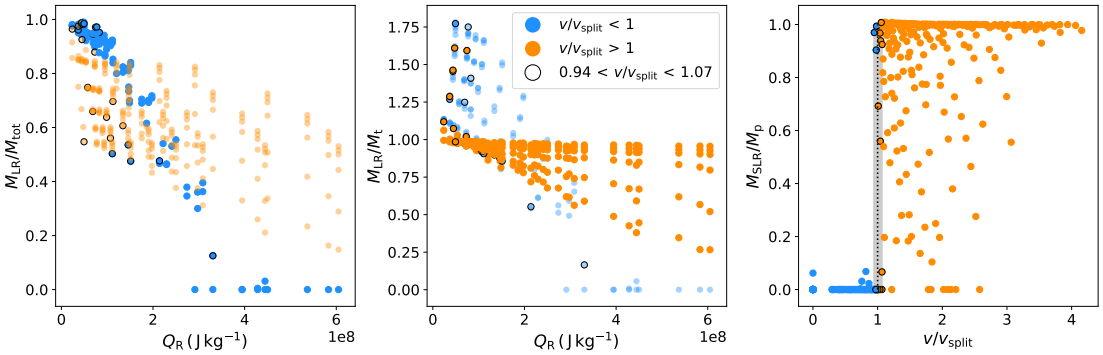

Figure 5.3: Left: The mass of the largest remnant as a fraction of total impactor mass compared with impact energy. The collisions with impact velocities below v_{split}, which are well described by Denman et al. (2020), are coloured in blue, other collisions are orange and partially transparent as their masses are not well described using this normalisation. Centre: The mass of the largest remnant as a fraction of target mass compared to impact energy. Collisions with impact velocities greater than v_{split} are coloured orange. The orange points being constrained to a small wedge in this normalisation implies it is a more useful tool for describing them. Other collisions are coloured blue and made partially transparent. Right: Second largest remnant mass in terms of the projectile mass compared with the ratio of the impact velocity to the critical velocity, v_{split}. The shaded region shows the values we chose to ignore for our fits to either regime; this selection gives the circled points in all three graphs.

between these two regimes can be well approximated by a simple escape velocity measure,

$$v_{\rm split} = \sqrt{\frac{2GM_{\rm tot}}{b(R_{\rm p} + R_{\rm t})}}, \tag{5.5}$$

which assumes spherical symmetry, and that the impact parameter, b, is a good approximation for the distance of closest approach.

These two collision regimes split by $v_{\rm split}$ correspond to situations where there is either one or two resultant large post-collision remnants, i.e. situations in which the cores of target and projectile either merge with one another or go their separate ways after impact. The simulations in the first of these regimes (blue points) result in one single large remnant formed from the combined cores of both target and projectile. The largest remnant (leftmost graph, Figure 5.3) is formed from the cores of the two planets combining leaving a low or negligible mass secondary remnant. The second of these regimes (orange points) is similar to hit-and-run, with a significant mass secondary remnant present due to the projectile bouncing off the target. The difference between these collisions and the classical definition of hit-and-run (i.e. no erosion of the target) is that, due to the presence of the lightly bound atmosphere, some erosion from the target is always observed (centre graph Figure 5.3). The energy cutoff between these two collision regimes is dependent on impact parameter with hit-and-run like collisions at higher b occurring at lower impact energies.

These two different collision outcomes are the reason why the remnant mass is best described using two different mass normalisations (left and centre panels in Figure 5.3). At lower velocities and impact parameters we have a regime with one single large remnant formed by a combination of both projectile and target so we normalise by the combined mass of projectile and target, $M_{\rm tot}$, as shown by the blue points in the leftmost graph of Figure 5.3. The largest remnant mass $M_{\rm LR}$ in these collisions behaves like the head-on collisions described in Denman et al. (2020) as shown in Figure 5.6. At higher impact energies, when most of the atmosphere is removed, the largest remnant mass in this regime behaves similarly to that described in Leinhardt & Stewart (2012), that is decreasing linearly with increasing $Q_{\rm R}$; at low energies atmosphere removal is less efficient and we, therefore, have a shallower gradient. The second regime occurs at higher velocities for each impact angle. All largest remnants in the second regime are less massive than the target – the target always suffers some erosion. We normalise

largest remnant mass by target mass in this regime (see orange points in the middle graph of 5.3) because the largest remnant mass can be considered to be less than the target mass by some impact energy dependent erosive factor as will be shown later in Figure 5.4.

While the rightmost graph in Figure 5.3 shows that $v_{\rm split}$ is a good approximation for the regime boundary, there are a few misdiagnosed results. There are three potential causes for these outliers: firstly the assumption of spherical symmetry, in reality there is some tidal distortion at this point; secondly, graze-and-merge collisions should occur at slightly lower velocity than this boundary, those on long orbits may not have had time to re-collide yet, meaning they may appear as hit-and-run collisions in our data even if their final result would be a merger; or thirdly, material dependent impact effects such as deflection or drag.

An important confusing factor for the boundary between collision regimes is the possibility of secondary collisions which occur when the secondary remnant does not have the energy to escape the target after collision. These secondary collisions could occur close to the end of the simulation, meaning we would not be able to measure the equilibrium bound mass. For planets orbiting close to the central star the simulation timescale we have used is sufficient for them to escape the Hill sphere of the largest remnant, but because we do not model a central star, they undergo a secondary collision. To keep our collision analysis agnostic to orbital distance and to account for the imperfect nature of this regime boundary measure, we have elected to ignore all simulations with velocities in the range $0.94 < v_{\rm split} < 1.07$ when fitting.

a) Erosive Hit-and-Run

For collisions with a velocity above $v_{\rm split}$ the projectile rebounds off the target causing erosion in one or both; following Gabriel et al. (2020) we call such collisions erosive hit-and-runs.

In these erosive hit-and-run collisions we observe an approximately linear decrease in largest remnant mass (normalised by the target mass) with increasing impact energy (top graph, Figure 5.4). This linear relationship is independent of projectile mass, but with a gradient that decreases with increasing impact parameter, meaning that more grazing collisions remove less material.

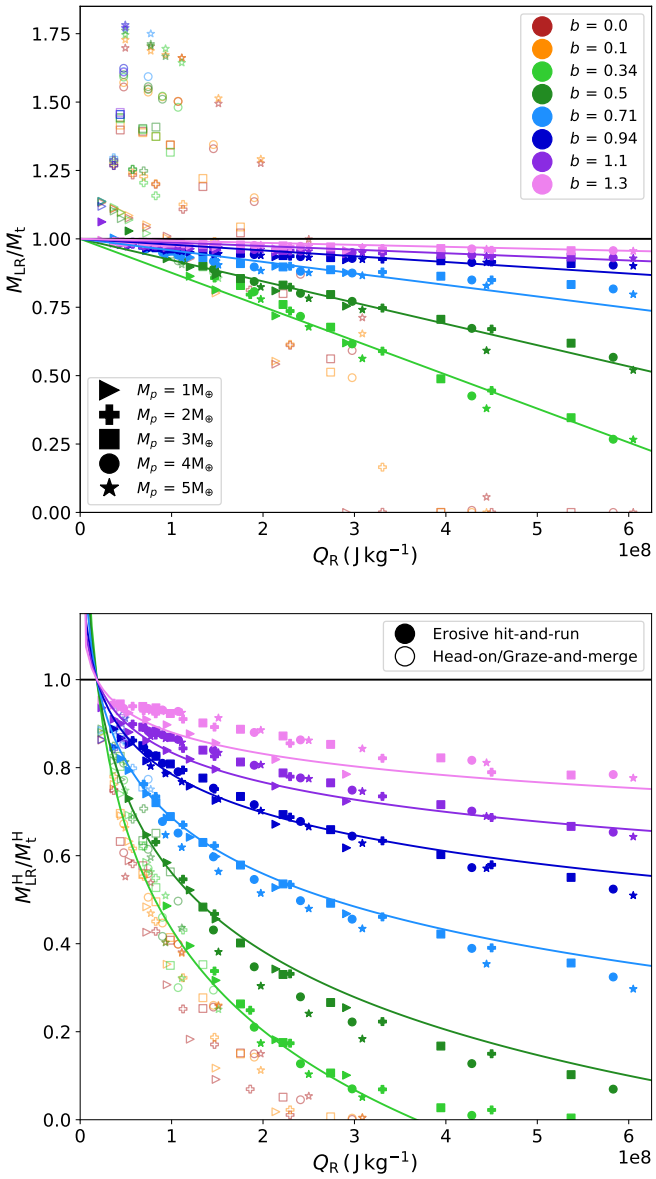

Figure 5.4: Top: Mass of the largest remnant relative to the target mass compared with specific impact energy. Erosive hit-and-runs are shown with filled symbols, open symbols indicate head-on or transition region collisions. Projectile mass is indicated by symbol shape; different impact angles are given in different colours. This graph illustrates the projectile mass independence of erosive hit-and-run collisions. The data has been fitted linearly with an intercept of the target mass and a gradient that is a power law function of impact parameter. The black horizontal line indicates the original target mass. Bottom: Mass of atmosphere in the largest remnant normalised by the initial atmosphere mass of the target compared to Q_R. The fit shown by the solid lines is a power law fit with a shared minimum energy for atmosphere loss Q_0, and a power law coefficient that is itself a power law function of impact angle.

Assuming a power law dependence of the gradient, $\Gamma_{\rm EHR}$, on impact parameter (see appendix 5.6.2), if we fit to all of the impact parameters simultaneously we obtain:

$$\frac{M_{\rm LR}}{M_{\rm t}} = -10^{(-1.28\pm0.02)b-8.47\pm0.01}Q_{\rm R} + 1. \tag{5.6}$$

We have set this model to pass through $M_{\rm LR} = M_{\rm t}$ at $Q_{\rm R} = 0$ so that we have no mass loss for zero input energy. A fit with a loose intercept (see appendix 5.6.2) gives an intercept slightly below one indicating that low energy mass loss is potentially non-linear, despite this we have still used a linear fit so as to provide the simplest description of the results.

Leinhardt & Stewart (2012), when studying impacts of atmosphere-less planets in the disruption regime, found a simple relation based on the geometry of the impact that described the dependence of the amount of impact energy the projectile deposits in the target on the impact parameter. They show the effective specific kinetic energy of a collision at a particular impact angle $Q_{\rm R}^{'}$, is related to the specific kinetic energy of a head-on collision at the same mass and velocity $Q_{\rm R}$ by

$$Q_{\rm R}^{'} = \frac{\mu_\alpha}{\mu}Q_{\rm R}, \tag{5.7}$$

where μ is the reduced mass and μ_α a modified version of the reduced mass determined from the mass of the projectile that interacts with the target. μ_α is given by

$$\mu_\alpha = \frac{\alpha M_{\rm p} M_{\rm t}}{\alpha M_{\rm p} + M_{\rm t}}, \tag{5.8}$$

where α is found by calculating the fraction of the projectile that is below the uppermost point of the target at the point of impact (see figure 2 in Leinhardt & Stewart 2012):

$$\alpha = \frac{3R_{\rm p}l^2 - l^3}{4R_{\rm p}}, \tag{5.9}$$

l here is the vertical distance between the base of the projectile and the top of the target. Note that $l = (R_{\rm p} + R_{\rm t})(1 - b)$. In this way the energy involved in the oblique impact is always smaller than (or equal to) the energy of the head-on impact.

This correction to the impact energy can be related to our gradient, $\Gamma_{\rm EHR} = -10^{-1.28b-8.47}$, above by considering the simultaneous equations of equation 5.6 and the equivalent equation we would get with the corrected impact energy, $Q_{\rm R}^*$:

$$\frac{M_{\rm LR}}{M_{\rm t}} = -\Gamma_0 Q_{\rm R}^* + 1. \tag{5.10}$$

This leaves us with

$$Q_{\mathrm{R}}^{*} = \frac{\Gamma_{\mathrm{EHR}}(b)}{\Gamma_0} Q_{\mathrm{R}}, \tag{5.11}$$

or in other words the reduced mass ratio we expect to observe in our collisions should be directly proportional to Γ_{EHR} and some constant scaling factor, Γ_0,

$$\frac{\Gamma_{\mathrm{EHR}}(b)}{\Gamma_0} = \frac{\mu_\alpha}{\mu}. \tag{5.12}$$

The exact correction from Leinhardt & Stewart (2012) cannot be used for our collisions with an atmosphere because atmospheres do not have a defined outer edge, instead they decrease roughly exponentially in density with distance from their base. Instead we assume the radius of the target is the outer radius of its mantle. The relation between reduced mass ratio and impact parameter predicted using this modified model is shown by the coloured lines in Figure 5.5.

When $\Gamma_{\mathrm{EHR}}(b)/\Gamma_0$ is scaled up such that Γ_0 is the largest measured gradient ($\Gamma_{\mathrm{EHR}}(b = 0.34)$, red points in Figure 5.5), the low impact parameter collisions ($b \leq 0.8$) agree well with the modified version of the Leinhardt & Stewart (2012) interacting mass measure using the mantle surface radius as the target radius (see Figure 5.5). This agreement indicates that the corrected Leinhardt & Stewart prediction of the relation between impact parameter and impact energy of the interacting mass still works well for collisions in which the majority of interaction between projectile and target is between core and mantle, even though the prediction does not include the effects of the atmosphere. The shock caused by the projectile passing through the atmosphere however means that the amount of material removed at higher impact angles is greater. The atmosphere-less bodies in Leinhardt & Stewart (2012) would no longer impact one another at impact parameters greater than one so there would be no energy deposition and no mass loss, whereas, due to our definition of the point of impact, the projectile dives into the target's atmosphere at these impact parameters (1.0 – 1.3) and we observe atmospheric erosion. This atmosphere material is removed preferentially to the mantle for two reasons: firstly, it is significantly less tightly bound than the core and mantle material, secondly, the impedance mismatch between atmosphere and mantle mean that any shockwaves in the mantle caused by atmospheric shocks are substantially weaker than the initial shock that caused them. This low level of mantle interaction is especially true for highly grazing ($b > 1$) collisions.

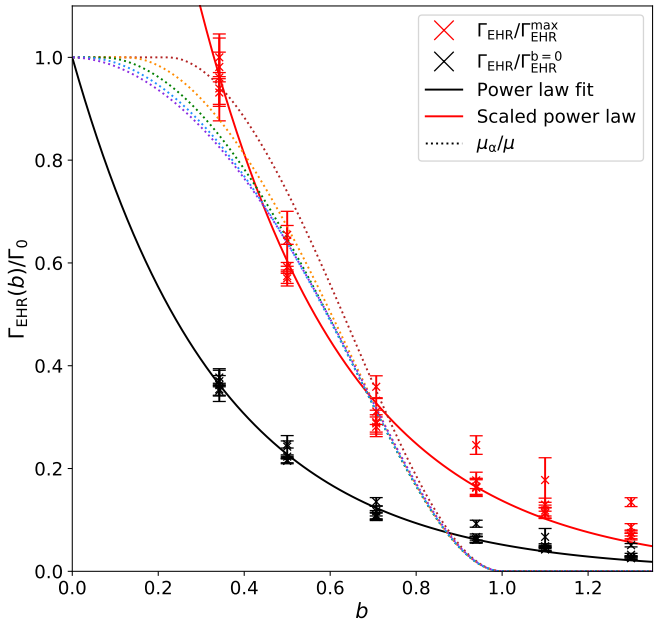

Figure 5.5: Two different scalings of the total mass loss gradient as a function of impact parameter. The scaling in black is with respect to the predicted gradient at $b = 0$ from the fit in equation 5.6. The data points are from the measured gradients for linear fits to individual projectile masses and impact parameters (see appendix 5.6.2). The red line and data points are scaled with respect to the greatest measured gradient. These are compared to our modified version of Leinhardt & Stewart (2012)'s reduced mass ratio modification to Q_{R}. Our results at the lower impact angles follow a pattern consistent with Leinhardt & Stewart (2012), but they diverge at higher impact angles due to the presence of an atmosphere.

b) Atmosphere Loss in the Erosive Hit-and-Run Regime

To understand how much atmosphere gets removed in erosive hit-and-run collisions we compare the specific impact energy, $Q_{\rm R}$, with the fraction of atmosphere remaining on the largest remnant after a collision, $M^{\rm H}_{\rm LR}/M^{\rm H}_{\rm t}$,where $M^{\rm H}$ is the mass of the hydrogen atmosphere and the subscripts t and LR indicate the target and the largest remnant respectively. Figure 5.4 shows that the amount of atmosphere in the largest remnant decreases with increasing impact energy and also with decreasing impact parameter. The amount of extra material removed for a small increase in energy also decreases with increasing energy. The data for each separate impact parameter thus follow convex curves downwards.

In the erosive hit-and-run regime each of the separate projectile masses (shown by different shapes in Figure 5.4) all follow the same loss curve if they collide at the same impact parameter. This means that any projectile mass dependency in the atmosphere mass loss from these impacts is characterised by $Q_{\rm R}$.

Physically the lack of additional dependence on projectile mass beyond specific impact energy is due to the proportionality of the amount of material ejected and the difference between input kinetic energy of the impact, and the gravitational potential energy of the material being ejected. For hit-and-run collisions the gravitational potential will be dominated by the target mass, $M_{\rm t}$, as the projectile rebounds quickly off the target.

Initial power law fits for each impact parameter (see appendix 5.6.2) crossed the initial atmosphere mass at a non-zero energy, this indicates that there is a minimum input energy required for atmosphere to be ejected from the planet. The precise value for this minimum energy, Q_0, is due to the energy required to accelerate atmosphere particles to a velocity where they can escape the largest remnant's Hill sphere. As such the precise value is likely to be dependent both on how efficiently collision energy is spread between atmosphere particles and also potentially for simulations, their resolution.

The power law coefficient was also found to itself have a power law dependence on impact parameter (see appendix 5.6.2). Fitting for all projectile masses and impact angles simultaneously with the function

$$\frac{M^{\rm H}_{\rm LR}}{M^{\rm H}_{\rm t}} = -10^{\delta b+\epsilon}\log_{10}\left(\frac{Q_{\rm R}}{Q_0}\right)+1, \tag{5.13}$$

(solid lines in the bottom graph of Figure 5.4) we obtained values of $\delta = -0.70 \pm 0.01$, $\epsilon = 0.13 \pm 0.01$ and $Q_0 = (1.8 \pm 0.1) \times 10^6\,\mathrm{J\,kg^{-1}}$.

The physical meaning of the impact parameter dependent power law coefficient, $\gamma_{\mathrm{atmos}} = -10^{\delta b + \epsilon}$, is related to the efficiency of the collision in removing atmosphere from the target. Collisions closer to head-on remove more atmosphere than more highly grazing ones as a greater amount of the projectile's momentum can be transferred to the target's atmosphere. In addition, for collisions with low b the projectile causes shockwaves that travel through the core and mantle, which can cause atmosphere ejection from all over the planet not just the parts close to the trajectory of the projectile. Atmospheric shockwaves from high b impacts, on the other hand, are unlikely to cause strong shocks in the mantle due to the impedance mismatch between atmosphere and mantle.

c) The Head-On-Like Regime

For collisions below the critical velocity, v_{split}, we compare the mass in the largest remnant to the specific impact energy normalised by the catastrophic disruption threshold Q^*_{RD} outlined in Denman et al. (2020), as shown in Figure 5.6. We observe an initial shallow decrease in mass with increasing impact energy, which sharply increases at about $0.5Q^*_{\mathrm{RD}}$; this is strongly consistent with the model derived in Denman et al. (black lines in Figure 5.6), as such we label all these collisions as 'head-on-like'. Denman et al. (2020) identify this transition with the minimum energy at which mantle will be excavated by the impact in addition to atmosphere.

We have also compared the fraction of atmosphere lost from the largest remnant for this set of head-on-like collisions to our predictions in Denman et al. (2020) (see bottom panel, Figure 5.6). Again the results are strongly consistent with the predicted values. There is, however, an impact angle dependent divergence from predicted atmosphere loss which increases at low impact energies. More grazing collisions ($b \gtrsim 0.3$) remove less atmosphere than predicted by the model. This is likely due to glancing collisions generating a lower magnitude shock in the core and mantle. Glancing collisions between planets without atmospheres (such as those detailed in Leinhardt & Stewart (2012) section 3.1.2) have been shown to have less efficient energy deposition at higher impact parameters. A less energetic shockwave in the core means less atmosphere being pushed

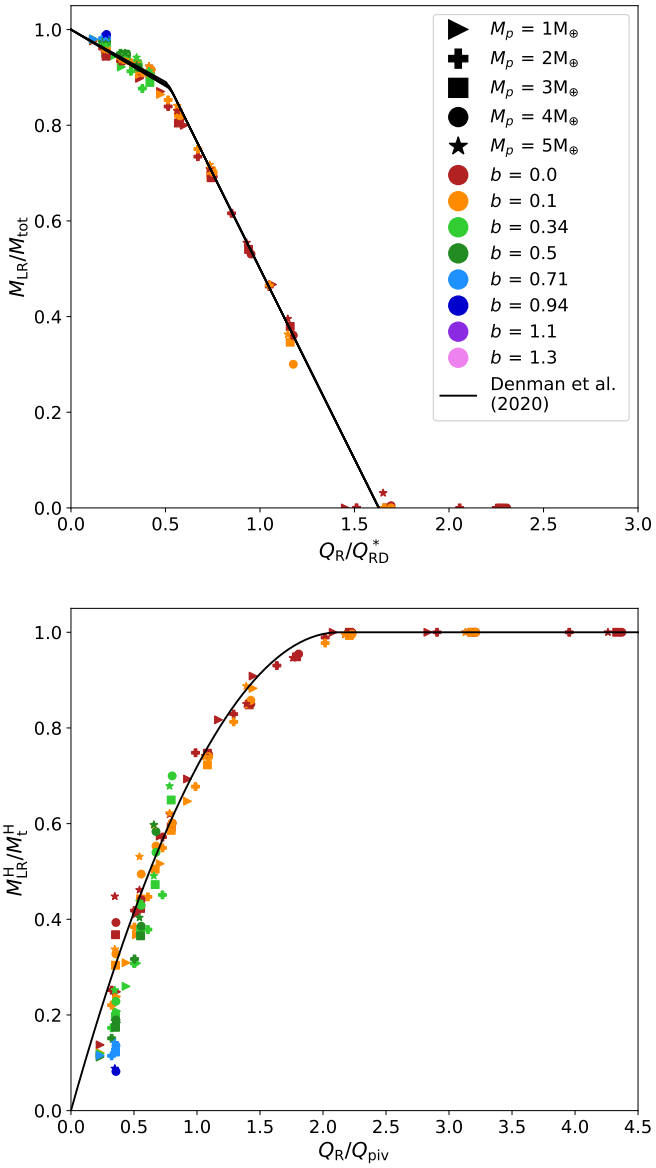

Figure 5.6: Top: Largest remnant mass as a function of normalized specific impact energy for all collisions in the head-on-like regime. Results are compared to the model from Denman et al. (2020) (the black line). Data and prediction show good agreement with one another. Bottom: The fraction of atmosphere lost by the largest remnant for all collisions with velocity below $v_{\rm split}$ (head-on-like) compared with impact energy normalised by $Q_{\rm piv}$ from Denman et al. (2020). The black line shows their predicted atmosphere loss fraction. The two results agree well with one another.

away by the shock as it reaches the target surface again on the other side of the planet.

This consistency between the results of this work and the model from Denman et al. (2020) occurs despite this chapter using a significantly increased atmosphere pseudo-entropy, $1.3 \times 10^{12}\mathrm{Ba\,g^{-\gamma}\,cm^{3\gamma}}$ as opposed to $5 \times 10^{11}\mathrm{Ba\,g^{-\gamma}\,cm^{3\gamma}}$, which resulted in a warmer, more extended atmosphere. Looking at these collisions in terms of energy, this consistency is likely because although the higher pseudo-entropy means the outermost atmosphere particles are higher up the potential well, the difference in energy required for them to be ejected is small compared to the differences in how efficiently the impact energy is spread between particles.

5.3.2 Remnant Composition

Preferential erosion or accretion of planet components during collisions will result in compositional change. Figure 5.7 shows the fraction of largest remnant that is comprised of each constituent material after a collision. The original mass fractions were, 26% iron, 53% forsterite and 20% hydrogen for the target, and, 33% iron and 67% forsterite for the projectile. We observe two different patterns: head-on-like collisions with $v < v_{\mathrm{split}}$ tend to clump around separate curves dependent on projectile mass; whereas the erosive hit-and-run collisions, for which $v > v_{\mathrm{split}}$, tend to all follow one single curve, this is true for the fractions of all material types (core, mantle, and atmosphere). The single line for erosive hit-and-runs is due to the collisions only eroding material from the target and barely depositing any.

Comparing the three graphs in Figure 5.7, looking at the erosive hit-and-run collisions, we see iron core content increasing with decreasing largest remnant mass (top), Hydrogen atmosphere content by comparison decreases with decreasing final mass (bottom), while forsterite mantle content increases with mass removed initially it reaches a turning point at $5.2 \pm 0.2\,\mathrm{M_\oplus}$ and starts to decrease again as more material is removed (middle). Whether a material fraction increases or decreases with decreasing final remnant mass depends upon if material is preferentially removed in an impact or not. In our simulations, first the lightly gravitationally bound outer atmosphere is removed, then the more tightly bound mantle layer underneath, and finally the strongly bound iron core material. This explains the turning point in mantle fraction, at lower final masses the

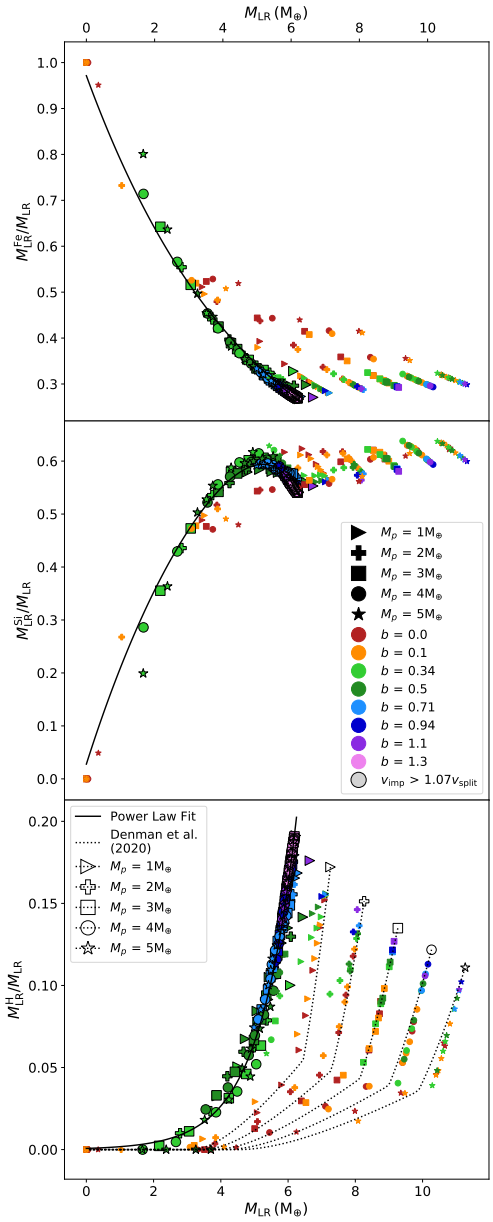

Figure 5.7: Top: Mass fraction of iron in the largest remnant as a function of the remnant mass. Iron fraction increases at low remnant masses because collisions preferentially remove material that is less well bound. Middle: Silicate mass fraction of the largest remnant. The mantle is less tightly bound than core material yet more strongly bound than atmosphere, we thus observe a turnover at the point where the majority of atmosphere has been eroded and mantle erosion begins in earnest. Bottom: The fraction of the largest remnant that is hydrogen atmosphere. Atmosphere is the least strongly bound part of the planet and thus is removed preferentially. We also show the predictions for head-on collisions from Denman et al. (2020) as dotted lines (open symbols at the end represent the projectile mass of the prediction). Colours and symbols have the same meanings as in previous Figures. For each of these graphs we have fit the $v_{\rm imp} > v_{\rm split}$ data with a power law (solid black lines).

majority of atmosphere has already been removed and mantle is then removed preferentially to iron core, but at higher masses atmosphere is still being removed preferentially to mantle.

An important result to take from all erosive hit-and-runs following the same pattern of final material fraction, is that the atmosphere fraction after an erosive hit-and-run collision can be calculated from the final remnant mass and vice versa.

The material fraction results were fitted with power laws; for the iron core we obtained:

$$f_{\mathrm{Fe}} = 10^{(-0.091\pm0.002)M_{\mathrm{LR}}-0.01\pm0.01}, \tag{5.14}$$

while for the hydrogen atmosphere we obtained,

$$f_{\mathrm{H}} = 10^{(0.39\pm0.01)M_{\mathrm{LR}}-3.14\pm0.05}, \tag{5.15}$$

finally we combine equations 5.14 and 5.15 for the fraction of the largest remnant that is silicate mantle:

$$f_{\mathrm{Si}} = 1 - f_{\mathrm{FE}} - f_{\mathrm{H}}. \tag{5.16}$$

These relations are shown in Figure 5.7 with solid black lines.

For the atmosphere fraction we have also added lines detailing the prescription from Denman et al. (2020) – the dotted lines with open symbols representing their projectile mass in the bottom panel of Figure 5.7. Because our head-on results show strong consistency with the model for total and atmospheric mass in the largest remnant, we again observe consistency here, with some deviation occurring for the $b = 0.34$ collisions which are close to the transition region, $v \approx v_{\mathrm{split}}$.

5.3.3 The Second Largest Remnant

The top panel of Figure 5.8 shows the dependence of the mass of the second largest remnant on impact velocity. At low relative velocities and impact angles we observe head-on like behaviour with no secondary remnant of more than a few particles in most cases. The most massive second largest remnants we observe are found at velocities just above the transition velocity, v_{split}. As the energy increases the projectile gets more and more eroded by the impact. For lower impact parameters, $b \sim 0.3 - 0.5$, eventually at sufficiently high energy the projectile will get disrupted. The degree to

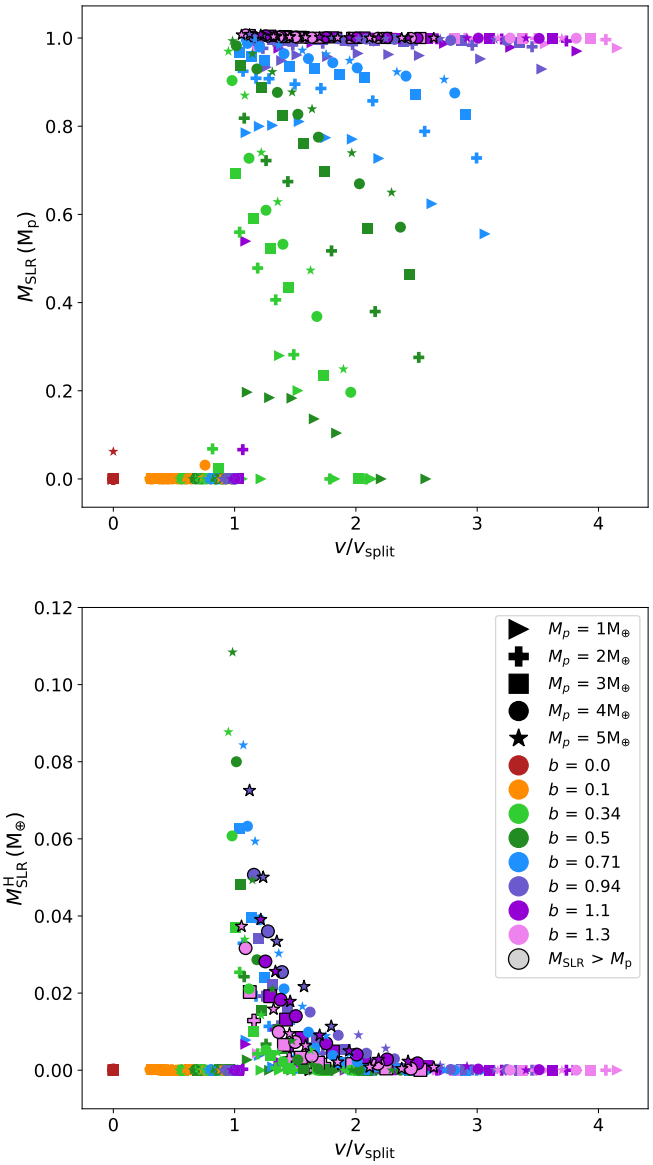

Figure 5.8: Top: Mass of the second largest remnant as a function of impact velocity in terms of the transition velocity, $v_{\rm split}$, showing the dependence on both projectile mass (different symbols) and impact parameter (different colours). More grazing impacts (e.g. blue and purple) result in less material lost from the projectile, as do lower velocity impacts, although sufficiently low velocity impacts will result in a merger ($v < v_{\rm split}$). Points with a black outline indicate those collisions in which the second largest remnant has increased in mass, typically by accreting atmosphere from the target. Bottom: The mass of target atmosphere accreted on to the second largest remnant as a function of impact velocity. The amount of accreted atmosphere peaks at a low energy close to the edge of the erosive hit-and-run regime at $v = v_{\rm split}$.

which the projectile is eroded is dependent on impact parameter, with more grazing impacts requiring more energy to remove the same amount of material. For the highly grazing impacts ($b > 1$) the amount of mass lost is negligible, and at lower impact energies the projectile can even gain mass. This mass gain comes from accretion of some of the comparatively lightly bound atmosphere of the target as the projectile passes through it (these collisions are highlighted by black outlines in Figure 5.8).

The bottom panel of Figure 5.8 shows the amount of atmosphere that is accreted onto the secondary remnant from the target. Like for the total secondary remnant mass, accreted atmosphere mass peaks at low impact velocities just above the critical impact velocity (v_{split}). The amount of atmosphere accreted decreases a lot more sharply after this point than the total mass of the secondary remnant though, with little to no atmosphere being accreted at velocities twice that of peak accretion.

All second largest remnants which have greater mass than the projectile have accreted atmosphere from the target during the collision. The outermost target atmosphere particles are loosely bound so the gravitational pull of the projectile can be sufficient to pull them away if they are not completely ejected by atmospheric shocks. This effect is likely exaggerated by the projectiles in our study being atmosphere-less, this means target atmosphere particles can approach closer to the projectile and thus experience a stronger gravitational pull towards it.

The collisions where mass increases also occur at the highest impact parameters where the projectile only barely grazes the target mantle, if at all, as core collisions are more erosive to the projectile. The collisions in which the secondary remnants accrete the most atmosphere, however, tend to be those of lower impact parameters (around $0.3 < b < 0.75$) where more of the core and mantle of the projectile is eroded, but the projectile passes through more of the atmosphere and thus can accrete more.

5.4 Discussion

5.4.1 The Erosive Hit-and-Run Regime

An important difference between collisions involving planets with and without an atmosphere is that, due to the lightly bound nature of the upper atmosphere, there is a very low probability of getting a ‘true’ hit-and-run collision in which target and projectile

mass are both affected negligibly. Instead we get 'erosive hit-and-runs' (Gabriel et al., 2020) where collisions resulting in two large remnants also erode the target.

In this erosive hit-and-run regime we normalise the mass of the largest post-collision remnant with respect to target mass as opposed to total mass. This is because in erosive hit-and-run collisions the largest remnant is formed from the partially eroded target with the remnants of the projectile rebounding, as opposed to projectile and target cores combining similar to what happens in a head-on collision.

Our results for the mass of the largest remnant in the erosive hit and run regime show negligible dependence on the projectile mass for our particular target mass. Because of this lack of projectile mass dependence we have elected not to describe our results in terms of accretion efficiency (Asphaug, 2010). In this regime the dependence of the amount of material excavated by the projectile on projectile mass is completely characterised by the specific impact energy, Q_{R}. The efficiency of this excavation is a strong function of impact parameter, with grazing impacts removing a lower proportion of the target's mass. This relation is also seen in the data provided by Gabriel et al. (2020) for atmosphere-less silicate-iron planets.

5.4.2 The Transition to Hit-and-Run

We find the transition between the merging and hit-and-run collision regimes to be strongly related to the mutual escape velocity of the two bodies at the point of closest approach, v_{split} defined in equation 5.5.

Earlier works on impacts such as Leinhardt & Stewart (2012) use the grazing angle measure of $b_{\mathrm{crit}} = R_{\mathrm{t}} / (R_{\mathrm{p}} + R_{\mathrm{t}})$ to approximate the transition to hit-and-run. b_{crit} is the boundary impact parameter where the velocity vector of the projectile's centre of mass no longer intersects the target. Gabriel et al. (2020) show that for larger planets $\approx 1\,\mathrm{M}_{\oplus}$, where there can be significant stratification of density due to both gravity and material types, this can cause the boundary between merging and hit-and-run to occur at substantially lower impact parameters. The smallest planets in this chapter are $1\,\mathrm{M}_{\oplus}$ and the targets all have large hydrogen atmospheres which are significantly less dense than the cores, we thus observe a transition to hit-and-run collisions at less than b_{crit}.

We use a different parametrisation of this boundary, one that has a simple functional form and physical motivation, i.e. the velocity required for the secondary remnant to

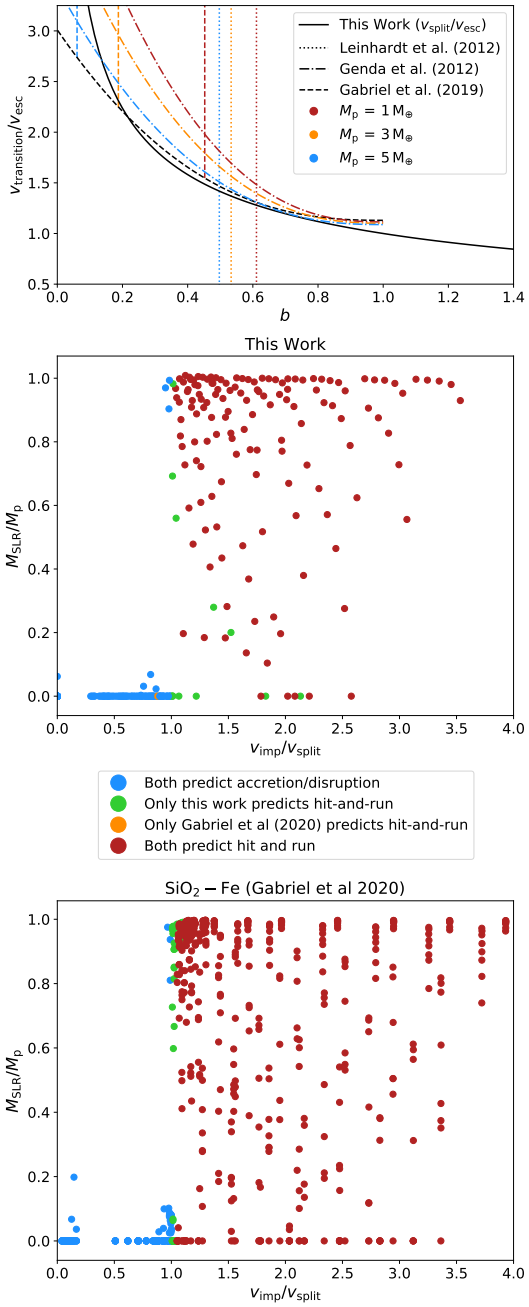

Figure 5.9: Top: Different methods of calculating the velocity of transition between merging and 'hit-and-run' and the dependence on b. Our model provides a close match to the Gabriel et al. (2020) prediction for impact angles greater than their predicted minimum hit-and-run impact angle (dashed lines). Middle: Comparison between the Gabriel et al. method for determining the erosive hit-and-run transition and our model applied to our simulations. Our results are in agreement apart from some collisions we classify as erosive hit-and-run (green points). Bottom: A comparison between our method for determining the erosive hit-and-run transition and the Gabriel et al. method, applied to their two component iron-silicate planets. Again our predictions identify more erosive hit-and-run collisions.

escape the system from its point of closest approach ($v_{\rm split}$). The top panel in Figure 5.9 shows comparisons between our model and the models from Gabriel et al. (2020), Genda et al. (2012) and Leinhardt & Stewart (2012) where we have replaced the target full radius with that of its surface due to the presence of an atmosphere. In the simplest model, like that used by Leinhardt & Stewart (2012), there is a sharp (mass ratio dependent) impact parameter cutoff above which all collisions are hit-and-run (dotted vertical lines). Both our model and that of Genda et al. (2012) (solid lines and dash-dotted lines respectively) describe the transition to the hit-and-run regime as impact parameter dependent, occurring at increasingly higher velocities at lower impact parameters, following a convex function. The model of Gabriel et al. (2020) (dashed lines) uses aspects of both descriptions, below a particular impact parameter threshold hit-and runs will not occur, but above that they will occur if they are above some transition velocity which decreases as a convex function of increasing impact parameter.

The bottom two panels compare which collisions both our method and that of Gabriel et al. (2020) classify as merge or hit-and-run for both our work and the two component bodies from their work. Red points are collisions that both methods classify as erosive hit-and-run, blue points are collisions in which both methods predict accretion or disruption, and green points are collisions that only this work classifies as erosive hit-and-run. Only one point (given in orange) was classified as erosive hit-and-run by Gabriel et al. but not by our model. The two panels show the two methods give broadly consistent results, with $v_{\rm split}$ from this work classifying more collisions as hit-and-run.

The minimum possible velocity of a collision between two planets with $b < 1$ is their mutual escape velocity, if the two planets are in isolation this is $v_{\rm esc} = \sqrt{2GM_{\rm tot}/(R_{\rm p} + R_{\rm t})}$. For highly grazing collisions ($b > 1$) the escape velocity from the point of closest approach is $v_{\rm split}$ which implies that they can only be erosive hit-and-run collisions. In our simulations, however, we observe some highly grazing collisions to result in mergers. These highly grazing mergers occur because the atmosphere also has a drag force on the projectile as it passes through it, if the projectile is moving slowly enough, this drag force can be sufficient to cause it to become a graze-and-merge collision. In the real world collisions slightly slower than mutual escape velocity can also occur due to the presence of the other bodies in the system, if we also consider the presence of the central star for example we only need to consider the projectile starting at zero velocity at the edge of

the Hill sphere (rather than at infinity).

Material properties may affect the accuracy of v_{split} as a predictor of the transition between head-on-like and erosive-hit-and-run collisions, for example by changing how much drag or deflection the projectile undergoes as it passes through the target. v_{split} seems to work well for both simulations despite differences in equation of state and the presence of an atmosphere. This agreement is likely due to collisions being deep in the gravity dominated regime Housen & Holsapple (1990).

5.4.3 Atmosphere Removal

Denman et al. (2020) show that the likelihood of a collision removing all the atmosphere from a planet in one go is low, and if it does so it will be sufficiently energetic to cause catastrophic disruption. The head-on collisions in this work are in strong agreement with their predictions for atmosphere loss, as shown in Figure 5.6.

Comparing our results for the mass remaining in the largest remnant for head-on collisions to those at higher impact parameters (given in Figure 5.4) we see that, for all cases where $b > 0.3$, higher impact parameters mean a lower efficiency of atmosphere erosion. Considering that higher impact parameters are more likely than head-on (Shoemaker & Hackman 1962 predict a most likely value of 45°), this means that a single impact removing the entirety of a Super-Earth's atmosphere is very unlikely. This implies that when we observe a Super-Earth mass planet with no substantial atmosphere it has likely either undergone multiple collisions or formed sufficiently close to its central star for photo-evaporation to have stripped the entire atmosphere.

5.4.4 Final Planet Radii

As in Denman et al. (2020), we have used Lopez & Fortney (2014)'s results to predict the final radii and densities of planets from their percentage composition post collision once all the bound material has settled back down, see Figure 5.10. The majority of higher impact parameter results (greens, blues and purples) cluster in a single group, these are the erosive hit-and-run collisions, the dash-dotted line here is Lopez & Fortney (2014)'s model applied to the material composition fit of equation 5.15. Lower impact parameter collisions on the other hand separate into multiple groups depending on their projectile mass (symbol shape); these groups agree with radius and density predictions using the

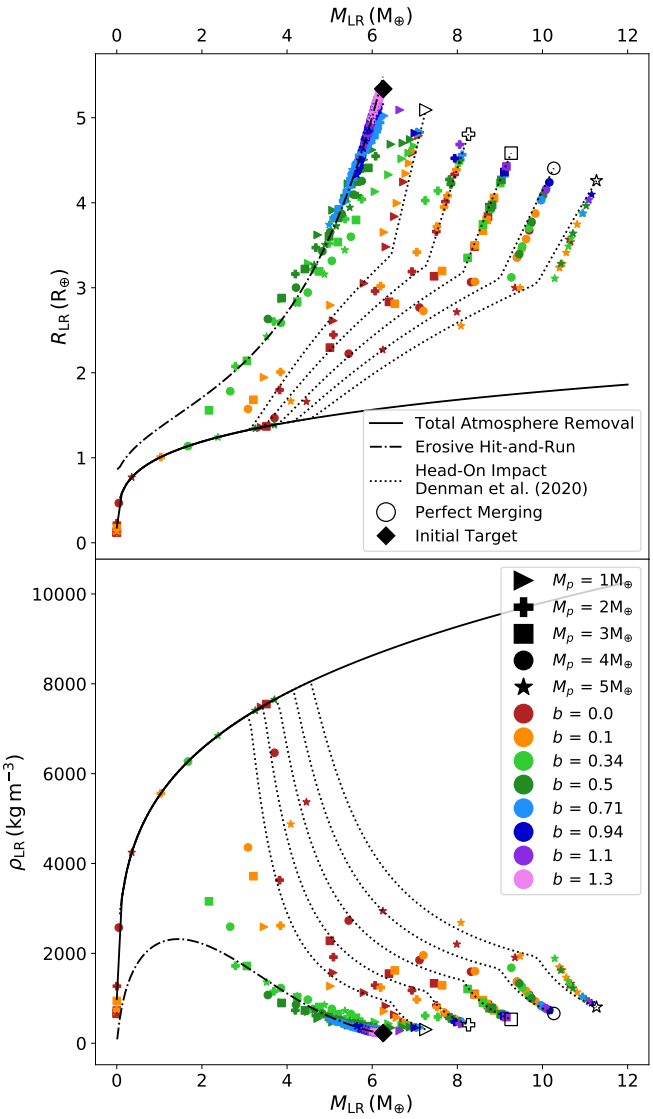

Figure 5.10: Top: The radii of the largest remnants generated by our collisions as a function of their masses. The colour of points indicates the impact parameter whereas the shape indicates the projectile mass. Lines indicate the expected results for total atmosphere erosion (solid line), and for partial atmosphere erosion in both the erosive hit-and-run (dash-dot) and head-on-like regimes (dotted lines, from Denman et al., 2020). The open symbol at the end of each dotted line shows which projectile mass the line represents. Bottom: Corresponding densities as a function of largest post-collision remnant mass. Note that for real systems the upper limit for density is likely also dependent on material types in the core. Highly erosive collisions will strip mantle more readily than core, leaving a denser remnant than would be expected if the same ratio of core to mantle was maintained.

Denman et al. (2020) prescription to predict material composition (dotted lines, with the shape of the open symbol at the end denoting projectile mass). The black line denotes the expected radius if the entirety of the atmosphere was eroded.

All simulated collisions result in ejection of atmosphere causing a reduction in planet radius typically leading to an increase in final density. Figure 5.7 shows that the the atmosphere fraction for the majority of collisions clusters around a single function of total mass, as such so do the final radii of planets. The majority of collisions that are not close to this erosive hit-and-run prediction line instead follow the predictions for atmosphere mass fraction from Denman et al. (2020) for merging collisions.

Although from Figure 5.10 it appears that these collisions could generate Earth analogues, i.e. objects with the Earth's mass and size, Figure 5.7 reveals that to erode enough material to reach this mass these collisions eject a significant fraction of the mantle and as such they result in a much higher iron fraction than the Earth. The model we are using to predict radius doesn't include core fraction for sake of simplicity, so we would expect these Earth mass planets to actually be smaller and denser. Considering the relationship between final iron content and final mass detailed in Figure 5.7, we expect the predictions here to underestimate density and overestimate radius by a factor that increases with decreasing final remnant mass.

Overall, Figure 5.10 shows that a collision between a single target-projectile pair (these are each denoted by a different symbol) can result in a wide variety of radii and densities in the remnant planets. These simulations therefore provide direct support to the conclusions of Inamdar & Schlichting (2016) that giant impacts can enrich the density diversity of Super-Earth planets.

5.5 Conclusions

Collisions between a Super-Earth sized target with an atmosphere, and a second Super-Earth sized projectile (with no atmosphere) tend to fall into two different collision regimes. At high impact parameter and velocity they have erosive hit-and-run collisions in which the target and projectile cores mostly remain intact and separate, but erosion and sometimes accretion occurs during the collision. For low impact angles and velocities we instead observe the projectile and target combining into a single large remnant,

following Denman et al. (2020). Between these two regimes we observe graze-and-merge collisions where the target and projectile eventually merge into one large remnant, but not on the first collision.

We observe the transition between these two regimes to be well described by a simple escape velocity measure, the minimum velocity required for an erosive hit-and run being

$$v_{\text{split}} = \sqrt{\frac{2G(M_{\text{p}} + M_{\text{t}})}{b(R_{\text{p}} + R_{\text{t}})}}.$$

For erosive hit-and-run collisions in which large secondary remnants arise, the dependence of the mass of the largest remnant on projectile mass is solely contained within the specific impact energy. In other words, all collisions in the erosive limit appear to follow the same pattern with regards to specific relative kinetic energy of impact regardless of projectile mass.

The results of the simulations outlined in this chapter reinforce the conclusion from Denman et al. (2020) that it is impossible to remove the entirety of the atmosphere of the target planet without removing a significant percentage of the mantle as well. Considering the higher probabilities of higher impact angles and lower velocity collisions, a giant impact being sufficiently energetic to remove the entirety of a planet's atmosphere is likely a rare occurrence.

Despite the low likelihood of removing the entire atmosphere of a planet with a single collision, the planets resulting from giant impacts cover a wide array of different radii and densities, reinforcing the hypothesis that planet-planet collisions are a cause of the large density diversity we observe in Super-Earth populations.

5.6 Appendices

5.6.1 Resolution Testing

An array of different resolution simulations were run to test the veracity of our results, the resolutions used for these tests were $10^4, 2 \times 10^4, 5 \times 10^4$ and 10^6 particles in the $5\text{M}_\oplus$ target core and mantle compared to the standard resolution of 10^5 particles in the target core and mantle.

A comparison of the results for these different resolutions is given in Figure 5.11. For mass of the largest remnant our results show agreement between the resolutions to

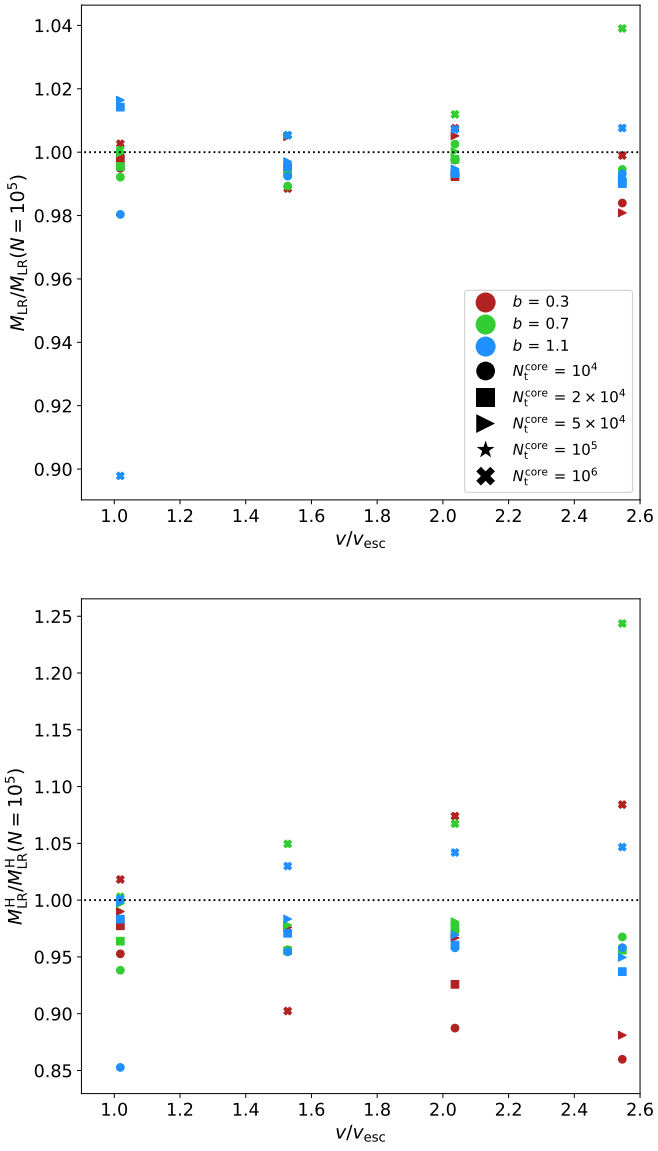

Figure 5.11: Top: The ratio of largest remnant mass for various simulation resolutions to the remnant mass for our standard resolution ($N = 10^5$) compared to impact velocity. The majority of runs here give results within 2% of the standard resolution chosen. Bottom: Atmosphere mass remaining as a fraction of the atmosphere mass obtained at our standard resolution at different impact velocities. Due to the lower resolution of the atmosphere compared to the total mass this shows less close agreement, the majority of results still fall within 6% of the values from the chosen resolution.

within 2% for all but two tests. For atmosphere mass remaining in the largest remnant the results detailed in Figure 5.11 show a greater spread between resolutions; the majority of results agree to within 6%, however there are some significant outliers which differ by up to 25%.

We also observe in our results that the amount of atmosphere remaining seems slightly dependent on resolution, with the higher resolution simulations typically retaining more atmosphere after an impact. One might assume that the reverse would be true, as the individual particles at higher resolutions would be lower mass and thus require less energy to eject. What is likely happening is that the greater spatial resolution for the higher resolution simulations means that atmosphere particles interact more frequently and there is thus more efficient energy partitioning between particles.

Overall these resolution tests show a good agreement with our standard resolution results for both mass of the largest remnant and also atmosphere mass.

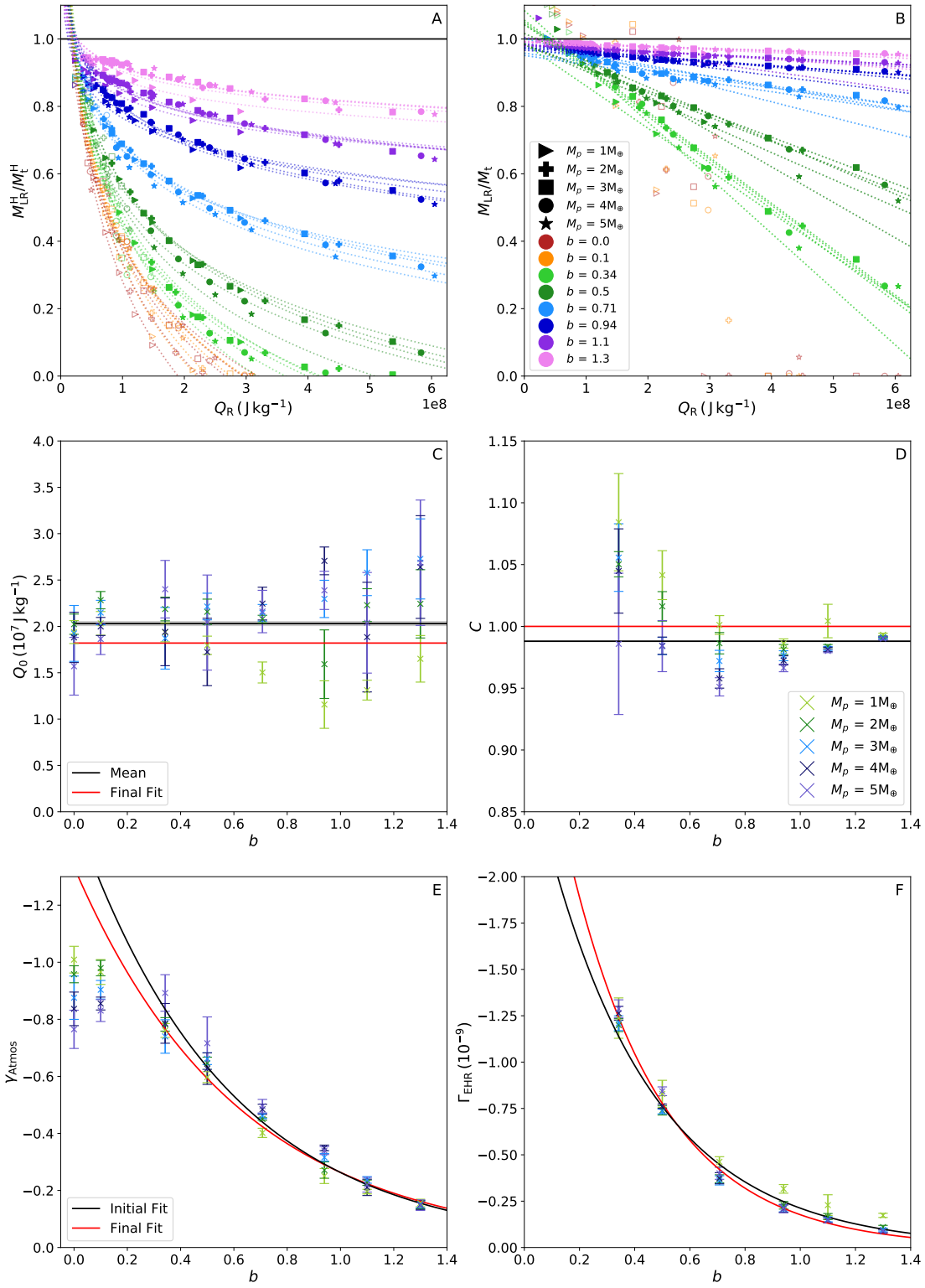
A
B
C
D
E
F
M_{LR}^{H}/M_t^{H}
M_{LR}/M_t
Q_R (J kg^{-1})
1e8
M_p = 1M$_\oplus$
M_p = 2M$_\oplus$
M_p = 3M$_\oplus$
M_p = 4M$_\oplus$
M_p = 5M$_\oplus$
b = 0.0
b = 0.1
b = 0.34
b = 0.5
b = 0.71
b = 0.94
b = 1.1
b = 1.3
Q_0 (10^7 J kg^{-1})
Mean
Final Fit
b
C
γ_{Atmos}
Initial Fit
Final Fit
Γ_{EHR} (10^{-9})

Figure 5.12: A: Atmosphere mass in the largest remnant as a function of Q_{R}; this has been fit for each impact parameter and projectile mass by a series of power law fits (dotted lines). Erosive hit-and-run collisions are given by filled symbols, all other collisions are open symbols. B: Largest remnant mass normalised by target mass compared to Q_{R}. The erosive hit-and-run collisions for impact parameter and projectile mass have been fit with linear fits. C: Minimum energy required for atmosphere to be ejected, Q_0, for each power law fit in A as a function of impact parameter. There is some scatter with no obvious physical cause so the final fit (red line) uses a common value for all impact angles and projectiles. The mean Q_0 is shown in black. D: The intercept of the linear fits to largest remnant mass versus impact energy as a function of impact parameter. Many of these intercepts fall below the target mass (the mean value is in black), implying that mass could be lost without input energy, this is un-physical so we set the intercept to the target mass (unity) for all fits. E: The coefficient for power law fits to atmosphere mass in the largest remnant versus impact energy, this itself follows a power law function of the impact parameter. An initial power law fit to these coefficients is shown in black. The final fit from figure 5.4, which fits for impact parameter and impact energy dependence at the same time, is shown in red. F: The gradient of linear fits to projectile mass in the largest remnant versus impact energy fixed to go through zero mass loss for zero impact energy. These gradients follow a power law (black line).

5.6.2 Erosive Hit-and-run fitting process

This section summarises the reasoning behind the functional forms of the final fits used for the total mass and atmosphere masses of the largest remnant in sections a) and b).

a) Atmosphere fitting

The left side of Figure 5.12 shows atmosphere mass in the largest remnant as a function of specific impact energy and the dependence of fit parameters on the impact parameter, *b*. The top left panel shows atmosphere mass normalised by initial target atmosphere mass compared to impact energy, Q_{R}. Data for each individual projectile mass and

impact parameter are fit with the following power law:

$$\frac{M_{\rm LR}^{\rm H}}{M_{\rm t}^{\rm H}} = \gamma_{\rm atmos} \log_{10}(Q_{\rm R}) + c_{\rm atmos}, \tag{5.17}$$

where $\gamma_{\rm atmos}$ and $c_{\rm atmos}$ are fit parameters.
Each of these fits (dotted lines in the top left graph of Figure 5.12) cross the target atmosphere mass at an impact energy of approximately $2 \times 10^7\,{\rm J\,kg^{-1}}$. The exact value of this collision energy is given by

$$Q_0 = 10^{\frac{1-c_{\rm atmos}}{\gamma_{\rm atmos}}}, \tag{5.18}$$

for each fit. This value has a reasonably low amount of scatter, that does not appear to show any impact parameter or projectile mass dependence, so we elected to use an impact parameter independent fit parameter for the final combined fit (section b). The Q_0 measured in the final fit is given by the red line in the left middle graph in Figure 5.12, the mean value of Q_0 from our separate fits for each proectile mass and impact parameter is given by the black line.
The power law coefficient $\gamma_{\rm atmos}$ for each of these individual fits is given in the bottom left graph of Figure 5.12. Apart from the head-on like collisions ($b < 0.2$), these have a power law dependence on impact parameter; the black line shows a power law fit to these coefficients, whereas the red line is the impact parameter dependence of the coefficient obtained for our final fit (equation 5.13) where we fit all the projectiles and impact angles simultaneously.

b) Largest Remnant mass fitting

The top right graph of Figure 5.12 compares largest remnant mass and impact energy, the erosive hit-and-run collisions are shown with solid symbols. These erosive hit-and-run collisions show a linear dependence of remnant mass on impact energy, each separate impact parameter and projectile mass was therefore fit with:

$$\frac{M_{\rm LR}}{M_{\rm t}} = \Gamma_{\rm EHR} Q_{\rm R} + C, \tag{5.19}$$

where $\Gamma_{\rm EHR}$ and C are the gradient and the intercept respectively.
The intercept for each of these fits is shown in the middle right graph of Figure 5.12. Many of these values are below the target mass (less than 1), as is the mean intercept (the

black line), this is unphysical as it implies material can be lost from the target without any impact energy. What we actually observe at low impact energies is a curve upwards away from the linear fit, so it is likely that mass loss for low impact energies, close to the transition region, is non-linear. However, we chose to use the simplest possible model to describe the data and so used a linear fit fixed to the target mass for zero impact energy (red line), i.e. $C = 1$, despite the low energy differences this shows good agreement with the majority of the data.

The bottom graph in Figure 5.12 details the dependence of the gradient of the largest remnant mass to impact energy relation on impact parameter. The gradient becomes less negative by a decreasing amount with increasing impact parameter, so we fit it with a power law (black line) which shows good agreement. The dependence of gradient on impact parameter obtained from our final fit (equation 5.6), which simultaneously fit to all projectile masses and impact parameters, is shown in red.

5.6.3 Graze-and-Merge re-collision time

To approximate the longest possible orbit time that could occur before re-collision, without the secondary remnant escaping the largest remnant's gravitational influence, we first need to calculate the Hill radius of the target planet r_{H}:

$$r_{\mathrm{H}} = a_{\mathrm{i}} \sqrt[3]{\frac{M_{\mathrm{t}}}{3M_0}}, \tag{5.20}$$

where a_{i} is the semi-major axis of the target about the star it orbits and M_0 that star's mass. The semi-major axis of an orbit about the target after a grazing collision is half the sum of the apoapsis and periapsis distance and so the longest possible orbit of the secondary remnant without it escaping is $a_{\mathrm{ii}} = (r_{\mathrm{H}} + R_{\mathrm{t}} + R_{\mathrm{p}})/2$. From this semi-major axis we can calculate the orbital period of this limiting orbit of the projectile about the target to be

$$T = 2\pi \sqrt{\frac{a_{\mathrm{ii}}^3}{G(M_{\mathrm{t}} + M_{\mathrm{p}})}}. \tag{5.21}$$

Applying this to our scenario, for a close orbiting super Earth 0.1 au from a sun-like star (like we use in section 5.4.4 for density estimates) this gives us re-collision times of $5 - 7$ hrs for Super-Earth mass projectiles. This time period is well within the time limit of 27.7 hrs of our simulations. So we would be able to model such re-collisions in our

simulations. We do not model the central star's gravity in our simulations, however, so our simulations include graze-and-merge collisions on longer re-collision timescales, as such we removed the graze-and-merge collisions from our collision fits so that they could remain agnostic to orbital distance.

5.6.4 Remeasuring the point of collision

For ease of comparison to previous works on cratering and giant impacts (for example Leinhardt & Stewart 2012; Marcus et al. 2009, 2010) and also to give a simple, reproducible approach that is independent of atmosphere scale height, we have chosen to measure our impact parameters at the point of collision between the mantle surfaces of projectile and target, or at the point of closest approach for highly grazing collisions. This method is not without its drawbacks however, the main one which needs to be considered is the effect of atmospheric drag.

To understand the difference caused by this drag we re-simulate the point of collision at a high snapshot output frequency and remeasure the relative velocity, separation, and impact parameter of the centre of masses at the point where the mantles collide (or reach their point of closest approach if $b > 1$).

Because of this atmospheric drag, the velocity at the point of collision for an impact is reduced slightly. This means that the measured specific relative kinetic energy of impact, $Q_{\mathrm{R}}^{\mathrm{meas}}$, is typically less than that initially predicted $Q_{\mathrm{R}}^{\mathrm{pred}}$. Figure 5.13 compares the ratio of measured to expected Q_{R} with various collision parameters it is likely to be dependent on. The top two graphs compare the energy ratio to relative velocity and projectile mass; as might be expected, lower velocities and projectile masses typically mean a greater difference in impact energy, because the change in momentum due to the drag force is a larger percentage of the overall momentum of the projectile. The decrease we see in measured Q_{R} for lower impact velocities is stronger than that for lower projectile masses, this is due to Q_R having a squared dependence on velocity (equation 5.1). The dependence of Q_R on projectile mass is somewhat more complicated, being somewhere between approximately zero proportionality for $M_{\mathrm{p}} \approx M_{\mathrm{t}}$ and approximately linear dependence for $M_{\mathrm{p}} << M_{\mathrm{t}}$.

Predicted impact parameter does not appear to have a significant effect on the amount of kinetic energy lost to atmospheric drag (see bottom panel Figure 5.13). We do,

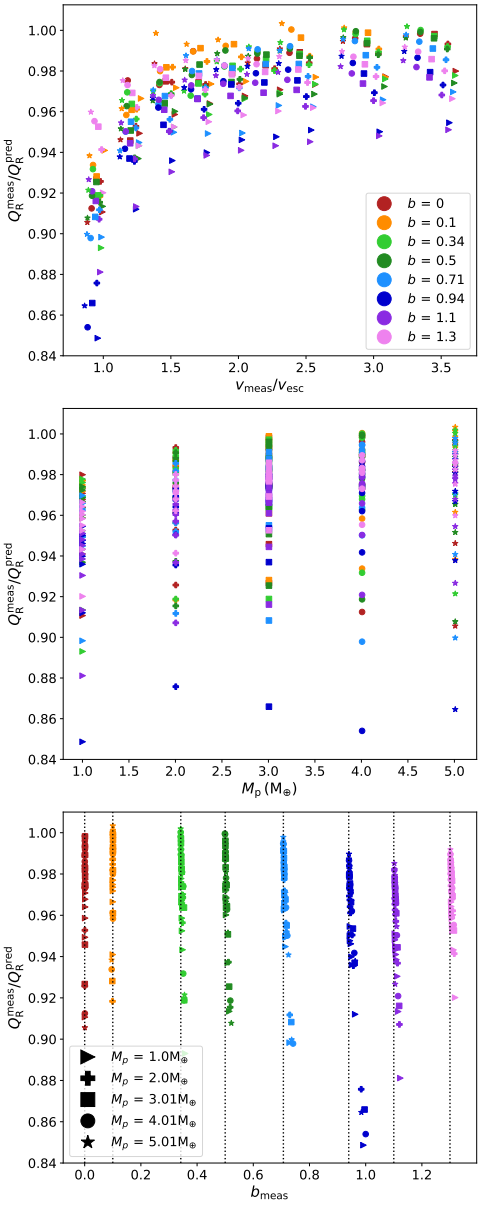

Figure 5.13: Variation of the specific impact energy as a function of other collision parameters. The colour of the points indicates the impact parameter, the shape indicates the mass of the projectile. Top: Ratio of measured to expected Q_R vs measured impact velocity. There is a significant decrease in energy compared to the prediction for low velocities where a change in momentum due to drag can cause a much larger proportional change in velocity and thus kinetic energy. Middle: Projectile mass compared with measured to expected Q_R ratio. Although there is a slight decrease in the mean impact energy for smaller projectiles due to lower momenta, projectile mass does not have a significant effect. Bottom: The measured to expected Q_R ratio compared with measured impact parameter. Impact parameter difference does not appear to cause a significant change to impact energy; note, however, that impacts with the largest change in kinetic energy tend to show the largest change from expected impact parameter (shown with dotted lines).

Table 5.1: Initial masses, M of each planet used in our simulations, as well as the masses of each component (Fe – iron, Si – forsterite, H – hydrogen) in each body, and the radius of the outermost simulation particle in each material layer.

Type	M	$M_{\rm Fe}$	$R_{\rm Fe}$	$M_{\rm Si}$	$R_{\rm Si}$	$M_{\rm H}$	$R_{\rm H}$
	$\rm M_\oplus$	$\rm M_\oplus$	$\rm R_\oplus$	$\rm M_\oplus$	$\rm R_\oplus$	$\rm M_\oplus$	$\rm R_\oplus$
Target	6.26	1.66	0.76	3.34	1.51	1.25	5.34
Projectile	1.00	0.33	0.50	0.67	0.96	0.00	-
Projectile	2.00	0.67	0.60	1.33	1.17	0.00	-
Projectile	3.01	1.01	0.68	1.99	1.32	0.00	-
Projectile	4.01	1.32	0.72	2.69	1.43	0.00	-
Projectile	5.01	1.66	0.77	3.34	1.52	0.00	-

however, observe that, especially at higher impact parameters, the greater the measured deflection from the intended impact parameter the larger the percentage decrease in impact energy. Atmospheric pressure is deflecting the projectiles away from the target causing them to spend more time passing through the atmosphere before collision, thus producing a greater decrease in projectile momentum and therefore impact energy.
For the majority of collisions, apart from those at the lowest impact velocity, the drag effects on kinetic energy are relatively small, typically causing a decrease of $< 6\%$. Since this effect is small we therefore used the expected parameters for our analyses in this chapter.

5.6.5 Data tables

We present here data tables, Table 5.1 provides details for each of the bodies we simulated collisions with, the other Tables each list the results of our simulations for a particular projectile mass. All collisions used a $6.25\,\rm M_\oplus$ target, the projectile mass for each of the collision results tables are as follows: Table 5.2 is for $1\,\rm M_\oplus$ projectiles, Table 5.3 is for $2\,\rm M_\oplus$ projectiles, Table 5.4 is for $3\,\rm M_\oplus$ projectiles, Table 5.5 is for $4\,\rm M_\oplus$ projectiles, and Table 5.6 is for $5\,\rm M_\oplus$ projectiles.

5.6.6 A Modified Prescription For The Mass Of the Largest Remnant

Using our new results we can now add to the collision prescription from Denman et al. (2020) to account for different impact angles, note that we have not yet tested the dependence of our modifications due to impact angle on target mass or target atmosphere

Table 5.2: A summary of the results of the simulations of collisions of the $1\,M_\oplus$ projectile with the $6.25\,M_\oplus$ target. Full planet data is given in Table 5.1, the rest of the collision results are in Tables 5.3, 5.4, 5.5, and 5.6.

b	v	$M_{\rm LR}$	$f_{\rm Fe}$	$f_{\rm Si}$	$f_{\rm H}$	$M_{\rm SLR}$
	$\rm km\,s^{-1}$	$M_\oplus$				$M_\oplus$
0.00	20.0	7.09	0.28	0.57	0.15	-
0.00	25.0	6.95	0.29	0.58	0.14	-
0.00	30.0	6.73	0.30	0.59	0.11	-
0.00	35.0	6.52	0.31	0.61	0.08	-
0.00	40.0	6.32	0.32	0.62	0.06	-
0.00	45.0	5.81	0.34	0.62	0.04	-
0.00	50.0	5.08	0.39	0.58	0.02	-
0.10	20.0	7.11	0.28	0.56	0.15	-
0.10	25.0	6.96	0.29	0.58	0.14	-
0.10	27.5	6.87	0.29	0.58	0.13	-
0.10	30.0	6.79	0.29	0.59	0.12	-
0.10	35.0	6.58	0.30	0.60	0.09	-
0.10	40.0	6.28	0.32	0.61	0.07	-
0.10	50.0	5.02	0.38	0.59	0.03	-
0.34	20.0	7.11	0.28	0.56	0.15	-
0.34	25.0	6.98	0.29	0.57	0.14	-
0.34	27.5	6.86	0.29	0.57	0.13	-
0.34	30.0	6.69	0.30	0.57	0.13	-
0.34	35.0	6.38	0.31	0.57	0.11	-
0.34	40.0	6.07	0.33	0.57	0.10	-
0.34	45.0	5.40	0.32	0.59	0.09	0.28
0.34	50.0	5.09	0.33	0.59	0.08	0.20
0.50	20.0	7.12	0.28	0.56	0.16	-
0.50	25.0	6.90	0.29	0.56	0.15	-
0.50	27.5	6.72	0.30	0.56	0.14	-
0.50	30.0	6.44	0.30	0.56	0.14	0.20
0.50	35.0	5.99	0.30	0.57	0.14	0.18
0.50	40.0	5.80	0.30	0.58	0.13	0.18
0.50	45.0	5.62	0.31	0.58	0.12	0.14
0.50	50.0	5.43	0.31	0.58	0.10	0.10
0.71	20.0	7.12	0.28	0.56	0.16	-
0.71	25.0	6.28	0.27	0.56	0.17	0.79
0.71	27.5	6.20	0.27	0.56	0.17	0.80
0.71	30.0	6.13	0.28	0.56	0.16	0.80
0.71	35.0	5.99	0.28	0.57	0.15	0.81
0.71	40.0	5.91	0.28	0.57	0.15	0.78
0.71	45.0	5.84	0.29	0.58	0.14	0.77
0.71	50.0	5.77	0.29	0.58	0.13	0.73
0.94	20.0	7.00	0.29	0.56	0.15	-
0.94	25.0	6.18	0.27	0.55	0.18	0.94
0.94	27.5	6.13	0.27	0.55	0.18	0.95
0.94	30.0	6.10	0.27	0.55	0.17	0.96
0.94	35.0	6.04	0.28	0.56	0.17	0.96
0.94	40.0	6.00	0.28	0.56	0.16	0.97
0.94	45.0	5.96	0.28	0.56	0.16	0.96
0.94	50.0	5.92	0.28	0.57	0.15	0.96
1.10	20.0	6.65	0.27	0.55	0.18	0.54
1.10	25.0	6.16	0.27	0.55	0.18	0.98
1.10	27.5	6.13	0.27	0.55	0.18	1.00
1.10	30.0	6.11	0.27	0.55	0.18	0.99
1.10	35.0	6.09	0.27	0.55	0.18	1.00
1.10	40.0	6.06	0.27	0.55	0.17	0.99
1.10	45.0	6.03	0.28	0.55	0.17	0.99
1.10	50.0	6.00	0.28	0.56	0.17	0.99
1.30	20.0	6.23	0.27	0.54	0.19	0.98
1.30	25.0	6.19	0.27	0.54	0.19	1.00
1.30	27.5	6.18	0.27	0.54	0.19	1.00
1.30	30.0	6.16	0.27	0.54	0.19	1.00
1.30	35.0	6.15	0.27	0.54	0.18	1.00
1.30	40.0	6.13	0.27	0.55	0.18	1.00
1.30	45.0	6.11	0.27	0.55	0.18	1.00
1.30	50.0	6.08	0.27	0.55	0.18	1.00

Table 5.3: A summary of the results of the simulations of collisions of the $2\,M_\oplus$ projectile with the $6.25\,M_\oplus$ target. Full planet data is given in Table 5.1, the rest of the collision results are in Tables 5.2, 5.4, 5.5, and 5.6.

b	v	$M_{\rm LR}$	$f_{\rm Fe}$	$f_{\rm Si}$	$f_{\rm H}$	$M_{\rm SLR}$
	$\rm km\,s^{-1}$	$M_\oplus$				$M_\oplus$
0.00	20.0	7.94	0.29	0.59	0.12	-
0.00	25.0	7.72	0.30	0.60	0.09	-
0.00	30.0	7.51	0.31	0.62	0.07	-
0.00	35.0	6.93	0.34	0.62	0.05	-
0.00	40.0	6.07	0.38	0.58	0.04	-
0.00	45.0	5.09	0.44	0.55	0.02	-
0.00	50.0	3.82	0.48	0.52	-	-
0.10	20.0	7.98	0.29	0.59	0.12	-
0.10	25.0	7.77	0.30	0.60	0.10	-
0.10	27.5	7.69	0.30	0.61	0.09	-
0.10	30.0	7.52	0.31	0.61	0.07	-
0.10	35.0	7.05	0.33	0.61	0.06	-
0.10	40.0	6.20	0.38	0.59	0.04	-
0.10	50.0	3.85	0.48	0.51	0.01	-
0.34	20.0	8.04	0.29	0.58	0.13	-
0.34	25.0	7.85	0.30	0.59	0.11	-
0.34	27.5	7.54	0.31	0.59	0.10	0.14
0.34	30.0	7.25	0.32	0.58	0.09	-
0.34	35.0	5.75	0.31	0.60	0.09	1.12
0.34	40.0	5.36	0.32	0.60	0.08	0.96
0.34	45.0	4.98	0.34	0.60	0.06	0.81
0.34	50.0	4.61	0.36	0.59	0.05	0.56
0.50	20.0	8.07	0.29	0.58	0.13	-
0.50	25.0	7.85	0.30	0.59	0.11	-
0.50	27.5	7.81	0.30	0.59	0.11	-
0.50	30.0	6.08	0.30	0.57	0.13	1.64
0.50	35.0	5.77	0.30	0.58	0.12	1.45
0.50	40.0	5.57	0.30	0.59	0.11	1.35
0.50	50.0	5.15	0.32	0.60	0.08	1.04
0.71	20.0	8.11	0.29	0.58	0.14	-
0.71	25.0	6.19	0.27	0.57	0.16	1.85
0.71	27.5	6.13	0.27	0.57	0.16	1.82
0.71	30.0	6.06	0.28	0.57	0.15	1.82
0.71	35.0	5.91	0.28	0.58	0.14	1.79
0.71	40.0	5.78	0.29	0.58	0.13	1.77
0.71	50.0	5.63	0.30	0.59	0.12	1.72
0.94	20.0	7.94	0.29	0.57	0.13	-
0.94	25.0	6.14	0.27	0.55	0.18	1.96
0.94	27.5	6.10	0.27	0.55	0.17	1.97
0.94	30.0	6.06	0.27	0.55	0.17	1.97
0.94	35.0	6.01	0.28	0.56	0.17	1.98
0.94	40.0	5.95	0.28	0.56	0.16	1.97
0.94	50.0	5.86	0.28	0.57	0.15	1.98
1.10	20.0	8.06	0.29	0.56	0.15	0.13
1.10	25.0	6.14	0.27	0.55	0.18	2.00
1.10	27.5	6.12	0.27	0.55	0.18	2.01
1.10	30.0	6.10	0.27	0.55	0.18	2.01
1.10	35.0	6.06	0.27	0.55	0.17	2.00
1.10	40.0	6.04	0.28	0.55	0.17	2.00
1.10	50.0	5.98	0.28	0.56	0.16	2.00
1.30	20.0	6.20	0.27	0.54	0.19	2.01
1.30	25.0	6.18	0.27	0.54	0.19	2.01
1.30	27.5	6.17	0.27	0.54	0.19	2.00
1.30	30.0	6.16	0.27	0.54	0.19	2.01
1.30	35.0	6.15	0.27	0.54	0.19	2.00
1.30	40.0	6.12	0.27	0.55	0.18	2.00
1.30	50.0	6.08	0.27	0.55	0.18	2.00

Table 5.4: A summary of the results of the simulations of collisions of the $3\,M_\oplus$ projectile with the $6.25\,M_\oplus$ target. Full planet data is given in Table 5.1, the rest of the collision results are in Tables 5.2, 5.3, 5.5, and 5.6.

b	v	$M_{\rm LR}$	$f_{\rm Fe}$	$f_{\rm Si}$	$f_{\rm H}$	$M_{\rm SLR}$
	$\rm km\,s^{-1}$	$M_\oplus$				$M_\oplus$
0.00	20.0	8.75	0.31	0.60	0.09	-
0.00	25.0	8.72	0.31	0.61	0.08	-
0.00	30.0	8.41	0.32	0.62	0.06	-
0.00	35.0	7.45	0.36	0.60	0.04	-
0.00	40.0	6.39	0.41	0.56	0.03	-
0.00	45.0	5.01	0.44	0.54	0.01	-
0.00	50.0	3.51	0.52	0.48	-	-
0.10	20.0	8.86	0.30	0.60	0.10	-
0.10	25.0	8.69	0.31	0.61	0.08	-
0.10	27.5	8.60	0.31	0.62	0.07	-
0.10	30.0	8.41	0.32	0.62	0.06	-
0.10	35.0	7.64	0.35	0.60	0.05	-
0.10	40.0	6.53	0.41	0.56	0.03	-
0.10	50.0	3.21	0.52	0.48	-	-
0.34	20.0	9.01	0.30	0.59	0.11	-
0.34	25.0	8.76	0.31	0.61	0.09	-
0.34	27.5	8.60	0.31	0.61	0.08	-
0.34	30.0	8.24	0.32	0.62	0.05	0.07
0.34	35.0	5.62	0.31	0.61	0.08	2.08
0.34	40.0	5.19	0.33	0.61	0.06	1.78
0.34	45.0	4.76	0.35	0.60	0.05	1.57
0.34	50.0	4.24	0.39	0.58	0.03	1.31
0.50	20.0	9.04	0.30	0.59	0.11	-
0.50	25.0	8.79	0.30	0.61	0.09	-
0.50	27.5	8.82	0.30	0.60	0.09	-
0.50	30.0	5.91	0.29	0.59	0.12	2.82
0.50	35.0	5.64	0.30	0.59	0.11	2.67
0.50	40.0	5.35	0.31	0.59	0.09	2.47
0.50	45.0	5.20	0.32	0.60	0.08	2.29
0.50	50.0	4.98	0.33	0.60	0.07	2.09
0.71	20.0	9.11	0.29	0.59	0.12	-
0.71	25.0	6.11	0.27	0.57	0.15	2.91
0.71	27.5	6.05	0.28	0.58	0.15	2.88
0.71	30.0	5.98	0.28	0.58	0.14	2.85
0.71	35.0	5.83	0.29	0.58	0.14	2.81
0.71	40.0	5.69	0.29	0.58	0.13	2.80
0.71	45.0	5.62	0.30	0.58	0.12	2.75
0.71	50.0	5.55	0.30	0.59	0.11	2.74
0.94	20.0	9.11	0.29	0.58	0.12	-
0.94	25.0	6.12	0.27	0.55	0.17	2.99
0.94	27.5	6.06	0.27	0.56	0.17	3.00
0.94	30.0	6.03	0.28	0.56	0.17	2.99
0.94	35.0	5.98	0.28	0.56	0.16	2.99
0.94	40.0	5.93	0.28	0.56	0.15	2.99
0.94	45.0	5.88	0.28	0.57	0.15	2.99
0.94	50.0	5.83	0.29	0.57	0.14	2.98
1.10	20.0	9.15	0.29	0.58	0.13	-
1.10	25.0	6.12	0.27	0.55	0.18	3.02
1.10	27.5	6.11	0.27	0.55	0.18	3.02
1.10	30.0	6.10	0.27	0.55	0.18	3.01
1.10	35.0	6.06	0.27	0.55	0.17	3.01
1.10	40.0	6.03	0.28	0.56	0.17	3.01
1.10	45.0	5.99	0.28	0.56	0.16	3.00
1.10	50.0	5.97	0.28	0.56	0.16	3.00
1.30	20.0	6.19	0.27	0.54	0.19	3.03
1.30	25.0	6.18	0.27	0.54	0.19	3.01
1.30	27.5	6.18	0.27	0.54	0.19	3.01
1.30	30.0	6.16	0.27	0.54	0.19	3.01
1.30	35.0	6.14	0.27	0.55	0.18	3.01
1.30	40.0	6.12	0.27	0.55	0.18	3.01
1.30	45.0	6.10	0.27	0.55	0.18	3.01
1.30	50.0	6.08	0.27	0.55	0.18	3.01

Table 5.5: A summary of the results of the simulations of collisions of the $4\,M_\oplus$ projectile with the $6.25\,M_\oplus$ target. Full planet data is given in Table 5.1, the rest of the collision results are in Tables 5.2, 5.3, 5.4, and 5.6.

b	v	$M_{\rm LR}$	$f_{\rm Fe}$	$f_{\rm Si}$	$f_{\rm H}$	$M_{\rm SLR}$
	$\rm km\,s^{-1}$	$M_\oplus$				$M_\oplus$
0.00	20.0	9.73	0.31	0.62	0.08	-
0.00	25.0	9.69	0.31	0.62	0.07	-
0.00	30.0	9.40	0.32	0.63	0.05	-
0.00	35.0	8.32	0.36	0.60	0.04	-
0.00	40.0	7.11	0.42	0.56	0.03	-
0.00	45.0	5.45	0.44	0.55	0.01	-
0.00	50.0	3.70	0.53	0.47	-	-
0.10	20.0	9.83	0.30	0.61	0.09	-
0.10	25.0	9.62	0.31	0.62	0.07	-
0.10	27.5	9.51	0.31	0.63	0.06	-
0.10	30.0	9.41	0.32	0.63	0.05	-
0.10	35.0	8.42	0.35	0.61	0.04	-
0.10	40.0	7.20	0.41	0.57	0.02	-
0.10	50.0	3.08	0.53	0.47	-	0.13
0.34	20.0	9.96	0.30	0.60	0.10	-
0.34	25.0	9.68	0.31	0.62	0.07	-
0.34	27.5	9.52	0.31	0.63	0.06	-
0.34	30.0	9.27	0.32	0.64	0.04	-
0.34	35.0	5.50	0.31	0.62	0.07	3.62
0.34	40.0	5.05	0.33	0.61	0.05	2.91
0.34	45.0	4.49	0.37	0.60	0.04	2.44
0.34	50.0	3.86	0.42	0.56	0.02	2.13
0.50	20.0	10.01	0.30	0.60	0.10	-
0.50	25.0	9.74	0.31	0.62	0.08	-
0.50	27.5	9.45	0.32	0.63	0.06	-
0.50	30.0	5.75	0.30	0.60	0.11	3.94
0.50	35.0	5.56	0.30	0.60	0.10	3.73
0.50	40.0	5.28	0.32	0.60	0.08	3.51
0.50	45.0	5.01	0.33	0.60	0.07	3.31
0.50	50.0	4.83	0.34	0.60	0.06	3.11
0.71	20.0	10.09	0.30	0.60	0.11	-
0.71	25.0	9.97	0.30	0.60	0.10	-
0.71	27.5	5.95	0.28	0.58	0.14	3.96
0.71	30.0	5.89	0.28	0.58	0.14	3.93
0.71	35.0	5.75	0.29	0.58	0.13	3.86
0.71	40.0	5.62	0.30	0.58	0.12	3.82
0.71	45.0	5.52	0.30	0.59	0.11	3.78
0.71	50.0	5.48	0.30	0.59	0.10	3.74
0.94	20.0	10.16	0.29	0.59	0.11	-
0.94	25.0	6.08	0.27	0.56	0.17	4.02
0.94	27.5	6.04	0.28	0.56	0.17	4.02
0.94	30.0	6.01	0.28	0.56	0.16	4.01
0.94	35.0	5.95	0.28	0.56	0.16	4.00
0.94	40.0	5.90	0.28	0.57	0.15	4.00
0.94	45.0	5.85	0.28	0.57	0.14	4.00
0.94	50.0	5.81	0.29	0.57	0.14	4.00
1.10	20.0	10.07	0.30	0.60	0.11	-
1.10	25.0	6.12	0.27	0.55	0.18	4.03
1.10	27.5	6.10	0.27	0.55	0.18	4.03
1.10	30.0	6.09	0.27	0.55	0.18	4.02
1.10	35.0	6.06	0.27	0.55	0.17	4.01
1.10	40.0	6.02	0.28	0.56	0.17	4.01
1.10	45.0	5.98	0.28	0.56	0.16	4.01
1.10	50.0	5.95	0.28	0.56	0.16	4.01
1.30	20.0	6.18	0.27	0.54	0.19	4.04
1.30	25.0	6.18	0.27	0.54	0.19	4.02
1.30	27.5	6.17	0.27	0.54	0.19	4.01
1.30	30.0	6.17	0.27	0.54	0.19	4.01
1.30	40.0	6.11	0.27	0.55	0.18	4.01
1.30	45.0	6.09	0.27	0.55	0.18	4.01

Table 5.6: A summary of the results of the simulations of collisions of the $5\,M_\oplus$ projectile with the $6.25\,M_\oplus$ target. Full planet data is given in Table 5.1, the rest of the collision results are in Tables 5.2, 5.3, 5.4, and 5.5.

b	v	$M_{\rm LR}$	$f_{\rm Fe}$	$f_{\rm Si}$	$f_{\rm H}$	$M_{\rm SLR}$
	$\rm km\,s^{-1}$	$M_\oplus$				$M_\oplus$
0.00	20.0	10.63	0.31	0.62	0.06	-
0.00	25.0	10.66	0.31	0.62	0.06	-
0.00	30.0	10.40	0.32	0.63	0.05	-
0.00	35.0	9.35	0.36	0.61	0.03	-
0.00	40.0	7.99	0.42	0.56	0.02	-
0.00	45.0	6.25	0.44	0.55	0.01	-
0.00	50.0	4.45	0.52	0.48	-	-
0.10	20.0	10.81	0.31	0.62	0.08	-
0.10	25.0	10.56	0.32	0.63	0.06	-
0.10	27.5	10.47	0.32	0.63	0.05	-
0.10	30.0	10.40	0.32	0.63	0.05	-
0.10	35.0	9.48	0.35	0.61	0.03	-
0.10	40.0	8.08	0.41	0.57	0.02	-
0.10	50.0	4.09	0.51	0.49	-	0.01
0.34	20.0	10.93	0.30	0.61	0.09	-
0.34	25.0	10.67	0.31	0.62	0.07	-
0.34	27.5	10.61	0.31	0.63	0.06	-
0.34	30.0	10.29	0.32	0.64	0.04	-
0.34	35.0	5.36	0.31	0.63	0.06	4.86
0.34	40.0	4.88	0.34	0.62	0.04	4.36
0.34	45.0	4.24	0.38	0.59	0.03	3.71
0.34	50.0	3.52	0.45	0.53	0.02	3.15
0.50	20.0	11.03	0.30	0.61	0.09	-
0.50	25.0	10.72	0.31	0.62	0.07	-
0.50	27.5	10.43	0.32	0.63	0.05	-
0.50	30.0	5.67	0.29	0.61	0.10	4.98
0.50	35.0	5.47	0.30	0.61	0.09	4.83
0.50	40.0	5.16	0.32	0.60	0.07	4.63
0.50	45.0	4.90	0.34	0.60	0.06	4.39
0.50	50.0	4.64	0.35	0.60	0.05	4.20
0.71	20.0	11.08	0.30	0.60	0.10	-
0.71	25.0	10.95	0.30	0.61	0.09	-
0.71	27.5	5.90	0.28	0.58	0.14	5.00
0.71	30.0	5.81	0.29	0.58	0.13	4.99
0.71	35.0	5.66	0.29	0.58	0.12	4.93
0.71	40.0	5.53	0.30	0.58	0.12	4.87
0.71	45.0	5.49	0.30	0.59	0.11	4.83
0.71	50.0	5.42	0.31	0.59	0.10	4.75
0.94	20.0	11.15	0.30	0.60	0.10	-
0.94	25.0	6.04	0.28	0.56	0.17	5.05
0.94	27.5	6.01	0.28	0.56	0.16	5.04
0.94	30.0	5.97	0.28	0.56	0.16	5.03
0.94	35.0	5.92	0.28	0.56	0.15	5.01
0.94	40.0	5.88	0.28	0.57	0.15	5.01
0.94	45.0	5.83	0.29	0.57	0.14	5.00
0.94	50.0	5.79	0.29	0.58	0.14	5.00
1.10	20.0	11.09	0.30	0.60	0.10	-
1.10	25.0	6.10	0.27	0.55	0.18	5.05
1.10	27.5	6.09	0.27	0.55	0.18	5.03
1.10	30.0	6.08	0.27	0.55	0.18	5.03
1.10	35.0	6.05	0.28	0.55	0.17	5.02
1.10	40.0	6.02	0.28	0.56	0.17	5.01
1.10	45.0	5.98	0.28	0.56	0.16	5.01
1.10	50.0	5.94	0.28	0.56	0.16	5.01
1.30	20.0	6.17	0.27	0.54	0.19	5.05
1.30	25.0	6.17	0.27	0.54	0.19	5.02
1.30	27.5	6.17	0.27	0.54	0.19	5.02
1.30	30.0	6.17	0.27	0.54	0.19	5.02
1.30	35.0	6.15	0.27	0.54	0.19	5.01
1.30	40.0	6.12	0.27	0.55	0.18	5.01
1.30	45.0	6.09	0.27	0.55	0.18	5.01
1.30	50.0	6.06	0.27	0.55	0.17	5.01

mass. The new prescription is as follows:

1. For a given collision scenario with a $6.25\,\mathrm{M}_\oplus$ target with 20% atmosphere by mass (M_p, v and b), first calculate the specific kinetic energy of the impact:

$$Q_\mathrm{R} = \frac{1}{2}\mu\frac{v^2}{M_\mathrm{tot}}. \tag{5.22}$$

2. Then calculate the transition velocity between erosive hit-and-run and accretion/disruption events, v_split, which is given by

$$v_\mathrm{split} = \sqrt{\frac{2G(M_\mathrm{t}+M_\mathrm{p})}{b(R_\mathrm{t}+R_\mathrm{p})}}. \tag{5.23}$$

3. If $v < v_\mathrm{split}$ then follow the prescription from Denman et al. (2020), outlined here, otherwise skip to 4.
   (a) Calculate the specific kinetic energy of the transition between the atmosphere loss and core and mantle loss regimes,

$$Q_\mathrm{piv} = \left(\frac{M_\mathrm{tot}}{M_\oplus}\right)\left(-2.45\frac{M_\mathrm{p}}{M_\mathrm{t}} + 14.56\right) \quad [10^6\,\mathrm{J\,kg^{-1}}]. \tag{5.24}$$

   (b) Calculate the catastrophic disruption threshold,

$$Q^*_\mathrm{RD} = c^*\frac{4}{5}\pi\rho_1 G R^2_\mathrm{C1}, \tag{5.25}$$

   where $\rho_1 = 1000\,\mathrm{kg\,m^{-3}}$, and $R_\mathrm{C1} = \left(\frac{3M_\mathrm{tot}}{4\pi\rho_1}\right)^{\frac{1}{3}}$ is the radius of a spherical body with a density of ρ_1 and mass M_tot. We use the value $c^* = 2.52$ predicted by Denman et al. (2020) to determine the catastrophic disruption threshold ($Q^{*(\mathrm{New})}_\mathrm{RD}$), as well as the value $c^* = 1.9$ from Leinhardt & Stewart (2012) for atmosphere-less planets which is used to predict energy dependence in the core and mantle dominated loss regime ($Q^{*(\mathrm{LS12})}_\mathrm{RD}$).

   (c) Then, calculate the specific energy gradient for largest remnant mass for the core and mantle loss regime:

$$m_\mathrm{c\&m} = \frac{-0.5(1+f^\mathrm{t}_\mathrm{H})}{Q^{*(\mathrm{LS12})}_\mathrm{RD}}. \tag{5.26}$$

   where f^t_H is the mass fraction of the target which is atmosphere.

(d) Next, calculate the gradient for the atmosphere loss dominated regime from the core and mantle loss gradient assuming zero impact energy means zero mass loss,

$$m_{\rm atmos} = \frac{m_{\rm c\&m}(Q_{\rm piv} - Q_{\rm RD}^{*(\rm New)}) - 0.5}{Q_{\rm piv}}. \tag{5.27}$$

(e) The next step is to calculate the super-catastrophic disruption threshold ($M_{\rm LR} < 0.1M_{\rm tot}$), we use the Leinhardt & Stewart (2012) method for this,

$$Q_{\rm supercat} = Q_{\rm RD}^{*(\rm New)} - \frac{0.4}{m_{\rm c\&m}}. \tag{5.28}$$

(f) From the above three steps the total mass in the largest remnant must therefore be:

$$\frac{M_{\rm LR}}{M_{\rm tot}} = \begin{cases} m_{\rm atmos}Q_{\rm R} + 1 & 0 < Q_{\rm R} < Q_{\rm piv} \\ \\ m_{\rm c\&m}(Q_{\rm R} - Q_{\rm RD}^{*(\rm New)}) + 0.5 & Q_{\rm piv} < Q_{\rm R} < Q_{\rm supercat}. \end{cases} \tag{5.29}$$

As neither this study nor Denman et al. (2020) probed the super-catastrophic disruption regime we do not predict results here, we recommend the Leinhardt & Stewart (2012) prescription for collisions in this regime.

(g) Finally, the mass of atmosphere in the largest remnant is given by:

$$\frac{M_{\rm LR}^{\rm H}}{M_{\rm t}^{\rm H}} = \begin{cases} 1 + \frac{0.94^2}{4}\left(\frac{Q_{\rm R}}{Q_{\rm piv}}\right)^2 - 0.94\frac{Q_{\rm R}}{Q_{\rm piv}} & \frac{Q_{\rm R}}{Q_{\rm piv}} < 2.12 \\ 0 & \frac{Q_{\rm R}}{Q_{\rm piv}} > 2.12. \end{cases} \tag{5.30}$$

4. If, on the other hand, $v > v_{\rm split}$ then we have an erosive hit-and-run collision and the following process should be used to predict largest remnant mass (note we have not tested the dependencies of these power laws on target mass or target atmosphere fraction):

(a) The total atmosphere mass remaining in the largest remnant is given by

$$\frac{M_{\rm LR}^{\rm H}}{M_{\rm t}^{\rm H}} = -10^{-0.76b+0.18}\log_{10}(Q_{\rm R}) + 10^{-0.54b+1.02}, \tag{5.31}$$

(b) and the mass remaining in the largest remnant is

$$M_{\rm LR} = -10^{-1.11b-8.56}Q_{\rm R} + M_{\rm t}. \tag{5.32}$$

6

Conclusion

6.1 Work in progress and future work

6.1.1 Different Mass targets and atmospheres

The results presented in chapter 5 are only for a single target mass, to generate a more effective scaling law, data for different targets is needed. Following the methods detailed in chapter 5 I have begun accumulating this data, preliminary results are shown in figures 6.1 and 6.2. The two new targets which I have begun simulating so far are a $3.27\,M_{\oplus}$ target with a $0.27\,M_{\oplus}$ atmosphere and a $10.43\,M_{\oplus}$ target with a $3.43\,M_{\oplus}$ atmosphere. These atmosphere masses were chosen following Bern model estimates for atmosphere mass (equation 2.28).

Figure 6.1 compares the mass of the second largest remnant post-collision to the escape velocity derived transition velocity, v_{split}, from chapter 5. Like for the original mass results (centre) the overwhelming majority of collisions that produce a non-negligible second largest remnant have a velocity greater than this transition velocity for all target masses, whereas collisions that don't produce a second largest remnant typically have collision velocities below the transition velocity (unless the collision is sufficiently energetic to disrupt the target). These results further reinforce the use of v_{split} as a model

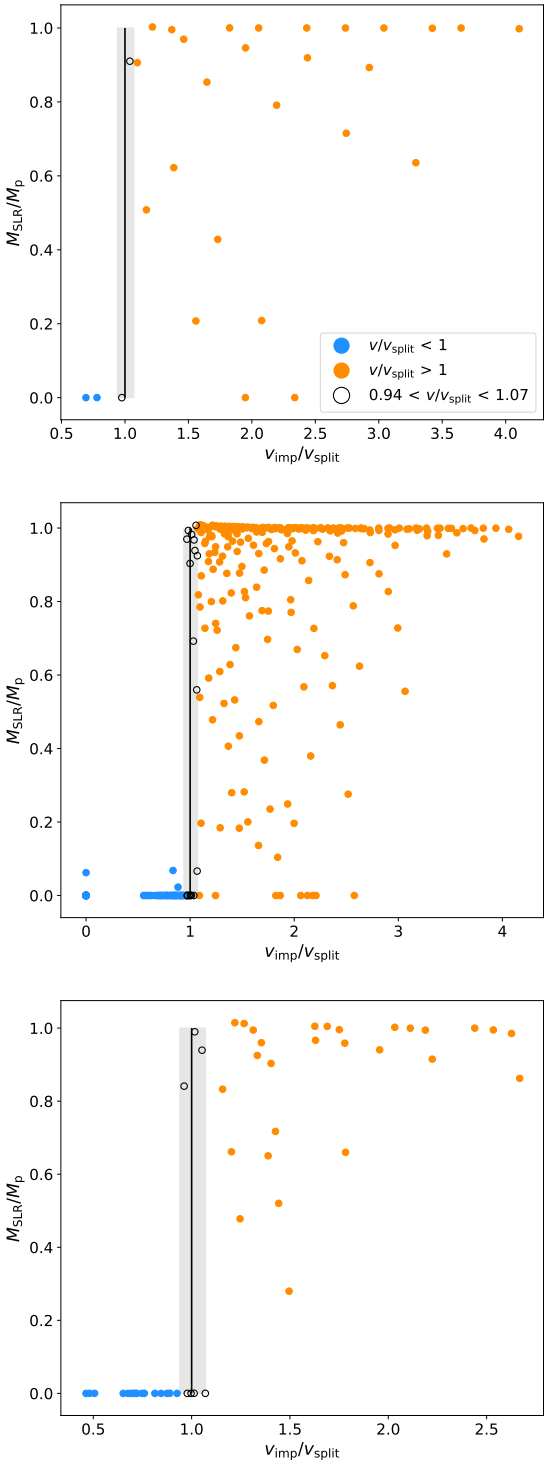

Figure 6.1: Comparisons of the mass of the second largest remnant of the collision to the velocity of transition to hit-and run predicted in chapter 5. Each graph is a different mass target, the top graph is $3.27\,M_\oplus$, the middle graph $6.25\,M_\oplus$ and the bottom graph $10.43\,M_\oplus$. All target masses appear to show a transition to hit-and-run at this velocity.

for the transition to hit-and-run.

Figure 6.2 on the other hand looks at the mass of the largest remnant for erosive hit-and-run collisions. The top graph looks at atmosphere remaining in the largest remnant (as a fraction of initial atmosphere). All target masses appear to follow the same general pattern as the original $5\,M_{\oplus}$ one from chapter 5 of decreasing mass with increasing impact energy following a convex curve. In all cases the higher mass targets lose a smaller atmosphere fraction than the smaller targets, they do however have a larger atmosphere to begin with, so further analysis is required to determine whether the un-normalised rate of mass loss of atmosphere follows the same pattern.

The bottom graph of figure 6.2 shows the total mass of the largest remnant (normalised by target mass). Like for atmosphere mass, the general pattern of a linear dependence of mass on impact energy appears to be true for all target masses. Unlike for atmosphere mass however, the effect of changing target mass is less clear. For the two higher impact angles a greater initial target mass results in a larger final loss, but for the lower impact angles the reverse is true. Potentially this is because of the thicker atmosphere of the largest target, which would dampen the effect of shockwaves through the core, but potentially be easier to directly eject through an atmospheric shock wave.

The next stage of the process with these different mass targets would be to ensure we have enough collisions that we can begin to fit to them, to start to generate scaling laws. It should be noted however, that, like in chapter 4 the targets used here have atmosphere fractions defined by their core and mantle mass. This means that we cannot effectively separate the effects of changing planet mass from changing atmosphere fraction. It would therefore be desirable, before fitting, to also run an array of simulations with different atmosphere fractions but the same core and mantle mass, so that these two effects can be distinguished.

6.1.2 Satellite Formation

Some of the oblique collisions which were run resulted in small chunks of mantle and sometimes core being spun off from the largest remnant. Often this occurred when the collision of the projectile was very oblique and resulted in it extending into a long filamentary structure as it spiralled into the target (see figure 6.3). These chunks were often of the order of the mass of the moon. A closer look at such collisions as a potential

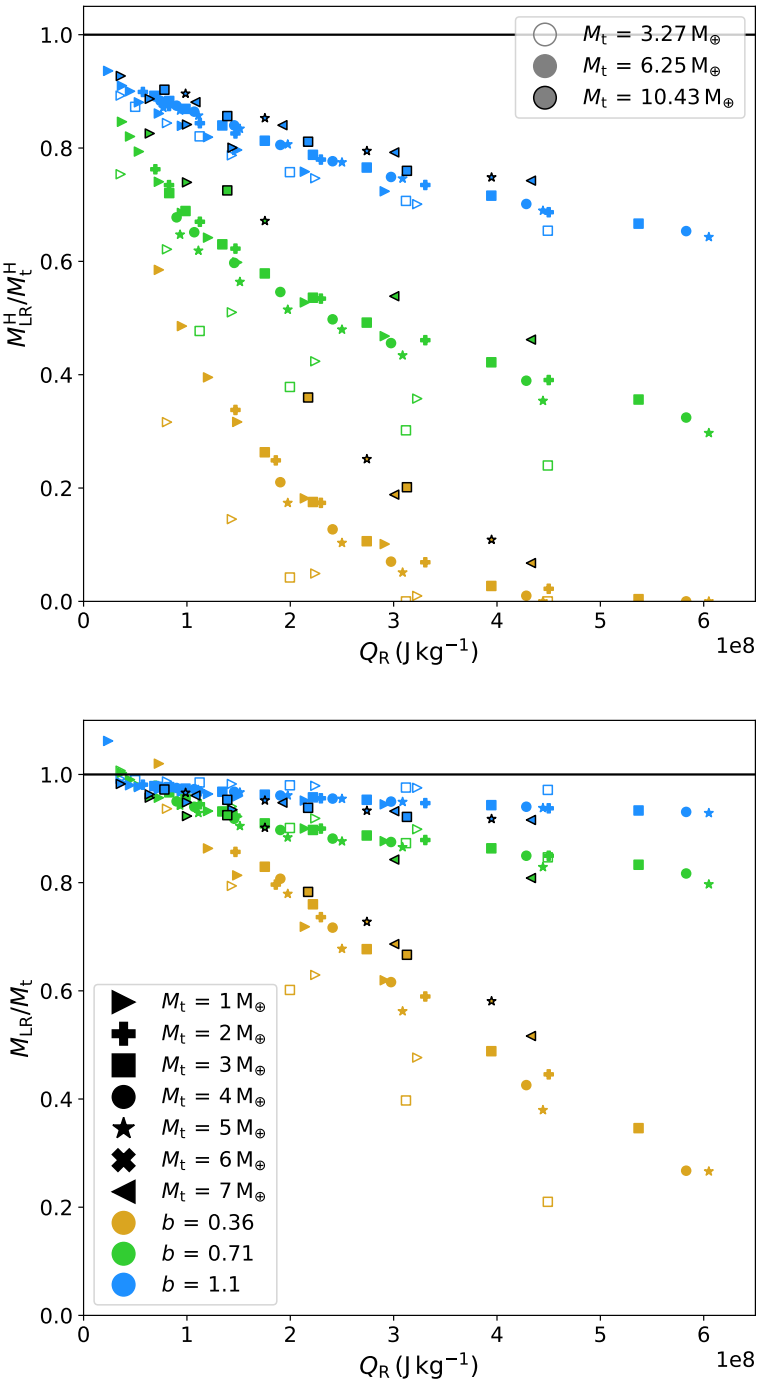

Figure 6.2: The total mass (bottom), and mass of the atmosphere (top) of the largest remnant as a function of specific energy of impact. Colours denote impact angles, shapes projectiles, and outline targets. Larger targets appear to always lose a lower atmosphere fraction, the pattern for total mass loss is less clear however.

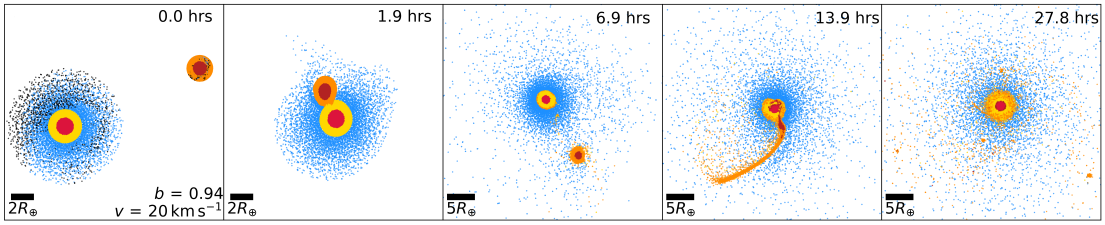

Figure 6.3: A Diagram of a potential satellite forming collision between a $6.25\,M_\oplus$ target and a $2\,M_\oplus$ projectile. This collision initially only barely grazes the target, the projectile gets torn to pieces by tidal forces on its second approach. Some of the clumps stripped off the projectile remain in orbit after the collision has finished.

route for satellite formation would therefore make sense. These moon sized chunks were however typically only of a few hundred particles so to properly look at the phenomenon we would need to run more high resolution collisions. Another difficulty that may arise in further study of this phenomenon is a result from Shimoni et al. (2021). They show in their analysis of collisions between Pluto-like bodies that the rate of formation of such small objects (which they call satellitesimals) can be dependant on choice of equation of state. Their analytic equations of state predicted lower pressure values in the ejecta generated which produced increased satellitesimal formation over their tabulated one. For our particular example cooling and drag from the extended atmosphere are also likely important. It is therefore vital that any further analysis of this region is done with well defined and accurate equations of state.

6.1.3 Tidal Forces from the Star

The strength of gravitational and tidal effects from the central star will be strongly dependent on the star's mass and the orbital distance of the collision. As such we haven't included the effects for the collisions detailed in this thesis as we wished our results to be generalisable to a wide array of different orbits. It should be reasonably easy however to add a modification to the GADGET-2 code which we can use to model a central star. Because GADGET-2 was created for cosmological simulations it can model other particle types which don't behave as fluids such as dark matter which only interacts with its surroundings gravitationally. We could potentially model tidal effects at different distances by using a single such non-interacting particle with a very high mass set at a long distance from other particles modelling the central star.

Including stellar gravity would allow us to model and understand the strength of a variety of effects. For example, for close orbiting planets we would expect them to experience tidal heating from the central star, this could potentially mean material is easier to remove as it is already more energetic.
Accurate modelling of stellar tidal forces will also improve bound material measurements by modelling the planet's Roche lobes (i.e. the regions where their gravitational forces dominate). The size of the Roche lobe is dependent on orbital distance, material that goes outside the Roche lobe is more tightly bound to the central star than to the collision. Closer collisions therefore require less energy to eject material as the Roche lobes are smaller. In terms of our simulations we could more accurately determine what is bound to the largest remnant by removing material that is more strongly bound to the central star as well as material with sufficient kinetic energy to escape to infinity.

6.1.4 Equation Of State

All the simulations in this work so far have used a simplified equation of state for describing the atmosphere. They have used the in-built ideal gas code in GADGET-2. Ideal gases work best at low temperatures and pressures where the particles that make up the gas interact with one another infrequently so the size of particles and elasticity of such collisions is unimportant. When dealing with planetary collisions however, and even dealing with the equilibrium surface pressures at the base of Super-Earth atmospheres, we have significantly higher pressures than ideal gases can effectively cope with.
There are two ways in which this problem can be rectified, either by introducing an analytical equation of state which accounts for the high pressures better, or by using a tabulated equation of state for hydrogen. I have already begun searching for tabulated equations of state to use as an alternative. The main issue I am coming up against at the moment is that none of the tables I have found cover the entire pressure-density range I need. Most of the tabulated hydrogen equation of states I have found were designed for use in stellar atmospheres or in the atmospheres of gas giants (e.g. Saumon et al. 1995), so they typically do not extend out into the low pressure and density regions this work requires to accurately deal with ejected atmosphere.
One potential solution to this that I am experimenting with due to the lack of data is using the ideal gas law to generate results for this low pressure region, as this is the

region where it is most applicable. For this to work I need some way of ensuring that the transition between the original tabulated EOS and this extension region is smooth, so that the transition doesn't create an unphysical phase change.

6.1.5 The effects of Thermal Escape

After a collision any remaining atmosphere (and some of the mantle if it is sufficiently energetic) will remain in a hot extended state around the collision remnant. Because the atmosphere is warm and expanded, the rate of thermal escape from it is significantly increased until it cools back down to equilibrium with its surroundings. Owen & Wu (2016) provide a theoretical model for thermal escape from such expanded atmospheres, their theory was intended to model the warm atmospheres that exist shortly after disc dissipation before they have had a chance to cool, but the same physics holds true here. They model the effects of such loss analogously to a Parker wind. Liu et al. (2015) use the Owen & Wu (2016) results to predict thermal escape losses from their simulations. We would also expect photo-evaporation, which is thermal escape due to XUV heating, to have a stronger effect in such atmospheres as the particles are already higher energy and thus more loosely bound. A full computational analysis of thermal loss would likely require an accurate chemical model of the atmosphere which would require a different sort of simulation to those being used here.

6.2 Conclusion

Overall this work shows that collisions between planets are an important part of their evolution, and they have a significant observable effect on the atmospheres of the planets involved. I shall summarise here what I feel are the most important results:

6.2.1 The Hit-and-Run Transition

Many previous papers have given estimates for where the boundary in impact velocity impact parameter space is, many of these being empirical fits from sets of simulations (e.g. Genda et al. 2012 or Gabriel et al. 2020). In chapter 5 I show that both these empirical models and my simulation results appear to be strongly correlated with the escape velocity from the point of closest approach of the two colliding objects, i.e the

minimum velocity, $v_{\rm split}$, required for a hit and run collision is:

$$v_{\rm split} = \sqrt{\frac{2G\left(M_{\rm p} + M_{\rm t}\right)}{b\left(R_{\rm p} + R_{\rm t}\right)}} \tag{6.1}$$

where b is impact parameter, $R_{\rm p}$ is the projectile surface radius, $R_{\rm t}$ the target surface radius, and $M_{\rm p}$ and $M_{\rm t}$ are the projectile and target masses respectively. This model implies a physical explanation for the regime boundary. If a projectile planet collides against a target with sufficient velocity to escape at that impact angle, then a significant fraction of it should escape assuming the collision isn't sufficiently energetic to disrupt it completely.

The drag forces experienced by the projectile as it collides with the target do not significantly affect the location of this boundary in either of the two sets of SPH simulations I have analysed with $v_{\rm split}$, despite differences in equation of state. The success of this $v_{\rm split}$ model is likely due to the dominance of gravitational binding forces at this scale (Housen & Holsapple, 1990).

This model has only been tested against a couple of different simulation sets so far both of which were SPH, so the next step should be to increase that range of tests to determine in what circumstances $v_{\rm split}$ is a good model for the hit-and-run boundary. If under greater scrutiny the relation still holds it would indicate that the the physical explanation it implies for the regime boundary is true.

6.2.2 Atmosphere Removal via Impact

All of the simulations which included atmosphere in this work showed at least some atmosphere erosion, this was true for both head-on collisions (chapter 4) and also those at higher impact angles (chapter 5). This is due to atmospheres being low density (compared to other planet constituents) and high up a planet's potential, meaning it takes less energy to remove them compared to core or mantle material. This leads to the interesting result for higher impact parameter collisions that 'true hit-and-run collisions' i.e those where the projectile erodes a negligible amount of the target and bounces away (Leinhardt & Stewart, 2012) are very unlikely due to how weakly bound the atmosphere is. When a projectile has sufficient energy to escape the target post collision we instead observe 'erosive hit-and-run' collisions where the target loses at least some small amount of mass (the majority of which is atmosphere).

In chapter 5 our best fit relation for atmosphere mass retained by the largest remnant as a function of energy does imply a non-zero minimum energy required for atmosphere to be lost. This implies that atmosphere loss is not a certainty. This energy is likely proportional to the minimum energy required to remove an atmosphere particle from its initial bound position to infinity, so our result may end up being dependent on simulation resolution. It should also be noted however, that collisions of this low an energy may be physically unlikely to occur, because the slowest speed a collision can occur between two planets is the mutual escape velocity to outside each others area of gravitational influence (for planets with a significant size difference this distance is the target's Hill sphere).

Despite the ease in which this work shows that collisions can remove at least some of the atmosphere, we also show that it is difficult for them to remove all of it. In chapter 4, for example, we show that for all the atmosphere to be removed it requires sufficient energy for catastrophic disruption, i.e the largest remnant must be less than half the total mass of the system. In other words, for the entire atmosphere to be removed by a collision the planet's mantle must also be significantly eroded. The simulations outlined in chapter 5 reinforce this result, collisions at higher impact parameters remove less atmosphere that those at lower impact parameters, making total atmosphere removal by a single collision even less likely.

This difficulty in removing the entire atmosphere is due to the mechanical processes which cause atmosphere erosion. Atmosphere erosion is caused by pressure shockwaves propelling particles away from the planet at a sufficient rate to escape its gravitational influence. There are two main shockwaves which need to be considered, those in the atmosphere caused by the projectile passing through it, and those in the core and mantle caused by the mantles colliding.

Atmospheres are much more compressible than mantle and so there is a significant impedance mismatch between the two materials. Because of this, shockwaves in the atmosphere do not cause significant shockwaves in the mantle. This means that the atmosphere behind the planet is effectively shielded by the mantle from these shockwaves. For highly grazing impacts where the mantles do not touch this is the only atmosphere erosion process caused by the collision and so not very much material is removed and all of it is atmosphere.

Shockwaves through the mantle however can produce shockwaves in the atmosphere when they reach the surface if they are sufficiently energetic, energy is still lost however due to the atmosphere's compressibility. These shockwaves can cause atmosphere loss to occur from above anywhere on the planet's surface, not just the impact site. Collisions sufficiently energetic to cause the entire planet's surface to have moved sufficiently to eject all the atmopshere above it are, in all the simulations run in this work, also sufficient to eject a significant fraction of the mantle as well.
In summary, due to the light and compressible nature of gas atmospheres it does not take much impact energy to lose some, but it takes a lot more energy to cause all of the atmosphere to be ejected.

6.2.3 Impacts As a Cause of Density Diversity

Returning to the original observation that inspired this analysis into Super-Earth collisions, can they be a cause of the large observed diversity in density of planets of this mass range?
Many of the systems we have observed so far with multiple Super-Earths have them orbiting close to, but just outside resonance (Fabrycky et al., 2014). Because of these observations one common theory of Super-Earth formation is that Super-Earths generally migrate inwards and get trapped in resonant orbits while the protoplanetary disc is present. When the disc dissipates, its circularising effects on the planets orbiting within is removed and these resonant chains can become unstable (Izidoro et al., 2017). In this stage of planet formation (the 'giant impact' phase), collision between neighbouring planets is thought to be common.
In the case of observation we also find systems where one or more collision provides the best possible explanation for the observed density. In cases such as Bonomo et al. (2019) for example, where they observe the Kepler-107 system and an inner planet (Kepler-107b) is less dense than an outer one (Kepler-107c), the density difference cannot be caused by other phenomena such as photo-evaporation because they would imply that the closer orbiting planet be more dense. Our simulations for this paper (outlined in chapter 3) show that it is possible for one or more collisions to have caused the enriched density of Kepler-107c.
The simulations in chapters 4 and 5 looked at collisions where the target planet had

an atmosphere but the projectile did not. In all of these collisions the resulting largest remnant ended up with a smaller atmosphere fraction meaning they would be denser than the target. This was in part because in all the simulated collisions at least some atmosphere was removed from the target, and in some of them denser core and mantle material from the projectile was accreted. The effects of mantle fraction change weren't considered in either of these chapters, but they likely would have increased the density enrichment per collision, as after atmosphere, mantle is the next most likely material to be removed, and it is less dense than iron.

For higher impact angle collisions in chapter 5 it was possible for the projectile to gain some atmosphere during the collision (The largest mass atmosphere gained being $> 0.1M_{\oplus}$), meaning it is also possible for planets to become less dense after a collision. Not all the atmosphere mass lost is accreted by the projectile however, so if the the period of orbital instability post gas-disc dissipation is sufficiently long for the planets in a system to undergo multiple collisions with neighbours of different sizes we would still expect the overall effect to be on average atmosphere loss and density enrichment.

Overall the simulations in this work show that because collisions will always preferentially eject lighter material higher up a potential well, they will tend to have an enriching effect on the densities of planets involved. Collisional events are far more stochastic than other effects like photo-evaporation (the strength of which is dependent on incident radiation) meaning that neighbouring planets in the same solar system can have very different collisional histories. Collisions are therefore an important process in creating the diversity in density we have observed in Super-Earth mass planets.

Bibliography

Abe Y., Matsui T., 1986, Journal of Geophysical Research, 91, E291

Alexander R. D., Clarke C. J., Pringle J. E., 2006a, Monthly Notices of the Royal Astronomical Society, 369, 216

Alexander R. D., Clarke C. J., Pringle J. E., 2006b, Monthly Notices of the Royal Astronomical Society, 369, 229

Alibert Y., Mordasini C., Benz W., Winisdoerffer C., 2005, Astronomy and Astrophysics, 434, 343

Armitage P. J., 2007, eprint arXiv:astro-ph/0701485

Armitage P. J., 2010, Astrophysics Of Planet Formation. Cambridge University Press, Cambridge

Asphaug E., 2010, Chemie der Erde, 70, 199

Asphaug E., 2014, Annual Review of Earth and Planetary Sciences, 42, 551

Bai X. N., 2013, The Astrophysical Journal, 772

Bai X. N., Stone J. M., 2013, The Astrophysical Journal, 769

Barnes R., Raymond S. N., 2004, The Astrophysical Journal, 617, 569

Benneke B., et al., 2019, The Astrophysical Journal, 887, L14

Benz W., Asphaug E., 1999, Icarus, 142, 5

Benz W., Slattery W. L., Cameron A. G., 1988, Icarus, 74, 516

Bitsch B., Morbidelli A., Johansen A., Lega E., Lambrechts M., Crida A., 2018, Astronomy and Astrophysics, 612, 1

Blum J., Wurm G., 2008, Annual Review of Astronomy and Astrophysics, 46, 21

Blum J., et al., 2000, Physical Review Letters, 85, 2426

Bodenheimer P., Stevenson D. J., Lissauer J. J., D'Angelo G., 2018, The Astrophysical Journal, 868, 138

Bonomo A. S., et al., 2019, Nature Astronomy, 3, 416

Cameron A., Ward W., 1976, in Abstracts of the Lunar and Planetary Science Conference, volume 7. p. 120

Carter P. J., Leinhardt Z. M., Elliott T., Stewart S. T., Walter M. J., 2018, Earth and Planetary Science Letters, 484, 276

Carter P. J., Lock S. J., Stewart S. T., 2019, Replication Data for: "The energy budgets of giant impacts", doi:10.7910/DVN/YYNJSX, https://doi.org/10.7910/DVN/YYNJSX

Carter P. J., Lock S. J., Stewart S. T., 2020, Journal of Geophysical Research: Planets, 125, 1

Chambers J. E., 2001, Icarus, 152, 205

Chambers J. E., 2013, Icarus, 224, 43

Chau A., Reinhardt C., Helled R., Stadel J., 2018, The Astrophysical Journal, 865, 35

Ćuk M., Stewart S. T., 2012, Science, pp 1047–1053

Davies E. J., Carter P. J., Root S., Kraus R. G., Spaulding D. K., Stewart S. T., Jacobsen S. B., 2020, Journal of Geophysical Research: Planets, 125, 1

Demory B. O., et al., 2016, Nature, 532, 207

Denman T. R., Leinhardt Z. M., Carter P. J., Mordasini C., 2020, Monthly Notices of

the Royal Astronomical Society, 496, 1166

Denman T. R., Leinhardt Z. M., Carter P. J., submitted 2021, Submitted to 'Monthly Notices of the Royal Astronomical Society'

Draine B. T., 2003, The Astrophysical Journal, 598, 1026

Dullemond C. P., Hollenbach D., Kamp I., D'Alessio P., 2007, in , Protostars and Planets V. University of Arizona Press, Chapt. VI: Circumstellar Disks, pp 555–572 (arXiv:0602619), http://arxiv.org/abs/astro-ph/0602619

Ebel D. S., Stewart S. T., 2018, in , Mercury. Cambridge University Press, Chapt. 18, pp 497–515 (arXiv:1712.08234), doi:10.1017/9781316650684.019, https://www.cambridge.org/core/product/identifier/9781316650684{%}23CN-bp-18/type/book{_}part

Elkins-Tanton L. T., 2012, Annual Review of Earth and Planetary Sciences, 40, 113

Elkins-Tanton L. T., Seager S., 2008, The Astrophysical Journal, 685, 1237

Emsenhuber A., Asphaug E., 2019a, The Astrophysical Journal, 875, 95

Emsenhuber A., Asphaug E., 2019b, The Astrophysical Journal, 881, 102

Fabrycky D. C., et al., 2014, The Astrophysical Journal, 790

Fang J., Margot J. L., 2013, The Astrophysical Journal, 767, 115

Fraine J., et al., 2014, eprint arXiv:1409.8349

Freedman R. S., Lustig-Yaeger J., Fortney J. J., Lupu R. E., Marley M. S., Lodders K., 2014, The Astrophysical Journal, Supplement Series, 214, 25

Fressin F., et al., 2013, The Astrophysical Journal, 766, 81

Gabriel T. S. J., Jackson A. P., Asphaug E., Reufer A., Jutzi M., Benz W., 2020, The Astrophysical Journal, 892, 40

Gardiner C., 2015, Blue Crystal Phase 3, https://www.acrc.bris.ac.uk/acrc/phase3.htm

Gardiner C., 2017, Blue Crystal Phase 4, https://www.acrc.bris.ac.uk/acrc/phase4.htm

Genda H., Abe Y., 2003, Icarus, 164, 149

Genda H., Kokubo E., Ida S., 2012, The Astrophysical Journal, 744, 4

Gillion M., et al., 2017, Nature, 542, 456

Ginzburg S., Schlichting H. E., Sari R., 2016, The Astrophysical Journal, 825, 29

Goldreich P., 1965, Monthly Notices of the Royal Astronomical Society, 130, 159

Haisch, Jr. K. E., Lada E. A., Lada C. J., 2001, The Astrophysical Journal, 553, L153

Hartmann W. K., Davis D. R., 1975, Icarus, 24, 504

Hirschmann M. M., Withers A. C., 2008, Earth and Planetary Science Letters, 270, 147

Holsapple K. A., Schmidt R. M., 1987, Journal of Geophysical Research, 92, 6350

Housen K. R., Holsapple K. A., 1990, Icarus, 84, 226

Hunten D. M., 1973, Journal of the Atmospheric Sciences, 30, 1481

Hunten D. M., 1982, Planetary and Space Science, 30, 773

Hwang J. A., Steffen J. H., Lombardi J. C., Rasio F. A., 2017a, Monthly Notices of the Royal Astronomical Society, 470, 4145

Hwang J., Chatterjee S., Lombardi J., Steffen J., Rasio F., 2017b, The Astrophysical Journal, 852, 41

Ikoma M., Hori Y., 2012, The Astrophysical Journal, 753

Inamdar N. K., Schlichting H. E., 2015, Monthly Notices of the Royal Astronomical Society, 448, 1751

Inamdar N. K., Schlichting H. E., 2016, The Astrophysical Journal, 817, L13

Izidoro A., Ogihara M., Raymond S. N., Morbidelli A., Pierens A., Bitsch B., Cossou C., Hersant F., 2017, Monthly Notices of the Royal Astronomical Society, 470, 1750

Jeans J. H., 1924, Monthly Notices of the Royal Astronomical Society, 85, 2

Jin S., Mordasini C., Parmentier V., Van Boekel R., Henning T., Ji J., 2014, The Astrophysical Journal, 795, 65

Johansen A., Lambrechts M., 2017, Annual Review of Earth and Planetary Sciences, 45, 359

Kato M., IIjima Y.-i., Arakawa M., Okimura Y., Fujimura A., Maeno N., Mizutani H., 1995, Icarus, 113, 423

Kegerreis J. A., et al., 2018, The Astrophysical Journal, 861, 52

Kegerreis J. A., Eke V. R., Gonnet P., Korycansky D. G., Massey R. J., Schaller M., Teodoro L. F., 2019, Monthly Notices of the Royal Astronomical Society, 487, 5029

Kegerreis J. A., Eke V. R., Catling D. C., Massey R. J., Teodoro L. F. A., Zahnle K. J., 2020, The Astrophysical Journal, 901, L31

Kite E. S., Fegley Jr. B., Schaefer L., Ford E. B., 2020, The Astrophysical Journal, 891, 111

Knutson H. A., et al., 2014, The Astrophysical Journal, 794

Kokubo E., Ida S., 1998, Icarus, 131, 171

Kokubo E., Ida S., 2000, Icarus, 143, 15

Korycansky D. G., Asphaug E., 2009, Icarus, 204, 316

Kouchi A., Kudo T., Nakano H., Arakawa M., Watanabe N., Sirono S.-i., Higa M., Maeno N., 2002, The Astrophysical Journal, 566, L121

Lambrechts M., Lega E., 2017, Astronomy and Astrophysics, 606

Lammer H., Selsis F., Ribas I., Guinan E. F., Bauer S. J., Weiss W. W., 2003, The Astrophysical Journal, 598, L121

Lee E. J., Chiang E., Ormel C. W., 2014, The Astrophysical Journal, 797

Leinhardt Z. M., Stewart S. T., 2012, The Astrophysical Journal, 745, 79

Linder E. F., Mordasini C., Mollière P., Marleau G. D., Malik M., Quanz S. P., Meyer M. R., 2019, Astronomy and Astrophysics, 623, 1

Liu S. F., Hori Y., Lin D. N., Asphaug E., 2015, The Astrophysical Journal, 812, 164

Lock S. J., Stewart S. T., 2017, Journal of Geophysical Research: Planets, 122, 950

Lock S. J., Stewart S. T., Petaev M. I., Leinhardt Z., Mace M. T., Jacobsen S. B., Cuk M., 2018, Journal of Geophysical Research: Planets, 123, 910

Lock S. J., Stewart S. T., Ćuk M., 2020, Earth and Planetary Science Letters, 530, 115885

Lopez E. D., Fortney J. J., 2013, The Astrophysical Journal, 776, 2

Lopez E. D., Fortney J. J., 2014, The Astrophysical Journal, 792, 1

Lopez E. D., Fortney J. J., Miller N., 2012, The Astrophysical Journal, 761, 59

Lynden-Bell D., Pringle J. E., 1974, Monthly Notices of the Royal Astronomical Society, 168, 603

Lyra W., Paardekooper S. J., Mac Low M. M., 2010, The Astrophysical Journal Letters, 715, 68

Madhusudhan N., 2019, Annual Review of Astronomy and Astrophysics, 57, 617

Marcus R. A., Stewart S. T., Sasselov D., Hernquist L., 2009, The Astrophysical Journal, 700, 118

Marcus R. A., Sasselov D., Stewart S. T., Hernquist L., 2010, The Astrophysical Journal Letters, 719, 45

Masset F. S., Morbidelli A., Crida A., Ferreira J., 2006, The Astrophysical Journal, 642, 478

Matsui T., Waza T., Kani K., Susuku S., 1982, Journal of Geophysical Research, 87, 10968

Mayor M., Queloz D., 1995, Nature, 378, 355

Melosh H. J., 2007, Meteoritics and Planetary Science, 42, 2079

Melosh H. J., Vickery A. M., 1989, Nature, 338, 487

Mills S. M., Fabrycky D. C., Migaszewski C., Ford E. B., Petigura E., Isaacson H., 2016, Nature, 533, 509

Mizuno H., 1980, Progress of Theoretical Physics, 64, 544

Monaghan J. J., 1997, Journal of Computational Physics, 136, 298

Monaghan J. J., Gingold R. A., 1983, Journal of Computational Physics, 52, 374

Morbidelli A., Lambrechts M., Jacobson S., Bitsch B., 2015, Icarus, 258, 418

Mordasini C., 2018, in , Handbook of Exoplanets. Springer International Publishing, pp 2425–2474 (arXiv:1804.01532), doi:10.1007/978-3-319-55333-7_143

Mordasini C., Alibert Y., Klahr H., Henning T., 2012, Astronomy and Astrophysics, 547, 1

Mordasini C., Klahr H., Alibert Y., Miller N., Henning T., 2014, Astronomy and Astrophysics, 566, A141

Movshovitz N., Nimmo F., Korycansky D. G., Asphaug E., Owen J. M., 2016, Icarus, 275, 85

NASA 2019, Nasa Exoplanet Archive: Confirmed Exoplanets, doi:10.26133/NEA1, https://exoplanetarchive.ipac.caltech.edu/cgi-bin/TblView/nph-tblView?app=ExoTbls{&}config=planets

NASA 2021, NASA Exoplanet Archive: Confirmed Exoplanets, doi:10.26133/NEA1, https://exoplanetarchive.ipac.caltech.edu/cgi-bin/TblView/nph-tblView?app=ExoTbls{&}config=planets

Ogihara M., Kunitomo M., Hori Y., 2020, The Astrophysical Journal, 899, 91

Ormel C. W., Klahr H. H., 2010, Astronomy and Astrophysics, 520, A43

Owen J. E., Wu Y., 2013, The Astrophysical Journal, 775, 1

Owen J. E., Wu Y., 2016, The Astrophysical Journal, 817, 107

Paardekooper S. J., Baruteau C., Crida A., Kley W., 2010, Monthly Notices of the Royal Astronomical Society, 401, 1950

Paardekooper S. J., Baruteau C., Kley W., 2011, Monthly Notices of the Royal Astronomical Society, 410, 293

Parker E. N., 1958, The Astrophysical Journal, 128, 664

Perri F., Cameron A. G., 1974, Icarus, 22, 416

Phillips C., Wang J., Kendrew S., Greene T. P., Hu R., Valenti J., Panero W. R., Schulze J., 2021, eprint arXiv:2109.12132

Pichierri G., Morbidelli A., Crida A., 2018, Celestial Mechanics and Dynamical Astronomy, 130, 1

Piso A. M. A., Youdin A. N., 2014, The Astrophysical Journal, 786

Pollack J. B., Hubickyj O., Bodenheimer P., Lissauer J. J., Podolak M., Greenzweig Y., 1996, Icarus, 124, 62

Raymond S. N., Morbidelli A., 2020, Planet formation: key mechanisms and global models (arXiv:2002.05756), http://arxiv.org/abs/2002.05756

Rogers L. A., Bodenheimer P., Lissauer J. J., Seager S., 2011, The Astrophysical Journal, 738

Safronov V. S., 1972, Evolution of the protoplanetary cloud and formation of the earth and planets. Keter Publishing House, Jerusalem

Sakurai Akira M. I. o. T., 1960, Communications on Pure and Applied Mathematics, 13, 353

Saumon D., Chabrier G., van Horn H. M., 1995, The Astrophysical Journal Supplement Series, 99, 713

Schaefer L., Parmentier V., 2021, eprint arXiv:2108.08387

Schlichting H. E., Mukhopadhyay S., 2018, Space Science Reviews, 214

Schlichting H. E., Sari R., Yalinewich A., 2015, Icarus, 247, 81

Seager S., Sasselov D. D., 2000, The Astrophysical Journal, 537, 916

Sedov L. I., 1946, Prikl. Mat. Mekh, 10, 241

Shimoni Y., Aharonson O., Rufu R., 2021, eprint arXiv:2109.05051, pp 1–15

Shoemaker E. M., Hackman R. J., 1962, Symposium - International Astronomical Union

Sinclair C. A., Wyatt M. C., Morbidelli A., Nesvorný D., 2020, Monthly Notices of the Royal Astronomical Society, 499, 5334

Sotzen K. S., et al., 2021, eprint arXiv:2109.02714

Springel V., 2005, Monthly Notices of the Royal Astronomical Society, 364, 1105

Springel V., Hernquist L., 2002, Monthly Notices of the Royal Astronomical Society, 333, 649

Stewart S. T., Leinhardt Z. M., 2009, The Astrophysical Journal, 691, L133

Stewart S. T., Leinhardt Z. M., 2012, The Astrophysical Journal, 751, 32

Süli Á., 2021, Monthly Notices of the Royal Astronomical Society, 503, 4700

Swain M. R., Estrela R., Sotin C., Roudier G. M., Zellem R. T., 2019, The Astrophysical Journal, 881, 117

Taylor G., 1950, Proceedings of the Royal Society of London, 201, 159

Tsiaras A., et al., 2016, The Astrophysical Journal, 820, 99

Udry S., Santos N. C., 2007, Annual Review of Astronomy and Astrophysics, 45, 397

Valencia D., O'Connell R. J., Sasselov D., 2006, Icarus, 181, 545

Volk K., Gladman B., 2015, The Astrophysical Journal Letters, 806, L26

VonNeumann J., Richtmyer R. D., 1950, Journal of Applied Physics, 21, 232

Wakeford H. R., et al., 2017, Science, 356, 628

Ward W. R., 1986, Icarus, 67, 164

Watt L., Leinhardt Z., Su K. Y. L., 2021, Monthly Notices of the Royal Astronomical Society, 502, 2984

Weber P., Benítez-llambay P., Gressel O., Krapp L., Pessah M. E., 2018, The Astrophysical Journal, 854, 153

Wetherill G. W., Stewart G. R., 1989, Icarus, 77, 330

Williams J. P., Cieza L. A., 2011, Annual Review of Astronomy and Astrophysics, pp 67–118

Wurm G., Blum J., Colwell J. E., 2001, Icarus, 151, 318

Wyatt M. C., Kral Q., Sinclair C. A., 2020, Monthly Notices of the Royal Astronomical Society, 491, 782

Yalinewich A., Remorov A., 2021, eprint arXiv:2107.01701, 11, 1

Yalinewich A., Schlichting H. E., 2018, Monthly Notices of the Royal Astronomical Society, 9, 1

Youdin A. N., Goodman J., 2005, The Astrophysical Journal, 620, 459

Zel'dovich Y. B., Raizer Y. P., 1967, Physics of shock waves and high-temperature hydrodynamic phenomena. New York: Academic Press, New York

Zeng L., Sasselov D., 2013, Publications of the Astronomical Society of the Pacific, 125, 227